Développement d'un procédé innovant d'épuration du biogaz par mise en oeuvre de contacteurs à membranes

Valentin Fougerit

NNT : 2017SACLC053

THESE DE DOCTORAT
DE
L'UNIVERSITE PARIS-SACLAY
PREPAREE A
CENTRALESUPELEC

ECOLE DOCTORALE N° (579)
Sciences mécaniques et énergétiques, matériaux et géosciences

Spécialité de doctorat : Génie des Procédés

Par

Valentin Fougerit

Développement d'un procédé innovant d'épuration du biogaz par mise en œuvre de contacteurs à membranes

Thèse présentée et soutenue à CentraleSupélec (Gif-sur-Yvette), le 17 octobre 2017 :

Composition du Jury :

HEBRARD Gilles	Professeur – INSA Toulouse, LISBP	Président du jury
GOURDON Christophe	Professeur – ENSIACET	Rapporteur
FAVRE Eric	Professeur – ENSIC/Université de Lorraine, LRGP	Rapporteur
ATHES Violaine	Professeure – AgroParisTech	Examinatrice
CHABANON Elodie	Maître de conférences – Université Lyon 1, LAGEP	Examinatrice
PAREAU Dominique	Professeure – CentraleSupélec, LGPM	Examinatrice
STAMBOULI Moncef	Professeur – CentraleSupélec, LGPM	Directeur de thèse
THÉOLEYRE Marc-André	Expert – CentraleSupélec, LGPM	Encadrant - Invité
PERRÉ Patrick	Professeur – CentraleSupélec, LGPM	Invité

To my parents for their unconditional love

To Ninon for our valuable friendship

A mes parents pour leur amour inconditionnel

A Ninon pour notre inestimable amitié

“I never lose. I either win or learn”

“Je ne perds jamais. Soit je gagne, soit j’apprends”

Nelson Mandela

Abstract

Development of an innovative biogas upgrading process by means of membrane contactors

Upgrading is an attractive pathway for biogas utilization. Yet, the costs associated to these processes are still an obstacle to a widespread development, specifically in the case of farm anaerobic digestion units.

This PhD has assessed membrane contactor, a technology derived from the artificial lung, for the development of a robust gas-liquid physical absorption process meeting the biogas industry expectations. A modular experimental pilot ($150 - 880\ NL_{biogas}.h^{-1}$) was designed to investigate the performances in terms of methane recovery R_{CH_4} and methane quality $y_{CH_4}^{out}$.

The membrane contactor technology turned out to be suitable to produce a gas-grid quality biomethane. Key operating parameters were identified through a Design of Experiments. Among known process limitations, membrane wetting was found to have little influence on CO_2 absorption (< 10.5%): a new pore wetting description was suggested. Gas composition was a stronger limitation: the CO_2 mass transfer coefficient was divided by a factor 2-3 in the presence of a gas mixture instead of as a pure gas. Process configurations and solvents were successively tested to improve the performances. The addition of a methane recycling loop and the replacement of water by a saline solution (KCl) were combined into a patent and reached the targeted performances ($R_{CH_4} = 98.7\%$, $y_{CH_4}^{out} = 97.5\%$): the corresponding absorbed flux is $42\ NL_{CO_2}.m^{-2}.h^{-1}$. Furthermore, the estimated process energy consumption is competitive with established technologies ($0.225\ kWh.Nm_{biogas}^{-3}$).

For a process upscaling purpose, an original mass transfer model was developed to describe the specific internal geometry of the membrane module. Firstly optimized and validated for the absorption of pure CO_2, this numerical tool has required an optimized additional correction inspired from diffusion laws to account for the mass transfer limitation observed for a binary gas mixture.

Process designs are suggested for 3 industrial cases (100, 250 and 500 $Nm_{biogas}^3.h^{-1}$) based on an available membrane contactor range. The process sizings resulting from the dimensional analysis methodology or numerical simulation differ from 25 to 40 % and must then be confirmed.

Keywords: Biogas upgrading; Gas-liquid absorption; Membrane contactor; Mass Transfer

Résumé

Développement d'un procédé innovant d'épuration du biogaz par mise en œuvre de contacteurs à membranes

L'épuration est une solution attractive pour la valorisation du biogaz. Néanmoins, les coûts associés à ces procédés constituent un frein au développement, en particulier pour l'épuration du biogaz d'origine agricole.

Ces travaux ont évalué le contacteur à membranes, technologie issue du poumon artificiel, pour le développement d'un procédé d'absorption physique, robuste et répondant aux exigences de la filière. Un pilote expérimental modulaire ($150 - 880\ NL_{biogaz}.h^{-1}$) a permis d'investiguer les performances du procédé en termes de rendement méthane R_{CH_4} et de qualité méthane $y_{CH_4}^{out}$.

Le contacteur à membranes permet de produire un biométhane répondant aux spécifications de l'injection réseau. Les paramètres opératoires clés ont été mis en évidence par un plan d'expérience. Parmi les limites connues du procédé, l'effet de l'humidification de la membrane sur le débit d'absorption du CO_2 reste limité (< 10.5%) : une nouvelle description de l'humidification des pores a été proposée. La composition du gaz est plus limitante : le coefficient de transfert du CO_2 est divisé par un facteur 2-3 lorsque celui-ci est présent en mélange plutôt qu'en gaz pur. Plusieurs configurations et solvants ont été testés pour améliorer les performances. L'intégration d'une boucle de recyclage et le remplacement de l'eau par une solution de sels (KCl) ont permis de déployer un procédé breveté atteignant les performances visées ($R_{CH_4} = 98.7\%$, $y_{CH_4}^{out} = 97.5\%$) : le flux membranaire est de $42\ NL_{CO_2}.m^{-2}.h^{-1}$. En outre, la consommation énergétique estimée du procédé est compétitive comparée à celle des procédés d'épuration disponibles ($0.225\ kWh.Nm_{biogas}^{-3}$).

En vue d'un dimensionnement industriel, un modèle original de transfert a été développé pour intégrer la géométrie interne spécifique du module membranaire. Optimisé et validé pour l'absorption de CO_2 pur, cet outil numérique a nécessité l'optimisation d'une correction additionnelle inspirée des lois de diffusion pour décrire la limite observée en présence d'un mélange de gaz.

Une mise à l'échelle est proposée pour 3 unités industrielles (100, 250 et $500\ Nm_{biogaz}^3.h^{-1}$) sur la base des équipements disponibles. Les dimensionnements obtenus par analyse dimensionnelle ou par modélisation numérique diffèrent de 25 à 40 % et doivent encore être validés.

Mots-clés : Epuration de biogaz ; Absorption gaz-liquide ; Contacteurs à membranes ; Transfert de matière

Contents

List of Figures

List of Tables

Nomenclature

Latin symbols

a	Specific exchange area
a_{P^i}	Effect of parameter P^i in the DoE
A_i	Absorption factor of specie i
c_p	Specific heat capacity
C_i^{φ}	Volumic molar concentration of component i in phase φ
d	Diameter
d_H	Hydraulic diameter
D_A^{φ}	Diffusivity of solute A in the phase φ
D_{AB}	Gaseous diffusivity of specie A in specie B
f_i^{φ}	Fugacity of component i in the phase φ
$FC_{1\to2}$	Mass flowmeter correction factor
Gz	Graetz number
H^{cc}	Henry coefficient relative to liquid and gas molar concentrations
ΔH_{dis}	Enthalpy of dissolution
ΔH_r	Enthalpy of reaction
HTU	Height of a Transfer Unit
J_{i}^{abs}/J_i	Absorbed flux of component i through the membrane
Kn	Knudsen number
$K_{\varphi,i}^0$	Overall mass transfer coefficient of specie i relative to the phase φ in $mol.m^{-2}.s^{-1}$
$K_{\varphi,i}$	Overall mass transfer coefficient of specie i relative to the phase φ in $m.s^{-1}$ ($i = CO_2$ if not specified)
$k_{\varphi,i}$	Mass transfer coefficient of specie i relative to the resistance of the phase φ in $m.s^{-1}$
k_H^{px}	Henry coefficient relative to gas partial pressure and liquid molar fraction
k	Membrane shape coefficient
$l_{pore,eff}$	Effective pore length
$l_{pore,wet}$	Wetted length of the pore
L_f	Length of the fiber
m_i	Partition coefficient of component i
M_i	Molar mass of specie i
n_i	Molar quantity of specie i
N_A	Molar flux of specie A
N_f	Number of fibers
NTU	Number of Transfer Units
P_{model}	Precision of the model
P_i	Gas partial pressure of component i
P_{φ}	Total pressure of phase φ
ΔP	Transmembrane pressure
q_g	Gas mass flowrate
Q_g	Gas volumetric flowrate
Q_i^P	Membrane permeability relative to component i
Q_l	Liquid flowrate
r	Radius

r_i	Source term of specie i
R	Ideal gas constant
R_i/R_o	Inner/Outer radius of the fiber bundle
R_{CH_4}	Methane recovery rate
R_φ	Mass transfer resistance of the phase φ
Re	Reynolds number
se_{P^i}	Standard error of the effect of parameter P^i
S	Exchange area
S_i	Solubility of component i
Sc	Schmidt number
Sh	Sherwood number
t_0	Time at which humidification starts
Δt	Time laps during which humidification occurs
T_φ	Temperature of phase φ
T_g	Glass transition temperature
T_m	Melting temperature
$\overrightarrow{u_\varphi}$	Velocity of the phase φ
U	Electric voltage
$W_{process}$	Process energy consumption
x_i	Molar fraction of component i in the liquid phase
Δx	Mass transfer potential
X	Reduced CO_2 molar fraction in the liquid phase
y_i	Molar fraction of component i in the gas phase
Y	Reduced CO_2 molar fraction in the gas phase
Z	Height of mass exchanger

Greek symbols

α	Process selectivity
β	Parameter of the DoE test table
γ	Surface tension
Γ	Sizing margin factor
δ	Thickness
ε	Porosity
$\varepsilon_{bed,\varphi}$	Porosity of the porous medium related to phase φ
ε_{rel}	Relative error
$\zeta_{is/poly}$	Isentropic/Polytropic compressor efficiency
η	Membrane wetting fraction
θ	Contact angle
Θ_i	Fugacity coefficient of component i
$\overline{\overline{\kappa_\varphi}}$	Permeability tensor of the porous medium related to phase φ
λ	Molecule mean free path
Λ	Numerical optimization factor
Φ	Packing fraction in the bundle of fibers (%)
μ_i^φ	Chemical potential of component i in the phase φ
μ_φ	Dynamic viscosity of phase φ
ν	Kinematic viscosity
ξ_i	Specie i mass imbalance
Ξ	Membrane selectivity
π_{CO_2/CH_4}	Solvent selectivity of CO_2 against CH_4
ρ	Volumetric mass density
σ	Geometric standard deviation
σ_{model}	Mean squared error of the DoE model
τ	Tortuosity
ψ_i	Loading rate of the gas specie i
Ω	Mass exchanger cross-section area

Superscripts

$*$	Equivalent molar fraction at equilibrium
0	Standard conditions
abs	Relative to the absorbed flow
$bulk$	Relative to the bulk
$corr$	Corrected factor
eff	Effective
$feed$	Relative to the feed side
$ideal$	Relative to an ideal phase
in	Relative to the inlet flow of the biogas upgrading process
$interface$	Relative to the gas-liquid interface
off	Relative to the offgas flow of the biogas upgrading process
out	Relative to the outlet flow of the biogas upgrading process
$perm$	Relative to the permeate side
rec	Relative to the recycling loop
sat	Relative to saturation

Subscripts

bed	Relative to the porous medium
c	Critical
CH_4	Methane
CO_2	Carbon dioxide
dry	Relative to the dry regime
eq	Equivalent
exp	Relative to the experiment
fi	Relative to the hollow fiber inner side
$fiber$	Relative to the hollow fiber
fo	Relative to the hollow fiber outer side
int	Relative to the intermediate degassing step
I	Inert fraction
i	Relative to the gas-liquid interface
$line$	Relative to the process line
m	Relative to the membrane
mod	Relative to the model
ML	Logarithmic mean
p	Relative to the pore
t	Relative to the triple point
th	Theoretical
tot	Total
vac	Relative to vacuum
wet	Relative to the wet regime

Abbreviations

AAS	Amino-Acid Salts
AD	Anaerobic Digestion
CA	Carbonic Anhydrase
CAPEX	Capital Expenditure
CFD	Computational Fluid Dynamics
CHP	Combined Heat and Power
CL	Closed-Loop
CSTR	Continuously Stirred-Tank Reactor
COP 21	21st Conference of the Parties
DEA	Diethanolamine
DGA	Diglycolamine
DoE	Design of Experiments
DETA	Diethylenetriamine
DMPEG	Dimethylether Polyethyleneglycol
EHT	Accelerating voltage
EU	European Union
FS	Full-Scale
GC	Gas Chromatography
GHG	Greenhouse Gas
HTU	Height of Transfer Unit
HFMM	Hollow Fiber Membrane Module
IL	Ionic Liquid
IPCC	Intergovernmental Panel on Climate Change
IR	Infra-Red
IRENA	International Renewable Energy Agency
LCA	Life-Cycle Analysis
LCV	Lower Calorific Value
LNG	Liquefied Natural Gas
LSU	Livestock Unit
MDEA	Methyl diethanolamine
MEA	Monoethanolamine
MeOH	Methanol
NDIR	Non-Dispersive Infra Red
NGV	Natural Gas Vehicle
NMP	N-methyl-2-pyrrolidone
NREAP	National Renewable Energy Action Plan
NS	Not Specified
NTU	Number of Transfer Units
OP	Open-Loop
OPEX	Operational Expenditure
ORC	Organic Rankine Cycle
OS	Organic Scrubbing
PC	Propylene Carbonate
PCC	Post Combustion Capture

PDMS	Polydimethylsiloxane
PEEK	PolyEtherEtherKetone
PEG	Polyethylene Glycol
PEM	Polymer Electrolyte Membrane
PID	Proportional-Integral-Derivative
PP	Polypropylene
PPO	Poly(Phenylene Oxide)
PS	Polysulfone
PSA	Pressure Swing Adsorption
PSO	Particle Swarm Optimization
PTFE	Polytetrafluoroethylene
PVDF	Polyvinylidene fluoride
PVTMS	Polyvinyltrimethylsilane
PZ	Piperazine
RD	Reading value
RES	Renewable Energy Share
RO	Reverse Osmosis
RSD	Relative Standard Deviation
SEM - FEG	Scanning Electron Microscope - Field Emission Gun
SNG	Synthetic Natural Gas
SRB	Sulfate-Reducing Bacteria
TCD	Thermal Conductivity Detector
TEA	Triethanolamine
TEPA	Tetraethylenepentamine
UCV	Upper Calorific Value
UK	United Kingdom
US	United States
VOC	Volatile Organic Compounds
WD	Working Distance
WS	Water Scrubbing

Introduction

The industrial era has brought a growing world energy consumption since 1800. According to the US Energy Administration, this on-going growth has reached $13.84 \times 10^3\ Mtoe$ in 2012 and a forecasted consumption of $20.54 \times 10^3\ Mtoe$ is expected in 2040 (Figure 0.1). Fossil fuels like petrol, coal or natural gas are the main energy sources at use today for their accessibilities and production prices. Though, with a still increasing energy consumption, the fossil fuels are depleting: it leads to a frantic scramble for an access to new fuels deposits such as non-conventional fuels (heavy oil, oil sand, oil shale).

According to Intergovernmental Panel on Climate Change (IPCC) experts, the use of fossil fuels are to be linked with the recent increase observed in the greenhouse gases (GHG) atmospheric measurements (Figure 0.2). It has triggered a global climate change which is expected to reach $2.6 - 4.8\ °C$ by 2100 in a business-as-usual scenario (RCP 8.5[1]) [1]: it could lead to long-lasting devastating effects on human societies (droughts, sea level rise, food production issues, modification of marine and terrestrial ecosystems, new diseases…). Despite these dramatic observations, the world consumption of liquid fuels and natural gas are still on the rise. Therefore, the most important challenge of the upcoming centuries is to shift from a time-limited and carbon-intensive to renewable and carbon-neutral energy production system.

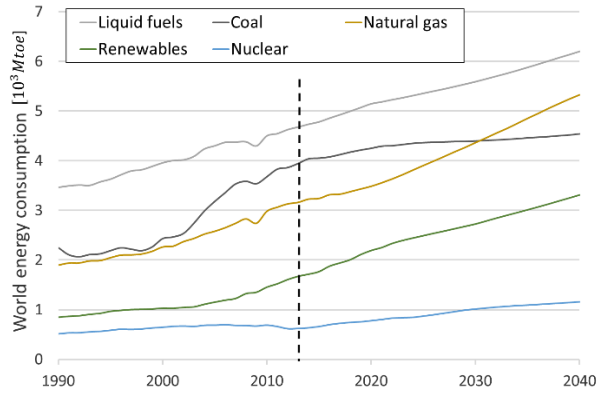

Figure 0.1 – World energy consumption by energy source 1990-2040 (data from [2])

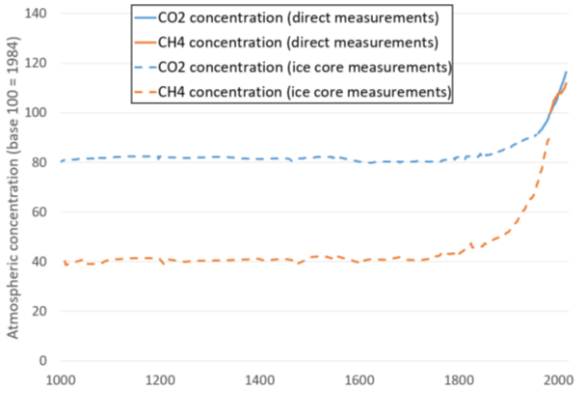

Figure 0.2 – Global atmospheric concentrations of carbon dioxide and methane (data from [3])

Base 100: $CO_2 = 344.58\ ppm$ - $CH_4 = 1656\ ppb$

In this challenge, biomass can offer a base energy production compared to intermittent renewable energies such as solar and wind. The International Renewable Energy Agency (IRENA) estimated that biomass would supply between $2.32 \times 10^3\ Mtoe$ and $3.51 \times 10^3\ Mtoe$ of the world energy consumption by 2030 with low and high scenarii (Figure 0.3). Energy crops hold the highest potential, notably in Latin America. The gap between the two scenarii is explained by a difference in the mobilization of the harvesting residues and processing residues. The development of fuel wood in Europe could also significantly increase the biomass energy supply. These figures are consistent with

[1] Representative Concentration Pathway with a radiative forcing of 8.5 $W.m^{-1}$ in 2100

the 2010 results which estimated that energy crops could supply $0.43 - 2.29 \times 10^3\ Mtoe$ by 2050 [4]. The estimation range is quite large since energy crops development is dependent on global political agreements regarding food security and sustainability. Despite a significant potential, biomass is still relying on political decisions regarding land-use conflicts. Moreover, bioenergy production from non-food crops is in need for administrative framework.

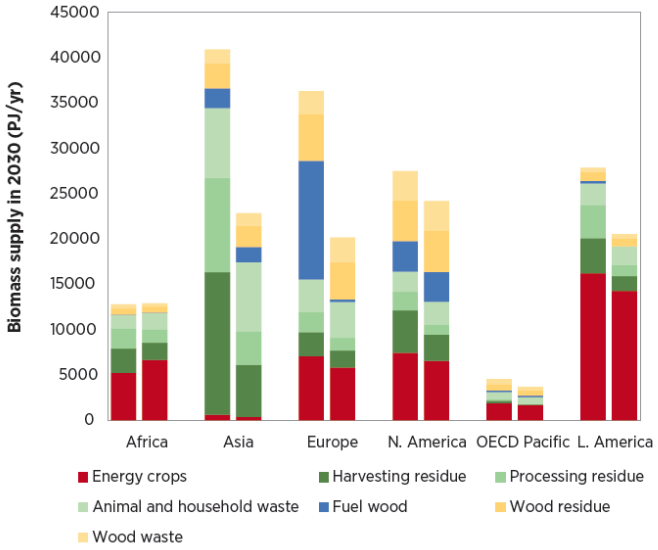

Figure 0.3 – Breakdown of biomass supply by type and region [5] - $1\ PJ = 2.39 \times 10^{-2}\ Mtoe$
Left bar: lower estimate with severe environmental restrictions – Right bar: higher estimate

The depletion of the fossil fuel deposits and the critical need for energy are an opportunity to drastically change our energy production system towards sustainable energies. The use of fossil fuels brought by the industrial era must only by looked at as a parenthesis in energy history (Figure 0.4). In this shift, biomass has a key role to play among renewable energies. Before the 19th century, biomass was used as an animal feed. It was thus essential for work and transportation. In the 21st century, biomass can recover its place in the energy and fuel production system.

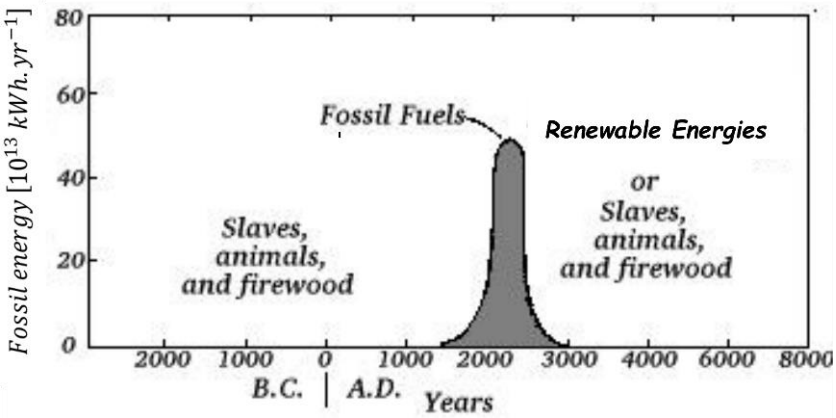

Figure 0.4 – History of fossil energy production systems - $10^{13}\ kWh = 859.8\ Mtoe$

The world agreement reached during the 21st Conference of the Parties (COP 21), recently weakened by the US withdrawal, is a first step towards this shift of paradigm. It must now be enforced

through national policies to lead an energetic transition built on 3 pillars: energy efficiency and consumption reduction, development of renewable energies, reduction of GHG emissions. While wind and solar energies can substitute for fossil fuels (coal, oil, gas and nuclear energy) for electricity generation, the replacement of fossil fuels in the transportation industry is harder to address. Indeed, this sector requires a fuel with a high energetic density and easy handling that only liquid and pressurized gases can offer (Figure 0.5): the volumetric energy density is the most important feature as the space for the fuel tank is limited. In this regard, hydrogen may be restricted to specific applications as it displays a volumetric energy density quite low compared to currently available fuels (despite its very high energy density per mass).

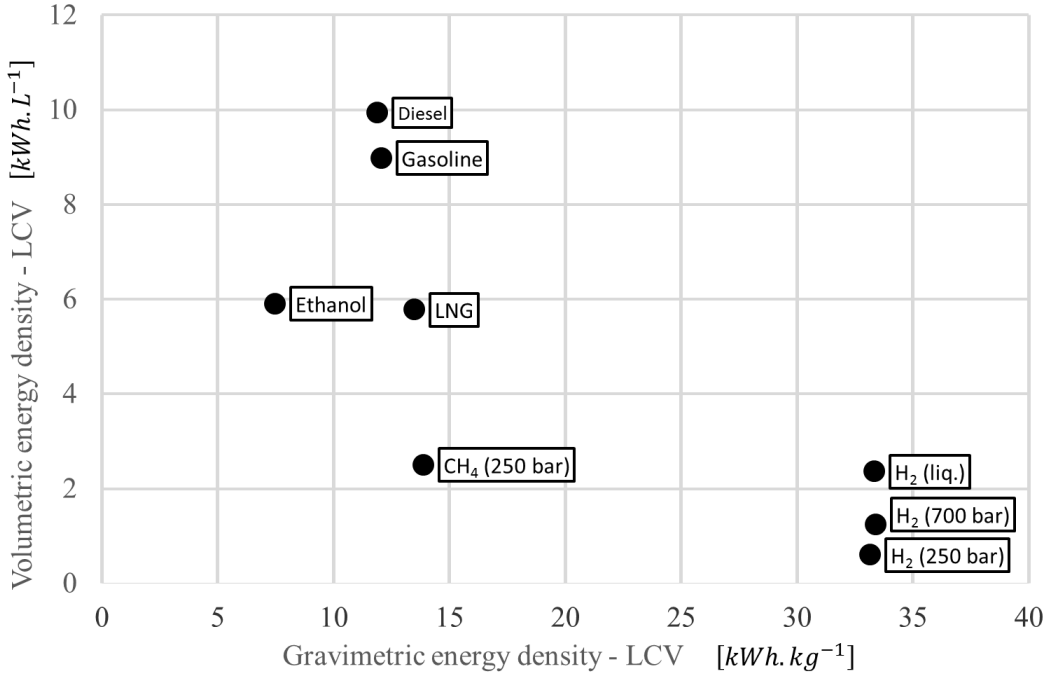

Figure 0.5 – Comparison of energy densities per mass and per volume of several liquid and gaseous fuels (LCV data from [6–8])

Anaerobic digestion (AD) can degrade organic matter into such a storable energy carrier under the form of methane. This biological process was known for long in history. For instance, it was observed in the form of an inflammable gas in marshes. The so-called biogas is essentially composed of methane and carbon dioxide. From the 20th century onward, men tried to get an industrial control over this degradation process for an energy production purpose. Indeed, performing under anaerobic conditions, this biological trophic chain has a low conversion speed. Nonetheless, its ability to treat a wide range of waste type such as agricultural waste, bio-waste or industrial waste makes it an attractive solution which also produces a high quality agricultural amendment. The produced biogas can be upgraded into biomethane by the separation of methane from carbon dioxide. Reaching a high methane purity, biomethane is comparable to natural gas. It then represents an attractive alternative to this fossil fuel.

Process engineering is the science designing, controlling and optimizing the transformation of fluxes into a complex system composed of unit operations. It is here a key field to take the full benefits from anaerobic digestion and bring biomass energy production to its complete potential. Process engineering works indeed at the intensification and robustness of the anaerobic digestion unit. Furthermore, this science applies to separation techniques, and has proved useful in the development of biogas upgrading processes. Process engineering tools were thus adopted in this PhD to set-up an innovative, robust and cost-effective separation process by means of membrane contactors.

The research and process developments carried out during the PhD are presented in this manuscript in the form of 5 chapters.

Chapter 1 presents the state-of-the-art relative to the different topics approached in this PhD work. As a starting point, energy production from anaerobic digestion is discussed with a general approach. Having identified biogas upgrading as key in the value chain, the available and emerging technologies are compared from economical and technical indicators based on a literature review. This introduction set the objectives for the research project. In the view of developing an absorption process utilizing hollow fiber membrane contactors, a literature review of the solvent applicable to the CO_2/CH_4 separation is carried out. At last, methods from process engineering are presented with the aim of a quick industrial upscaling of the developing process. With this regard, a focus is made on the mass transfer modelling strategies to build up a reliable numerical model.

Chapter 2 presents the experimental apparatus and related methods to characterize the state and the performances of the biogas upgrading process. At first, the membrane module used throughout the experimental work is described and characterized. The pilot process equipment with its regulation is then extensively described. A focus is brought on the analytical devices relative to the gas phase. In the end, the methods utilized for the characterization of the process performances and state are detailed, with the introduction of a specific apparatus for dissolved gas content and Henry coefficient measurements.

Chapter 3 compiles the successive experimental campaigns carried out to understand how operating parameters are driving the mass transfer in the membrane contactor module and to develop a competitive biogas upgrading process. After assessing the suitability of membrane contactor for biogas upgrading, a Design of Experiment (DoE) methodology explored the influence of the process parameters in a reference architecture. Then, the mass transfer limitation due to membrane wetting and gas composition are investigated. The process optimization strategy is finally presented: the exploration of architecture and solvent led to a biomethane production ($y_{CH_4}^{out} = 97.5$ %) with satisfying recovery rate ($R_{CH_4} = 98.7$ %).

Chapter 4 introduces the original modelling approach developed with a process upscaling purpose. The choice for a modelling strategy combining 1D mass transfer with a local hydrodynamic description in 2D is initially presented. The model is developed, optimized and validated for pure CO_2 absorption. The description of membrane wetting picked from the literature is questioned as a

significant deviation from experimental data is observed. Then, numerical adaptations are carried out to describe the absorption of a gas mixture and fit experimental results.

Chapter 5 applies two methods for process upscaling: dimensional analysis and mass transfer modelling. After setting the specifications for the biogas upgrading unit in three different cases ($100, 250$ and $500\ Nm^3_{biogas}.h^{-1}$), a focus is made on the commercially available membrane modules. Dimensional analysis is suggesting two different configurations to upscale the experimental results obtained with the KCl solution and water respectively. The validated mass transfer model is also used to size the process using water as the absorbent. In the end, the results from both methods are compared and discussed to suggest the most reliable industrial set-up at this stage of development: general remarks and points of attention regarding the integration of the CO_2/CH_4 separation unit into the whole biogas upgrading process are provided.

Objectives

The assigned objective of this research project is to design a biogas upgrading unit adapted to an agricultural context. Europe, and France in particular, holds the potential to cover half of its domestic natural gas demand by means of anaerobic digestion (AD). Though, biomethane development faces two technical shortcomings, detailed in Chapter 1:

- organic waste are mainly scattered over rural territories in agricultural farms. Their activities (animal dejection, crop residues and energy crops) are estimated to provide 91.8% of AD substrate available by 2030 in France [9]. Among them, small and medium farms with less than 200 Livestock Units (LSU[2]) hold a significant potential since they represent 54.3% of the total livestock in France. Though, available biogas upgrading technologies are not adapted to this rural environment and to the low biogas flowrates produced from these AD units;
- the specific investment cost of both the AD and biogas upgrading units rises as the biogas flowrate decreases. A comparative technological study showed that the specific investment cost is doubled as the biogas flowrate drops from 500 $Nm^3_{biogas}.h^{-1}$ to 100 $Nm^3_{biogas}.h^{-1}$ [10].

The process performance objectives were set according to the available technologies and the gas-grid specifications ($R_{CH_4} > 97$ %, $y^{out}_{CH_4} > 97$ %). In order to answer the current market demand, project developments were carried out according to 4 choices:

- the process would be based on an absorption principle as water scrubbing proved to be simple and robust for biogas upgrading;
- the use of hollow fiber membrane modules (HFMM) generally leads to a constant specific investment cost. Therefore, the membrane contactor technology was selected to be the gas-liquid contacting device. Derived from the artificial lung development, it offers a much higher specific area compared to conventional devices (Figure 0.6);
- based on the lab skills, the focus was set on the process developments by investigating the operating parameters, the nature of the solvent and the module arrangement. Work on the nature of the hollow fiber material or on the module geometry itself were not in the scope of this PhD;
- a rapid process industrialization was forecast. Therefore, the HFMM used in the experimental pilot campaigns had to be selected from an industrial range. By doing so, geometric similarity between the modules would ease the process upscaling.

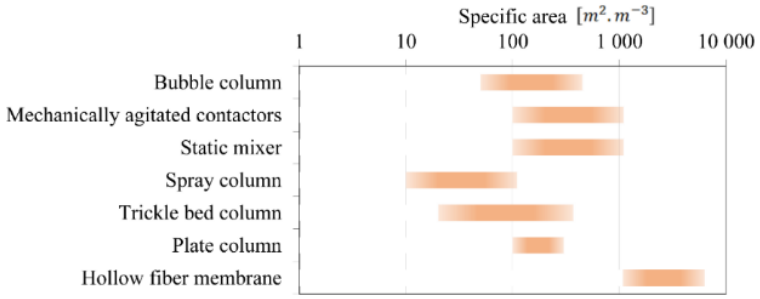

Figure 0.6 – Specific area of gas-liquid contacting devices (adapted from [11–13])

[2] LSU is an aggregated unit for livestock which integrates its nature and its age. 1 dairy cow = 1 LSU.

Chapter 1

State of the art

Chapter 1 State of the art

1.1 Introduction

This chapter is divided into 6 paragraphs. The first paragraph is an introduction to biogas (1.2): production by anaerobic digestion, biogas characterization, energy production from biogas and integration in the agricultural context. The two following paragraphs presents the state-of-the-art of the biogas upgrading technologies (1.3) and discusses the selection of an appropriate solvent in the view of a gas-liquid absorption process in polymeric hollow fiber membrane contactors (1.4). Then, the engineering methods to size the process are presented (1.5). The chapter ends with a focus on mass transfer modelling in the hollow fiber modules to provide an efficient tool for process scale-up (1.6).

1.2 Anaerobic digestion and energy production

1.2.1 Anaerobic digestion and biogas production

Anaerobic digestion (AD) refers to the degradation of organic matter by a consortium of microorganisms in anaerobic conditions. This biological degradation produces a gas mainly composed of methane and carbon dioxide, called biogas. This process has historically been used to reduce the organic content of cattle manure before its use as an organic amendment. Various substrates holds organic content and are therefore used as an input of the AD process (agricultural waste, crop residues, waste from the agroindustry, bio-waste, sewage sludge, landfill, energy crops…) [14, 15].

The degradation of organic macromolecules occurs through a complex trophic chain presented in Figure 1.1. The overall AD reaction generally takes the degradation of glucose in Eq. 1.1 as an example:

$$C_6H_{12}O_6 \rightarrow 3CH_4 + 3CO_2 \qquad \text{Eq. 1.1}$$

The mineralization of carbon into biogas is classically described in four successive steps involving the specific metabolisms of different bacteria populations:

- during hydrolysis, bacteria are producing decomposition enzymes. The complex carbonated chains are degraded into monomers;
- acidogenesis is a complex step which transforms the monomers resulting from hydrolysis. Various biochemical mechanisms can occur and produce short-chain fatty acids (acetic, propionic, butyric…), alcohol (ethanol), organic acids (lactic acid), hydrogen and carbon dioxide. The growth rate of corresponding bacteria is generally high with doubling times between 30 minutes and several hours [16];

- acetogenesis is the conversion of the intermediate products previously formed into acetate, hydrogen and carbon dioxide. This production relies on two main biochemical pathways (Figure 1.1):
  - ❖ the heterofermentative way is carried out by synthrophic acetogenic bacteria which are responsible for hydrogen and carbon dioxide production. Their reactions are thermodynamically favored only under very low hydrogen partial pressures ($P_{H_2} = 10^{-4} - 10^{-6}\ atm$) [17]. An accumulation of hydrogen inhibits the reaction and the anaerobic digestion might be stopped. Their doubling times is rather long and in the range of 1 to 7.5 days [16];
  - ❖ the homoacetogenic bacteria can synthetize acetate from the reduction of carbon dioxide or a longer organic molecule (volatile fatty acids) by hydrogen.
- methanogenesis is the final step in which intermediate products are converted into methane. The doubling time of these bacteria is ranging from 3.4 hours to 12 days, with a growth acknowledged slightly faster than the acetogenic population [16, 18]. Two main populations of bacteria exist:
  - ❖ the acetoclastic methanogens which produce methane mainly from acetic acid, though they can transform a wider range of substrates (methanol, methylamines, carbon dioxide and hydrogen). Those reactions are slow and slightly exothermic [17].
  - ❖ the hydrogenophilic methanogens which use hydrogen and carbon dioxide continuously produced by the acetogenic bacteria: these methanogens play a key role in maintaining a low hydrogen partial pressure. Both populations are living in syntrophy.

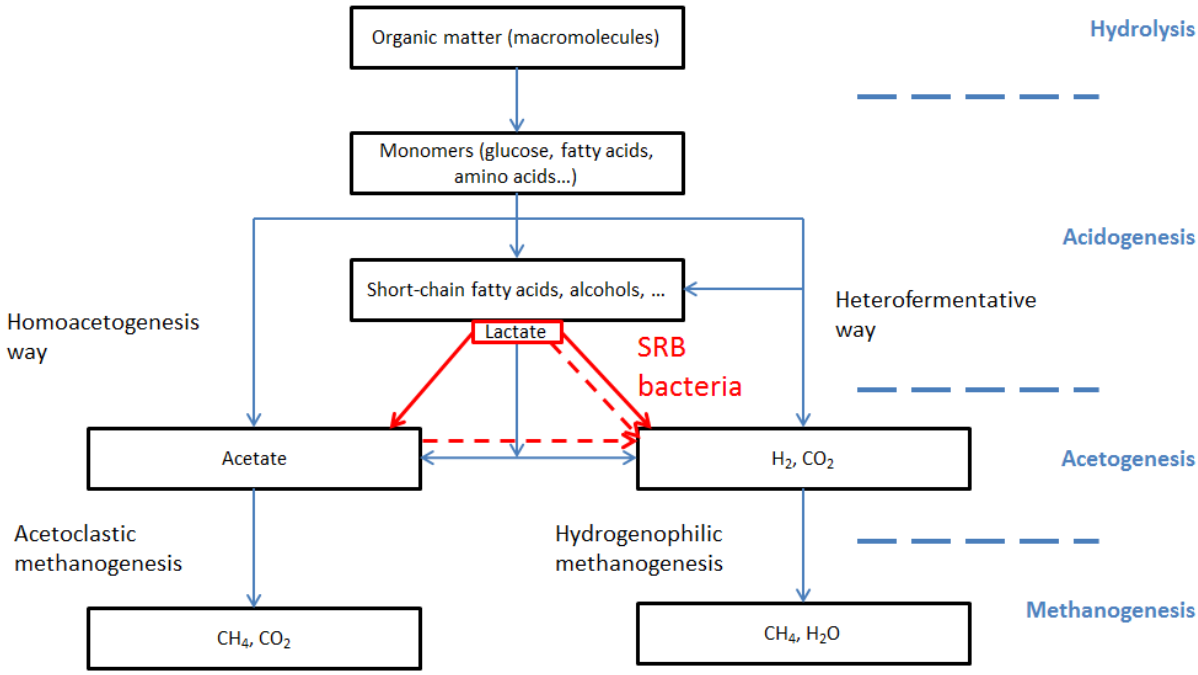

Figure 1.1 – Main steps of anaerobic digestion (adapted from [17])

The sulfate-reducing bacteria (SRB) are to be mentioned since they produce hydrogen sulfide which is an unwanted trace compound in the biogas (1.2.2). The SRB draw their energy from the oxidation of organic matter or dihydrogen while reducing sulfate-containing molecules. They negatively impact the methanogenic population due to direct inhibition or to precipitation of the metal essential for their growth [19]. Moreover, SRB demonstrate higher growth rates for those substrates [17, 20].

The predominant biochemical pathway depends on the operating conditions (fermenter technology, temperature, agitation). Three temperature regimes are identified for AD and the predominant biological consortium differs according to the temperature range (Figure 1.2). As a general rule, a higher temperature provides a more efficient degradation thanks to faster biological growth rates: with a lower residence time, the organic loading can be increased for the same AD unit. From an operational point of view, the higher the fermenter temperature, the more important is its heat demand. Due to this heat demand, the net energy production is decreased by 27.8 $kWh.m^{-3}$ for a 20 $°C$ increase [21].

The initial substrates also influence the predominant biochemical pathway. Animal dejections are reported to produce methane mainly by the hydrogenophilic way while the acetoclastic way is preferred in the digestion of activated sludge from wastewater treatment [15].

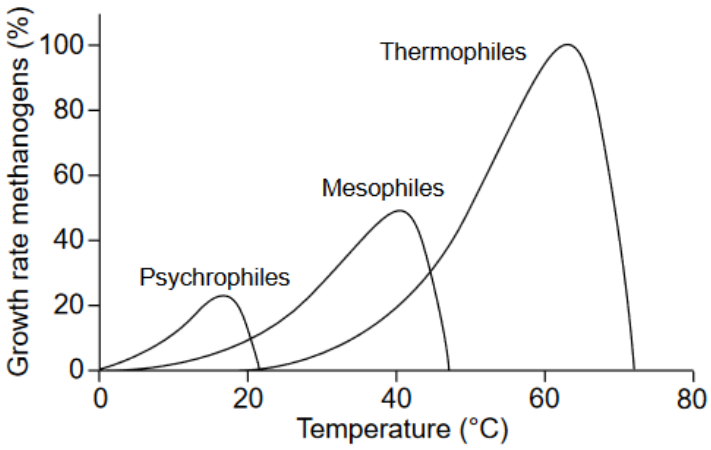

Figure 1.2 – Relative growth rates of psychrophilic, mesophilic and thermophilic methanogens [22, 23]

Relative growth is defined by comparison to the thermophilic population at its fastest growth rate

Four conditions are required for the biological degradation to be efficient [24]: absence of air, uniform temperature, optimum nutrient supply, optimum and uniform pH. These operating parameters drive the choice for an adapted equipment and a proper design for the digester. One should refer to dedicated literature [15, 17, 25].

1.2.2 Biogas description

Biogas has a matrix of methane (which contains its calorific value) and carbon dioxide with small amounts or traces of other gases, called impurities. Its composition depends on the feedstock and on the

digestion process (Table 1.1). Biogas from agricultural feedstock has typically a 50-60 %vol. methane content. Nitrogen is also sometimes reported due to the air injection in the digester to oxidize the hydrogen sulfide content [26]. Among the reported impurities, the hydrogen sulfide concentration is highly dependent on the type of substrate from 50 ppmv for some agricultural AD units to up to 10 000 ppmv for landfill gas. Ammonia is sometimes found in traces in agricultural biogas. In addition, biogas is saturated with water regardless of the AD process. Finally, compared to natural gas, the main differences are the significant concentration in carbon dioxide and the presence of impurities. The presence of carbon dioxide with no calorific value explains the lower energy content of biogas compared to natural gas ($5 - 8$ against $11.7\ kWh.Nm^{-3}$).

Components	**Bio-waste**	**Activated sludge**	**Agricultural feedstock**	**Landfill**	**Natural gas**
$\boldsymbol{CH_4}$ [% $\boldsymbol{vol.}$]	55-65	60-70	45-70	35-60	81-97
$\boldsymbol{CO_2}$ [% $\boldsymbol{vol.}$]	35-45	30-40	30-55	30-50	1
$\boldsymbol{H_2S}$ [$\boldsymbol{ppmv}$]	100-6000	500-1500	50-5000	600-10000	5
$\boldsymbol{NH_3}$ [$\boldsymbol{mg.Nm^{-3}}$]		< 0.05	< 2		-
$\boldsymbol{Siloxanes}$ [$\boldsymbol{mg.Nm^{-3}}$]	1 – 2	< 50	< 1	0 - 50	
$\boldsymbol{Halogenated\ hydrocarbons}$ [$\boldsymbol{mg.Nm^{-3}}$]	Traces	Traces	Traces	0-150	
$\boldsymbol{Calorific\ value}$ [$\boldsymbol{kWh.Nm^{-3}}$]	5 - 8				11.7

Table 1.1 – Natural gas and average biogas composition from various feedstocks [27, 28]
A more complete version of this Table is presented in Appendix A

The case of landfill gas is the most specific. The nitrogen and oxygen contents are higher due to airtightness issues in the gas collection permeable tubes [26]. Siloxanes ($< 50\ mg.Nm^{-3}$) and halogenated hydrocarbons ($< 150\ mg.Nm^{-3}$**)** are also more concentrated due to the presence of cosmetics and pharmaceuticals in the substrate, similarly to biogas from activated sludge digestion.

A specific feature of AD from agricultural waste is the stability of the biogas composition over time [29, 30]. This observation is explained by a lower variability in the substrate feed for the AD unit despite its seasonal variability. Regarding the composition in trace contaminants, two studies have characterized farm biogas from different sources with very low levels of volatile organic compounds (VOC) (Table 1.2).

	Halogenated compounds $[\mu g.m^{-3}]$	**Organic silicon compounds** $[mg.m^{-3}]$	**Benzene** $[mg.m^{-3}]$	**Toluene** $[mg.m^{-3}]$
Cow manure	b. d.	< 0.4	0.7 – 1.3	0.2 – 0.7
Pig slurry	< 3	NS	< 0.17	< 0.21

Table 1.2 – Concentrations in trace contaminants in biogas from agricultural feedstock [29, 31]

b.d. below detection limit

Components	Concentration	Impacts
CO_2	$25 - 50\ \%\ vol.$	Reduction of the calorific value Corrosion issues if the gas is humid
H_2S	$100\ -\ 10\,000\ ppmv$	Important corrosion in the equipment (compressors, engines, storage tank) Poisoning effect on catalysts[3] Formation of SO_2 due to combustion Safety issues
H_2O	$1 - 5\ \%\ vol.$	Indirect corrosion due to acid formation (reactions with H_2S, CO_2 and NH_3 form acids) Condensation in pipes
NH_3	$< 1\ \%\ vol.$	Corrosion issues if the gas is humid Formation of NO_x due to combustion
N_2	$0 - 5\ \%\ vol.$	Low calorific value Formation of NO_x due to combustion
O_2	$0\ -\ 5\ \%\ vol.$	Potential risk of explosion
Siloxanes	$0\ -\ 100\ mg.Nm^{-3}$	Formation of SiO_2 and microcrystalline quartz due to combustion → abrasion
Dust	-	Clogging in the equipment
Halogenated hydrocarbons	$0\ -\ 150\ mg.Nm^{-3}$	Corrosion in engines due to the formation of by-products during combustion

Table 1.3 – Concentrations and effects of biogas impurities [26, 28]

[3] Activated carbon filters or solvents are poisoned by H_2S.

Despite their low concentrations, the impurities can however affect the equipment dedicated to biogas use (1.2.3.1) [32]. Table 1.3 summarizes the effects of the various components of biogas. The major issues regarding impurities are:

- the low calorific value of some gases (carbon dioxide) which diminishes the calorific content;
- the degradation of equipment (compressors, engines, pipes) due to corrosion;
- the formation of polluting gases due to combustion (SO_2, NO_x).

1.2.3 Energy production from biogas

1.2.3.1 Biogas applications

Raw biogas produced from AD process holds a calorific content (Table 1.1) which finds different applications as summarized in Figure 1.3 [25]: These applications can be classified according to the end-use of biogas (heat, electricity or substitution of natural gas in the gas grid or as vehicle fuel). Converting biogas into heat in a boiler is the easiest application. Biogas can also be used for grid-electricity generation in Combined Heat and Power (CHP) units thanks to specific gas engines. A specific attention must be brought to the presence of trace impurities leading to corrosion in the engine during combustion and therefore to the equipment material. For instance, H_2S is partially converted to sulphur oxides SO_2 and SO_3 in the engine, which react with the water vapour to form sulphurous acid H_2SO_3 and sulphuric acid H_2SO_4 [33]. Electricity production from biogas is a more sustainable solution, with a lower primary energy consumption compared to fossil fuels. Figures[4] from Life-Cycle Analysis (LCA) database indicate $0.37\ kWh_{prim}.kWh_{el}^{-1}$ for biogas against 2.00 for natural gas and 2.72 for lignite [34]. In the recent decade, upgrading of raw biogas has gained attention since enriched biomethane provides a direct substitute for fossil fuels (natural gas either in the grid or as vehicle fuel). The Lower Calorific Value (LCV) of biomethane at 97 $\%vol.$ is indeed comparable to the one of natural gas (9.67 against $11.0\ kWh.Nm^{-3}$) [14]. The difference is explained by the presence of a small fraction of longer hydrocarbons (ethane C_2H_6, propane C_3H_8, butane C_4H_{10}) in the natural gas with a higher LCV than CH_4 itself. Finally, on-site gas storage is a technological option to take full benefits of the storable nature of this energy carrier.

The biogas upgrading pathway leads to a higher overall energy efficiency than heating and CHP applications [35]. This assertion is explained by comparison of the energy conversion efficiency (Table 1.4). Biomethane upgrading indeed displays a methane recovery rate up to 99% (1.3), while the best energy efficiency for both thermal and electric conversions recorded for CHP units are close to 90 % [36]. Moreover, the utilization of heat is highly dependent on the AD unit environment. An industrial unit is more likely to answer an on-site heat demand than a farm AD one implanted in a rural environment. Therefore, biogas utilization in CHP is rarely reaching its maximum energy efficiency. The anaerobic digestion is though requiring a constant heat demand for substrate heating (Figure 1.3) accounting for 10 to 15 % of the total energy produced [35, 37]. In the biogas upgrading pathway, the conversion to the final energy form is still to achieve. However, the location for this conversion can be

[4] It considers the extraction, production , refining and distribution processes.

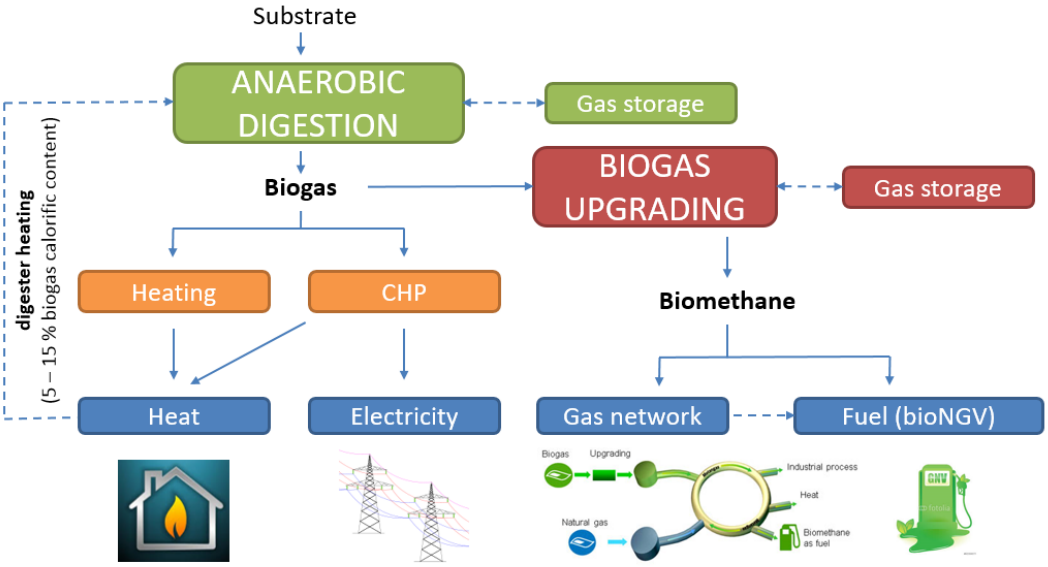

Figure 1.3 – Biogas applications in energy systems

	Heating	CHP		Biogas upgrading
Energy product	Heat	Heat	Electricity	Chemical
Energy efficiency ratio [%]	80 – 85	35 – 45	30 – 42[5]	81 – 95*

Table 1.4 – Energy efficiency according to biogas utilization pathway [10, 38, 39]

** These figures include the energy consumption of the upgrading process*

chosen along the gas grid at a place combining a heat and an electricity demand such an industrial site: the energy conversion in the CHP will thus be maximized.

Beyond its energy efficiency, biogas upgrading also offers the flexibility of energy storage. Biomethane takes advantage of the gas-grid infrastructure available in some European countries (UK, France, Germany, Italy…) to store and distribute energy to the end-user (gas turbine power, heat or transport fuel). As for natural gas, storage as compressed or liquefied biomethane are available options [40]. An integration with other intermittent renewable energies (wind and solar) is a promising technological option to make the whole energy system more sustainable and efficient [41].

Incentive regulatory schemes of the different utilization pathways were made in the EU member states accordingly to the national energy production strategy. Eurofores offers a broad report on the

[5] Organic Rankine Cycle (ORC) systems can increase the efficiency by converting heat into electricity. It provides an additional 5 to 8 points to the electricity efficiency ratio.

situation of each EU member states on the developments of renewable energies toward the binding 2020 NREAP[6] targets [42].

1.2.3.2 Gas-grid injection: an European perspective

Biomethane injection into the gas grid implies a new paradigm for the gas-grid operating companies: to a few huge methane terminals are added a constellation of small injection points. Specifications were issued to control gas quality in the network (Table 1.5).

Major parameters regarding biomethane vary among national regulations. The quality of the gas is most commonly specified by the Wobbe Index which is the ratio of its Upper Calorific Value (UCV) and the square root of its density against air. High quality biomethane (Wobbe Index > 13 $kWh.Nm^{-3}$) is required for Austria, Switzerland, as well as for the H gas[7] grid in France and Germany. Yet, The Netherlands operate a gas grid with a lower calorific content. The total sulphur and hydrogen sulfide contents are critical parameters (1.2.2) which find homogeneous specifications. However, the tolerance of oxygen is highly variable, with a very low threshold in France (0.01 % $vol.$) compared to other countries ($0.5 - 3$ % $vol.$).

Components	France	Austria	Germany	The Netherlands	Switzerland
$\boldsymbol{UCV}$[8] $[\boldsymbol{kWh.Nm^{-3}}]$	10.7-12.8 (H) 9.5-10.5 (L)	11.0-12.8	8.4-13.1	9.6-10.0	10.7-13.1
$\boldsymbol{Wobbe\ Index}$ $[\boldsymbol{kWh.Nm^{-3}}]$	13.6-15.7 (H) 12.0-13.0 (L)	13.3-15.7	12.8-15.7 (H) 10.5-13.0 (L)	12.1-12.3	13.3-15.7
$\boldsymbol{Water\ dew\ point}$ $[°\boldsymbol{C}]$	< -5	< -8 (8 bar)		< -10 (8 bar)	
$\boldsymbol{Total\ sulphur}$ $[\boldsymbol{mg.Nm^{-3}}]$	30	10	30	45	30
$\boldsymbol{H_2S}$ $[\boldsymbol{mg.Nm^{-3}}]$	5	5	5	5	5
$\boldsymbol{CO_2}$ [% $\boldsymbol{vol.}$]	2.5	2	6	10.3	6
$\boldsymbol{O_2}$ [% $\boldsymbol{vol.}$]	0.01	0.5	3	0.5	0.5

Table 1.5 – Specifications for the injection of non-conventional gases in the natural distribution gas grid in some European countries [43, 44]

Complete biomethane specifications for France are provided in Appendix B

[6] National Renewable Energy Action Plans
[7] High quality gas (as opposed to L gas in Europe or B gas in France)
[8] Upper calorific value

Actors from the gas industry and EU countries are working together for the development of a harmonized European standard for H gas [43]. Such a project will help for a better integration of biomethane in the energy production systems.

1.2.3.3 Biogas and biomethane potential in Europe

Among renewable energies, biogas and biomethane can play a key role for both their flexibility (storage) and their potential in Europe. A 2007 extensive study assessed the technical potential for biogas in EU-27 to 151 – 246[9] billions $Nm^3_{CH_4}/yr$ (Table 1.6). It could account for up to 52 % of the 472 billion Nm^3 natural gas consumption in 2015 [45]. Together with Synthetic Natural Gas[10] (SNG), biomethane from AD has the opportunity to meet the current demand for natural gas in Europe [46]. Despite this potential, its development faces some constraints: increasing competition for land (vs. food production) and biomass uses via other pathways (electricity and/or heat production), instability of political strategies, limited technical maturity, biomass production and supply, and social acceptance.

Resource	Billion Nm^3	%
Woody biomass	66	43,7 - 26,8
Herbaceous biomass	11	7,3 - 4,5
Wet biomass residues	26	17,2 - 10,6
Energy crops	48 – 143	31,8 - 58,1
Total	151 – 246	100,0

Table 1.6 – EU-27 technical biomethane potential [47]

These figures combine the potential of SNG and biogas production pathways.

Additional details on biomethane production potential are provided in Appendix C

The NREAP targets for 2020 were set to 16 % of the 151 billions $Nm^3_{CH_4}/yr$ lower technical potential. In addition, it is estimated that the objective of 48-50 billion $Nm^3_{CH_4}/yr$ could be reached by 2030 in EU-27 out of AD and SNG production (32 % of the lower technical potential) [47].

The situation regarding biogas developments is though quite different in European countries (Figure 1.4 and Figure 1.5). Germany, UK and Italy are already close to reach their 2020 targets with the utilization of 30 % of their biogas potential while France and the Netherlands are still on their way. France has indeed the highest biogas potential in Europe with 59.7 TWh [48]. A specific study on the biogas potential use in France by 2030 evaluated the production to 55.9 TWh [9].

On an EU-28 perspective, biogas energy production showed a strong 19 % growth on the 2005-2013 period (from 1.10 to 4.55 Mtoe). Only a 3 % growth is needed to meet the 2020 target [49]. Unfortunately, the EU 27 Renewable Energy Share (RES) target for 2030 was not declined into national objectives to support the development of renewable energies.

[9] Variability in the figures from different scenarios are mainly due to the level of energy crop use/
[10] Synthetic natural gas can be converted to biomethane through methanation

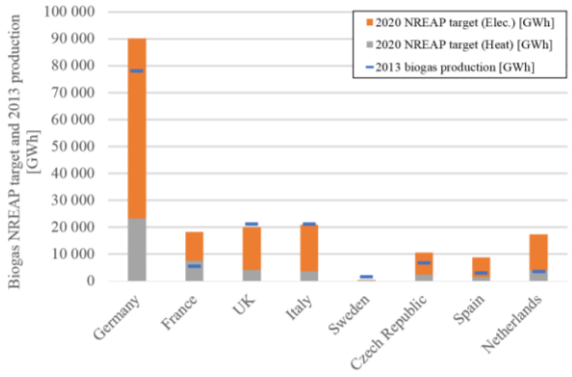

Figure 1.4– Comparison of biogas production and 2020 NREAP targets in some European countries

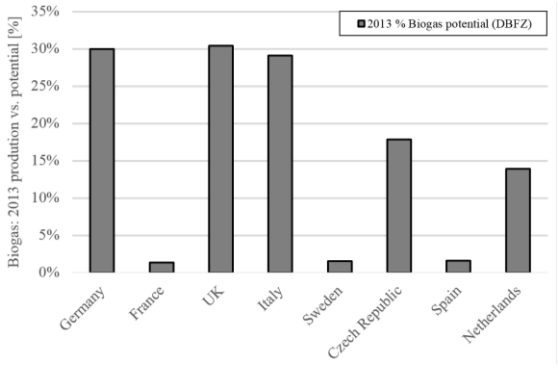

Figure 1.5 – Current production against biogas potential in some European countries

Figures from [50, 51]

Regarding the utilization pathways of biogas, industrial actors expect the share of biomethane applications to reach the one of electricity production by 2030 [47].

1.2.4 Integration of an anaerobic digestion unit on the farm

The case of agricultural AD is specific since the unit integration to the farm may lead to changes in operational and strategic management. In this case, the AD process provides a solution to manage waste streams, extra-revenue from energy production, extra-heat in the case of CHP utilization, and a high-quality organic amendment (Figure 1.6).

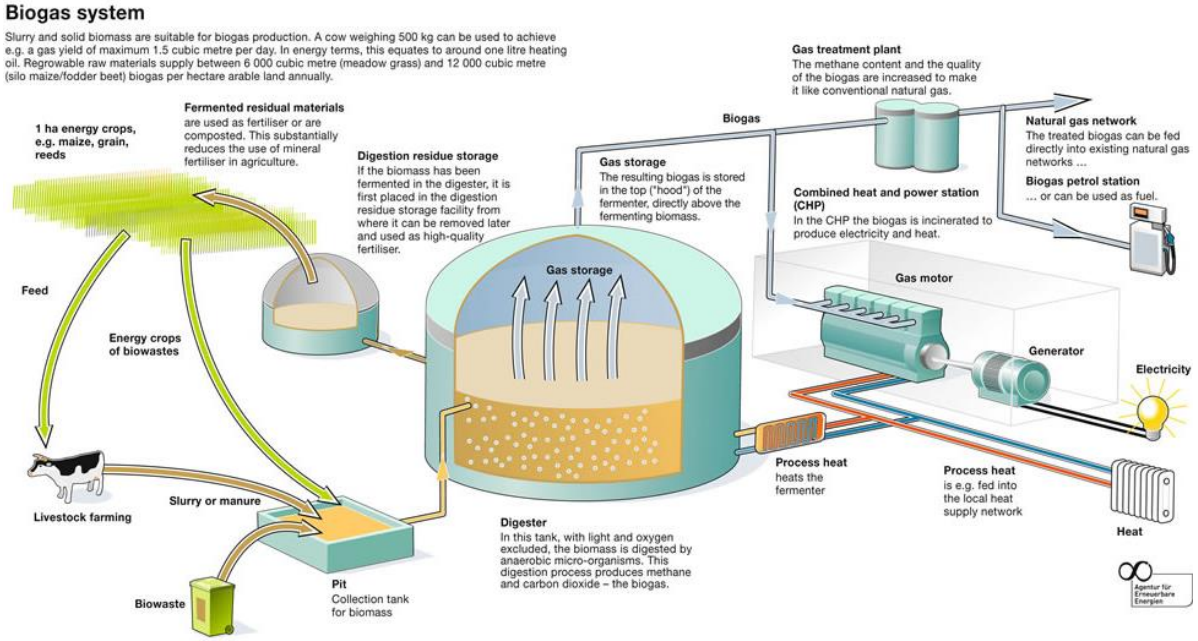

Figure 1.6 – Anaerobic digestion process (Source: Wheatleys)

Several business models are reported for AD integration into farm operations. Farm units offer less operational problems, a better control over the substrate supply, but higher energy production costs than small or large collective agricultural units [52]. The choice is driven by the local context: the geographical location is indeed a crucial factor. Substrates show variable energetic density: manure has a short critical collection radius (20 km) while energy crops and municipal solid wastes can be transported over a longer distance (respectively 50-70 and 425 km) [35].

Integration of an AD unit into a farm brings four main advantages:

- Renewable energy production relying on local biomass supply (in the view of energy autonomy);
- Reduction of greenhouse gases (GHG) emissions;
- Production of a valuable organic fertilizer [17, 25];
- Creation of non-transferable economic activity (382 000 direct and indirect jobs in the world, 66 000 in the EU and 4 000 in France in 2015 [53]).

1.3 Biogas upgrading processes: a review

This paragraph lists the different biogas upgrading processes available as commercial or emerging technologies. Biogas upgrading separates a mixed CO_2/CH_4 stream into a methane-rich biomethane and a CO_2-rich offgas streams (Figure 1.7). For each process, the separation principle is presented with a process flow diagram and the range of operating conditions.

Figure 1.7 – Biogas upgrading flow diagram

Two key indicators assess the biogas upgrading process performances: the biomethane quality $y_{CH_4}^{out}$ and the methane recovery rate R_{CH_4}. In the case of a strict binary mixture, these indicators are expressed by:

$$y_{CH_4}^{out} = \frac{Q_{g,CH_4}^{out}}{Q_{g,tot}^{out}} = \frac{Q_{g,CH_4}^{out}}{Q_{g,CH_4}^{out} + Q_{g,CO_2}^{out}} \quad \text{Eq. 1.2}$$

$$R_{CH_4} = \frac{Q_{g,CH_4}^{out}}{Q_{g,CH_4}^{in}} \quad \text{Eq. 1.3}$$

where $Q_{g,i}$ refers to the flowrate of specie i and y_i to its molar fraction.

The process selectivity α is may also be used as a process indicator.

$$\alpha = \frac{Q_{g,CO_2}^{off}}{Q_{g,CH_4}^{off}} \qquad \text{Eq. 1.4}$$

1.3.1 Available technologies

A wide number of reviews are dedicated to biogas upgrading in the literature [26, 54–62][11]. The technologies are presented in Figure 1.8 according to their separation principle.

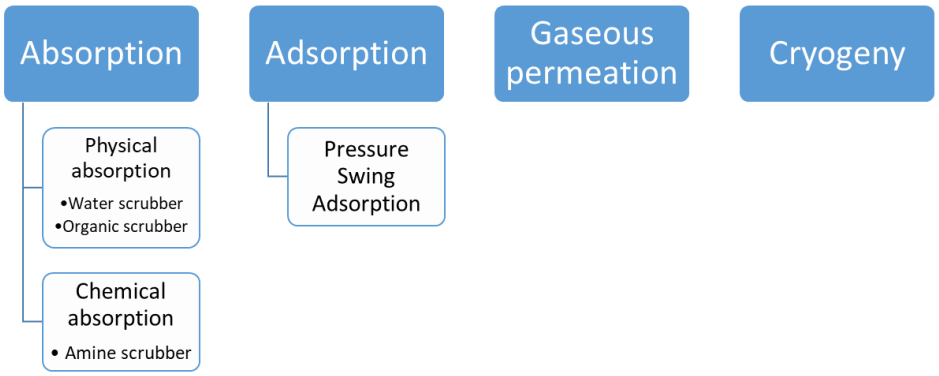

Figure 1.8 – Available biogas upgrading technologies according to their separation principle

1.3.1.1 Physical absorption

Physical absorption takes advantage of the solubility difference of carbon dioxide and methane in a solvent.

Water Scrubbing (WS)

Water scrubbing is a robust and widely established technology for biogas upgrading [10, 12]. The solubility in water is about 25 times higher for carbon dioxide than for methane (1.4.2.1). Carbon dioxide is absorbed into water in a packed tower under moderate pressure (6 to 10 bar g) while the methane-rich gas flow exits in the upper part of the column (Figure 1.9). The CO_2-rich water is then regenerated by air stripping in a desorption column under atmospheric pressure. An intermediate flash tank under lower pressure ($2.5 - 3.5\ bar\ g$) is sometimes installed to recover part of the dissolved methane which can thus be recycled at process inlet.

[11] References [58, 61] deserves special attention.

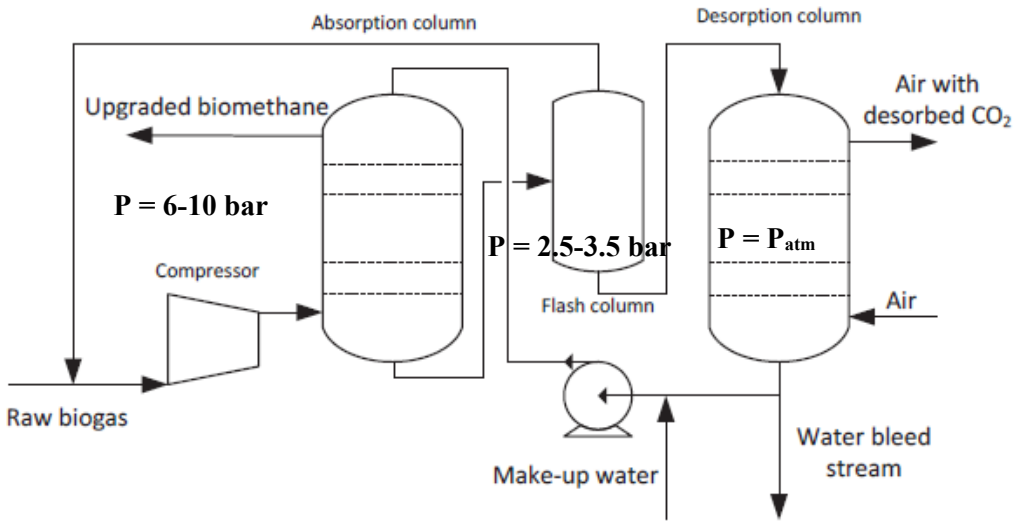

Figure 1.9 – Simplified process flow diagram of a water scrubber [59]

Despite its popularity, this system is poorly documented with experimental data in the scientific literature. Recently, Benizri performed an original pilot-scale study, replacing the desorption column by a static mixer, but the biomethane quality only reached a maximum of 85 % [63]. To characterize the mass transfer efficiency of this WS technology, the overall mass transfer coefficient was estimated based on this available dataset ($K_L a \cong 0.009 - 0.011\ s^{-1}$). A theoretical study demonstrated that the presence of a flash tank can increase the biomethane quality to 98 % with a methane recovery rate of 98.7 % [54]. A simulation study was performed at a gas/liquid ratio (Q_g/Q_l) of 5.41 $Nm^3.m^{-3}$ with an absorption column operating under 8 $bar\ g$; the flash tank pressure was optimized to 4.4 $bar\ g$, minimizing specific energy consumption at 0.212 $kWh.Nm^{-3}_{biogas}$.

Due to its operational simplicity (no consumable material and chemical-free process), WS is adapted to the constraints of an agricultural environment. However, the investment cost remains high at low biogas flowrates (about $500 - 600$ k€ for 100 $Nm^3.h^{-1}$ raw biogas [53]). An increase in the raw biogas flowrate significantly impacts the payback time and the net value of a gas-grid injection project. In the Italian legislative framework, Bortoluzzi stated that a 250 $Nm^3_{CH_4}.h^{-1}$ project was barely profitable while doubling the biomethane flowrate increased the project net value from 0.6 to 8.2 $M€$ [64]. In this framework, smaller upgrading units (120 $Nm^3_{CH_4}.h^{-1}$) produce biomethane at a overall specific cost[12] of 0.54 €. $Nm^{-3}_{CH_4}$ and 0.73 €. $Nm^{-3}_{CH_4}$ for grid injection and bio-Natural Gas Vehicle (NGV) respectively [65]. The difference is essentially due to the additional compression cost up to 250 bar a in the case of bioNGV.

Organic Scrubbing (OS)

Organic scrubbing relies on the same separation principle as WS. The solvent is generally based on polyethylene glycol (PEG) which has a higher carbon dioxide absorption capacity. The Selexol® commercial solution has five times more affinity to CO_2 than water [55]. A more efficient solvent allows

[12] Includes OPEX and CAPEX with a depreciation life of 20 years

process intensification (smaller equipment or smaller solvent flowrate). This process is more widespread in the carbon capture industry: almost no scientific reports were dedicated to its application for biogas upgrading.

The process involves a temperature swing to enhance the performances: carbon dioxide is absorbed at $20\ °C$ while the absorbent is heated up to $40 - 80\ °C$ prior to the desorption column (Figure 1.10). The solvent is stripped either with inert gas or steam (in case of high H_2S content) [26]. PEG has a low vapour pressure which limits the requirements for solvent make-up. Contrary to WS, the raw biogas needs to be dried and pre-conditioned: H_2S is treated (typically adsorbed on activated carbon) to avoid solvent degradation.

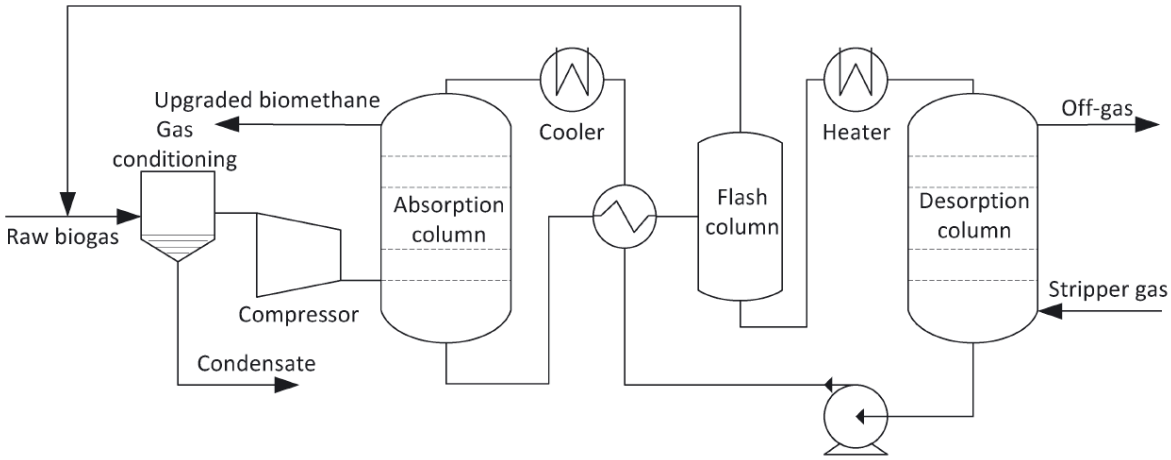

Figure 1.10 – Simplified flow diagram process of an organic solvent scrubber [58]

1.3.1.2 Chemical absorption

Similarly to physical absorption, chemical absorption operates in an absorption/desorption cycle. The use of a chemical reaction between the absorbent and CO_2 implies high loading rates and faster mass transfer (dissolved CO_2 quickly reacts with the absorbent, thus the mass transfer driving force is kept high). Available technologies are based on MEA or MDEA. Other amines or blends of amines are considered like DEA, TEA, PZ or DGA [66]. The choice of the amine depends on its CO_2 absorption capacity but also on its thermal and chemical stability [67]. Tertiary amines like MDEA have a low heat of reaction making regeneration less energy demanding [68] while primary or secondary amines have faster reaction rates: blends of MDEA/MEA or MDEA/PZ are good industrial candidates [10, 69].

Carbon dioxide reacts with amines in two routes [66, 70, 71]: it can covalently link to the amine to form a carbamate or exchange a proton with the amine to form bicarbonate (Figure 1.11).

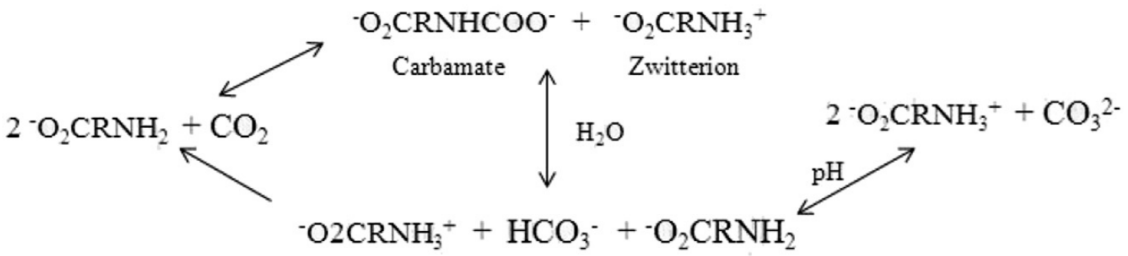

Figure 1.11 – Reaction scheme for CO_2 absorption in aqueous amine or amino acid salt solution [71]

Carbon dioxide is absorbed under moderate pressures (6-7 bar g). Due to a strong affinity with carbon dioxide, amine is regenerated with steam and carbon dioxide desorption requires a high energy amount (Figure 1.12). Depending on the nature of the amine, the temperature in the desorption column can vary from 115 °C up to 180 °C [61]. This heat demand (0.55 $kWh.Nm^{-3}$ [58]) can be met by large upgrading units thanks to thermal integration [37] but is prohibitive for small units. In contrast with physical absorption, amine process does not need an intermediate flash tank with a methane recycling loop. As for organic scrubbing, hydrogen sulfide must be removed prior to upgrading since amines are poisoned by H_2S.

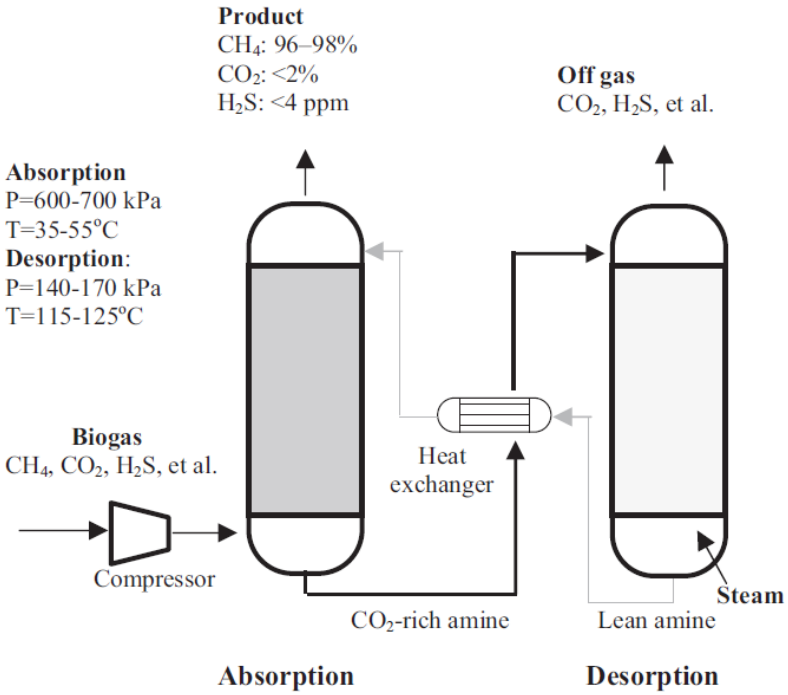

Figure 1.12 – Simplified process flow diagram of an amine scrubber [61]

Due to its high absorption ratio (mol_{CO_2}/mol_{amine}), amine absorption is the process reported with the higher methane recovery rate and biomethane quality (R_{CH_4}, $y_{CH_4}^{out}$). Compared to WS, it also leads to process intensification: the use of thermodynamical models demonstrated that liquid flowrate could be divided by 8.9 in the case of 30 %wt. MEA [54].

1.3.1.3 Pressure Swing Adsorption (PSA)

PSA process is based on the use of porous materials with high specific surface areas. Two different separation principles are at stake: kinetic selectivity with molecular sieves and thermodynamic selectivity with equilibrium adsorption [72]. CO_2 has a lower molecular size than methane (3.4 against 3.8 Å): molecular sieves with average pore size of 3.7 Å retain carbon dioxide molecules while methane molecules flow through the interstitial spaces [55]. Adsorbents such as activated carbons and zeolites take advantage of a higher CO_2 solid-gas partition coefficient to selectively separate CO_2 and CH_4 [73, 74].

PSA process is typically operated at $4-7\ bar\ g$ to increase the retention of CO_2 molecules (Figure 1.13). It comprises 4, 6 or 9 adsorbent cylinders for process optimization purpose [59]. Once one column is saturated with CO_2, its regeneration phase starts: the exiting gas is used to increase the pressure of the adjacent column (to limit energy consumption), the pressure is decreased to ambient pressure and the adsorbent bed is finally purged with biomethane (this final exhaust gas can be recirculated with raw biogas). The cycle lasts for 2-10 minutes [10]. Biogas pre-conditioning units are required to eliminate gas moisture and prevent adsorbent poisoning by H_2S and siloxanes.

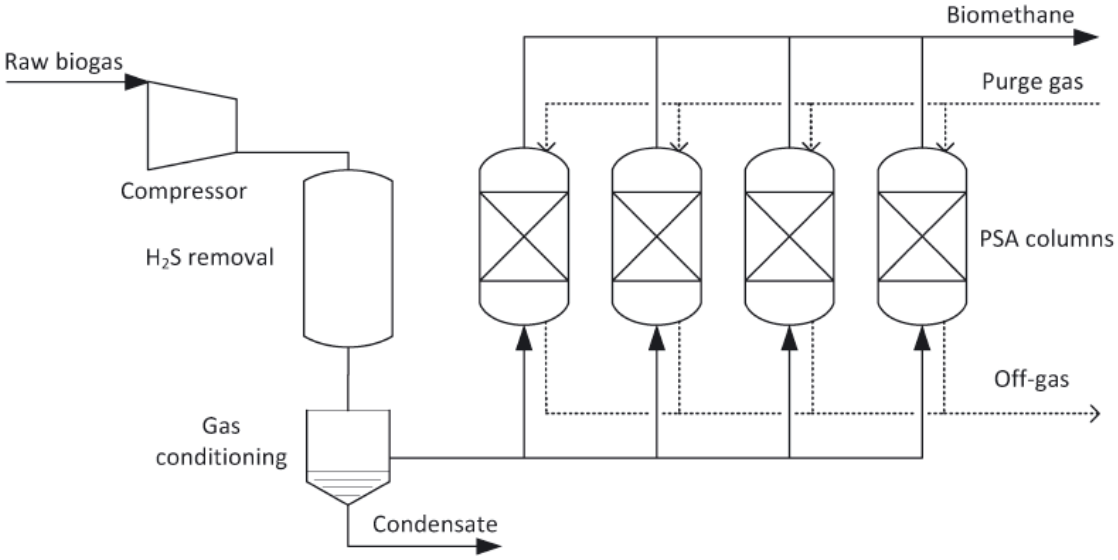

Figure 1.13 – Simplified process flow diagram of a PSA unit [59]

This technology is attractive for its compactness and the absence of consumable material. Based on industrial units, the energy consumption ($0.2-0.3\ kWh.Nm^{-3}$) is reported to be comparable to WS [10]. Recently, lower consumption ($0.15\ kWh.Nm^{-3}$) was achieved using a double-stage PSA process packed with equilibrium adsorbent Zeolite 5A: biomethane ($y_{CH_4}^{out} = 98.8\ \%vol.$) was produced with a high methane recovery rate ($R_{CH_4} > 99\ \%$). The main limitations of this technology are its specific investment cost, especially towards small units (see below 1.3.2), and its consumption of chemicals (replacement of zeolites and activated carbons).

Besides process optimization, research for new adsorbents is on-going (metal-organic frameworks, enhanced zeolites or activated carbons). Wet impregnation or immobilization onto the porous surface of amines or polyamines increases the CO_2 sorption capacity: $4.26\ mmol_{CO_2}.g_{sorbent}^{-1}$ is reached for TEPA[13]-impregnated activated carbon against $3.06-3.6\ mmol_{CO_2}.g_{sorbent}^{-1}$ for standard absorbents (Zeolite 13X and zeolite 4A) [75].

1.3.1.4 Gas permeation

Gas permeation membranes have been applied to natural gas treatment for three decades. With a similar gas mixture, the technology has been transferred to biogas upgrading units. Separation occurs thanks to different diffusion rates through the membrane [76]. Partial pressure difference ΔP_i between feed and permeate sides is the permeation driving force [77]:

$$\Delta P_i = y_i^{feed} P^{feed} - y_i^{perm} P^{perm} \qquad \text{Eq. 1.5}$$

where P is the total gas pressure with superscripts $feed$ and $perm$ referring respectively to the feed and permeate side of the membrane.

For biogas upgrading, methane is retained in the feed flow while carbon dioxide permeates through the membrane (Figure 1.14). Water vapour, oxygen and hydrogen are also removed from biomethane. The membrane materials are typically compared according to their CO_2/CH_4 selectivity Ξ_{CO_2/CH_4} based on the respective permeability Q^P of the species to separate:

$$\Xi_{CO_2/CH_4} = \frac{Q_{CO_2}^P}{Q_{CH_4}^P} \qquad \text{Eq. 1.6}$$

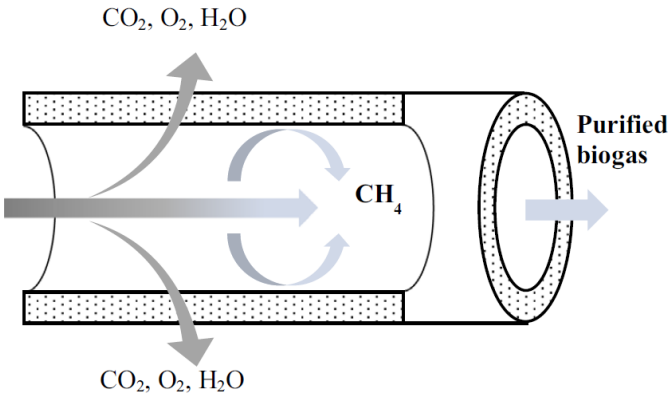

Figure 1.14 – Principle of membrane permeation [61]

Gas permeation has become a major process for biogas upgrading due to its ease-of-use (no water or chemicals) and the ability to downscale the unit without efficiency losses [58]. However, industrial units require drastic biogas preconditioning to prevent water condensation and exposition of

[13] Tetraethylenepentamine

the membrane material to pollutants (H_2S and VOC) which lead to membrane degradation [78]. The feed biogas is compressed to $4 - 19\ bar\ g$ according to the unit specifications. One single membrane module cannot meet biomethane production requirements and therefore, commercial units are designed with two or three membrane modules and a gas recirculation loop (Figure 1.15). For small scale units ($< 250\ Nm^3.h^{-1}$ raw biogas), the investment cost remains comparable to WS [10].

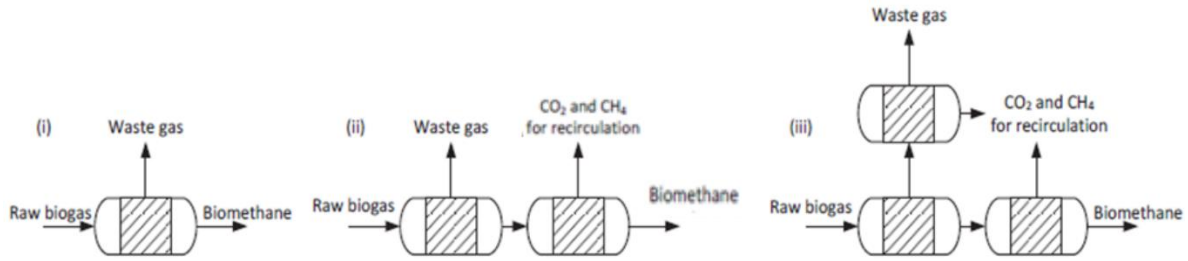

Figure 1.15 – Commercially available designs for membrane-based process [10]

Commercial units are operated with polymeric membrane materials (polyimide) but other types of membranes are under development (facilitated transport membranes, inorganic membranes and mixed matrix membranes). The key indicators for membrane development are high permeability and selectivity, chemical compatibility, long-term stability and cost. Development status and performances of the different materials are presented in the literature [77, 79]. The trade-off between CO_2 permeability $Q^P_{CO_2}$ and selectivity Ξ_{CO_2/CH_4} is typically compared to the state-of-the-art Robeson upper bound (Figure 1.16).

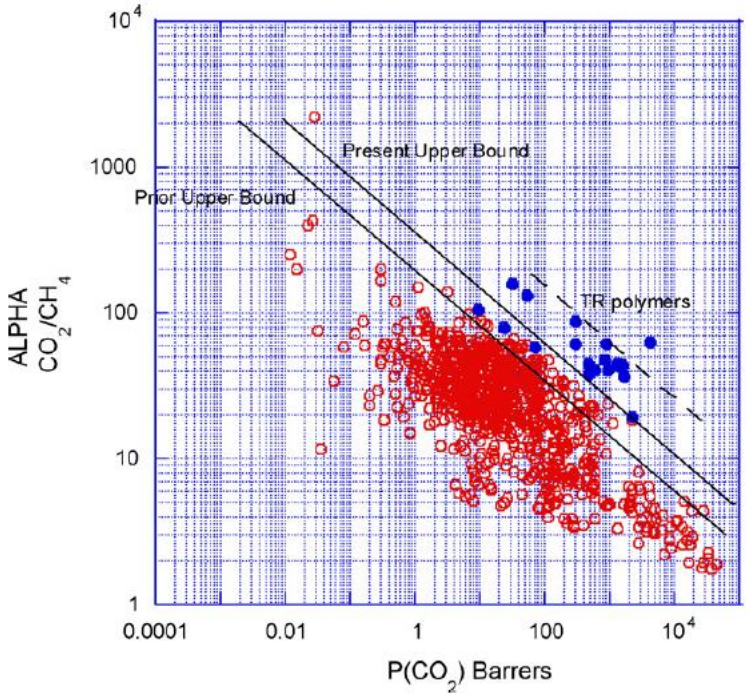

Figure 1.16 – Upper bound correlation for CO_2/CH_4 separation [80]

TR = Thermally rearranged

Polymeric material is 5-10 times less selective than inorganic material but it has been adopted in the industry for its low cost and high processability. Polymer plasticization can occur at high CO_2 partial pressure due to CO_2 sorption in the polymer matrix: this phenomenon enhances mass transport for all compounds, thus reducing the membrane selectivity [77].

1.3.1.5 Cryogenic separation

The cryogenic process takes advantage of the different liquefaction/solidification temperatures to perform an efficient separation (Figure 1.17). The temperature is decreased in successive steps to remove different biogas components.

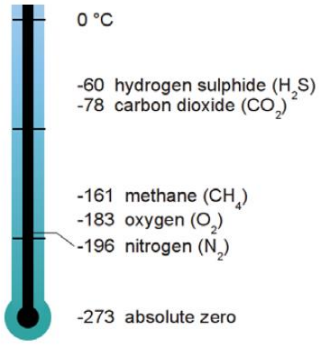

Figure 1.17 – Boiling point at atmospheric pressure for pure gases present in biogas [10]

Several firms (GtS, Prometheus Energy, Acrion and CryoPur) have designed plants at a significant scale [81, 82]. The operating pressure and the number of modules depend on the unit technology and the unit specifications. Carbon dioxide antisublimates in a first vessel and is separated from gaseous methane. In a second step, solid CO_2 is melted to produce liquid bio-CO_2. The upgrading biomethane can either by injected in the gas network or liquefied thanks to an additional temperature decrease. The thermodynamic diagram is presented in Appendix D for the binary $CO_2 - CH_4$ mixture based on the comparison between two thermodynamical models and experimental data from the literature [83].

The main operational issue faced by the GtS plants (operating around 10 bar a) was clogging of pipelines or heat exchangers due to CO_2 solidification [55]. The CryoPur® technology operates in a similar range $2 - 15\ bar\ a$ depending on the specifications.

Despite its promising perspectives, very few biogas upgrading facilities are based on this process due the lack of industrial experience and to its high energy-consumption. The energy efficiency in reaching low temperatures is crucial for its competitiveness [84]. GtS expected an electricity consumption of $0.45\ kWh.Nm^{-3}$ though the figure $0.60\ kWh.Nm^{-3}$ from CryoPur appears more realistic (including both upgrading and liquefaction). This process turns valuable when methane is used as bio-LNG since the cooling required for purification reduces the energy-demand for liquefaction [26].

1.3.2 Economical and technical comparison of commercially available technologies

The strengths and weaknesses of the available technologies are summarized in Table 1.7 and the technical performances reported in the literature are compared. All technologies produce high quality biomethane satisfying the grid specifications ($y_{CH_4}^{out} > 96.7\ \%vol.$) and the methane slip is comparable ($< 2\ \%$). Amine scrubbing exhibits a very low methane slip (0.1 %). The process choice finally depends on the unit specifications (biogas flowrate and quality, presence of impurities, use of biomethane).

An European benchmark for capital expenditures (CAPEX) and operational expenditures (OPEX) was established by Bauer [10]. The specific investment cost severely increases in the range of flowrates produced by an agricultural AD unit ($< 250\ Nm^3.h^{-1}$ raw biogas) due to downscaling issues (Figure 1.18). According to this study, the investment is comparable for all techniques in their availability range. In particular, WS and gas permeation membranes are competing for small-scale units.

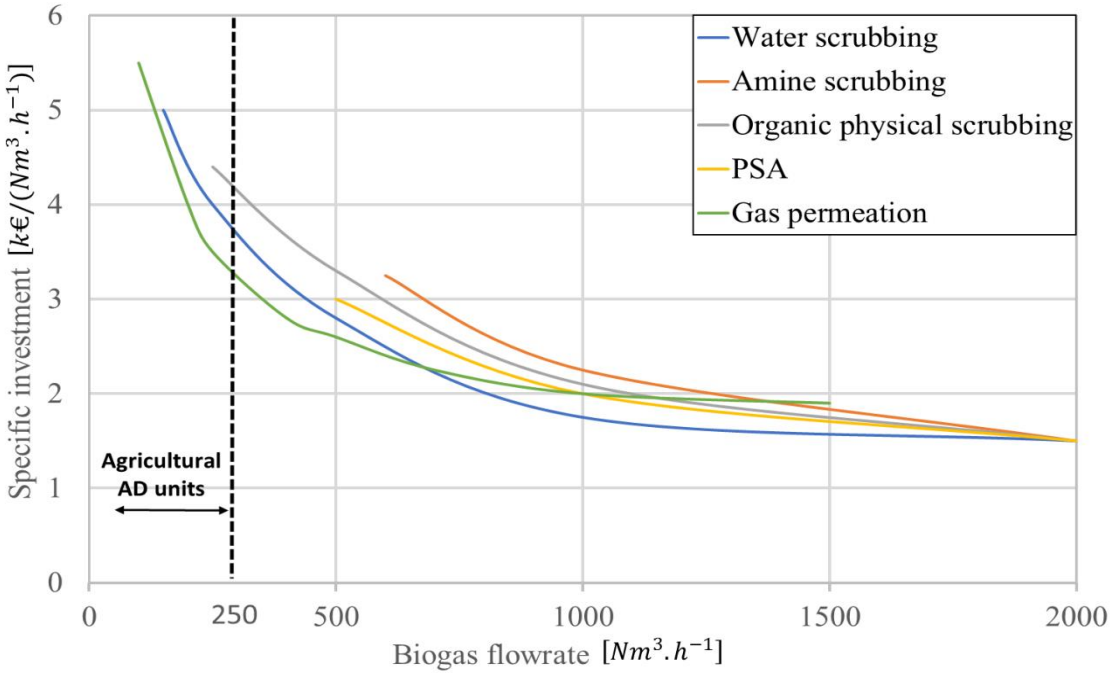

Figure 1.18 – Specific investment for a biogas upgrading unit according to the biogas flowrate [10]

This technology review has identified points of attention for future process developments:

- The biogas upgrading market is highly competitive and therefore the process costs (CAPEX and OPEX) must always be kept in mind;
- Available technologies demonstrate satisfying technical performances: the developed process should meet at least the same performances;
- For the agricultural AD units, the process must comply with a rural environment (ease of operation, ease of maintenance and robustness).

	Water scrubber	*Amine scrubber*	*PSA*	*Gas permeation*	*Cryogeny*
Advantages	Robustness Ease-of-operation Tolerant to impurities	Compactness High selectivity	Compactness	Compactness Modularity High reliability Ease of maintenance	Production of bio-LNG and bio-CO_2 High flexibility
Drawbacks	Limited downscaling	Required biogas preconditioning (H_2S, VOC) Chemical consumption High heat demand for regeneration	Required biogas preconditioning (H_2S, siloxanes, water)	Drastic biogas preconditioning Little operational experience	High energy demand High capital cost
Operational issues	Clogging due to bacterial growth Foaming	Degradation of amines by O_2 and H_2S	Solenoid valve tightness		Clogging due to CO_2 ice
Methane slip [%]	1	0.1	2	0.5	
Methane purity [%]	98	>99	98	>97	>99.4
Water consumption [$L.Nm^{-3}$ biogas]	0.04 - 0.4	0.03	0	0	0
Electricity demand [$kWh.Nm^{-3}$]	0.23 - 0.3	0.12 - 0.14 + 0.55 $kWh_{th}.Nm^{-3}$	0.2 - 0.3[1]	0.2 - 0.3	0.60
Chemical consumption	Anti-foaming agent	Activated carbon Anti-foaming agent Amine	Activated carbon	Activated carbon	Activated carbon

Table 1.7 – Comparison of the technical performances achieved by the existing upgrading systems (adapted from [10, 26, 61, 82])

1.3.3 Emerging technologies

Various works are aiming at the development of innovative biogas upgrading processes. They use new separation principles or combine available technologies together or with new devices. A selection is presented here.

1.3.3.1 Hollow fiber membrane contactors

A hollow fiber membrane module (HFMM), also named hollow fiber membrane contactor, is a contacting device which found its first application in blood oxygenator forty years ago [85, 86]. Since then, membrane contactors have been transferred to various applications such as liquid/liquid extraction of aroma compounds, recovery and purification of pharmaceuticals, metal ion extraction, ultrapure water production, osmotic distillation and beverage carbonation [86–89]. Thanks to hydrophobic properties, hollow fiber membrane offers a non-dispersive contact to gas-liquid absorption systems with valuable advantages: operational flexibility (independent control of gas and liquid flowrates and pressures), a known interfacial area supported by the membrane, modularity (linear scale-up and ease of maintenance) and compactness [90, 91]. Compared to traditional gas-liquid devices (Figure 0.6), it also offers a higher specific area ($> 1\,000\, m^2.m^{-3}$) which paves the way for process intensification with a reactor volume ratio from 4 to 10 compared to conventional packed column [92–94]. Applied to CO_2 capture, polypropylene (PP) and polytetrafluoroethylene (PTFE) hollow fibers demonstrated a 4-fold increase in the overall mass transfer coefficient ($K_G a$) compared to a packed column [95]. This intensification factor is lowered over long period of operations due to membrane wetting (1.6.3). A more recent study distinguished the performances of PP and PTFE fibers using MEA solution as a chemical absorbent [92]. PP fibers resulted in a higher intensification factor at short time scale (4.0 against 1.2 for PTFE fibers) due to the typical hollow fiber diameter, but this factor decreased at long time scale (2.0 against 1.1). Then, four key challenges are identified to overcome current limitations to carbon capture: avoid the mass transfer limitation due to membrane wetting (1.6.3) which is not present in conventional scrubbers, develop stable membrane material (thermal and chemical resistances) to guarantee long-term performances, find an environmental-friendly absorbent which allow energy-efficient regeneration and CO_2 recovery, identify potential process interactions with other gas compounds [90, 91].

Different membrane types are referred to as hollow fiber contactors [86]: the main distinction has to be made between dense and porous membranes since the transport mechanism differs (pure diffusion through the polymer and mass transfer across the porous structure respectively). Then, among the porous membranes, a thin dense polymeric layer can be added to the porous structure to tackle pore wetting issues. These hollow fiber membranes are named as asymmetric or dual layer according to the number of thin dense layers.

The polymeric membranes are the most promising for porous hollow fibers [90]. According to the challenges identified above, the membrane polymer must have a good thermal, chemical and mechanical stability as well as a strong hydrophobic behaviour. The melting temperature T_m is a good

indicator of the polymer thermal stability while the glass transition temperature T_g helps to identify its physical structure. Table 1.8 presents these temperatures for the most current polymers used for membrane material. PTFE and PEEK are the more robust polymers with melting temperatures above 300°C. Care must also be brought to the stability of the potting material [91]. Fabrication and processability of the membrane material are also an issue for the industrial diffusion of hollow fiber modules. With this regard, PP and PTFE are popular membrane materials since they are produced respectively by thermal and stretching methods. As stated in the objectives, consideration on membrane developments are not of interest in this work. Numerous studies are focusing on the developments of membrane-based technology. One should refer to a specific review on the development of membrane materials [79, 91].

Polymer	Type	T_g (°C)	T_m (°C)
Polytetrafluoroethylene (PTFE)	Semi-crystalline	127	327
Polypropylene (PP)	Semi-crystalline	−20	176
Polyvinylidene fluoride (PVDF)	Semi-crystalline	~−30	~170
Polyethylene (PE)	Semi-crystalline	−115	137
Polyether ether ketone (PEEK)	Semi-crystalline	145	335

Table 1.8 – Glass transition and melting temperatures of polymers used as membrane material [91]

The use of porous membranes and dense membranes in gas-liquid absorption systems for biogas upgrading are presented separately.

Absorption

In the recent years, growing interest was shown on the promises of HFMMs applied to gas-liquid absorption. Most of the studies focused on carbon capture [86, 90–92, 96] but a few of them experimentally explored its potential for biogas [97–101] or natural gas upgrading [71, 101–103] (Table 1.9). The largest membrane areas reported were tested with PP hollow fibers (highly available for processability and cost considerations) by two research teams. All these studies evaluated the impact of the absorbent type and the operating conditions (inlet gas flowrate Q_g, liquid absorbent flowrate Q_l, gas pressure at absorption P_g, CO_2 inlet molar fraction y_{CO_2}) on absorption performances. However, in a

Ref.	Conf.	Membrane material	Membrane area [m^2]	y_{CO_2} [% $vol.$]	P_g [$bar\ g$]	Absorbent	Q_g [$mL.min^{-1}$]	Q_l [$mL.min^{-1}$]
[98]	Abs. Abs./Des.	PP (SepraTek Inc.)	0.25 / 0.75	50	1.5 – 4.5	Water	150 – 300	200 – 800
[97]	Abs.	PP (Membrana)	0.58	40	NS[14]	Water / NaCl / NaOH	210 – 581 NmL. min^{-1} (0.0017 – 0.0047 $m.s^{-1}$)	0.0054 – 0.024 $m.s^{-1}$
[99]	Abs.	PP (Membrana)	0.79	40	NS	Ammonia	750	100
[100]	Abs.	PVDF	0.084	20-40	NS	Water / MEA	400 – 600 (0.017 – 0.0254 $m.s^{-1}$)	0.019 – 0.076 $m.s^{-1}$
[101]	Abs.	PVDF (Memcor Australia)	0.019	20 - 50	NS	Water / NaOH (+NaCl) / MEA	200 – 400	0.7 – 2.5 $m.s^{-1}$
[102]	Abs.	ePTFE (Markel Corp.)	NS	9.5	1 - 50	Water / NaOH / MEA / DEA / DETA	200 – 800	100
[103]	Abs.	ePTFE (Sumitomo) / PFA (Entegris)	0.314 / 0.034	5	1 - 50	Water / NaOH / MEA / DEA / DETA	600 – 1000	10 – 25
[71]	Abs. Des. Abs./Des.	28% PVDF	0.0034	10	NS	MEA / NaOH / Sarcosine / Glycine	10 – 100	10 – 40

Table 1.9 – Review of the experimental conditions tested for biogas/natural gas upgrading using gas-liquid absorption hollow fiber membrane modules

process development perspective, only one recent study carried out experimental work to implement an absorption/desorption cycle applied to biogas upgrading, as initially presented by Teplyakov [104].

McLeod proved that the carbon dioxide absorbed flow $Q_{CO_2}^{abs}$ in water was driven by the liquid velocity when a physical absorbent was used [97]. Considering only absorption, 85 % biomethane was produced but the methane slip was already significant ($R_{CH_4} = 94.78$ %). Using a 1 M NaCl solution instead of pure water, R_{CH_4} was increased to 96 % thanks to the salting out effect (1.4.2.2). With water as the absorbent, Kim produced a gas-grid quality biomethane ($y_{CH_4}^{out} = 98$ %) though with a lower recovery rate ($R_{CH_4} = 85$ %) [98]. Coupling absorption and desorption steps, R_{CH_4} was further decreased to 75 %. Nonetheless, the process stability was confirmed over 50 hours. The use of chemical solvents to enhance carbon dioxide absorption is an interesting way that will be developed in paragraph 1.4.3.

Patents relative to the application of hollow fibers to gas separation have also been delivered. The Dutch research institute TNO filed the patent application WO 2012/096576 to protect the combination of HFMMs and gas-liquid absorption to separate a gas mixture into fractions but the demand was withdrawn in 2016 [105]. Another TNO patent (EP 1 778 388) refers to the degassing of a CO_2-rich solvent [106]. Older patents refer to the natural gas sweetening using chemical absorption [107–109]. In 2016, the patent EP 2 714 243 was delivered to the German company Ingenieurbüro Buse GmbH for a methane enrichment process based on CO_2 absorption in water using HFMMs [110, 111]. A first plant was already commissioned (Figure 1.19) but no process performances were published up to now.

[14] Not Specified (NS)

Figure 1.19 – Small scale biogas upgrading unit using hollow fiber membrane contactors
Plant capacity: 6 $Nm^3_{CH_4}.h^{-1}$ - *Germany*

The implementation of gas-liquid absorption in HFMMs is promising as it can take advantage of the modularity and compactness of membranes combined with the robustness and ease-of-operation of WS technology. As another advantage, the use of membrane contactors in both absorption and desorption steps avoids the depressurization of the solvent generally needed for desorption in the liquid closed-loop; this represents a significant energy saving as the solvent recompression is considered to account for 20-30 % of the process energy requirement [86]. A better understanding of gas-liquid mass transfer as well as sizing tools for scale-up are needed to support the technology developments.

Mixed systems

Besides porous hollow fiber membranes, research projects assessed the combination of gas permeation membranes with gas-liquid absorption to take advantage of a dense selective membrane layer that would also avoid wetting.

Dense PDMS[15] demonstrated a high CO_2 permeability ($1.25 \times 10^{-4}\ mol.m^{-2}.s^{-1}$) if used as an ultrathin wall without a support layer [112]. Compared to porous PP membrane, the limiting mass transfer resistance is transferred from the liquid phase to the membrane: the selectivity and mass transfer rate are thus controlled by the membrane features. The comparison of two membranes with similar permeability and selectivity features (a PDMS coated and a Teflon-AF coated composite membranes) gave evidence that wetting could still be observed: PDMS material overcomes Teflon-AF with a respective permeability of $1.35 \times 10^{-3}\ mol.m^{-2}.s^{-1}$ and $7.50 \times 10^{-4}\ mol.m^{-2}.s^{-1}$ for a 40/60 CO_2/CH_4 mixture under 5 $bar\ g$ feed pressure [113]. Despite dense skin PPO[16] hollow fiber membranes showed a lower CO_2 absorption flux ($2.5 \times 10^{-5}\ mol.m^{-2}.s^{-1}$), the methane losses were minimized and the process performances are encouraging ($y^{out}_{CH_4} = 92\ \%, R_{CH_4} = 97\ \%$) [114].

[15] Polydimethylsiloxane
[16] Poly(Phenylene Oxide)

1.3.3.2 Hydrate formation

Gas hydrates are crystalline compounds which trap gas molecules to form a stable solid similar to ice. Water molecules form polyhedral cages which are occupied by guest gas molecules. The solid structure is stabilized by hydrogen bonds between the host water molecules and by Van der Waals forces between the gas molecules and the cages [115, 116]. Methane hydrates were naturally found under the sediments on the ocean floors. The formation of hydrates has been applied to selective gas separation since the hydrate formation characteristics vary according to the guest molecule features (such as size and shape) [117]. Hydrates typically form in moderate conditions (low temperature and high pressure): CO_2 hydrates are formed above $10\ bar\ a$ at $T = 20°C$ (Figure 1.20) while CH_4 hydrates require higher pressures. Additives are often considered to enhance the hydrate rate formation and the gas storage capacity of hydrates.

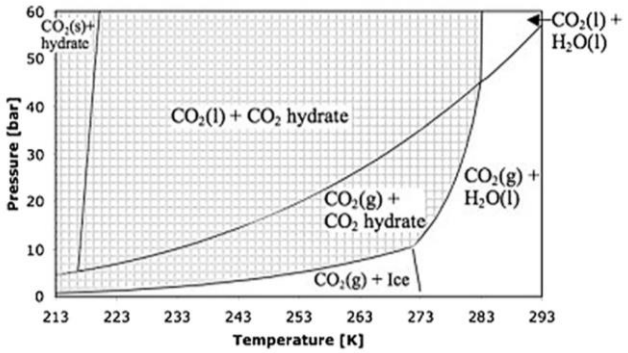

Figure 1.20 – Pressure-temperature projection of the CO_2 phase diagram with the region of CO_2 hydrate stability shaded [116]

A feasibility study enriched $1.16\ Nm^3_{biogas}$ from $y_{CH_4} = 61.6$ % to 71.2 % in 30 minutes using water combined with SDS[17] additive under high pressure ($P = 60\ bar\ a$) and at a temperature above zero ($T = 5\ °C$) [116, 118]. With an ideal energy consumption of $0.306\ kWh.kg^{-1}_{biogas}$, the process performances are far from those of available biogas upgrading technologies (1.3.2). Other studies explored the combination of several additives (TBAB[18], THF[19], TBPO[20], TBPT[21]) and their synergic effects (combined with DMSO[22]) by characterizing kinetics and phase equilibrium [115, 117, 119]. However, up to now, the separation efficiency remains limited.

1.3.3.3 Biological processes

Some microorganisms use CO_2 as their carbon source. Two biological groups attract growing interest for the bioconversion of carbon dioxide: methanothrophic bacteria and microalgae.

[17] Sodium Dodecyl Sulfate
[18] Tetra-n-butyl ammonium bromide
[19] Tetrahydrofuran
[20] Tributylphosphine oxide
[21] Tetra-n-butyl phosphonium bromide
[22] Dimethyl sulfoxide

Hydrogenophilic methanogens belong to one of the microbial population producing methane from CO_2 and H_2 injection during the AD trophic chain (Figure 1.1). Their metabolism acts as a biogas upgrading mechanism thanks to H_2 injection according to the Sabatier methanation reaction:

$$CO_2 + 4H_2 \rightarrow CH_4 + 2H_2O \qquad \Delta H_r^0 = -167\ kJ.mol^{-1} \qquad \text{Eq. 1.7}$$

Two pathways are considered for the injection of H_2: in the anaerobic digester for *in-situ* upgrading or in an external bioreactor dedicated to biological methanation. Most projects worldwide are developed according to the latter set-up (Figure 1.21). Compared to catalytic methanation, biological systems are less intensive but operate under moderate temperatures (40-70 against 600-800 °C) and are more resistant to trace contaminants (H_2S, NH_3, VOC…) [120].

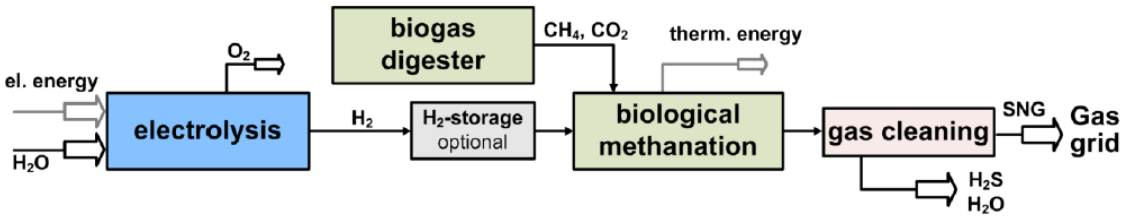

Figure 1.21 – Process flow diagram for biological methanation in a separate reactor as upgrading unit [121]

The combination of CO_2 and H_2 provides a long-term solution for renewable electricity surplus storage when H_2 is produced from water electrolysis. It also increases the production capacity for methane and thus for decarbonized high density fuels for transportation (as long as the electricity used in the electrolysis is from renewable sources) [122]. Three projects are worth noticing:

- **Electrochea** is leading a demonstration project (BioCat) in Denmark with a pre-commercial unit (10 m^3 bioreactor, 250 kW_e PEM[23] electrolyser) [122]. The thermophilic methanogenic archea strain was selectively evolved at lab-scale. The development strategy reached a methane productivity of 21 $Nm^3_{CH_4}.m^{-3}_{reactor}.d^{-1}$ and a 62 % H_2 conversion efficiency with an elevated biomass concentration ~ 8 $g_{biomass}.L^{-1}$ when fed with raw biogas [123].
- **MicrobEnergy**, subsidiary of the Viessman Group, set up the first biological methanation commercial reactor (BioPower2Gas) in Germany. The dimensions are comparable to the BioCat project (5 m^3 bioreactor, 300 kW_e PEM electrolyser). Produced biomethane ($y^{out}_{CH_4}$ = 98 %) is injected into the gas-grid. The unit is dimensioned to upgrade 30 $Nm^3_{biogas}.h^{-1}$ with a 60 $Nm^3_{H_2}.h^{-1}$ injection [124].
- **ETOGAS - Audi** is a major industrial Power-to-Gas facility under operation since 2013. Hydrogen is provided by alkaline electrolysers powered by wind energy (3 × 2.0 MW_e) and combined to a CO_2-rich stream coming from the neighbouring biogas upgrading unit (amine

[23] Polymer Electrolyte Membrane

scrubber). The process has a 54 % energy efficiency and is expected to produce roughly 1 000 $t_{CH_4}.y^{-1}$ [122].

Trickle-bed reactors have also been investigated at pilot scale. CH_4-rich biogas (77 %) was successfully converted to biomethane (96 %) by an immobilized archea consortium in a 61 L reactor. A lower methane productivity (1.49 $Nm^3_{CH_4}.m^{-3}_{reactor}.d^{-1}$) was observed than for the previous projects. Though, this figure could be improved by increasing the 3.76:1 $H_2{:}CO_2$ ratio [120]. In addition, the stability of the trickle-bed reactor was confirmed by continuous biomethane production over 240 days ($y^{out}_{CH_4} > 96$ %) with quantitative CO_2 conversion (> 96 %) [44].

Microalgae are other candidates for biological biogas upgrading thanks to their photosynthetic metabolism. A vast literature is indeed available on CO_2 fixation [125–129]. Major issues for the adaptation of microalgae cultures to biogas upgrading are the low conversion efficiency, the production of O_2 during photosynthesis (not adapted to gas-grid injection, see 1.2.3.2) and the impact of the daylight cycle. A recent study assessed the combination of a 50 L open-photobioreactor with a water absorption column. Biomethane was continuously produced during 7 days at any time regardless of day/night cycle ($y^{out}_{CH_4} = 96 - 98$ %) but the biogas load was limited (1.0 $m^3_{CH_4}.m^{-3}_{reactor}.d^{-1}$). Moreover, mass balances demonstrated that a transfer of CO_2 from the liquid to the atmosphere was the main phenomenon responsible for its removal [130].

Biological methanation is then a more promising way than microalgae cultures. It offers the possibility for a better integration of energy production systems. Though, more economical data are needed to confirm its interest as a biogas upgrading process on its own. In parallel, research on *in-situ* biological methanation should be conducted to assess if the existing AD units could be upgraded by H_2 injection.

1.4 Selection of a solvent adapted to CO_2/CH_4 separation: a review

As for the available biogas upgrading technologies, the suitable solvents for biogas upgrading are divided into physical and chemical absorbents. This paragraph compares their performances in terms of their CO_2/CH_4 selectivity, CO_2 solubility, and compatibility with polymeric hollow fiber membranes.

1.4.1 Thermodynamical properties: gas-liquid equilibrium

Gas-liquid mass transfer is driven toward equilibrium between both phases. A gas-liquid system is in equilibrium when chemical potential equality is reached for every chemical species i:

$$\mu_i^g = \mu_i^l \qquad \forall i \qquad \text{Eq. 1.8}$$

where μ_i^g and μ_i^l are the chemical potentials of specie i in gas and liquid phases respectively.

The notion of fugacity f_i^{φ} was introduced and defined for each phase φ by Lewis in 1901 to describe the non-ideality of a system [131]:

$$\mu_i^{\varphi}\left(T, P, x_i^{\varphi}\right) = \mu_i^{\varphi,0}(T) + RT\ ln\left(\frac{f_i^{\varphi}\left(T, P, x_i^{\varphi}\right)}{f_i^{\varphi,0}(T)}\right) \quad \text{Eq. 1.9}$$

where T and P are respectively the temperature and the total pressure, superscript 0 represents the reference state (atmospheric pressure, pure compound) and x_i^{φ} the molar fraction of i in the corresponding phase φ.

The chemical potential equality (Eq. 1.8) is thus equivalent to fugacity equality:

$$f_i^{g}(T, P, y_i) = f_i^{l}(T, P, x_i) \quad \text{Eq. 1.10}$$

where x_i and y_i are the molar fractions in liquid and gas phases respectively.

The fugacity in the gas phase is expressed thanks to the fugacity coefficient Θ_i which describes the volumetric behaviour:

$$f_i^{g}(T, P, y_i) = y_i P \Theta_i(T, P, x_i) \quad \text{Eq. 1.11}$$

This coefficient is estimated by thermodynamical models among which Peng-Robinson, Soave-Redlich-Kwong and Lee-Kesler-Plöcker are the most common. This fugacity coefficient is equal to 1 when the gas phase is ideal. It significantly decreases below 1 when the pressure increases over several bars or when the temperature is close to the critical temperature of the component i. According to the nature of the biogas mixture and the investigated range of conditions ($P_g \leq 5\ bar\ g$ and $T_g \leq 30\ °C$), the gas mixture is considered ideal [11].

For a condensed phase (liquid or solid), the chemical potential is less dependent on the pressure. In 1923, Lewis introduced the fugacity of an ideal solution $f_i^{l,ideal}$ which is independent on the pressure [131]:

$$f_i^{l,ideal}(T, P, x_i) = x_i\ f_i^{l,0}(T) \quad \text{Eq. 1.12}$$

The deviation to ideality was described by the activity coefficient of the component i, γ_i:

$$f_i^{l} = \gamma_i\ f_i^{l,ideal} \quad \text{Eq. 1.13}$$

The reference state is commonly set to a pure solvent and an infinite dilution of the solute in the temperature and pressure conditions of the considered system. In practice, a solution is considered ideal when the total concentration of the species is below $5 \times 10^{-2}\ mol.L^{-1}$ [11]. According to the solubility of methane and carbon dioxide in water (Table 1.10), the solution is considered ideal.

The thermodynamical equilibrium is thus simplified by combining Eq. 1.10, Eq. 1.11 and Eq. 1.12 into:

$$y_i P = x_i \, f_i^{l,0}(T) \qquad \text{Eq. 1.14}$$

The above equilibrium equation was already found by Henry in 1802. He introduced the Henry's law which describes the dissolution of a gas in a liquid [132]:

$$y_i P = x_i \, k_H^{px}(T) \qquad \text{Eq. 1.15}$$

The Henry coefficient k_H^{px} has the dimension of a pressure. A dimensionless form of the Henry coefficient H^{cc} can be related to k_H^{px} thanks to the ideal gas law:

$$H^{cc}(T) = \frac{C_i^l}{C_i^g} = \frac{C_{tot}^l \, RT}{k_H^{px}(T)} \qquad \text{Eq. 1.16}$$

where C_i^{φ} is the volumic molar concentration of component i in the phase φ and R is the ideal gas constant.

At equilibrium, the partition coefficient m_i for specie i is thus dependant on pressure and temperature according to:

$$m_i \overset{\text{def}}{=} \frac{y_i}{x_i} = \frac{k_H^{px}(T)}{P} \qquad \text{Eq. 1.17}$$

All the above equations are valid between the molecules of component i in the gas phase and the molecular form dissolved in the liquid phase. If the molecular form dissociates in the solvent or reacts with another chemical compound, the subsequent reaction products are not considered (such as carbonate and bicarbonate ions for CO_2 dissociation). The total concentration of component i in the liquid $C_{i,tot}^l$ is introduced.

1.4.2 Physical absorption

1.4.2.1 Water

Water shows a stronger affinity with CO_2 than CH_4 due to its polarity [63]. On top of its low environmental impact, its availability and cost make it the first candidate to consider.

Absorption of carbon dioxide in pure water is widely documented [12, 133]. Carbon dioxide in solution forms unstable carbonic acid H_2CO_3 (ratio $CO_2 : H_2CO_3 > 99$ % [134, 135]). This diprotic acid dissociates into carbonate and bicarbonate ions (Eq. 1.18 and Eq. 1.19). The temperature dependency is described according to empirical models [136, 137].

$$H_2CO_3 \rightarrow HCO_3^- + H^+ \qquad pKa_1^{CO2} = 6.38 \ (@20\,°C) \qquad \text{Eq. 1.18}$$

$$HCO_3^- \rightarrow CO_3^{2-} + H^+ \qquad pKa_2^{CO2} = 10.38 \ (@20\,°C) \qquad \text{Eq. 1.19}$$

Experimental data on Henry coefficients are available in the literature for both CO_2 and CH_4. The exhaustive survey performed by Carroll on a CO_2-water system led to an empirical correlation valid at low pressure ($P_g < 10\ bar\ a$) and moderate temperatures ($273 < T < 433\ K$) [133]; at higher pressure ($P_g < 100\ MPa$), thermodynamic models are available [138]. Regarding methane, dissolution was assessed under intermediate pressures ($5 < P_g < 90\ bar\ a$) [139]. A wider thermodynamic model was established from a large survey of experimental data [140]. In the meantime, Sander is leading a project compiling Henry coefficients for more than 3 000 species [141]. The temperature dependence of Henry coefficient is described with the van't Hoff equation. The model is in accordance with the above experimental studies and therefore CO_2 and CH_4 dissolution will be described according to Sander for consistency reasons (Figure 1.22). Additional details on the compilation project of Sander is presented in Appendix E.

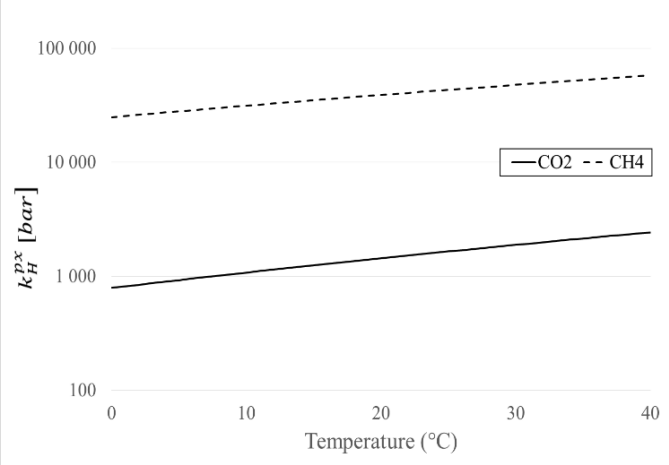

Figure 1.22 – CO_2 and CH_4 Henry coefficients between 0 and 40 °C

Gas	k_H^{px} [MPa]
CO_2	143.9
CH_4	3896
O_2	3963
N_2	8543
H_2S	57.22

Table 1.10 – Henry coefficients at 20°C [141]

The determination of Henry coefficients is carried out using pure gases. Then, the tabulated data do not take into account the potential interactions between the species. With regard to CO_2 and CH_4, Benizri proved the Henry coefficients to be not significantly affected by the CH_4-CO_2 interactions [63].

Both absorption of CO_2 and CH_4 are exothermic processes. The survey of Carroll suggested a correlation to estimate the enthalpy of dissolution for carbon dioxide $\Delta H_{dis,CO_2}$ according to the temperature [133]. The correlation is in accordance with calorimetric measurements $\Delta H_{dis,CO_2}(25\ °C) = -19.57 \pm 0.17\ kJ.mol^{-1}$ [142]. CH_4 dissolution is slightly less exothermic $\Delta H_{dis,CH_4}(25\ °C) = -13.18 \pm 0.07\ kJ.mol^{-1}$ [143]. Therefore, gas absorption may lead to a local increase in the water temperature. However, in a closed-loop process, the enthalpy variations at the absorption and desorption steps are compensating one another: no temperature rise is expected in the process steady state.

$$\Delta H_{dis,CO_2} = 106.56 - 6.2634 \times \frac{10^4}{T} + 7.475 \times \frac{10^6}{T^2}\ kJ.mol^{-1} \quad \text{Eq. 1.20}$$

1.4.2.2 Mineral salts

Addition of mineral salts to an aqueous solvent decreases the solubility of gases via the salting out effect. Water molecules indeed prefer to dissociate ionic species than hydrate the uncharged gas molecules [97].

The use of the salting out effect appears as counterintuitive but the reduced CO_2 solubility is compensated by an increased CO_2/CH_4 selectivity π_{CO_2/CH_4}.

$$\pi_{CO_2/CH_4} = \frac{C^l_{CO_2}}{C^l_{CH_4}} \qquad \text{Eq. 1.21}$$

The carbon dioxide dissolution in brine is widely studied for carbon capture applications [144–147]. Harned and Davis assessed the solubility of carbon dioxide at $P_{CO_2} = 1\ atm$ and in a low temperature range ($0 - 50\ °C$) [137]. Schumpe suggested an empirical correlation to estimate solubility of various gases in different electrolytes [148, 149]. The model is in good accordance with the experimental values reported by Harned but a deviation is observed for $T < 15°C$ (Figure 1.23).

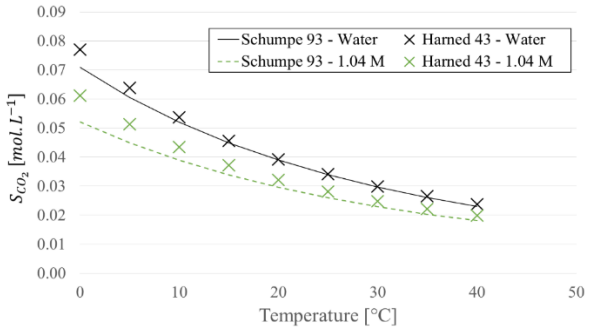

Figure 1.23 – CO_2 solubility in water and NaCl solution according to temperature ($P_{CO_2} = 1\ atm$)

Harned 1943: Experimental measurements [137]

Schumpe 1993 : Model for gas solubility in electrolyte solution [148, 149]

As there are no experimental data for CH_4, the model of Schumpe is adopted to estimate π_{CO_2/CH_4} (Figure 1.24). Na_2SO_4 is expected to have a higher selectivity compared to KCl or NaCl salts. However the CO_2 absorption capacity is significantly reduced (Table 1.11) and thus NaCl and KCl salts are preferred to avoid a decrease in the CO_2 absorption flowrate.

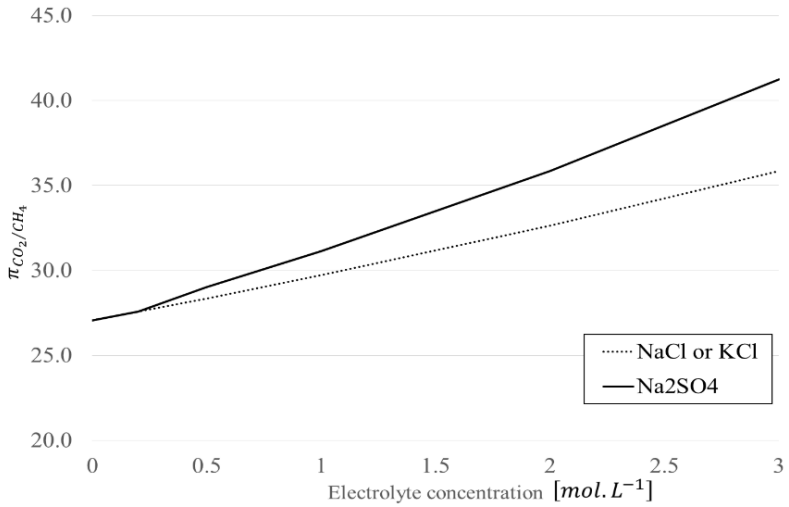

Figure 1.24 – CO_2/CH_4 selectivity according to electrolyte concentration (model from [149])

Absorbent	**Water**	**1M NaCl**	**1M KCl**	**1M Na_2SO_4**
S_{CO_2} $[10^{-3}\ mol.L^{-1}]$	39.0	29.9	31.5	19.8

Table 1.11 – Carbon dioxide solubility in different salt solutions (1M)
$P_{CO_2} = 1\ atm$ / $T = 20°C$ - model from [149]

The use of NaCl to biogas upgrading purposes was reported to increase the CH_4 recovery rate by 23 % when 1 M NaCl was added to deionized water without significantly impacting CO_2 absorption rate [97]. It was also noticed that the water vapour content was diminished in outlet biomethane due to a decrease in water activity [101]. However, these results have not been confirmed yet in an absorption/desorption cycle.

1.4.2.3 Organic solvents

The need for different gas separations has required to investigate a batch of organic molecules. Several have been selected and commercialized for carbon capture and natural gas sweetening applications thanks to their CO_2 solubility at least 3.5 times higher compared to water (Table 1.12).

	PC[24]	MeOH[25]	NMP[26]	DMPEG[27]	Water
Tradename	Fluor	Rectisol	Purisol	Selexol	
CO_2 solubility $[m^3.m^{-3}]$	3.4	14.4	3.57	3.63	0.96
CO_2/CH_4 selectivity	26	20	14	15	26.7
Boiling point $[°C]$	240	65	202	275	100
Surface tension $[N.m^{-1}]$	42	22.2	34.4	40.7	73.0
Viscosity $[mPa.s]$	3	0.6	1.65	5.8	1

Table 1.12 – Comparison of organic physical solvent properties for biogas upgrading [86, 150]

But compared to water, despite this higher CO_2 solubility, they exhibit a slightly lower CO_2/CH_4 selectivity. In addition, both the changes in surface tension and viscosity are questioning the combination of organic physical solvents with hollow fiber membranes, as explained below:

- the lower surface tension increases membrane wetting and thus mass transfer resistance;
- the higher solvent viscosity increases the pressure drop over the membrane module and enhance mass transfer resistance in the liquid phase.

For these reasons, very few studies in the literature have focused on gas-liquid separation processes involving organic physical solvents [86]. Moreover, the temperature required to favour their regeneration is incompatible with some hollow fiber material (PP polymer for instance).

1.4.2.4 Ionic liquids

Ionic liquids (ILs) are molten salts with a melting point lower than $100\,°C$. Contrary to common solvents, they are exclusively composed of ions. The research interest for ionic liquids has grown since the publication of an article in 1998 underlining their potential as solvents [151]. They are good candidates for carbon dioxide absorption due to their properties such as high CO_2 solubility, high thermal stability, negligible volatility and non-flammability. Research on ionic liquids is in addition pulled by post combustion capture. The absorption mechanism depends on the nature of the ionic liquid. Physical absorption is the most common one but solvent designers are also working on the functionalization of ionic liquids with amine groups to improve CO_2 absorption capacity. For ionic liquids where physical absorption is at stake, the anion is believed to play a key role though the cation also impacts CO_2 solubility. The CO_2 interaction with IL is suggested to be of Lewis acid-base type. Nonetheless, the free volume mechanism is also involved: similarly to hydrates (1.3.3.2), CO_2 molecules are hosted in the free cavities formed by the liquid molecules. An exhaustive review reports

[24] Propylene carbonate
[25] Methanol
[26] N-methyl-2-pyrrolidone
[27] Dimethylether Polyethyleneglycol

CO_2 Henry constants to be 5 orders of magnitude below the Henry coefficient for water [150], then indicating a very high solubility.

The combination of ionic liquids with membrane contactors for both post-combustion capture (PCC) and biogas upgrading applications still needs a proof-of-concept. The use of ionic liquids brings several challenges that must be addressed:

- high viscosity of ionic liquids, especially when loaded with CO_2, increases the liquid mass transfer resistance which is the limiting one;
- relatively low surface tensions which favours membrane wetting and consequently adds another mass transfer resistance. In addition, ionic liquids could degrade polymeric membrane materials by dissolution;
- toxicity and potential environmental impacts of IL are still unclear;
- high current prices of ionic liquid (~ $\$\,1\,000\,/kg$), far from those of conventional organic solvents [150].

PCC by several ionic liquids in different hollow fiber membrane materials was carried out by a Spanish team from the University of Cantabria [96, 152, 153]. The overall mass transfer coefficient is still one order of magnitude lower than water (Table 1.13). Regarding biogas upgrading, a numerical study reported that the use of imidazolium-based ionic liquids could reduce solvent circulation and energy consumption by 54 and 11% respectively while maintaining a satisfactory biomethane purity [154]. Similarly, the use of [bmim][Tf_2N] was assessed to reduce the solvent recirculation by 24 % while the specific energy consumption was comparable ($0.218\ kWh.Nm_{biogas}^{-3}$ against $0.212\ kWh.Nm_{biogas}^{-3}$) [54].

Reference	Membrane material	Absorbent	$K_{g,tot}$ $[10^{-5}\ m.s^{-1}]$
[153]	PP	Water	2.4 – 4.0
	PP	MDEA	2.0 – 3.3
	PP	GLY	10.0 – 17.0
	PP	GLY + PZ	13.0 – 23.0
	PP	[emim][EtSO4]	0.071
	PP	[emim][Ac]	0.11
[96]	PS[28]	[emim][Ac]	0.24 – 0.37
[152]	PVDF-[emim][Ac]	[emim][Ac]	1.7

Table 1.13 – Comparison of the overall mass transfer coefficients for ionic liquids

Ionic liquids have promising properties for carbon capture. Nonetheless, several challenges must be overcome before their industrial application. The price of ionic liquids is the major issue to develop an economical biogas upgrading process. Compared to conventional industrial processes with organic

[28] Polysulfone

solvents already existing, the development of biogas upgrading processes based on ionic liquids seems dubious.

1.4.3 Chemical absorption

1.4.3.1 Amines

Available chemical scrubbers for biogas upgrading are most often based on MEA, a primary amine or MDEA, a tertiary amine. Thermal swing is the separation principle for these amine-based processes. While CO_2 absorption can be performed at ambient temperature and low pressure, the CO_2-rich amine aqueous solution is conventionally regenerated under temperature above $120\,°C$ [10]. These temperatures being not suitable for polymeric hollow fibers, a packed column is necessary to perform solvent desorption, losing the advantages of HFMMs for this step (compactness and energy saving) (1.3.3.1).

1.4.3.2 Amino-acid salts (AAS)

AAS have been considered to replace alkanolamines in CO_2 absorption processes. The carboxylate group (-COOH) is neutralized by alkaline salts to form AAS [66]. The reaction mechanism is similar to the amine-CO_2 one presented in Figure 1.11. Despite a higher price, AAS offer several advantages compared to conventional amines:

- thanks to their high molecular weight, AAS have a low volatility. The need for solvent make-up due to absorbent loss in the regeneration unit ($\$0.19 - 1.31/ton_{CO_2}$ in PCC [150]) is thus considerably reduced;
- naturally occurring, AAS are more resistant to oxidative degradation which is an industrial issue in chemical absorption [67];
- they have a higher biodegradability which is a point of vigilance in the context of a rural environment to enable environment safe disposal [155, 156].

Song performed a systematic comparison of absorption and desorption performances of 16 AAS [157]. Sterically hindered AA are the most promising since they demonstrate increased cyclic capacities, slower initial absorption rates and faster initial desorption rates. It favours a higher operational CO_2 loading with equivalent CO_2 fluxes in the absorption and desorption units. In addition, desorption was carried out by stripping at lower temperatures almost compatible with the polymeric hollow fiber materials ($80\,°C$).

The use of AAS for biogas upgrading has been scarcely investigated [66]. Table 1.14 lists the values of absorbed CO_2 fluxes $J_{CO_2}^{abs}$ mentioned in experimental studies involving AAS and HFMMs. Potassium glycinate used in a HFMM proved to capture carbon dioxide from flue gas with a removal efficiency above 90 %. Promotion by PZ increases the absorption performance of the solvent [158]. An experimental study demonstrated potassium arginate to have a superior CO_2 removal performance compared to several amines. 97 % biomethane quality was achieved but the solvent regeneration was not investigated [159]. The cation of the alkaline salt turns out to have a significant role in the CO_2

absorption mechanism. Na^+ salts showed an increase by $10-15$ % in the CO_2 absorbed flux compared to K^+ salts [71].

Reference	Membrane material	Membrane area $[m^2]$	Gas composition	Absorbent	$J_{CO_2}^{abs}$ $[10^{-3}\ mol.m^{-2}.s^{-1}]$
[159]	PP	0.565	CO_2/CH_4 $y_{CO_2}=30-50$ %	20% wt K-arg	3.80 – 5.50
				20% wt MEA	3.39 – 4.67
				20% wt DEA	3.19 – 3.83
				20% wt TEA	0.56 – 0.94
[158]	PP	0.176	CO_2/N_2 $y_{CO_2}=8.6$ %	1 M K-Gly	0.4 – 2.0
				0.75 M K-Gly + 0.25 M PZ	0.6 – 2.2
[71]	28% PVDF	0.0034	CO_2/CH_4 $y_{CO_2}=10$ %	0.5 M K-Gly	1.60 – 1.78
				0.5 M K-Sar	1.62 – 1.82
				0.5 M Na-Gly	1.83 – 1.95
				0.5 M Na-Sar	1.90 – 1.97
				0.5 M MEA	1.50 – 1.72

Table 1.14 – Comparison of the absorbed CO_2 flux for AAS

Arg=Arginige, Gly= Glycine, Sar=Sarcosine

AAS are promising CO_2 absorbents which present the advantages of amines in chemical absorption and avoid some of their operational issues (solvent loss, degradation, biodegradability). Nonetheless, the question of the solvent regeneration has not been addressed yet. It is the major barrier to the development of a biogas upgrading process utilizing HFMMs at the desorption step.

1.4.3.3 Alkali salts: potassium carbonate

Alkali salts react with CO_2 according to an acid-base reaction and therefore demonstrate high absorption rates. Caustic solvents (sodium hydroxide, potassium hydroxide and calcium hydroxide) are the second most abundant class of chemical absorbers after amine solutions [66]. Though the stronger the chemical affinity, the more energy is required to regenerate the alkali solution. For instance, alkaline scrubbing with regeneration applied to landfill biogas is not economically feasible. Operational costs are high due to low solvent regeneration rates (61%) and the price of NaOH ($0.79\ €_{2012}.kg^{-1}$) [160].

Among these alkali salts, there is a growing interest for potassium carbonate for its potential as green CO_2 absorbent. Compared to amine solutions, a potassium carbonate solution needs a lower regeneration energy [161], displays lower degradation rates and is less corrosive. In the view of industrial development, potassium carbonate processes can also operate on a pressure swing cycle as opposed to amines which operate on a temperature swing cycle [162]. The main issue of potassium carbonate is related to its slower reactions. Among the set of reactions at stake (Eq. 1.23-Eq. 1.26), Eq. 1.23 is fast but still the limiting step of the absorption process [163].

$$CO_{2(g)} \rightleftarrows CO_{2(aq)} \quad \text{Eq. 1.22}$$

$$CO_{2(aq)} + OH^-_{(aq)} \rightleftarrows HCO_3^-{}_{(aq)} \quad \text{Eq. 1.23}$$

$$HCO_3^-{}_{(aq)} + OH^-_{(aq)} \rightleftarrows CO_3^{2-}{}_{(aq)} + H_2O_{(aq)} \quad \text{Eq. 1.24}$$

$$CO_{2(aq)} + H_2O_{(aq)} \rightleftarrows H_2CO_3{}_{(aq)} \quad \text{Eq. 1.25}$$

$$H_2CO_3{}_{(aq)} + OH^-_{(aq)} \rightleftarrows HCO_3^-{}_{(aq)} + H_2O_{(aq)} \quad \text{Eq. 1.26}$$

Among the numerous process parameters, a temperature rise increases the absorption kinetic rate [164].

In the sake of process efficiency, several promoters have also been studied to enhance mass transfer. They are classified into two categories: inorganic promoters (acids or salts) and organic promoters (amines and AA) [163]. In the last decade, enzyme promotion was investigated with carbonic anhydrase (CA) or metal compounds mimicking its active site [165–169]. Literature reviews underline the need for thermal and chemical stability [163, 170]. In this regard, AAS are promising but long-tests over a range of industrial conditions are still needed.

Compared to amine solutions, a solution of 1M K_2CO_3 gives a lower absorption flux by one order of magnitude for PCC applications (Table 1.15). Though, its combination with dense membranes (PVTMS[29]) is efficient to remove CO_2 for PCC applications [171]. In the same study, investigation of the desorption performance demonstrated that it depends on temperature and liquid flowrate. Promotion by PZ was significant: the desorbed flow was doubled. The higher flux recorded (2.9×10^{-4} mol. m^{-2}. s^{-1}) is slightly below the absorbed CO_2 flux presented in Table 1.15. It is likely that a porous membrane will improve this result.

Absorbent	$J_{CO_2}^{abs}$ [10^{-3} $mol.m^{-2}.s^{-1}$]
1 M MEA	4.5
1 M PZ	9.8
1 M K_2CO_3	0.5

Table 1.15 – Comparison of the absorbed CO_2 flux for K_2CO_3 and amine solutions [172]
PP membrane, membrane area $S = 6.53 \times 10^{-3}\ m^2$; $y_{CO_2} = 15\ \%$

Enzymatic promoters offer promising possibilities to improve K_2CO_3 absorption and desorption kinetics. CA is extremely efficient to catalyse both ways Eq. 1.23 [165, 173, 174]. Its use in industrial processes faces the challenges of its thermal and chemical stabilities as well as its high price. To avoid denaturation and minimize the quantity of CA, immobilization strategies are investigated [91]. Immobilization on hollow fibers improves the absorbed CO_2 flux by 36 % in an artificial lung device [175, 176]. Mimic enzyme based on divalent metals are more competitive cost wise, thermally more stable but less active. 10 mM Zn-cyclen increased by 10-fold the kinetic rate constant of a 0.5 M K_2CO_3

[29] Polyvinyltrimethylsilane

solution when used in a porous tubular glass membrane contactor [167]. For a 10 % CO_2 gas mixture, the absorbed CO_2 flux was in a range comparable to Table 1.14 ($1.4 - 1.8 \times 10^{-3}\ mol.m^{-2}.s^{-1}$).

1.4.4 Economical and technical comparison

The various solvents available for biogas upgrading are compared from a techno-economic point of view (Table 1.16). As physical solvents, water and mineral salt solutions are easy to operate but have the lowest absorbed CO_2 flux reported in the literature. Their combination with HFMMs is of interest because membrane wetting is limited thanks to higher surface tension and contact angle. Several organic solvents have a good absorption potential but their higher viscosity and lower surface tension might significantly reduce mass transfer in hollow fiber membranes. Though, no experimental work has been reported for biogas upgrading application to confirm this assertion. Regarding the use of ILs, the production price is a big barrier towards an industrial development. In addition, their high viscosity significantly limits mass transfer and might be a strong obstacle to reach a satisfying absorption efficiency.

Chemical absorbents have the advantage to maintain a high mass transfer potential. Though, the temperature and energy requirements for the absorbent regeneration are the main issues. AAS present the advantages of an amine group and avoid some of the amine operational problems (biodegradability and toxicity, high temperature at desorption, volatility, stability). A systematic study of the desorption performance by means of pressure swing in hollow fiber modules should be conducted. Last but not least, potassium carbonate is a promising reactive that can be regenerated by pressure swing. Its industrial use is conditioned by a techno-economic viable promotion to improve the absorption and desorption kinetics.

Water and mineral salts solution are selected to develop a robust and cost-effective process with very limited chemical consumption. Among chemical absorbents, AAS solution was also selected for experimental testing.

	Water	Mineral salts	Organic solvents	ILs	MEA	AAS	K_2CO_3
Advantages	Chemical-free Tolerant to pollutants	Improved CO_2/CH_4 selectivity Tolerant to pollutants	High CO_2 solubility	High CO_2 solubility	High CO_2 solubility Highly reactive	Highly reactive Low volatility Resistant to oxidative degradation High CO_2 solubility	High CO_2 solubility Desorption can be operated by pressure swing
Drawbacks	Low CO_2 solubility	Low CO_2 solubility	Poisoned by H_2S Low surface tension Higher solvent viscosity	High current price High viscosity Low surface tension	High temperature at desorption (T > 120 °C) Poisoned by H_2S Low surface tension Moderate viscosity	Elevated price Low surface tension Moderate viscosity Poisoned by H_2S	Slow kinetics
$J_{CO_2}^{abs}$ [10^{-3} $mol.m^{-2}.s^{-1}$]	0.08 – 0.16	0.08-0.15		NS	1.50 – 4.67	0.4 – 5.5	0.5
Solvent cost [$\$.kg^{-1}$]	-	KCl: 0.2	MeOH: 0.7 NMP: 4 DMPEG: 2.5	1 000 (lab scale) 40 (large scale)	1.5-2	> MEA	2.4

Table 1.16 – Solvent suitability for a biogas upgrading process using hollow fiber membrane contactors [10, 71, 97, 150, 158, 172, 177]

1.5 Sizing of an industrial gas-liquid absorption unit

1.5.1 Dimensioning solvent flowrate

In a gas-liquid absorption process, the flowrates ratio Q_g/Q_l is a crucial operating parameter. The minimal solvent flowrate required to absorb a given CO_2 flowrate is calculated by a carbon dioxide mass balance on the absorption module (Figure 1.25).

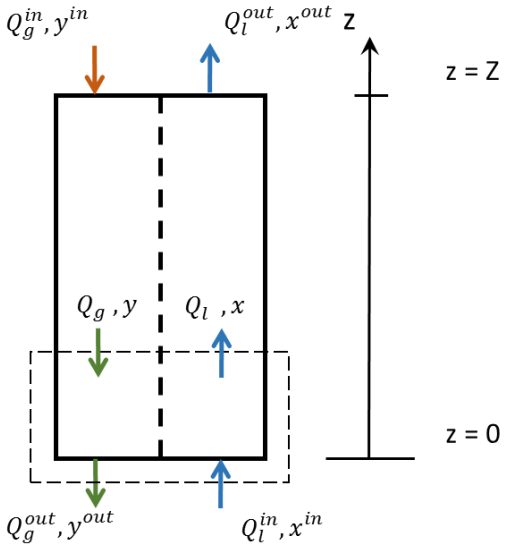

Figure 1.25– Counter-current absorption in a gas-liquid exchanger

The composition of the inlet biogas, considered as a binary mixture of CO_2 and CH_4, is set to $y_{CO_2}^{in} = 40$ %. Therefore, the total gas flowrate Q_g significantly varies across the absorption module. The absorption of methane is neglected; methane is then considered as inert and noted I. Its flowrate G_I is constant across the module and reduced variables for molar fractions X and Y (related to CO_2) are introduced. The liquid flowrate is constant as the dissolved CO_2 quantity is rather low compared to the water flowrate.

$$Q_{g,I} = y_I^{in} Q_g^{in} = y_I^{out} Q_g^{out} = y_I \; Q_g \qquad \text{Eq. 1.27}$$

$$Y = \frac{y}{1-y} \qquad \text{Eq. 1.28}$$

$$X = \frac{x}{1-x} \qquad \text{Eq. 1.29}$$

Fixing y^{in}, y^{out} and x^{in} (the molar fractions of CO_2 in the different phases), the carbon dioxide mass balance on the absorption unit links the inert flowrates ratio to the outlet molar fraction X^{out}:

$$\frac{Q_{g,I}}{Q_{l,I}} = \frac{X^{out} - X^{in}}{Y^{in} - Y^{out}} \qquad \text{Eq. 1.30}$$

In an infinite exchanger, the outlet liquid would be at equilibrium with the inlet biogas ($X^{out} = X^{sat}$). The minimal liquid flowrate Q_l^{min} is then given by the following equation:

$$\frac{Q_l^{min}}{Q_{g,I}} = \frac{Y^{in} - Y^{out}}{X^{sat} - X^{in}} \quad \text{Eq. 1.31}$$

where X^{sat} is the reduced CO_2 molar fraction relative to the saturation (hypothetic equilibrium with the inlet biogas).

In industrial columns the liquid flowrate is generally oversized by 40 % [11] and thus the theoretical optimized ratio Q_g^{in}/Q_l is derived according to:

$$\left(\frac{Q_g^{in}}{Q_l}\right)_{th} = \frac{1}{1.4} \times \frac{Q_{g,I}/\left(1 - y_{CO_2}^{in}\right)}{Q_l} = \frac{1}{1.4\left(1 - y_{CO_2}^{in}\right)} \frac{X^{sat} - X^{in}}{Y^{in} - Y^{out}} \quad \text{Eq. 1.32}$$

The theoretical ratio Q_g^{in}/Q_l obtained with water or 1M KCl solution is displayed in Figure 1.26. These curves suppose that the solvent entering the absorption column is CO_2-free ($x^{in} = X^{in} = 0$) and that CO_2 is completely removed from the gas stream ($y_{CO_2}^{out} = Y^{out} = 0$ %). The lower CO_2 absorption capacity of 1 M KCl solution explains the decrease of the theoretical Q_g^{in}/Q_l ratio compared to water.

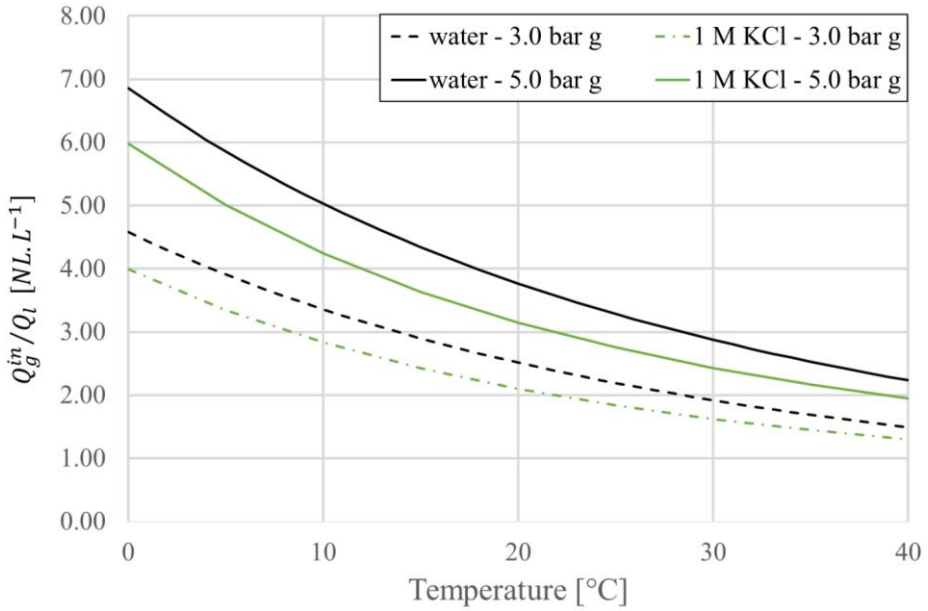

Figure 1.26– Q_g^{in}/Q_l ratio required for complete CO_2 removal according to temperature and pressure conditions - according to Eq. 1.32

After the solvent flowrate has been determined for a given biogas flowrate, the CO_2 removal efficiency depends on mass transfer kinetics and equipment size.

1.5.2 Scale-up

In the experimental section (3.5), the process will be optimized according to the process indicators (operating conditions and process configurations). The upscaling of these experimental results to an industrial unit will be carried out according to two different methods:

- dimensional analysis which is a typical Process Engineering method relying on dimensionless numbers;
- predictive tools such as the method of transfer units (HTU Height of a Transfer Unit, NTU Number of Transfer Units) or mass transfer models.

1.5.2.1 Dimensional analysis method

Dimensional analysis provides a methodology to set up a successful roadmap from bench-scale experimental design to industrial unit sizing. It is relying on a fundamental assertion: "a mathematical formulation of a physicotechnological problem can be of general validity only when the process equation is dimensionally homogenous" [178]. This method is especially relevant for process sizing when the physical mechanisms at stake in the process are known.

Dimensional analysis can be carried out in 4 steps:

1. Relevance list and reduction of the number of parameters;
2. Scale-up of the desired operating conditions;
3. Identification of different process regimes;
4. Establishment of an experimental roadmap.

In a scale-up perspective, focus was made on stages 1 and 2. Nonetheless, attention was paid to the conservation of the process regime.

During the first step, all the relevant physical parameters describing the process are listed. The physical parameters can be classified according to the target quantity, the geometrical parameters, the physical properties and the process related parameters [178]. Then, the number of different dimensions occurring in the parameter units is derived from this relevance list. The Pi theorem formulated by Buckingham is then applied:

"Every physical relationship between n physical quantities can be reduced to a relationship between $m = n - r$ mutually independent dimensionless groups, where r stands for the rank of the dimensional matrix" (generally equal to the number of the basic quantities contained in them) [178, 179]

From this theorem, the relationship between dimensionless numbers is investigated at the pilot scale.

In the second step, the scale-up is relying on the theory of models:

"Two processes may be considered completely similar if they take place in similar geometrical space and if all the dimensionless numbers necessary to describe them have the same numerical value" [178]

The geometric similarity and the conservation of dimensionless numbers are thus sufficient for a proper scale-up.

1.5.2.2 Predictive scale-up with simulation models

An improved understanding of the mass transfer mechanisms in the system lead to the development of predictive models for scale-up purposes.

A typical 1D method for packed column systems is the method of transfer units [65]. The overall mass transfer coefficient is expressed in the resistance-in-series model [11, 177]. The carbon dioxide mass balance on the liquid phase over a slice dz of the mass exchanger gives:

$$Q_l\, dx = K_L^0 (x^* - x)\, a\Omega dz \qquad \text{Eq. 1.33}$$

where Q_l is the liquid molar flowrate, x is the liquid molar fraction in the slice, x^* is the equivalent liquid molar fraction at equilibrium with the gas phase in the slice, K_L^0 is the overall mass transfer coefficient relative to the liquid phase in $mol.m^{-2}.s^{-1}$, Ω the section area of the mass exchanger and a its specific exchange area.

By integration over the absorption unit (the mass transfer coefficient is considered constant over the mass transfer unit), the height of the module is expressed by the product of the height of a transfer units (HTU_L) and the number of the transfer units (NTU_L):

$$Z = \frac{Q_l}{K_L^0 a\Omega} \times \int_{x^{in}}^{x^{out}} \frac{dx}{x^* - x} = HTU_L \times NTU_L \qquad \text{Eq. 1.34}$$

The NTU required for a given separation performance measures the difficulty of the separation. It depends on the physico-chemical equilibrium and on the separation performance. The HTU is characteristic of an equipment and its hydrodynamics: it measures its separation efficiency.

For the sizing of the industrial unit, the NTU value achieved at the pilot scale is conserved to obtain similar performances. The NTU value is derived from Eq. 1.34 applied at the experimental pilot scale. a, Ω and Z being geometrical parameters provided by the manufacturer, the overall mass transfer coefficient K_L^0 is the only parameter that must be obtained from experimental measurements It is estimated by means of the logarithmic mean of the exchange potential Δx_{ML} [180–182]:

$$Q_l\left(x^{out} - x^{in}\right) = K_L^0 a\, \Delta x_{ML}\, \Omega Z \qquad \text{Eq. 1.35}$$

$$\Delta x_{ML} = \frac{(x^{out,*} - x^{out}) - (x^{in,*} - x^{in})}{\ln(x^{out,*} - x^{out}) - \ln(x^{in,*} - x^{in})} \quad \text{Eq. 1.36}$$

The mass transfer unit method is widespread for the upscaling of separation techniques. The consistency of the method is conditioned by a good estimation of the overall mass transfer coefficient. This parameter is highly dependent on the hydrodynamic conditions (1.6.2.1). Therefore, special care must be taken to keep the same Reynolds number from the pilot to the industrial module.

Predictive mass transfer models can also provide tools for the process scale-up. A model properly describing the local mass transfer phenomena in good agreement with the pilot scale experimental results is relevant for process upscaling. A multi-scale model is though essential to avoid the scale dependency of the predictive model. The mass transfer phenomena and the various modelling strategies are presented in the next paragraph.

1.6 Mass transfer modelling in hollow fiber membrane contactors

Mass transfer modelling is presented with the objective to develop a predictive multi-scale model.

1.6.1 Mass transfer in a membrane contactor

The membrane is a support to the gas-liquid interface. Due to its hydrophobic nature, the membrane pores are occupied by the gas phase (Figure 1.27). Mass transfer is therefore occurring in three different domains: the gas phase, the membrane phase and the liquid phase.

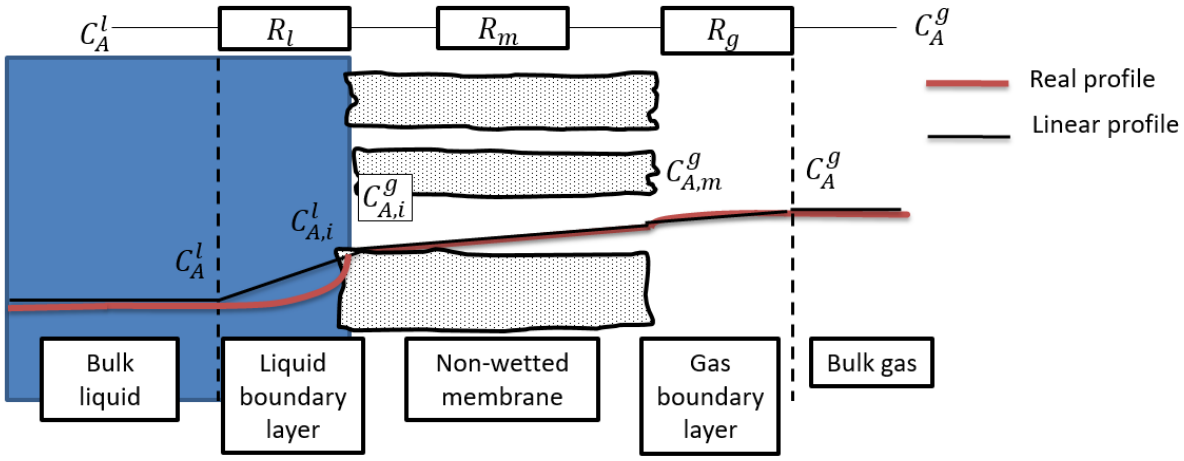

Figure 1.27– Concentration profile at the gas-liquid interface during absorption

With $\boldsymbol{R_l}$, $\boldsymbol{R_m}$, $\boldsymbol{R_g}$ being the resistances in the liquid, membrane and gas phases respectively. $\boldsymbol{C_A^l}$ and $\boldsymbol{C_A^g}$ are the concentrations of specie A in the liquid and gas bulks respectively. Subscripts $\boldsymbol{i}$ and $\boldsymbol{m}$ are relative to the gas-liquid interface and to the membrane inner diameter.

The equations of continuity are governing mass transfer in the successive domains. Its general expression expressed in molar units for the specie A is [183]:

$$\frac{\partial c_A}{\partial t} + \left(\vec{\nabla} \cdot c_A \, \vec{u}\right) = -\left(\vec{\nabla} \cdot \overrightarrow{J_A}\right) + r_A \qquad \text{Eq. 1.37}$$

where c_A is the molar concentration of A ($mol.m^{-3}$), $\vec{u}$ is the velocity vector ($m.s^{-1}$), $\overrightarrow{J_A}$ is the diffusion flux of A ($mol.m^{-2}.s^{-1}$) and r_A the source term ($mol.m^{-3}.s^{-1}$).

Two assumptions allow to simplify Eq. 1.37 into Eq. 1.38:

- industrial units will be operated at steady state. Therefore, the variables are independent on time;
- only physical absorption is considered: the reaction term r_A vanishes.

$$\left(\vec{\nabla} \cdot c_A \, \vec{u}\right) = -\left(\vec{\nabla} \cdot \overrightarrow{J_A}\right) \qquad \text{Eq. 1.38}$$

Descriptions of the diffusion flux and of the flow are now needed. The membrane module has to be described more specifically.

Several options are available in the design of HFMMs. First, the hollow fiber lumenside can be occupied by the gas or the liquid phase, depending on the application. Then, different flow configurations occur in membrane modules: counter-current flows, co-current flows and cross-flows. Choice was made to develop a biogas upgrading process based on a membrane module commercially available at an industrial size for future industrial upscaling (Liqui-Cel® Extra-Flow module produced by Membrana presented in Figure 1.28). In its design, each module comprises a diverting baffle at its center to enhance mass transfer efficiency. It leads to complex hydrodynamics in the shellside, an intermediate between the counter-current flow and the cross-flow configurations. Technical specifications require the liquid to flow in the shellside to minimize pressure drop.

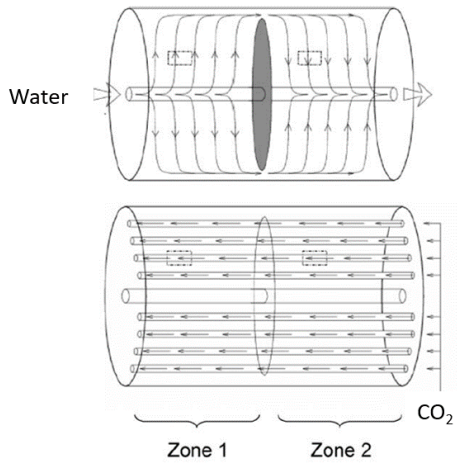

Figure 1.28– Flow configuration in the Liqui-Cel® Extra-Flow membrane contactor (adapted from [184])

In the liquid phase, the diffusion term is expressed by Fick's law and Eq. 1.38 is transformed into Eq. 1.40 assuming that the diffusion coefficient in the liquid phase D_A^l is constant:

$$\overrightarrow{J_A} = -D_A^l \vec{\nabla} c_A \qquad \text{Eq. 1.39}$$

$$\left(\vec{\nabla} \cdot c_A \, \vec{u}\right) = D_A^l \nabla^2 c_A \qquad \text{Eq. 1.40}$$

1.6.2 Modelling strategies

Different hypotheses are made to simplify the mass transfer equations presented above. The subsequent modelling strategies present a variable level of complexity. Table 1.17 summarizes the main assumptions and advantages.

Modelling strategy	Flow regime assumption		Advantages	Comments
	Gas phase	*Liquid phase*		
Resistance-in-series (1D)	Plug flow	Plug flow	Classical approach	Relies on a good prediction of mass transfer coefficients
1D-2D model	Plug flow	Axial convection and radial diffusion	Compromise in terms of complexity	Supposes a parallel flow configuration
Convection diffusion (2D)	Axial convection and radial diffusion	Axial convection and radial diffusion	Influence of solvent and hydrodynamics can be investigated separately	Supposes a parallel flow configuration

Table 1.17 – Summary of the different modelling strategies reported in the literature (adapted from [91, 185])

The liquid temperature (on which the gas-liquid equilibrium is dependent) is often considered constant for physical absorption. Though, chemical absorption of CO_2 in amine solutions is exothermic and heat mass transfer should be considered [186]. In these absorption systems in which higher operating temperatures occur, the water loss due to evaporation may be significant.

Pressure of both phases are important parameters to describe gas-liquid equilibrium and membrane wetting (1.6.3). The liquid phase is more subject to pressure drop in the membrane module due to its higher dynamic viscosity. Gas phase pressure drops in such systems reported in the literature are often below $0.05\ bar\ g$, which is negligible against the pressure applied in the experiments. Regardless of the phase, the pressure drop in the lumenside is commonly described by the Hagen-Poiseuille equation:

$$\frac{dP_\varphi}{dz} = -\frac{8\mu_\varphi \bar{u}_\varphi}{r_{fi}^2} \quad \text{Eq. 1.41}$$

where P_φ is the pressure in phase φ, μ_φ is the dynamic viscosity of phase φ, $\bar{u}_\varphi$ is the average velocity of phase φ and r_{fi} is the inner radius of the hollow fiber.

The pressure drop in the shellside is described by Darcy's law, as the fiber bundle is considered as a porous macroscopic medium. The permeability of the fiber bundle is estimated thanks to Kozeny-Carman equation [185–187].

The 1D and 2D modelling strategies are specifically presented with corresponding studies. The 1D-2D model is a combination of both: the gas and the membrane phases are described by a mass transfer coefficient.

1.6.2.1 Resistance-in-series (1D)

The resistance-in-series model introduced by Lewis and Whitman is applicable to gas-liquid or liquid-liquid systems [188]. It assumes that for each phase, the mass transfer resistance is located in a thin diffusion layer close to the interface in which the solute concentration profile is linear; the concentration in the bulk outside the thin layer is constant (Figure 1.27). At the interface the phases are supposed in equilibrium. It is a common model for gas-liquid absorption in HFMMs [180, 182, 185, 187, 189–191].

In a diffusion layer, the diffusion flux $\overrightarrow{J_A}$ is therefore proportional to the concentration difference; J_A is positive or negative depending on the direction of transfer:

$$J_A = k_A \left(c_A^{bulk} - c_A^{interface}\right) \quad \text{Eq. 1.42}$$

For mass transfer in HFMMs, the overall resistance relative to the liquid phase R_L is expressed as the sum of three different resistances in series R_g, R_m and R_l respectively in the gas phase, the membrane and the liquid phase (Figure 1.27). The expression of the overall resistance depends on the nature and geometry of the membrane. Dupuy detailed the different forms of the resistance for liquid-liquid extraction using HFMMs [192]. Liqui-Cel® Extra Flow modules require the gas to flow in the lumenside while water is flowing in the shellside. In this case, the overall mass transfer coefficient relative to the liquid phase K_L is defined by:

$$\frac{1}{K_L\ d_{fo}} = \frac{1}{k_l d_{fo}} + \frac{H^{cc}}{k_m\ d_{ML}} + \frac{H^{cc}}{k_g\ d_{fi}} \quad \text{Eq. 1.43}$$

where H^{cc} is the dimensionless Henry coefficient (Eq. 1.16), d_{fo}, d_{fi}, d_{ML} are respectively the outer, inner and logarithmic mean diameters of the hollow fiber, and k_l, k_m, k_g the mass transfer coefficients of the liquid, membrane and gas phases respectively.

The mass transfer coefficients are generally considered as constant over the membrane module; this assumption is valid as long as the hydrodynamic conditions and fluid and membrane properties are not significantly modified in the module.

This mass transfer description requires a reliable estimation of the respective mass transfer coefficients. Empirical correlations with dimensionless numbers are used to predict them. These correlations are in the following general form, named Chilton-Colburn equation [191, 193]:

$$Sh = f(Re, Sc) = \omega Re^{c} Sc^{\frac{1}{3}} \quad \text{Eq. 1.44}$$

where Sh is the Sherwood number, Re is the Reynolds number and Sc is the Schmidt number. ω and c are dimensionless parameters of the correlation; they depend on the system geometry.

The lumenside mass transfer coefficient is often estimated by the theoretical Lévêque correlation [182, 189–191, 194, 195]:

$$Sh = 1.62 \left(Re\, Sc\, \frac{d_{fi}}{L_f} \right)^{1/3} = 1.62\, Gz^{1/3} \quad \text{Eq. 1.45}$$

where d_{fi} and L_f are respectively the inlet diameter and length of the hollow fiber, and Gz is the Graetz coefficient.

For low Graetz number ($Gz < 6$), another equation was suggested [184, 196]:

$$Sh = 0.5\, Gz \quad \text{Eq. 1.46}$$

Gabelman and Hwang listed the correlations established in various HFMM geometries [87]. Relevant correlations are presented in Table 1.18 for the liquid phase flowing in the shellside. Experimental correlations are determined by the Wilson plot method from the expression $Sh = f(Re)$ [180, 197].

N°	Flow	Flowrate Q_l $[10^{-6}\ m^3/s]$	Correlation	Reference
1	Parallel flow	10 − 50	$Sh = 0.32\, Re^{0.61} Sc^{0.33}$ (1) $Sh = 0.39\, Re^{0.59} Sc^{0.33}$ (2)	[198, 199]
2		0.2 – 200	$Sh = 1.76\, Re^{0.82} Sc^{0.33}$	[200]
3		0.2 – 200	$Sh = 0.56\, Re^{0.62} Sc^{0.33}$	[201]
4		32 – 13 279	$Sh = 2.15\, Re^{0.42} Sc^{0.33}$	[193]
5		0.57 − 1.58	$Sh = 0.34\, Re^{0.67} Sc^{0.33}$	[197]
6	Cross-flow	NS	$Sh = 1.38\, Re^{0.34} Sc^{0.33}$	[195]

Table 1.18 – Empirical mass transfer correlations for liquid flowing in the shellside

The correlation parameters presented in Table 1.18 are variable ($\omega = 0.32 - 2.15, c = 0.34 - 0.82$). It is dependent on the flow configuration and the membrane module geometry such as the packing

fraction of the fiber bundle ϕ. Based on the experimental data from Sengupta [202], the correlation (4) was suggested and validated for commercial Extra-Flow® modules of different sizes.

But the definition of the dimensionless numbers is also of prime importance for consistency [193]. As presented in Figure 1.28, in the commercial Extra-Flow® modules, the flows are neither parallel nor crossed; it is the major difficulty to overcome. For instance, the correlation (5) established by Mavroudi for pure CO_2 absorption in water assumed a completely cross-flow pattern with two distinct zones (distribution and collection tubes); in contrast, the dimensionless numbers were calculated with a parallel flow assumption [197]. A broad review of these correlations by Shen stated that the following expression was valid assuming a parallel flow configuration (regardless of the intern geometry) [203]:

$$Sh = 0.55\, Re^{0.72} Sc^{1/3} \qquad \text{Eq. 1.47}$$

This correlation is valid in a large range of conditions ($0.1 < Re < 250;\ 0.32 < \phi < 0.45$). The hydraulic diameter d_H used in dimensionless number calculations can be estimated with Eq. 1.48[30].

$$d_H = \frac{4 \times S_{wet}}{d_{fo}} \qquad \text{Eq. 1.48}$$

where S_{wet} is the surface wetted by the absorbent and d_{fo} is the outer diameter of the hollow fiber.

Nevertheless, the assumption of a parallel flow in membrane modules including a center diverting baffle is questionable; indeed the correlation suggested by Shen results in 20 % deviation [203]. In this type of module, hydrodynamic is complex and the liquid mass transfer coefficient is likely to vary across the module. The consideration of the local hydrodynamic conditions could improve the estimation of the liquid shellside mass transfer coefficient.

To estimate its mass transfer coefficient k_m, the membrane is assimilated to a network of non-connected cylindrical pores [204]:

$$k_m = \frac{D^{eff} \varepsilon_m}{\tau_m \delta_m} \qquad \text{Eq. 1.49}$$

where D^{eff} is the effective diffusion coefficient within the membrane pores, $\varepsilon_m, \tau_m, \delta_m$ are respectively the porosity, the tortuosity and the thickness of the membrane material.

The diffusion mechanisms at stake in the pores and the estimation of the effective diffusivity are discussed in Appendix G. The description of membrane wetting which has an influence on mass transfer is discussed in the relevant paragraph (1.6.3).

[30] For the calculation of the wetted surface S_{wet}, the section of the collection/distribution tube must be withdrawn from the module cross-section.

1.6.2.2 Convecto-diffusive models (2D)

Convecto-diffusive models simplify the mass transfer equations of the different domains (Eq. 1.38 and Eq. 1.40) to particular directions as presented in Table 1.19. A reactive term is added to these equations to consider chemical absorption. Figure 1.29 provides a schematic representation of the different domains with concentration and velocity profiles.

Domain	Differential mass balance
Gas phase	$u_{z,g}\frac{\partial C_A^g}{\partial z} = \frac{1}{r}\frac{\partial}{\partial r}\left(rD_A^g\frac{\partial C_A^g}{\partial r}\right)$
Membrane phase	$0 = \frac{1}{r}\frac{\partial}{\partial r}\left(rD_A^m\frac{\partial C_A^g}{\partial r}\right) + \frac{\partial}{\partial z}\left(D_A^m\frac{\partial C_A^g}{\partial z}\right)$
Liquid phase	$u_{z,g}\frac{\partial C_A^l}{\partial z} = D_A^l\frac{1}{r}\frac{\partial}{\partial r}\left(r\frac{\partial C_A^l}{\partial r}\right)$

Table 1.19 – Mass balance equation in the different domains

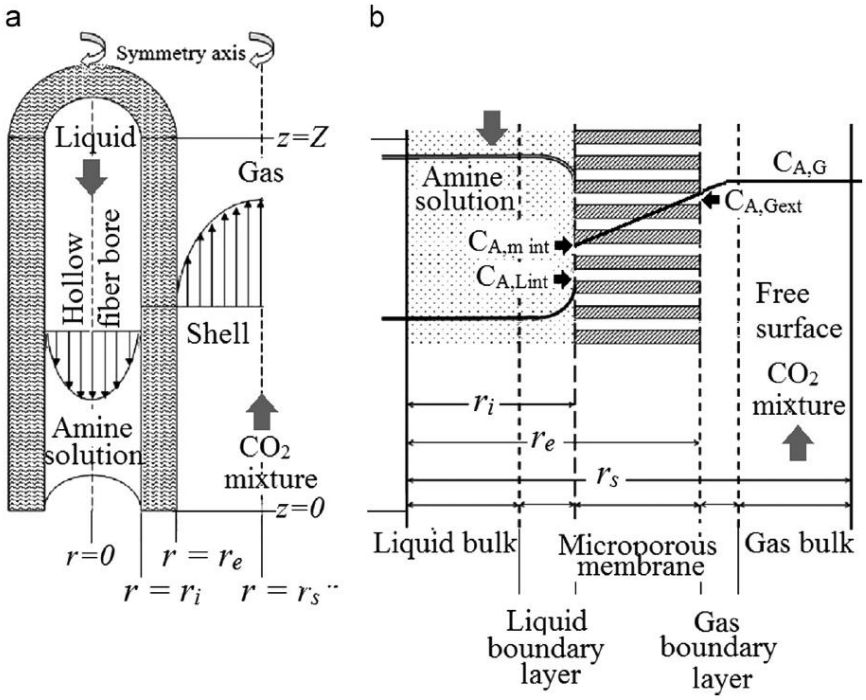

Figure 1.29– Schematic representation of the mass transfer domains in a hollow fiber membrane [205]
(a) velocity profiles of gas and liquid phases; (b) local concentration gradients

Convection is reduced to the axial direction which assumes a parallel flow configuration. Diffusion is considered in the radial direction [206, 207]. Sometimes, axial diffusion is also added to the mass balance equation [186, 205, 208]. In the case of the liquid phase, the diffusion coefficient can be considered constant. However, the diffusion coefficient in the gas phase may vary according to its composition.

Boundary conditions must be set at the limit of the different domains. They are presented in Table 1.20.

Boundary	Condition	
Bulk gas – Gas layer	Axial symmetry	$\frac{\partial C_A^g}{\partial r} = 0$
Gas layer - Membrane	Continuity at interface	$C_A^g = C_A^m$
Membrane – Liquid layer	Gas-liquid equilibrium	$C_A^l = H_A^{cc} C_A^m$
Liquid layer – Liquid bulk	Axial symmetry	$\frac{\partial C_A^l}{\partial r} = 0$

Table 1.20 – Boundary conditions for 2D mass transfer model

The velocity profile in the lumenside is described by a Hagen-Poiseuille flow with no-slip conditions which leads to a fully developed velocity profile. Happel's free surface theory is used to express the velocity in the shellside [186, 205, 207–209].

The application of the 2D strategy was developed to compare chemical solvents for biogas upgrading purposes [208]. In non-wetted conditions, potassium arginate demonstrated a higher absorption flux than MEA, DEA and TEA amine solutions. Furthermore, the 2D model is a helpful tool to study the influence of geometrical parameters such as fiber diameters, contactor length and membrane thickness. Multicomponent absorption with convector-diffusive mass transfer was explored for natural gas sweetening and post-combustion capture [186, 205, 206].

The comparison of the 1D and 2D strategies performed by Albarracin Zaidiza demonstrated both strategies result in similar simulated absorbed CO_2 fluxes [205]. The combination of heat transfer to the mass transfer models revealed the existence of a peak temperature for CO_2 absorption in amine solution. This behaviour was described in both 1D and 2D models [186]. Therefore, the 1D approach must be preferred when applicable for process sizing since its calculation time is significantly reduced.

1.6.3 Membrane wetting

In order to avoid phase mixing, the liquid phase pressure is kept higher than the gas phase one. The hydrophobic properties of the membrane prevent water from flowing across the membrane. Nonetheless, a mass transfer reduction occurring at long time scales (from some hours to some days) has been reported in the literature [197, 204]. Absorbed CO_2 flux was divided by 2 after 800 hours of operation with 30 %wt MEA solution [92]. The overall mass transfer resistance was increased by 21-53 % in the case of pure CO_2 absorption in water after some hours of operation [197].

This limitation has been attributed to a partial membrane wetting. Pores of the hydrophobic membrane are partially filled with solvent, thus increasing the membrane mass transfer resistance. It is a main concern for industrial applications of HFMMs [210].

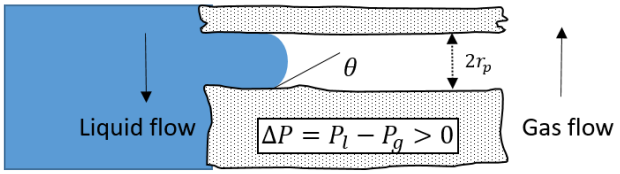

Figure 1.30– Gas-liquid interface and wetting in a membrane pore

The critical pore radius r_c above which wetting occurs is therefore a crucial parameter to estimate. It can be derived from the Laplace-Young equation [211]:

$$r_c = -\frac{2\gamma \cos\theta}{\Delta P} \qquad \text{Eq. 1.50}$$

where γ is the surface tension of the solvent, θ the contact angle between the solvent and the membrane material and ΔP the operating transmembrane pressure between the two phases.

The choice of the membrane material and of the absorbent type is therefore crucial in order to maximize the factor $\gamma \cos\theta$. Indeed a high critical radius limits membrane wetting. The systematic characterization of hollow fibers immersed in different absorbent solutions demonstrated that amine molecules can diffuse into the polymer leading to membrane swelling and reducing its hydrophobic properties. In the case of deionized water, the contact angle decreased only from 121.6° to 99° in 90 days [212]. In this regard, additional treatments (hydrophobic surface treatment or deposition of a thin dense layer) are potential strategies to limit membrane wetting [92, 210]. The membrane pore size distribution is the other membrane feature of prime importance. Lognormal distributions are typically adopted for mathematical modelling but several forms can be encountered [213].

Only the pores with a radius larger than the critical threshold ($r > r_c$) could be subject to wetting. However, Eq. 1.50 provides indications neither on wetting kinetics nor on the degree of solvent penetration in the larger pores: for a single pore with $r > r_c$, the wetted pore length δ_{wet} may be inferior to the membrane thickness δ_m. A physical balance on the gas-liquid interface in a straight cylindrical pore concludes that the pore is systematically fully wetted at equilibrium ($\delta_{wet} \cong \delta_m$) [207]. The wetting ratio η can thus be derived from the pore size distribution $g(r)$:

$$\eta = \frac{V_{wet}}{V_{tot}} = \frac{\int_{r_c}^{r_{max}} \pi r^2 \delta_m \tau_m g(r)\, \mathrm{d}r}{\int_{r_{min}}^{r_{max}} \pi r^2 \delta_m \tau_m g(r)\, \mathrm{d}r} \qquad \text{Eq. 1.51}$$

The description of membrane wetting in the 1D strategy is lumped in the membrane mass transfer coefficient k_m. In the extreme case of a fully wetted membrane, the diffusivity in the gas in Eq. 1.49 is replaced by the diffusivity in the liquid D^l:

$$k_{m,wet} = \frac{D^l \varepsilon_m}{\tau_m \delta_m} \qquad \text{Eq. 1.52}$$

In most cases, the membrane is working under partially wetted conditions. The membrane is then divided into dry and wet domains. An equivalent membrane mass transfer coefficient is calculated using the wetting ratio η [182], considering a resistance-in-series model:

$$\frac{1}{k_{m,eq}} = \eta \frac{1}{k_{m,wet}} + (1-\eta)\frac{1}{k_{m,dry}} \quad \text{Eq. 1.53}$$

In the case of the 2D model, the membrane is also divided into dry and wet domains. The position of the gas-liquid interface at steady-state can be derived from the wetting ratio η [207]. Its dynamic progression within each pore has been suggested from a force mass balance [190]:

$$l_{pore,wet}(t) = \sqrt{\frac{2k}{\mu_l}\left(\frac{2\gamma cos\theta}{r} + \Delta P\right)t} \quad \text{Eq. 1.54}$$

where $l_{pore,wet}$ is the length of the pore filled with liquid, t the time elapsed since humidification started and k is a shape coefficient of the microporous material.

Despite these attempts to model this wetting mechanism, there is a lack of a systematic and reliable characterization method. Indeed, the role of process operating parameters like gas and liquid velocities is only investigated through indirect mathematical modelling [190, 207, 210, 212]. The development of a non-intrusive method determining the degree of wetting is of interest to provide a better description of the underlying phenomenon [214].

1.7 Conclusion

The aim of this chapter was to provide a techno-economic background for the development of a robust and cost-effective biogas upgrading process. Biogas production and subsequent conversion into biomethane hold a significant potential ($151 - 246$ billions $Nm^3 CH_4/yr$) to bring Europe energy production towards a sustainable energy mix. Though, the review of the available technologies evidenced that the biogas upgrading unit is still a financial and operational concern, especially for small-scale farm AD units ($< 250\ Nm^3_{biogas}.h^{-1}$). To overcome this barrier, membrane contactors technologies are promising devices to intensify gas-liquid absorption processes. In a process development perspective, solvents were reviewed according to their features: CO_2/CH_4 selectivity, absorbed CO_2 fluxes, low energy requirements for solvent regeneration and solvent cost. Two physical absorbents (water and mineral salt solutions) and one chemical absorbent (amino-acid salt solutions) were selected for experimental investigation. Though, potassium carbonate solutions were also identified as good candidates.

For absorption processes, a global mass balance on carbon dioxide provides a systematic method to estimate the required liquid flowrate to efficiently upgrade a given biogas flowrate. Then, two different methods based on dimensional analysis and predictive numerical modelling were identified in the view of industrial scale-up (1.5). Mass transfer modelling in hollow fiber membrane

contactors pointed out that membrane wetting is a main concern for industrial applications since it significantly decreases the absorbed CO_2 flux.

This PhD study will experimentally investigate the development of an innovative biogas upgrading process. While literature mainly focuses of the absorption efficiency of solvents, the desorption process will be here systematically studied in combination with the absorption step (Chapter 3). The modelling of mass transfer with a special concern on membrane wetting will also be carried out to support the process development and scale-up (Chapter 4).

Chapter 2

Material and methods

Chapter 2 Material and methods

2.1 Introduction

This chapter presents the experimental apparatus and related methods to characterize the state and the performances of the biogas upgrading process. This first paragraph is a presentation of the membrane contactor module which has been used in the experimental section. Membrane porosity and pore size distribution from manufacturer data are confronted to experimental characterization in the view of numerical modelling (2.2). Paragraph 2.3 is an overview of the pilot process with details on the process measurements and regulations. Then, the analytical methods and equipment used for gas composition analysis and gas flow metering are presented (2.4). At last, the experimental data processing for process characterization is detailed (2.5.1 and 2.5.2). Experimental techniques specifically developed to estimate the dissolved gas content of a liquid or the Henry coefficient of an absorbent are presented (2.5.3 and 2.5.4).

2.2 Hollow fiber membrane contactor module

Choice was made to develop a biogas upgrading process based on a membrane module commercially available at an industrial size for future industrial upscaling (Liqui-Cel® Extra-Flow module produced by Membrana and presented in Figure 1.28). This module comprises a diverting baffle at its center to enhance mass transfer efficiency.

The features of different membrane types are presented in this paragraph and some of them are compared to experimental characterization (porosity and pore size distribution).

2.2.1 Manufacturer data

The geometrical features of the 2.5" x 8" Extra-Flow module used in the experimental section are summarized in Table 2.1, from the data sheet presented in Appendix H. It is the smallest item of the Liqui-Cel® industrial range.

Parameter		Value	Source
External fiber area $\boldsymbol{S}$		$1.4\ m^2$	Appendix H
Inner radius of the fiber bundle $\boldsymbol{R_i}$		$1.10 \times 10^{-2}\ m$	[192, 202]
Outer radius of the fiber bundle $\boldsymbol{R_o}$		$2.32 \times 10^{-2}\ m$	[192]
Thickness of the annular gap between the cartridge and the fiber bundle		$3 \times 10^{-3}\ m$	Manufacturer
Fiber length $\boldsymbol{L_f}$		$0.203\ m$	[192, 202]
Fiber effective length $\boldsymbol{L_f^{eff}}$		$0.146\ m$	[192]
Number of fibers $\boldsymbol{N_f}$		10 200	[202]
Specific area $\boldsymbol{a}$	External fiber area against effective fiber bundle volume	$7\ 334\ m^2/m^3$	Calculated
	External fiber area against module external volume	$4\ 089\ m^2/m^3$	Calculated

Table 2.1 – Geometric features of the 2.5" x 8" Extra-Flow module

Two types of polypropylene hollow fibers have been used for the process (Table 2.2). X-50 fibers offer a higher porosity compared to X-40 fibers which present more mechanical resistance due to their lower porosity and larger thickness. Therefore, X-50 fibers are selected to perform the absorption step while X-40 fibers are set to the desorption process in which the membrane is exposed to a stronger transmembrane pressure ($4 - 6\ bar\ g$ against $0.5 - 2.5\ bar\ g$).

Parameter	X-40	X-50
Applications	Degassing of other gases	CO_2 degassing
Material	Polypropylene (PP)	Polypropylene (PP)
Inner fiber diameter $\boldsymbol{d_{fi}}$ $[\boldsymbol{\mu m}]$	200	220
External fiber diameter $\boldsymbol{d_{fo}}$ $[\boldsymbol{\mu m}]$	300	300
Porosity[31] $\boldsymbol{\varepsilon_m}$ [%]	$20 - 25$	$40 - 45$
Tortuosity $\boldsymbol{\tau_m}$ $[-]$	$2 - 3$	$2 - 3$
Average pore diameter $\boldsymbol{d_{p,mean}}$ $[\boldsymbol{\mu m}]$	0.03	0.03
Maximum liquid operating pressure (for $\boldsymbol{T < 40\ °C}$) $[\boldsymbol{bar\ g}]$	7.2	7.2

Table 2.2 – Data on hollow fiber membranes from manufacturer

[31] Data from membrane provider

The membrane tortuosity τ_m is a geometric parameter used to calculate the effective pore length $l_{pore,eff}$:

$$l_{pore,eff} = \tau_m \delta_m \quad \text{Eq. 2.1}$$

The characterization of porous medium tortuosity is not reliable yet. The estimation is derived from the value of the porosity ($\tau_m = \frac{1}{\varepsilon_m}$) [215].

2.2.2 Methods for membrane characterization

Characterisation of the membrane porosity and pore size distribution was carried out to validate manufacturer data in the view of mass transfer modelling.

2.2.2.1 Mercury intrusion porosimetry

Mercury intrusion porosimetry is a measurement technique based on the Laplace-Young equation (Eq. 1.50). A sample of the porous medium is immerged in mercury. Pressure is gradually increased by steps and thus mercury penetrates smaller and smaller pores (Figure 2.1). The volume of mercury is measured in the capillary by conductivity (Figure 2.2). These experiments were performed at the facility of the IEM Montpellier with the collaboration of Dr. Sanchez-Marcano.

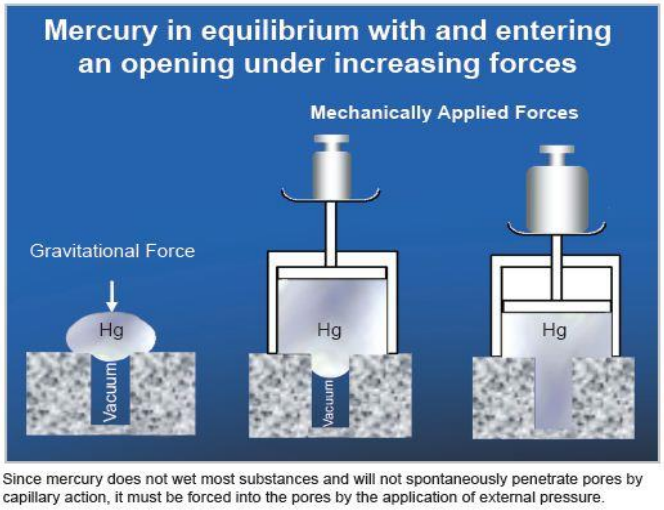

Figure 2.1– Mercury intrusion porosimetry principle (source: Micromeritics)

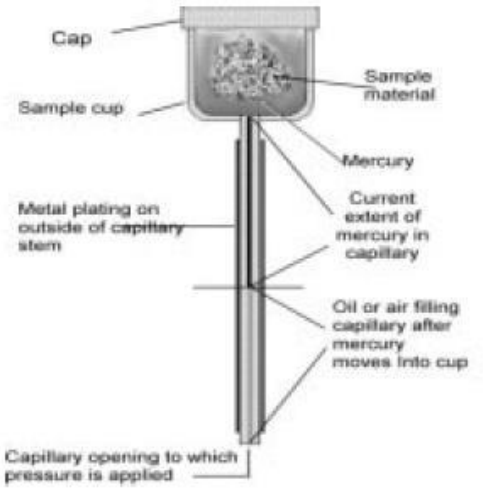

Figure 2.2 – Cross-section of a penetrometer (source: Micromeritics)

The pore size distribution is derived from the successive pressure steps. A pressure up to 4 200 bar is applied on the sample (corresponding to the intrusion of mercury into smaller pores of diameter $d_p = 3.5\ nm$ in the case of our samples). At these extreme pressures, the polymeric structure of the sample may be deformed and thus the measurements may not be representative. Therefore, the results must be handled with care.

The experimental porosity value was in accordance with manufacturer specifications for X-40 (21 % for the experimental value against 20-25 % for specifications). However, the experimental value was lower for X-50 membrane (29 % against 40-45 %).

The pore size distribution could not be precisely derived from experimental results (Figure 2.3 and Figure 2.4). The peak of the pore distribution is actually at the detection limit of the device corresponding to high pressures applied to the sample. Though, the mean pore diameter was found to be smaller than the manufacturer specifications for the 3 samples tested ($\sim 11\ nm$ against $30\ nm$). Scanning Electron Microscope (SEM) imagery was then performed to corroborate these experimental results. The pore size distribution weighted by the pore volume is more evenly distributed from 10 to 100 nm (Figure 2.4): it indicates that the pores in this range are equally contributing to the exchange area.

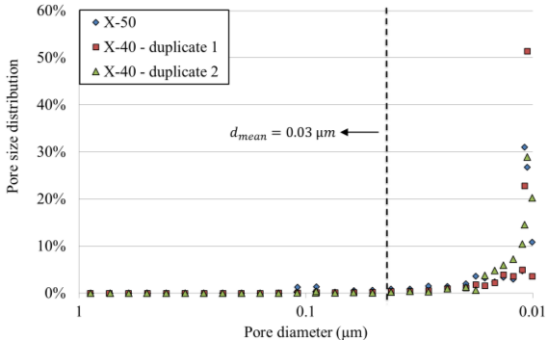

Figure 2.3– Pore size distribution results from Hg porosimetry

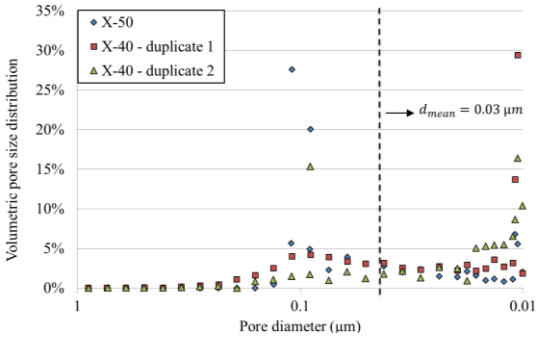

Figure 2.4 –Volumetric pore size distribution results from Hg porosimetry

2.2.2.2 Morphological study with SEM-FEG

Morphology of both X-40 and X-50 fiber types was investigated by SEM imagery (Leo Gemini 1530 equipped with Field Emission Gun-FEG). Samples coated with gold were observed perpendicularly to the hollow fiber outer surface (Figure 2.5). More pores were observed on the X-50 fiber type which confirms its higher porosity. In both samples, the membranes pores have a similar ellipsoidal shape with an elongation in the fiber axis direction. The ratio of the major and minor axes of the ellipsoidal pores ranges from 3 to 10-15. This observation questions the use of a cylindrical pore model.

Complementary pictures with an oblique angle show a highly interconnected pore network. They indicate that the perpendicular views of the membrane must be handled with care; the thickness of the sample may indeed disturb the interpretation.

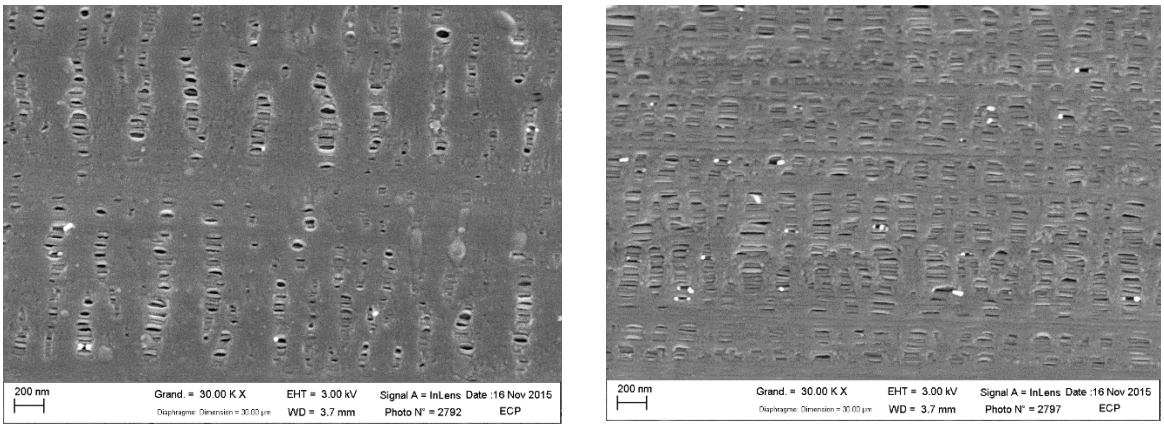

Figure 2.5 – Comparison of porosity according to membrane type
SEM-FEG images – Left: X-40 fiber – Right: X-50 fiber

SEM images were post-processed with the Fiji software in several steps:

- pore segmentation with contrast threshold;
- image despeckling;
- analysis of the pore area and determination of the equivalent pore diameter.

The equivalent pore diameter $d_{p,eq}$ is the diameter of the cylindrical pore with a section area equivalent to the surface S_p of the actual pore (Eq. 2.2).

$$S_p = \pi \left(\frac{d_{p,eq}}{2} \right)^2 \qquad \text{Eq. 2.2}$$

The resulting pore selection (Figure 2.6) is in accordance with the visual identification of pores one can have from Figure 2.5.

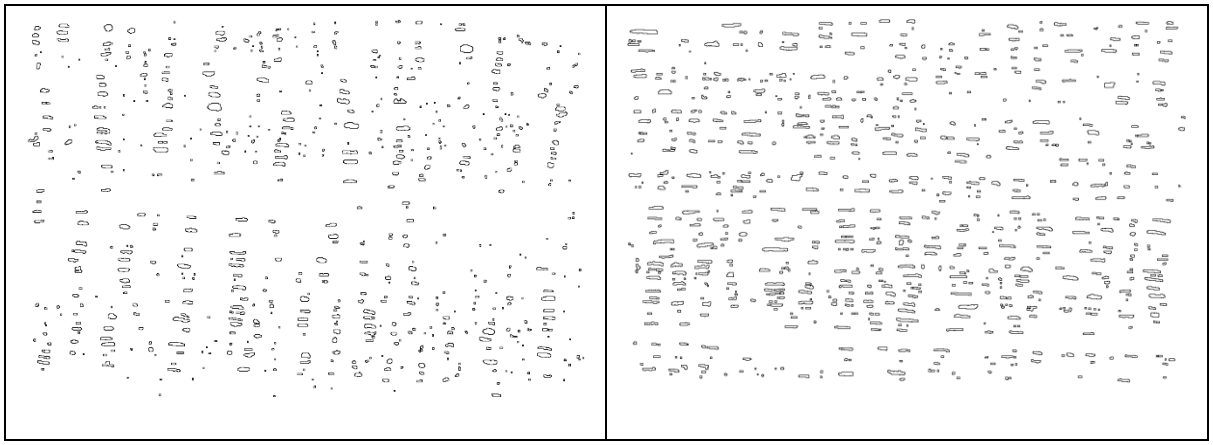

Figure 2.6 – Pore identification from SEM-FEG images
Left: X-40 fiber – Right: X-50 fiber

The magnification level impacts the resulting equivalent pore size distribution (Figure 2.7). With a finer resolution ($3.57\ nm.px^{-1}$), a little shift towards a smaller pore size distribution is

observed. Therefore, the higher magnification of the SEM device (x30 000) is used for the comparison of both fiber types: its resolution is more adapted to the size of the geometric features.

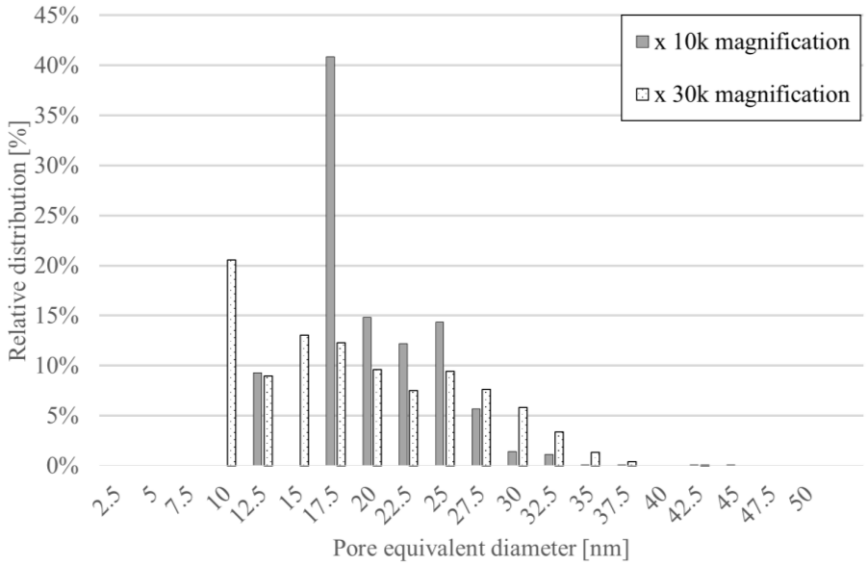

Figure 2.7 – Influence of SEM-FEG magnification on relative pore size distribution derived from image processing

X-40 fibers – EHT=3.00 kV – WD=3.7mm – Diaphragm=30.00 µm

The equivalent pore size distribution is comparable for both membranes types (Figure 2.8). Only the total observed number of pores (porosity) is significantly changing. The distribution peak is at an equivalent pore diameter of 10 nm for both membranes. Though, the distribution is comparable for pore diameter comprised between 10 and 30 nm.

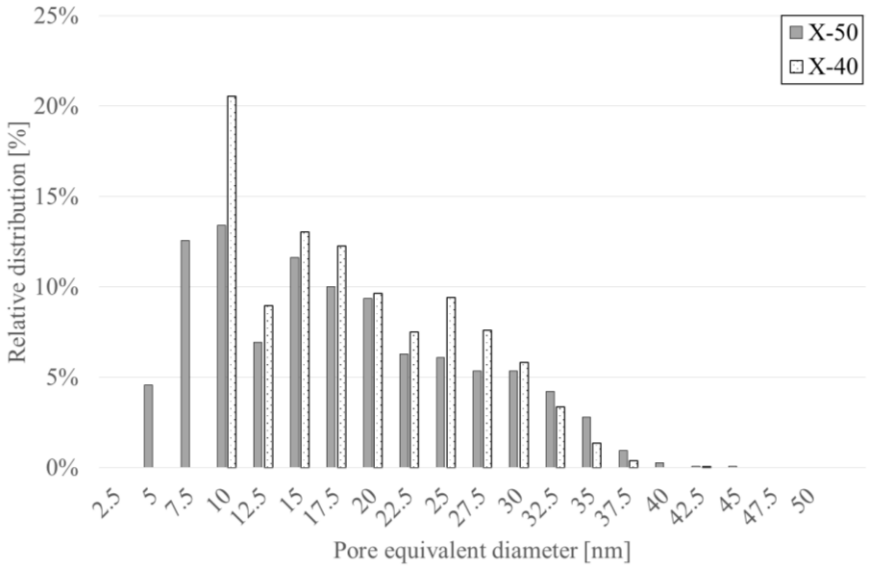

Figure 2.8 – Relative pore size distribution according to fiber type derived from image processing

X 30k magnification – EHT=3.00 kV – WD=3.7mm – Diaphragm=30.00 µm

2.2.2.1 Comparison to manufacturer data in the view of numerical modelling

Despite their respective limitations, both characterization methods agree on a smaller mean pore diameter $d_{p,mean}$ than the manufacturer data ($10-15\ nm$ against $30\ nm$). Moreover, the shape of the distribution established by SEM-FEG images questions the lognormal distribution reported in the literature (1.6.3).

To explain these discrepancies and ascertain our results, a specific work could have been carried out on membrane characterization to systematically compare several techniques on various porous samples. However, this study focuses on the process developments. Therefore, as suggested in literature, a lognormal pore size distribution $g(r)$ with the manufacturer mean pore size diameter ($d_{p,mean} = 30\ nm$) was adopted for numerical modelling [213].

$$g(r) = \frac{1}{r\sqrt{2\pi}}\left[\ln\left(1+\sigma^2\right)\right]^{-0.5} exp\left[-\frac{\left(\ln\left((r/r_{p,mean})(1+\sigma^2)^{0.5}\right)\right)^2}{2\ln(1+\sigma^2)}\right] \qquad \text{Eq. 2.3}$$

where σ is the geometric standard deviation and $r_{p,mean}$ the mean pore radius.

The corresponding pore volume distribution is presented in Figure 2.9 and has to be compared to the experimental results from Figure 2.4.

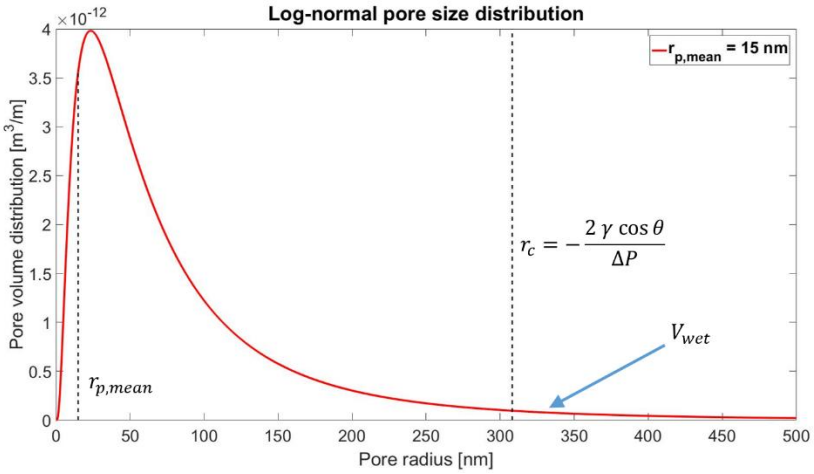

Figure 2.9 – Membrane log-normal pore size distribution

Nomenclature is introduced in paragraph 1.6.3

2.3 Pilot equipment

2.3.1 System overview

The pilot process was progressively developed to reach the final experimental set-up presented in Figure 2.10. It comprises 5 distinct parts: one chassis for gas regulation, the gas composition analytical system, two chassis for liquid regulation and the gas-liquid absorption/desorption units with two membrane contactors. The technical description of the pilot process is provided in Appendix I.

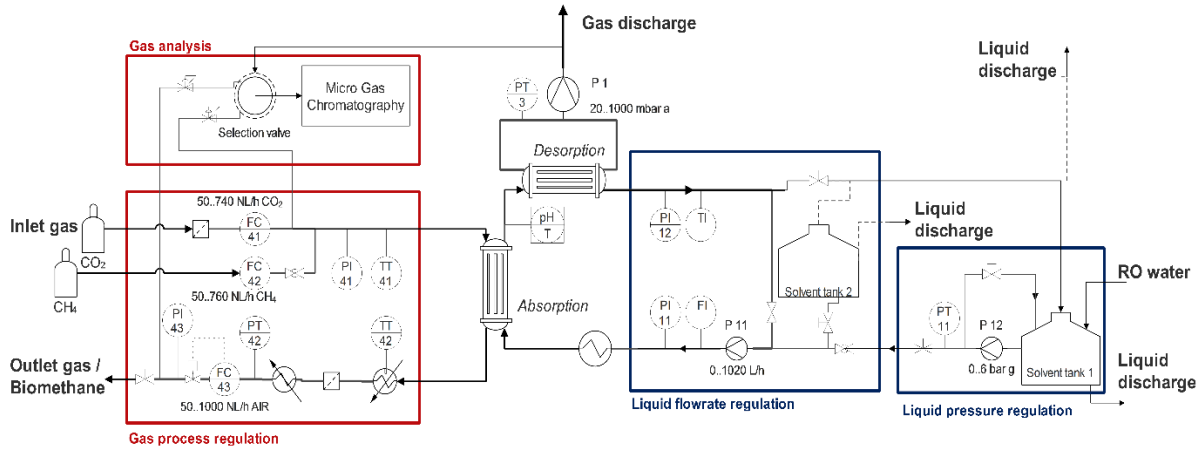

Figure 2.10 – Process flow diagram for the reference process architecture 1:1

Several process architectures have been investigated in the closed-loop configuration. The reference case in Figure 2.10 presents an equivalent exchange area in the absorption and desorption steps, referred to as 1:1 (one membrane module each). Other investigated architectures are referenced in Appendix J.

2.3.2 Gas regulation and measurements

The inlet gas flowrate and its composition are controlled by a 2-way mixer equipped with mass flow controllers (Bronkhorst In-Flow CTA). Pure gases (CO_2, CH_4, N_2 - Air Liquid AlphaGaz 1 standard) were used to produce synthetic mixtures. If not specified, the synthetic biogas has a composition of 60 $\%vol.CH_4$ and 40 $\%vol.CO_2$. After CO_2 removal, the outlet gas flowrate is measured in another mass flow controller (Bronkhorst Low-ΔP-Flow). The process gas pressure is regulated with a PID controller connected to the solenoid valve of the outlet mass flow controller. It takes about 5 minutes for the gas flows and pressure to stabilize at their setpoints. The control interface is presented in Figure 2.11.

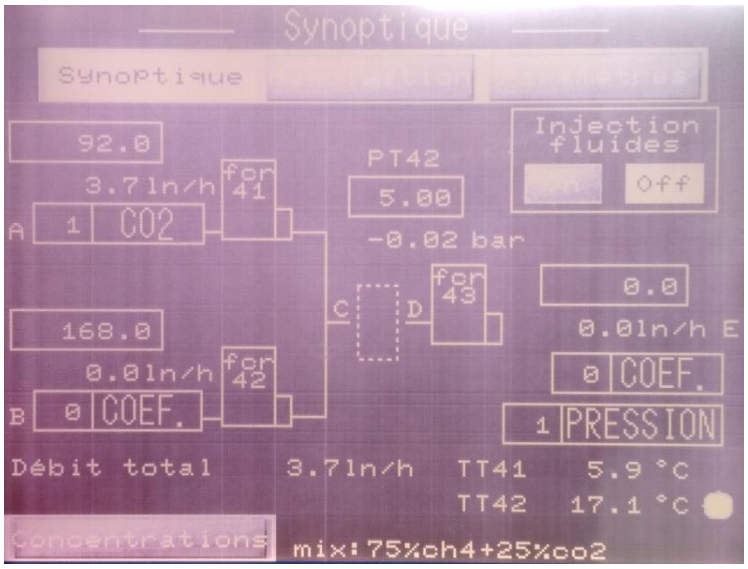

Figure 2.11 – Control interface of the gas chassis

The inlet gas flowrates are limited by the calibration range of the thermal mass flow controllers (Table 2.3).

Parameter	Operating range
Gas pressure at absorption $\boldsymbol{P_g}$	$0 - 7\ bar\ g$
Inlet $\boldsymbol{CO_2}$ volumetric flowrate $\boldsymbol{Q_{CO_2}}$	$74 - 739\ NL.h^{-1}$
Inlet $\boldsymbol{CH_4}$ volumetric flowrate $\boldsymbol{Q_{CH_4}}$	$70 - 530\ NL.h^{-1}$

Table 2.3 – Operating ranges for gas pressure and inlet flowrates

2.3.3 Liquid regulation and measurements

Open-loop and closed-loop configurations have been investigated (Figure 2.12 and Figure 2.13). In the open-loop configuration, reverse osmosis (RO) water is fed into the solvent tank 1 and is discharged after CO_2 removal. In the closed-loop configuration, the absorbent solution is loaded into the solvent tank 1: it then circulates in the process without passing through any solvent tank. Two pumps are respectively regulating the pressure and the flowrate. They are controlled by a pressure transmitter PT 11 and a vortex flowmeter FI (Liqui-View) through frequency converters. The range of operating conditions are presented in Table 2.4.

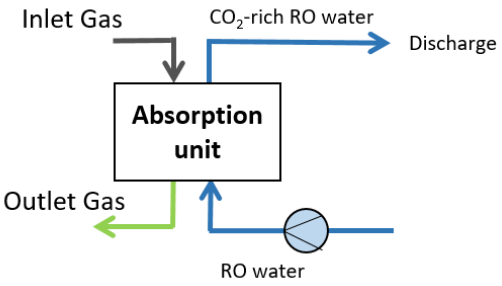

Figure 2.12– Open-loop configuration

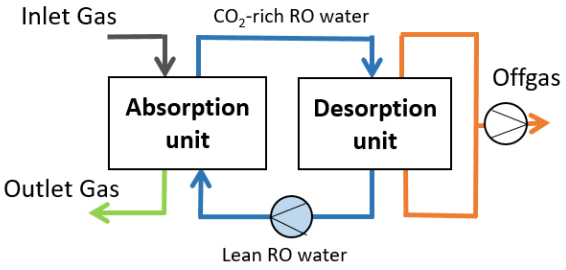

Figure 2.13 – Closed-loop configuration

Parameter	Operating range
Liquid pressure at absorption $\boldsymbol{P_l}$	$0 - 8\ bar\ g$
Liquid flowrate $\boldsymbol{Q_l}$	$30 - 240\ L.h^{-1}$

Table 2.4 – Operating ranges for the liquid pressure and flowrate

Liquid pH is measured in a flow-through fitting positioned either before or after CO_2 absorption step (Mettler-Toledo InPro 4262i). Solvent temperature is regulated with a cryostat through a plate heat exchanger (AlfaLaval).

2.4 Analytical equipments

2.4.1 Gas composition analysis

2.4.1.1 Micro Gas Chromatography

A Micro Gas Chromatography (micro-GC) is a gas chromatography analytical equipment with miniaturized components (injector, detector, columns). The principle of gas chromatography is to separate the components of the sample according to their velocities in a specific column. The separation column is chosen in accordance with the components to be analyzed. The gas sample is injected in the column with a carrier gas. At the end of the column, the presence of the components is detected by comparing the signal of the sample against that of the carrier gas.

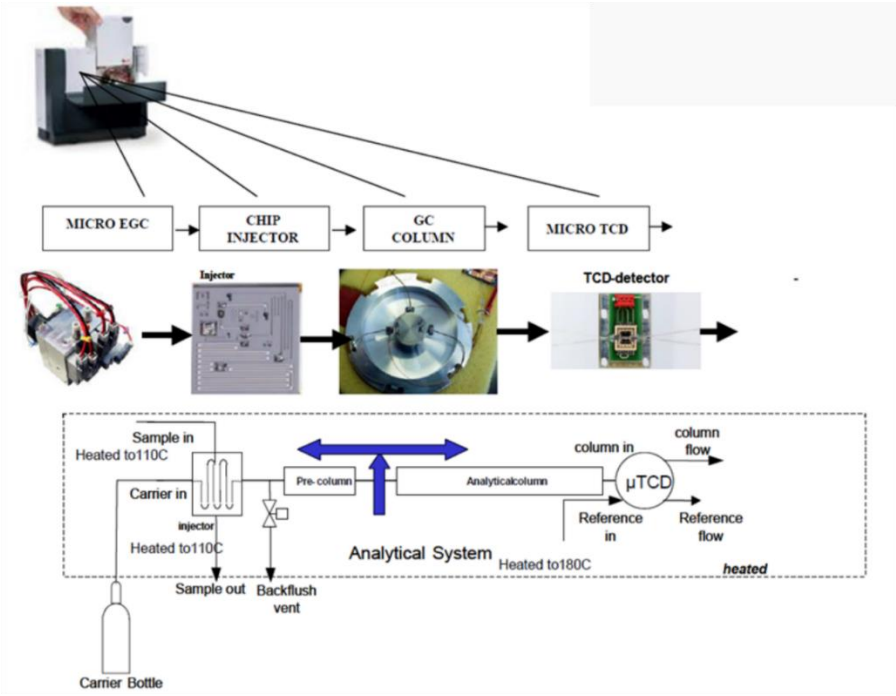

Figure 2.14 – Presentation of the Agilent 490 micro Gas Chromatography [216]

The micro-GC equipment is an Agilent 490 presented in Figure 2.14. It is equipped with two columns (Table 2.5). The detector is a Thermal Conductivity Detector (TCD).

Column	Component analyzed
10m Molsieve 5Å	O_2, N_2, CH_4
10m PoraPLOT U	CO_2, H_2S

Table 2.5 – Separation columns of the Agilent 490 micro GC

The injection method has been optimized to limit the time required for one gas analysis to 120 seconds. The method conditions are presented in Appendix K.

The method was calibrated with 4 standard gases: the respective concentrations are presented in Table 2.6. The calibration range had to cover a large range of concentrations for both CO_2 and CH_4 $(0 - 100\ \%)$.

Standard gas	CH_4	CO_2	O_2	N_2
1	60.00	40.00		
2	99.95			
3		99.95		
4		5.00	20.00	75.00

Table 2.6 – Standard gas mixtures for micro-GC calibration

A captioned chromatogram for a synthetic biogas is presented in Figure 2.15. The O_2 and N_2 peaks are absent. The CH_4 peak is the last one of the Molsieve 5Å chromatogram gas.

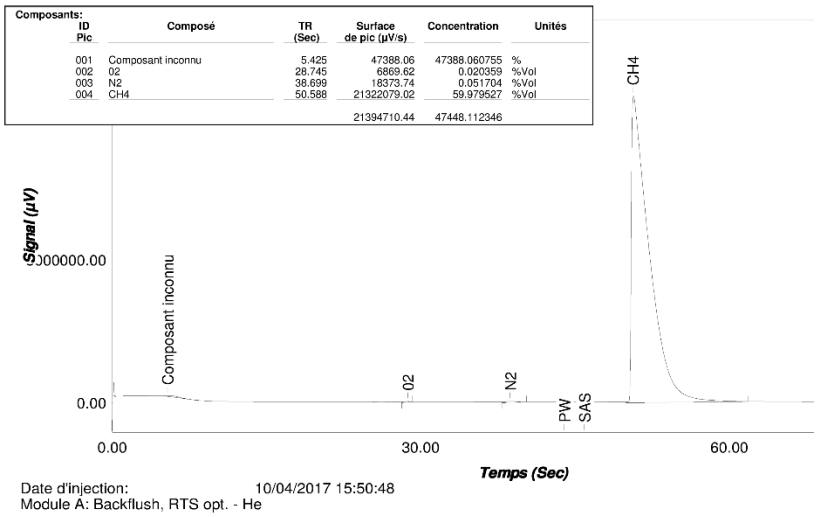

Figure 2.15 – Chromatogram of Molsieve 5Å column for a synthetic biogas sample

The micro-GC equipment was combined with a flow-through selection valve (VICI 6-streams selector valve). Gas analysis was typically performed at three process locations (Figure 2.10): biogas inlet, biomethane outlet and off-gas outlet. The Agilent 490 specifications impose the pressure of the sample to be between $50\ mbar\ g$ and $1\ bar\ g$. Therefore, the biogas inlet and biomethane outlet sampling lines have been equipped with pressure reducing controllers ($200\ mbar\ g$). Flow-through outlet in the selection valve was blocked for these lines to minimize the gas loss in the view of mass balances.

The error on the gas analysis is attributed to three causes: the sampling system, the standard gas mixtures used for calibration and the precision of the gas analyser. The micro-GC is a reliable gas analysis equipment with a high repeatability (< 0.5 % RSD[32]). Despite the special care given to the tightness of the sampling system and to the development of the analytical sequences, the uncertainty of the analysis was only of $\pm$ 0.3 %.

The analytical sequences were developed to have a sufficient sweeping time in the sampling system. Moreover, the sample was successively analysed twice to ensure reliable results.

2.4.1.2 Portable analyser: GEMBIO

A portable biogas analyser was scarcely used in some specific experimental campaigns or for punctual gas analysis. The device analyses four compounds present in biogas (Table 2.7). The precision specified by the manufacturer is limited for CO_2 and CH_4 (± 5 %RD[33]). Though, the analytical results provided by the portable analyzer were always within 0.5 % of the micro-GC results.

[32] Relative Standard Deviation
[33] Reading value

Gas	O_2	CO_2	CH_4	H_2S
Unit	%vol.	%vol.	%vol.	ppm
Range	0 - 25	0 - 100	0 - 100	0 - 2000
Precision	± 0.2 %vol.	± 5 %RD	± 5 %RD	± 10 %RD
Cell type	Electro-chemical	NDIR	NDIR	Electro-chemical

Table 2.7 – Analytical specifications of GEMBIO portable analyzer. (Manufacturer data)

O_2 and H_2S concentrations are measured with electro-chemical sensors while CO_2 and CH_4 measurements use Non-Dispersive Infrared-Red (NDIR) cells. A NDIR gas sensor measures the concentration in the sample chamber by quantifying the infrared signal absorbed by the sample [217]. The absorbance is proportional to the gas concentration. The sensor emits at a specific wavelength defined by the absorbance signature of the gas specie to be analyzed (Figure 2.16).

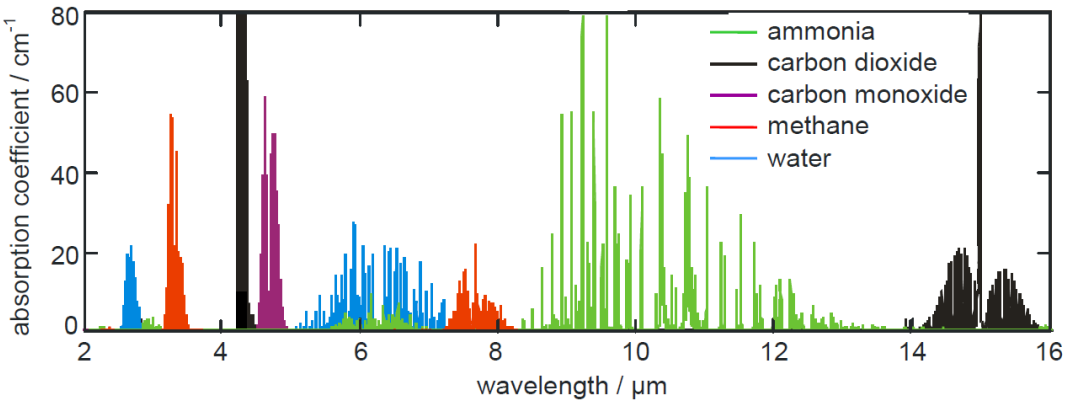

Figure 2.16 – Absorption spectra for 5 gases in the mid IR region of the spectrum [217]

Gases are all at 100 %vol.

2.4.1.1 Normalisation of gas analysis

Synthetic biogas was only composed of CO_2 and CH_4. Traces of atmospheric gases (< 0.05 %) could also be found (inlet gas quality, air tightness of the gas analytical system). Though, the sum of the analysed molar fractions might not be strictly equal to 100 %. The analytical composition was therefore corrected by normalisation to 100 %.

With respect to the calibration of each gas species, the analytical results were directly used to evaluate the concentration of every gas compounds (methane for instance). However, normalisation results were used in the process mass balance calculations.

This remark is valid for both gas analysers and adds to the measurement uncertainty.

2.4.2 Gas flow metering

2.4.2.1 Thermal mass thermal flowmeter

Two technologies of thermal mass flowmeters are present in the pilot equipment. The mass flow controllers at the gas inlet are less sensitive to gas particles and humidity (Bronkhorst In-Flow CTA). At the gas outlet, the mass flowmeter is protected with a coalescing filter (Classic Filters 5CK) and a more precise and reliable technology was preferred (Bronkhorst Low-ΔP-Flow). Its principle is presented here.

The gas flow is transformed into a laminar flow by geometric elements. A by-pass capillary samples a representative fraction of the total gas flow in the flowmeter. Sensors are located in this by-pass (Figure 2.17). Two temperature probes are set in a straight section of the capillary. Combined with the first temperature probe, a measured heat flux is provided by a heating element. The mass flow is then derived from the temperature measurements and the specific heat of the gas flow (Figure 2.18). Though, the specific heat of a gas is composition-dependant: its composition must therefore be precisely known. The electric signal U (the temperature difference) is proportional to heat capacity c_p and the gas flow by:

$$U = K\, c_p\, q_g = K\, c_p\, \rho\, Q_g \qquad \text{Eq. 2.4}$$

where K is the proportional factor, q_g the gas mass flowrate, Q_g the gas volumetric flowrate and ρ the gas volumetric density.

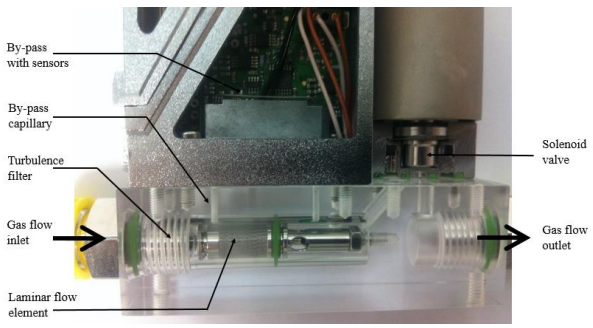

Figure 2.17 – Cross-sectional view of a thermal mass flow controller

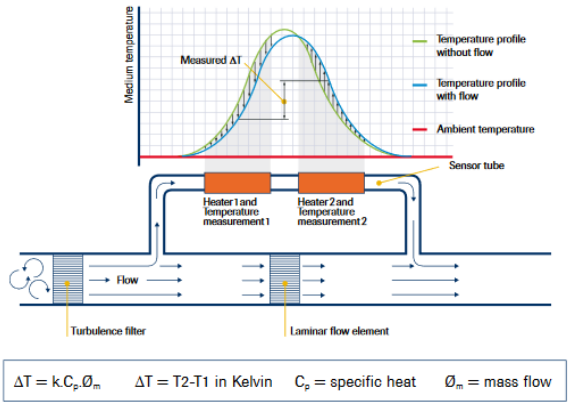

Figure 2.18– Principle of a thermal mass flowmeter [218]

In the In-Flow CTA flowmeter, the two temperature probes and the heater protrude directly in the main straight tube (Figure 2.19).

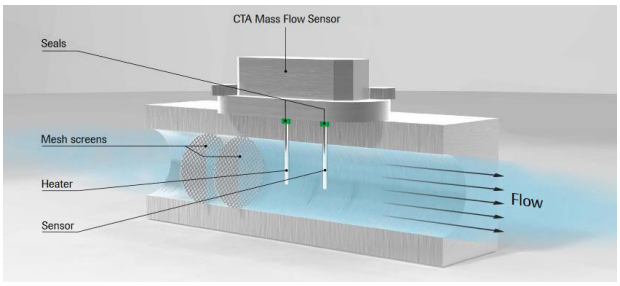

Figure 2.19 – Principle of the In-Flow CTA flowmeter [219]

Thermal mass flowmeters are typically calibrated at the production plant. Standard gases are however limited (air, N_2, CO_2). Theoretical correction factors are provided by the manufacturer for calibration with other gas mixtures. It introduces an additional uncertainty factor. This correction factor FC is the ratio of heat capacities c_p and densities ρ:

$$Q_{g,2} = FC_{1\to2}\, Q_{g,1} \qquad \text{Eq. 2.5}$$

$$FC_{1\to2} = \frac{(c_p\,\rho)_1}{(c_p\,\rho)_2} \qquad \text{Eq. 2.6}$$

Four types of uncertainties are related to thermal mass flowmeters (Table 2.8). The Low-ΔP-Flow offers more precision than the In-Flow CTA. The correction factors are estimated from thermodynamic models provided by the manufacturer but the uncertainty associated with it significantly increases the global uncertainty.

	In-Flow CTA	**Low-ΔP-Flow**
Range $[NL_{N_2}.h^{-1}]$	100 - 1000	100 - 1000
Precision	± (1 %RD + 1 %FS[34])	± (1 %FS)
Repeatability	± (0.2 %FS)	± (0.2 %RD)
Calibration uncertainty	± 0.5 %RD	± 0.3 %RD
Correction factor	± 2.0 %	± 2.0 %

Table 2.8 – Uncertainties of thermal mass flowmeters

The relative uncertainty of the 2 flowmeters composing the inlet gas mixer is respectively of 9.9 and 12.4 % at 100 $NL.h^{-1}$ for pure CH_4 and CO_2. Figure 2.20 shows that this significant figure decreases with the gas flowrate (4.8 and 5.3 % at 500 $NL.h^{-1}$). CH_4 and CO_2 do not have the same flow range for a similar flowmeter calibrated with N_2 since they have different thermal properties.

[34] Full-Scale

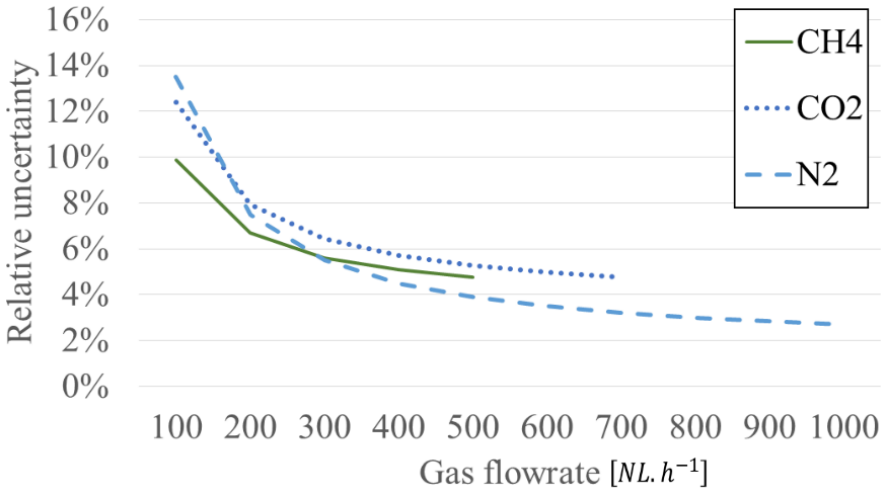

Figure 2.20 – Relative uncertainty according to gas component and gas flowrate in the In-Flow CTA flowmeters

2.4.2.2 Rotameters

Rotameters were used when the targeted gas flow was above the calibration range of the thermal mass flowmeters. They provide a visual indication of the gas flow. A float is maintained in suspension by the gas flow in a tube with variable cross-section (Figure 2.21).

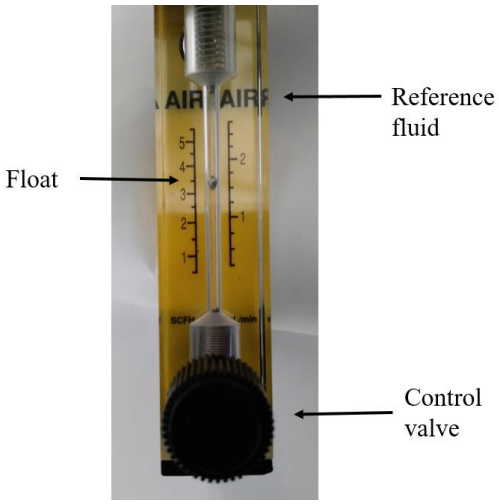

Figure 2.21 – Rotameter equipped with a control valve

The speed of the fluid is derived from the dynamic equilibrium between the buoyant force, the upward force and the float weight. Similarly to mass thermal flowmeters, the scale of the rotameter is calibrated for a specific gas under given pressure and temperature conditions. For a different gas mixture and/or under process operating conditions, a correction factor must be applied. The calculation of this factor is detailed in Appendix K.

The uncertainty specifications provided by the manufacturer in Table 2.9 are almost equivalent to the ones reported for thermal mass flowmeters.

	Aalborg rotameter
Precision	± (2 %FS)
Repeatability	± (0.25 %FS)
Calibration uncertainty	± (1 %FS)

Table 2.9 – Uncertainties of rotameters

2.5 Methods for process characterization

2.5.1 Process performance indicators

The biomethane quality $y_{CH_4}^{out}$ and the methane recovery rate R_{CH_4} are the two key performance indicators identified in paragraph 1.3. Experimental results are compared according to these indicators. Then, the specific energy consumption $W_{process}$ is estimated for selected experimental results: it accounts for the essential operational cost of the process.

The process is evaluated in the steady state regime. Gas composition analyses were performed 20 minutes after the process parameters reached their setpoints. Similar stabilization times are reported in the literature.

Experiment repeatability was checked in a first experimental campaign. The gas composition analysis deviation was within $\pm 0.5\ \%vol.$ When a stronger deviation was observed, the membrane contactor washing procedure allows to recover the initial performances (successive washing with a basic solution and an acidic solution).

Drying of membrane contactors was not performed systematically between two process points. Though, care was taken to systemically inert the gas atmosphere of the membrane contactor with CH_4 to prevent overnight biofilm development on the membrane.

2.5.1.1 Biomethane quality

The biomethane quality was monitored by the unnormalized analytical result (2.4.1.1).

2.5.1.2 Methane recovery rate

The methane recovery rate can be derived from inlet and outlet gas flowrates and molar fractions in the gas phase (Eq. 2.7).

$$R_{CH_4} = \frac{Q_{CH_4}^{out}}{Q_{CH_4}^{in}} = \frac{y_{CH_4}^{out} Q^{out}}{y_{CH_4}^{in} Q^{in}} \qquad \text{Eq. 2.7}$$

Though, the uncertainties were stronger on the gas flowrates than on the gas composition analysis. Therefore, a method based on the composition of the three gas flows was preferred. The combination of two mass balances (total gas and methane only) based on Figure 1.7 leads to:

$$R_{CH_4} = \frac{y_{CH_4}^{out}}{y_{CH_4}^{in}} \frac{\left(y_{CH_4}^{in} - y_{CH_4}^{off}\right)}{\left(y_{CH_4}^{out} - y_{CH_4}^{off}\right)} \quad \text{Eq. 2.8}$$

Unnormalized gas composition are used in Eq. 2.8.

2.5.1.3 Energy consumption

Once a biogas upgrading process has reached the required biomethane quality $y_{CH_4}^{out}$ with a satisfying methane recovery rate R_{CH_4}, the process energy consumption $W_{process}$ is an important indicator that characterizes the process efficiency. In the case of water scrubbing (WS) which do not require chemical consumption, operational costs are essentially occurring from energy consumption.

Energy consumption is calculated on the biogas upgrading process considering three steps:

- inlet biogas compression to process absorption pressure P_g;
- vacuum pump compression work on the degassed offgas flow;
- work of the liquid circulation pump to compensate the pressure losses ΔP_l in the liquid closed-loop.

This energy consumption assessment is indicative. Thermal integration of both the AD unit and biogas upgrading may reduce the overall energy consumption [37]. For instance, heat from the biogas compression can be used to answer the digester heat demand. This assessment do not include the energy consumption for biomethane grid conditioning (water removal, final compression to grid pressure …). It is considered that the biomethane is exiting the process at the operating absorption pressure P_g.

The absorption of CO_2 and CH_4 into water is an exothermic process (1.4.2.1). Though, the induced temperature variation is compensated between the absorption and desorption steps in the process steady state regime. The enthalpy variation is thus not considered in the calculations.

The isentropic approach is preferred over the polytropic approach. A polytropic transformation is a succession of isentropic infinitesimal transformations: it is a local description which accounts for the heat dissipation. The isentropic efficiency ζ_{is} compares the energy conversion of the real case to the ideal isentropic transformation from an overall point of view. For compressors, they are characterized by Eq. 2.9.

$$\zeta_{is} < \zeta_{poly} < 1 \quad \text{Eq. 2.9}$$

Electrical efficiency (75 %), mechanical efficiency (90 %) and isentropic efficiency (75 %) are successively considered. The details of the calculations are presented in Appendix M.

As a general rule, the work of compression is the most energy intensive: $0.134\ kWh.Nm^{-3}_{biogas}$ are needed to bring the raw biogas from atmospheric pressure to $P_g = 5.0\ bar\ g$. The vacuum pump generally accounts for a third of the energy consumption. For a typical 60/40 CH_4/CO_2 biogas, if all the CO_2 were to be removed, it would require $0.075\ kWh.Nm^{-3}_{biogas}$. The energy consumption associated to the pressure losses in the liquid closed-loop is negligible. It confirms the energy saving advantage of the hollow fiber membrane modules (HFMMs) over conventional WS as previously outlined in paragraph 1.3.3.1.

The analysis of process energy consumption was carried out for the most attractive process points in paragraphs 3.5.1, 3.5.2.3 and 3.5.4.

2.5.2 Overall mass transfer coefficient

The efficiency of the CO_2 mass transfer has been assessed for some experiments. First, the logarithmic mean of the mass transfer potential Δx_{ML} is calculated (Eq. 1.36). Thus, a constant overall mass transfer coefficient relative to the liquid phase K_L^0 is derived from experimental data. It is related to K_L coefficient expressed in $m.s^{-1}$ by Eq. 2.11.

$$K_L^0 = \frac{Q_l\left(x^{out} - x^{in}\right)}{a\ \Delta x_{ML}\ \Omega Z} \qquad \text{Eq. 2.10}$$

$$K_L\ = \frac{K_L^0}{C_{tot}^l} \cong \frac{K_L^0}{C_{H_2O}^l} \qquad \text{Eq. 2.11}$$

where x^{in} and x^{out} are the liquid molar fractions at the inlet and outlet of the absorbing membrane contactor, a, Ω, Z are respectively the specific area, the cross-section area and the height of the membrane module.

The molar fraction at the liquid outlet is derived from a CO_2 mass balance on the absorption unit, considering that Q_l is constant in the contactor:

$$x^{out} = \frac{Q_g^{in}}{Q_l} y_{CO_2}^{in} - \frac{Q_g^{out}}{Q_l} y_{CO_2}^{out}\ \left(+x^{in}\right) \qquad \text{Eq. 2.12}$$

The K_L^0 estimation is carried out with the hypothesis of a gas-free inlet absorbent ($x^{in} = 0$).

2.5.3 Measurement of dissolved gas content

The hypothesis of a negligible dissolved gas content at the liquid inlet of the absorption unit is questionable in the closed-loop configuration. Indeed, some dissolved gas could remain in the recycled liquid with an incomplete solvent desorption. An initial gas load in the absorbent can affect its mass transfer performances. The loading rate ψ of a gas component i is introduced by:

$$\psi_i = \frac{x_i}{x_i^{sat}(\mathrm{P}_i, \mathrm{T})} \qquad \text{Eq. 2.13}$$

where x_i is the dissolved gas content (molar fraction) in the liquid and x_i^{sat} the same parameter when the liquid is saturated. x_i^{sat} is calculated from thermodynamical data and operating conditions P_i, T.

As the gas and liquid phases are entering the absorption module counter-currently, the partial pressure P_i considered for calculating the final loading rate is the partial pressure at the gas inlet. Then, the loading rate would be of 100 % if the liquid outlet was at equilibrium with the gas inlet (reached for a mass exchanger of infinite dimension). The loading rate is used as an indicator of the gap to equilibrium at the gas inlet. An analytical method was developed to monitor the dissolved gas content in the absorbent.

The liquid with a dissolved gas content to be analysed flows through a membrane contactor in the shellside (Figure 2.22). The gas lumenside is a closed atmosphere: it is flushed 3 times before an analytical measurement to remove the initial atmosphere. The gas composition and pressure are progressively reaching the equilibrium conditions with the dissolved gas content. The partial pressure of each gas component is derived both from the manometer value and the gas analysis. Application of Henry's law provides an estimation of the liquid molar fraction x_i.

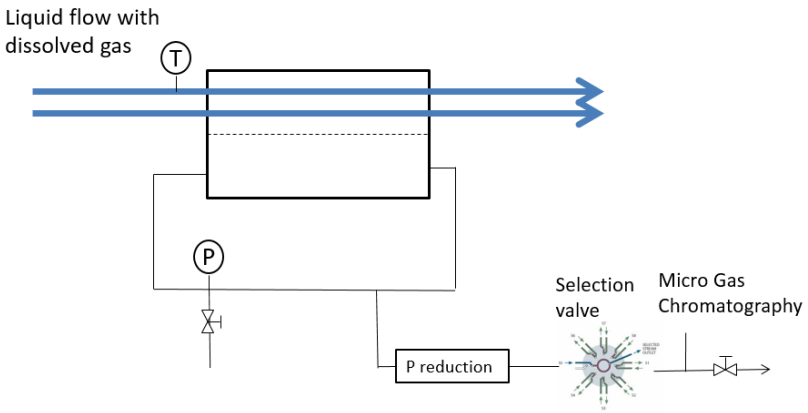

Figure 2.22 – Dissolved gas analytical module set-up

This apparatus can be connected at any position on the liquid closed-loop: before the absorption step to assess the loading rate of the inlet absorbent or after the absorption step to evaluate the solvent absorption capacity effectively used. Though, due to the micro-GC specifications, the gas must reach an equilibrium pressure above atmospheric pressure. The device was then mainly used after the absorption step.

Another method based on an absorption unit mass balance also provides an estimation of the liquid outlet molar fraction (Eq. 2.12). It measures the solvent absorption capacity used during the absorption step and does not consider the potential dissolved gas content at the contactor liquid inlet.

Both methods are detailed in Appendix N.

2.5.4 Determination of Henry coefficients

Experimental techniques to measure Henry coefficients are primarily based on the mixing of entirely determined gas and liquid volumes (pressure and temperature conditions, compositions) [63]. An experimental set-up has been developed in which the gas-liquid interface is materialized by a membrane module (Figure 2.23). This method is inspired by the protocol for absorption of a single gas [220].

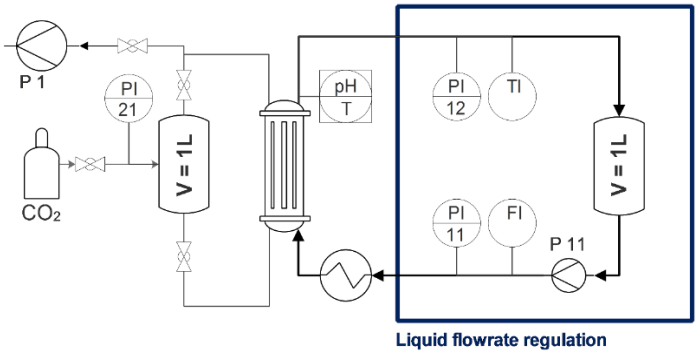

Figure 2.23 – Experimental set-up for the measurement of Henry coefficient

Firstly, the circulation of a known volume of liquid is started in a closed-loop. The gas cylinder is flushed 3 times prior loading, to get rid of contaminants, and the pressure of the gas cylinder $P_{g,cylinder}$ is noted down. Then, vacuum is established in the gas pipes and the contactor lumenside by the vacuum pump P1. After isolation by a ball valve, the experiment is ready to start.

The gas volume of known composition is put in contact with the liquid phase through the membrane contactor. Gas is absorbed in the circulating liquid until it reaches equilibrium. Gas pressure is noted down and the gas phase is analysed by micro-GC.

A gas phase mass balance on specie i between the initial and final states of the experiment leads to an estimation of the liquid molar fraction x_i:

$$x_i = \frac{\Delta n_i}{n_{solvent}} \qquad \text{Eq. 2.14}$$

$$\Delta n_i = \left(\frac{y_i P_g}{RT_g}\right)_{ini} - \left(\frac{y_i P_g}{RT_g}\right)_{final} \qquad \text{Eq. 2.15}$$

where Δn_i is the molar quantity absorbed from the initial to the final states and $n_{solvent}$ is the molar quantity of circulating solvent.

The initial depressurization of the gas cylinder is assumed to be isentropic. Therefore, the initial gas pressure $P_{g,ini}$ is derived from the Laplace law:

$$P_{g,ini} = P_{g,cylinder}\left(\frac{V_{cylinder}}{V_{gas}}\right)^{\gamma} \quad \text{Eq. 2.16}$$

where γ is the Laplace coefficient of the gas, $V_{cylinder}$ is the volume of the cylinder only and V_{gas} is the total volume of the gas phase (including the gas piping and the volume within the membrane contactor).

The initial composition of the gas phase must be precisely known before it is injected in the gas cylinder. Therefore, Henry coefficient measurements can only be performed with pure gases or preconditioned gas mixtures.

2.6 Conclusion

This chapter presented the experimental set-up of the biogas upgrading pilot process. The geometry of the membrane contactor module which is the angular stone of this work was detailed. The membrane material was characterized by mercury porosimetry and SEM imagery. The observed deviation from manufacturer data must be confirmed by a specific study. Regarding the biogas upgrading process, a synthetic biogas flow is generated from pure gases. The regulation system allows us to investigate the process operating conditions and the process configuration thanks to the set-up modularity. A special care must be given to gas composition analysis and gas flow metering to obtain equilibrated mass balances for both methane and carbon dioxide. The biogas upgrading process is evaluated according to biomethane quality, methane recovery rate and specific energy consumption. The overall liquid mass transfer coefficient is also an indicator of the mass transfer efficiency. In addition, two methods were specifically developed to measure the Henry coefficients of considered gases in absorbents and to provide an online measurement of the dissolved gas content in the liquid flow. This pilot set-up should allow the development and the optimization of a robust biogas upgrading process.

Chapter 3

Developing a process-scale biogas upgrading unit

Chapter 3 Developing a process-scale biogas upgrading unit

3.1 Introduction

This chapter compiles the successive experimental campaigns carried out to understand how operating parameters are driving the mass transfer in the membrane contactor module and to develop a competitive biogas upgrading process. In a preliminary campaign, the ability of membrane contactor to successfully produce gas-grid quality biomethane is assessed in an open-loop configuration (3.2). Then, a reference closed-loop configuration is investigated by a design of experiment methodology to identify the key process parameters, their relative influence and potential interactions (3.3). Paragraph 3.4 separately evaluates the influence of membrane wetting and gas composition in order to evidence the corresponding mass transfer limitation. At last, the results from the process optimization strategy leading to a proof-of-concept are presented in paragraph 3.5.

3.2 Achieving gas grid quality

A preliminary campaign was set to experimentally confirm the potential of a membrane contactor device to upgrade biogas into biomethane meeting gas grid specifications ($y_{CH_4}^{out} > 97$ %). In this chapter, the synthetic biogas has a composition of 60 $\%vol.CH_4$ and 40 $\%vol.CO_2$ if not specified. The influence of the inlet gas flowrate was investigated in an open-loop configuration with a constant liquid flowrate (Figure 3.1). As expected, the methane content of the outlet gas is negatively impacted by an increasing gas to liquid ratio. A biomethane quality up to $y_{CH_4}^{out} = 99.5$ % was obtained at a low gas to liquid ratio of 0.56 $NL.L^{-1}$. These initial experiments confirmed the potentiality of membrane contactors to upgrade raw biogas into biomethane.

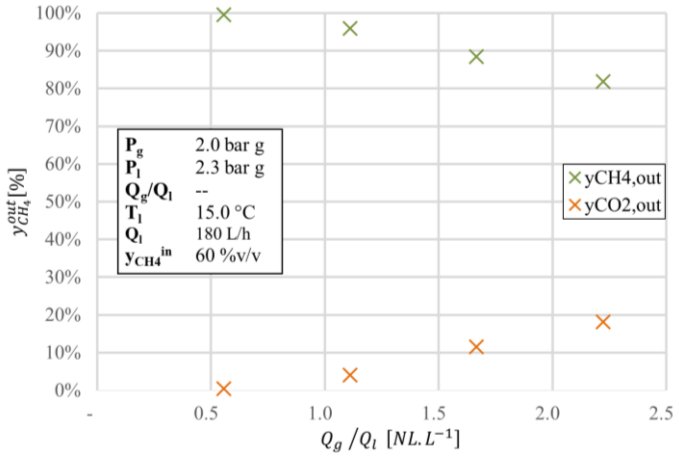

Figure 3.1 – Influence of biogas flowrate in open-loop configuration

3.3 Reference architecture: influence of the process operating conditions

The reference process architecture 1:1 is composed of a single absorption module and a single desorption module connected in a liquid closed-loop. A design of experiments (DoE) was set to investigate the relative influence of selected process parameters (3.3.2.1). Due to a limited reliability in the resulting DoE model (3.3.2.4), a deeper investigation of the main parameter (the flowrates ratio Q_g/Q_l) was carried out and its results compared to theoretical results (3.3.3). The exchange surface was then increased to overcome the evidenced mass transfer limitation (3.3.4).

3.3.1 Expected influence of process parameters

In a first approach, the process parameters and their expected influence on the performances have been summarized in Table 3.1. The flowrates Q_g and Q_l are the main parameters of the gas-liquid absorption processes, typically described by their ratio Q_g/Q_l. The gas pressure at absorption P_g and the liquid temperature T_l impact equilibrium (i.e. the partition coefficient m). According to Henry's law, the liquid pressure P_l has no impact on equilibrium. However, its impact on the gas absorption process is related to the increase of transmembrane pressure: membrane wetting (1.6.3) which is indeed enhanced by a high transmembrane pressure is a limitation to mass transfer. At desorption, a low vacuum level P_{vac} applied increases the mass transfer potential. Therefore, a more efficient solvent regeneration is expected.

The methane fraction of the inlet gas $y_{CH_4}^{in}$ necessarily impacts the process performances. Though, at industrial scale, the biogas quality is an input parameter which depends on the substrates and on the AD[35] process (1.2.2).

[35] Anaerobic Digestion

Parameter	Influence	$y_{CH_4}^{out}$	R_{CH4}
Q_g	Increase the CO_2 flow to be removed	-	+
Q_l	Increase the potential gas removal both for CO_2 and CH_4	+	-
P_g	Decrease the partition coefficient m, thus the liquid potential gas removal is increased (1.4.1)	+	-
P_l	Increase the membrane wetting and consequently the mass transfer resistance (1.6.3)	-	+
P_{vac}	The lower the pressure at desorption, the higher the mass transfer potential to regenerate the absorbent	-	+
T_g	Influence of gas temperature is not known but likely not to be significant	?	?
T_l	A lower temperature enhances the absorption capacity (1.4.2.1)	+	-
$y_{CH_4}^{in}$	Lower the CO_2 flow to be removed Decrease the CO_2 mass transfer potential $(x^* - x)$	+	-

Table 3.1 – Expected influence of process parameters

Among the listed parameters, five are selected for further investigation for their supposed influenced on the biogas upgrading process: both gas and liquid flowrates Q_g and Q_l, gas absorption and vacuum pressures P_g and P_{vac}, and inlet biogas composition $y_{CH_4}^{in}$.

3.3.2 Design of experiments

3.3.2.1 Definition

The Design of Experiment (DoE) methodology was adopted to compare the relative influence of these parameters and their interactions in a large range of operating conditions. Five parameters were selected and three levels were defined to investigate the quadratic influences and interactions (Table 3.2). The temperature of the absorbent was measured but not regulated ($T_l = 25°C \pm 3°C$). The influence of liquid pressure on membrane wetting was specifically studied in a different campaign (3.4.1.2).

Level	Q_l $[L.h^{-1}]$	Q_g $[NL.h^{-1}]$	P_g $[bar\ g]$	P_{vac} $[mbar\ a]$	$y_{CH_4}^{in}$ $[\%vol.]$
Parameter	P1	P4	P3	P2	P5
-β= -2.378	60	205.0	1.10	100.0	30.0
-1	103.5	355.7	2.2	157.9	47.4
0	135	465.0	3.0	200.0	60.0
+1	166.5	574.3	3.8	242.1	72.6
+β = +2.378	210	725.0	4.90	300.0	90.0

Table 3.2 – Definition of parameters' levels for the Design of Experiments

A central composite design was used to reduce the number of experiments (243 tests initially). The complete table with the parameters values and the experimental response is provided in Appendix O. The central composite design is divided into 3 matrices:

- A factorial design with 2 levels (-1 and +1): 32 tests;
- A series of tests at the center of the domain: N_0 tests;
- A series of tests on the axis of the domain (-β and +β for each parameter): 10 tests.

The value of β is chosen from tables (Table 3.3) to satisfy the optimality criteria: rotability, orthogonality and uniform precision. These criteria are defined in Appendix O. The criteria of orthogonality and uniform precision cannot be satisfied at the same time. Therefore, the design is qualified as quasi-orthogonal instead of orthogonal.

For a given number of parameters (k = 5), the number of tests N_0 at the center of the domain is defined according to the criterion that must be satisfied (Table 3.3). In practice, 15 tests were performed at the center of the domain to satisfy the uniform precision criteria.

Number of parameters (k)	**2**	**3**	**4**	**5** (2^5)	**5** (2^{5-1})	**6** (2^6)	**6** (2^{6-1})
N_0 *orthogonality*	8	9	12	17	10	24	15
N_0 *uniform precision*	5	6	7	10	6	15	9
β	1.414	1.682	2.0	2.378	2.0	2.828	2.378

Table 3.3 – Definition of the experimental design according to number of parameters

Among the five responses considered for data analysis, only the biomethane composition provided consistent results with an informative precision. Measurements precision was too limited on other responses (recovery rate R_{CH_4}, CO_2 molar fraction in the offgas $y_{CO_2}^{off}$, loading rates after absorption ψ_{CH_4} and ψ_{CO_2}). Therefore, only the results regarding biomethane quality are discussed.

3.3.2.2 Statistical processing

A quadratic model with interactions was used to interpret the experimental data. The statistical analysis is performed using the function *regstats* of MATLAB software. Three models are successively constructed:

- model1 which is the raw model with all the coefficients considered;
- model2 which is the model1 with only the coefficients of the significant parameters;
- model3 which is the model2 with an optimization of the significant parameter coefficients.

To determine whether the effect of the parameter P^i is significant, the ratio of its effect a_{Pi} against its standard error se_{Pi} is compared to a Student law coefficient with $N - C$ degrees of freedom

(N number of experiments, C number of coefficients in the model). The model standard error is estimated by:

$$\left|\frac{a_{P^i}}{se_{P^i}}\right| > t^{student}_{1-\alpha/2,(N-C)} \quad \text{Eq. 3.1}$$

The value of α determines the confidence interval. $\alpha = 0.05$ is a typical choice which describes the confidence interval at 95 %.

The same student coefficient and the mean squared error σ_{model} determines the precision of the model P_{model} by:

$$P_{model} = t^{student}_{1-\alpha/2,(N-C)} \cdot \sqrt{\sigma_{model}} \quad \text{Eq. 3.2}$$

3.3.2.3 Data rejection

The tests have been performed at different time periods by two different operators, with membranes subject to degradation. To perform an efficient statistical analysis, systematic mass balances (total gas, methane and carbon dioxide) have tested the consistency of the results. The mass balance errors ξ were calculated according to:

$$\xi_{tot} = \frac{Q_g^{out} + Q_g^{off} - Q_g^{in}}{Q_g^{in}} \quad \text{Eq. 3.3}$$

$$\xi_i = \frac{y_i^{out} Q_g^{out} + y_i^{off} Q_g^{off} - y_i^{in} Q_g^{in}}{y_i^{in} Q_g^{in}} \quad \text{Eq. 3.4}$$

where ξ_{tot} is the mass balance error on the total gas flow, ξ_i the one on the flow of component i, Q_g refers to the total gas flowrate and y_i to the molar fraction of component i in the gas phase.

Most of the experiments display a very good mass balance ($\xi < 5$ %) for the three indicators (Figure 3.2). Even a 15 % error can be considered admissible. As a general trend, the CH_4 and CO_2 errors tend to be positive and negative respectively. Eight tests have a stronger CO_2 error ($10 - 25$ %); these tests are performed at the extremity of the parameter axis. Luckily, three of them have replicates with a better mass balance. Therefore, no experiment with a mass balance error over 15 % was integrated in the statistical analysis.

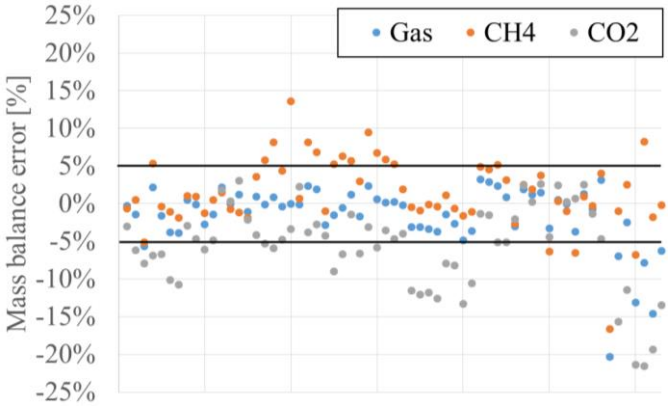

Figure 3.2 – Mass balance errors on the DoE experiments

3.3.2.4 Results

The residuals of the DoE model e represent the difference between the model estimation $\hat{y}$ and the experimental value y of the process response.

$$e = \hat{y} - y \qquad \text{Eq. 3.5}$$

The residual distribution of the quadratic model with interactions fits a normal density function (Figure 3.3): the error is randomly distributed within the domain. Moreover, no deviation of these residuals was observed neither with the order of the experiments nor with the measured response. The analysis of the model response in Figure 3.4 shows that the model is in agreement with the measured response in a 95 % confidence interval. The precision is though limited to $P_{model} = \pm 4.0$ % (Eq. 3.2).

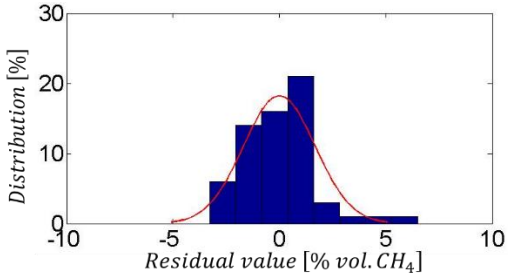

Figure 3.3 – Residuals distribution for the methane content response (quadratic model with interactions)

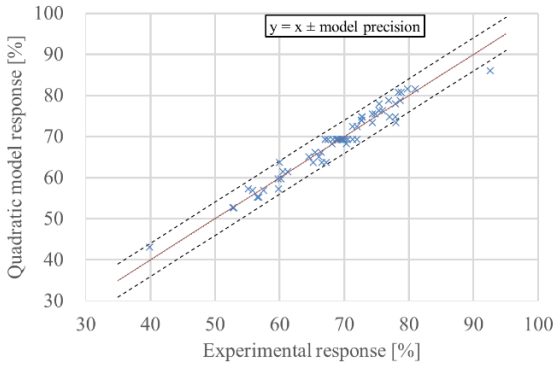

Figure 3.4– Model response against measured response and 95 % confidence interval

Most of the experimental results are concentrated in the range $y_{CH_4}^{out} = 55 - 80$ % which is below the targeted biomethane quality. The only experiment with a recorded biomethane quality above 90 % ($y_{CH_4}^{out} = 92.6$ %) is not in the confidence interval of the model. This is due to a lower precision of the model at the boundaries of the model: outside of the n-sphere (domain boundaries), the model is only an extrapolation. The model precision is therefore limited in the domain of interest.

The observed effects of the process parameters displayed in Figure 3.5 are in accordance with the preliminary discussion (Table 3.1). Only the pressure applied at the desorption step P_{vac} (P2) is not found to be significant in the domain ($100 - 300\ mbar\ a$). The inlet biogas quality (P5) is strongly significant both in the first order, the second order and by its interactions with other parameters (Q_l and P_g); the process performances are then highly dependent on the inlet biogas quality. The flowrates (P1 and P4) have limited quadratic effects: the gas flowrate quadratic effect is barely significant ($a_{\cdot P4^2} = 0.39$). It indicates that both parameters can be aggregated into a single parameter, the Q_g/Q_l ratio, for the next experimental campaigns.

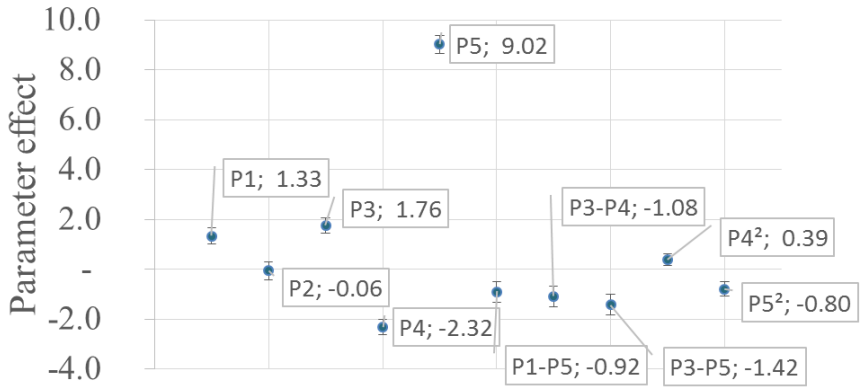

Figure 3.5 – Significant parameters retained in the quadratic model with interactions
P1=Q_l, P2=P_{vac}, P3=P_g, P4=Q_g, P5=$y_{CH_4}^{in}$

In order to optimize the biomethane quality, P_g (P3) must be set high while the Q_g/Q_l ratio must be low.

3.3.3 Influence of Q_g/Q_l ratio

The DoE confirmed the gas-to-liquid ratio to be a significant parameter to control the process performances. To further investigate the role of this aggregated parameter, the response of the DoE model was plotted against the performances of an ideal mass transfer exchanger (complete carbon dioxide removal) in Figure 3.6. The inlet biogas composition was set to a typical biogas composition ($y_{CH_4}^{in} = 60\ \%$) and the absorption pressure was set high ($P_g = 5\ bar\ g$) in order to improve the biomethane quality.

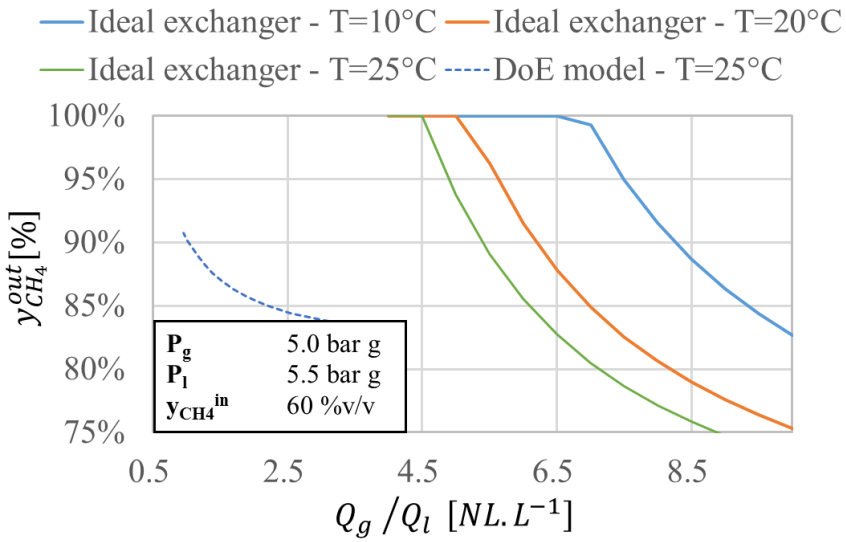

Figure 3.6 – Influence of Q_g/Q_l ratio on the biomethane quality: comparison of the DoE quadratic model with ideal exchanger performances

DoE model is applied with $Q_g = 205\ NL.h^{-1}$

In an ideal exchanger, a decrease in the water temperature improves the absorption performance. It is a way towards process intensification. Under $T_l = 20°C$, a theoretical Q_g/Q_l ratio of 5.29 $NL.L^{-1}$ is needed to obtain a 97 % quality biomethane. The DoE model built from experimental data at a constant temperature ($T_l = 25°C \pm 3$) reaches 90 % CH_4 biomethane only for ratios below 1.10 $NL.L^{-1}$. It is well below the performances of an ideal exchanger.

Two hypotheses are possible explanations for this observation. Firstly, the process was operating in a closed-loop configuration. As a result, the inlet absorbent may not be fully regenerated before entering the absorption module, leading to a decrease in its efficiency. On the contrary, the ideal exchanger curves suppose that the inlet liquid is free of dissolved gases. Secondly, the experimental set-up used in the DoE campaign (i.e. a X-50 absorption module) may be limited by mass transfer and therefore cannot meet the performances of an ideal exchanger. In this case, an increase of the exchange surface could improve the process performances. The first hypothesis is tested in this paragraph and the second hypothesis in the following one (3.3.4).

The liquid closed-loop results were compared to the open-loop performances with a varying Q_g/Q_l ratio under a fixed liquid flowrate ($Q_l = 210\ L.h^{-1}$). In these latter tests, the inlet liquid is free of any dissolved gas content. In both set-up, the developed module analysing the dissolved gas content in the liquid flow (2.5.3) was placed at the liquid absorption outlet to monitor the CO_2 loading rate.

In accordance with the DoE results, the biomethane composition increases with a decreasing Q_g/Q_l ratio in both configurations (Figure 3.7). The quality indicator culminates at 90.3 and 95.5 % for closed-loop and open-loop architectures respectively at $Q_g/Q_l = 0.7\ NL.L^{-1}$. Though, the recovery rate follows the opposite trend with a high methane loss at low Q_g/Q_l ratios (80 and 76 % respectively).

The open-loop configuration results in higher biomethane quality (up to 5 points) while high methane losses are observed (up to 4 points difference). Compared to the closed-loop configuration, the liquid inlet is CO_2-free and therefore, the driving force for mass transfer is enhanced. More carbon dioxide is removed which leads to a higher biomethane quality, especially for $Q_g/Q_l < 2\ NL.L^{-1}$. According to a similar reasoning and in the same flowrates ratio range, more methane is also absorbed in the open-loop configuration, thus decreasing the methane recovery rate.

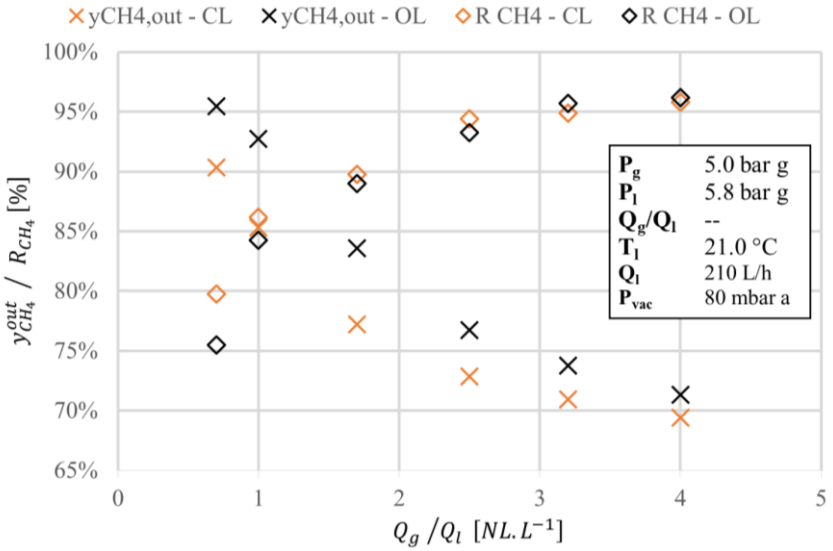

Figure 3.7 – Influence of Q_g/Q_l ratio on the biomethane quality and methane recovery rate

Reference configuration 1:1

In these experiments, the CO_2 loading rate ψ_{CO_2} is calculated as the ratio of the liquid outlet composition and the theoretical composition at equilibrium with gas inlet (2.5.3). It is monitored according to two methods presented in Appendix N. Method 1 is derived from a direct measurement using the analytical apparatus presented in paragraph 2.5.3. Method 2 is derived from a mass balance calculation: the result of this method assumes the absorbent to be free of dissolved gas at the liquid inlet.

As expected, Figure 3.8 displays a positive effect of Q_g/Q_l ratio on the CO_2 loading rate for both methods and configurations. In the open-loop configuration, the CO_2 loading rate shows a similar trend with both methods but lower results for the mass-balance method 2 (3 to 7 points). This negative offset is however within the measurement precision.

In the closed-loop configuration, the gas loads according to method 1 are about 5 to 10 points above the results obtained in the open-loop configuration. It seems to confirm that solvent is not fully degassed during the regeneration step. This pre-loading affects the concentration gradient during absorption and consequently decreases the absorption efficiency. This observation is confirmed by method 2: ψ_{CO_2} decreases by up to 5 points in the closed-loop compared to the open-loop configuration.

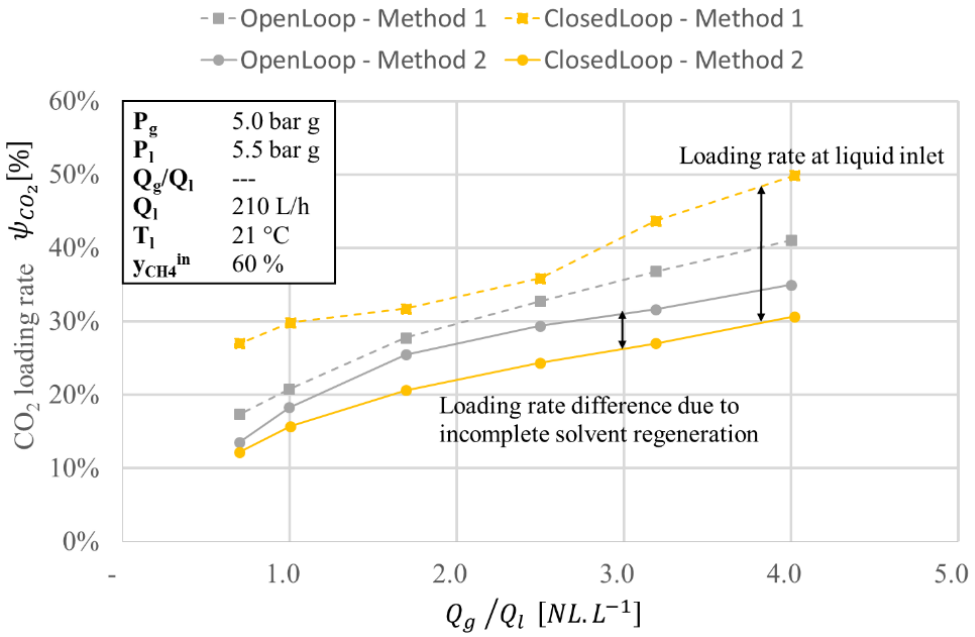

Figure 3.8 – Influence of Q_g/Q_l ratio and process configuration on the CO_2 loading rate at the absorption liquid outlet

Method 1: Direct analytical measurement – Method 2: Mass balance

This experimental campaign evidenced that the desorption step is not fully efficient in the reference architecture. Despite this fact, operating in the open-loop configuration led to a maximum CO_2 loading rate of $\psi_{CO_2} = 50$ %. Therefore, the incomplete solvent regeneration in the closed-loop configuration is only a partial explanation of the difference observed between experimental performances and results of ideal mass transfer exchangers (Figure 3.6). The second assumption of a mass transfer limitation is then investigated in the next paragraph.

3.3.4 Influence of absorption surface

The gap in the results between experimental and ideal exchangers may be explained by a too small exchanger. According to the transfer unit method, a longer exchanger leads to an improved NTU (Eq. 1.34). Therefore, two membrane modules were set in series to double the exchange surface and test the mass transfer limitation hypothesis. An open-loop configuration was set to avoid the question of the desorption efficiency.

The biomethane quality increases by 10-15 points when the exchange surface is doubled (Figure 3.9) but the behaviour according to the Q_g/Q_l ratio is the same. These results are compared to simulated results from a 1D model describing both CO_2 and CH_4 absorption. The constant overall mass transfer coefficient relative to the liquid phase K_L is an adjustable parameter of the 1D model. The adjusted K_L values are satisfactorily close (1.9×10^{-5} and 2.5×10^{-5} $m.s^{-1}$ respectively for one and two membrane modules) compared to the experimental uncertainty (2.4).

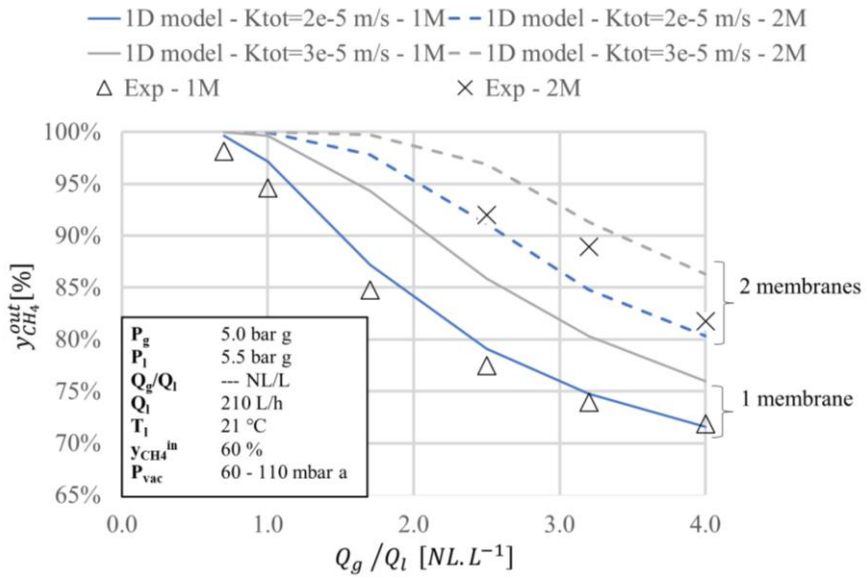

Figure 3.9 – Comparison of biomethane quality at different Q_g/Q_l ratio with one or two membrane modules (1M and 2M)

Open-loop configuration – Ktot = K_L

In addition, these adjusted values of K_L are consistent with the overall mass transfer coefficient derived from the calculation of the average mass transfer potential by Eq. 2.10 (Table 3.4). K_L is constant for the 1-module series ($2.02 \pm 0.07\ 10^{-5} m.s^{-1}$). It slightly increases during the 2-module series and a higher standard deviation is observed ($2.80 \pm 0.19\ 10^{-5} m.s^{-1}$). The corresponding overall mass transfer coefficient relative to the gas phase is very slightly below literature values ($2.4 - 4.0\ 10^{-5} m.s^{-1}$) [153].

N modules	Q_l $[L.h^{-1}]$	Q_g/Q_l $[NL.L^{-1}]$	P_g $[bar\ g]$	$y_{CH_4}^{in}$ $[\%vol.]$	K_L $[10^{-5} m.s^{-1}]$	K_G $[10^{-5} m.s^{-1}]$
1	210	0.7	5.0	60.1	2.02	1.85
	210	1.0	5.0	60.0	2.02	1.85
	210	1.7	5.0	59.8	1.96	1.80
	210	2.5	5.0	59.9	1.94	1.78
	210	3.2	5.0	60.0	1.99	1.80
	210	4.0	5.0	60.0	2.15	1.92
2	210	2.5	5.0	59.8	2.58	2.38
	210	3.2	5.0	60.3	3.03	2.73
	210	4.0	5.0	60.0	2.81	2.59

Table 3.4 – Overall mass transfer coefficients calculated from experimental data

The increase of the membrane area S could improve the biomethane composition and bring the behaviour of the mass exchanger closer to an ideal one. Though, simulations with the 1D model in the open-loop configuration indicate that 7 membrane modules in series are required to reach the targeted

biomethane quality ($y_{CH_4}^{out} > 97$ %) under $Q_g/Q_l = 4.0\ NL.L^{-1}$. This ratio was chosen to be slightly below the ratio needed in the case of an ideal mass exchanger (Figure 3.6).

This important number of modules is a consequence of the reduced average absorbed CO_2 flux J_{CO_2}. Figure 3.10 indeed shows that this flux is reduced by 20 % from the 1-module series to the 2-module series. In the second module, CO_2 has already been largely removed from the gas flow and therefore the mass transfer potential is lower than in the 1-module serie. As a comparison, in the membrane-wet regime, similar fluxes were reported for the absorption of pure CO_2 under atmospheric pressure in water ($0.9 - 1.4 \times 10^{-3}\ mol.m^2.s^{-1}$) [197]. In the literature review, chemical absorbents like amine or amino-acid salt solutions were reported in Table 1.14 to possibly improve this absorbed flux ($J_{CO_2} = 3.0 - 5.0 \times 10^{-3}\ mol.m^2.s^{-1}$).

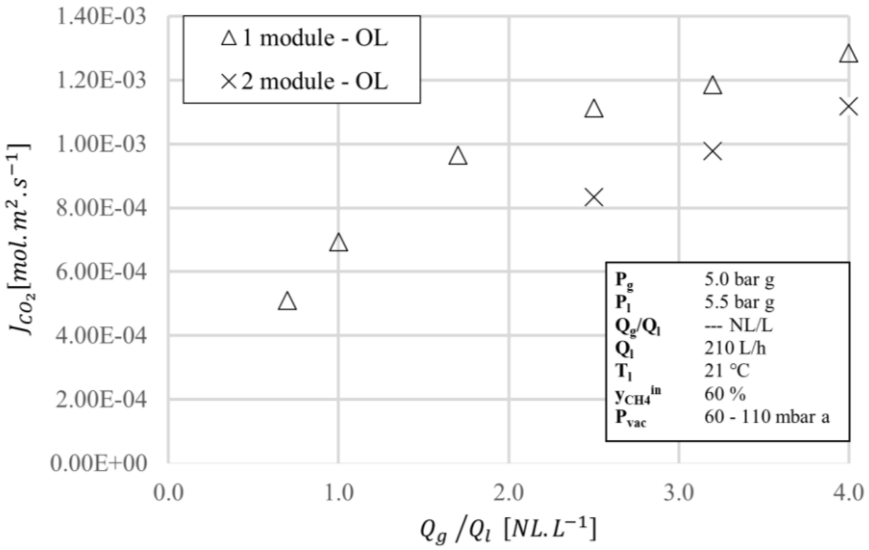

Figure 3.10 – Absorbed CO_2 flux at different Q_g/Q_l ratios with one or two membrane modules

Open-loop configuration

3.4 Determination of an average mass transfer coefficient

The average mass transfer coefficient K_L is the key parameter accounting for the mass transfer efficiency. Its dependency to process operating conditions was investigated. The cases of pure CO_2 and biogas absorptions were separated. In a first approach, the effect of membrane wetting on mass transfer was assessed with pure CO_2 absorption. Then, the absorption of CO_2 in a gas mixture was studied to determine the impact of the gas composition.

3.4.1 CO_2 absorption as a pure gas

To characterize the mass transfer limitation due to membrane wetting (1.6.3), the absorption of pure CO_2 was monitored over 7-8 hours in the open-loop configuration. Since pure gas absorption is considered, the resistances to mass transfer are located in the liquid phase and in the potential wet region

of the membrane (1.3.3.1). Different operating conditions (flowrates, pressures) were investigated in order to:

- obtain a data set in dry regime to optimize the parameters of the Chilton-Colburn equation for this device (Eq. 1.44);
- test the influence of operating conditions and notably the transmembrane pressure ΔP on membrane wetting.

The membrane drying procedure reported by Mavroudi was used [197]. Before each experiment, the membrane module was dried overnight ($> 6h$) with a constant dry air flow ($900\ NL.h^{-1}$) at atmospheric pressure and room temperature.

The reproducibility of the experimental results was assessed by comparison of two duplicates of a control experiment. At the beginning and at the end of the campaign, an experiment was performed under the control operating conditions after overnight membrane drying. Both duplicate resulted in the same flow profiles. There was indeed only a negligible decrease in the absorbed flowrate at the end of the campaign within the precision range of the gas flowmeters ($5.56 \times 10^{-6}\ Nm^3.s^{-1}$ for the second duplicate accounting for 1.0 % of the inlet flowrate).

The establishment of steady state was monitored by data acquisition. The gas flowrates at the inlet and outlet of the membrane contactor were recorded every 30 seconds. Two steady states regimes were obtained for each experiment: the dry mode which operates initially and the wetted mode afterwards (Figure 3.11). Similar behaviors were observed by Mavroudi [197]. The wetting kinetics was observed but only the gas flowrates in both dry and wetted regimes are used in the present work. The absorbed gas flowrate $Q_{CO_2}^{abs}$ is derived from the CO_2 total mass balance.

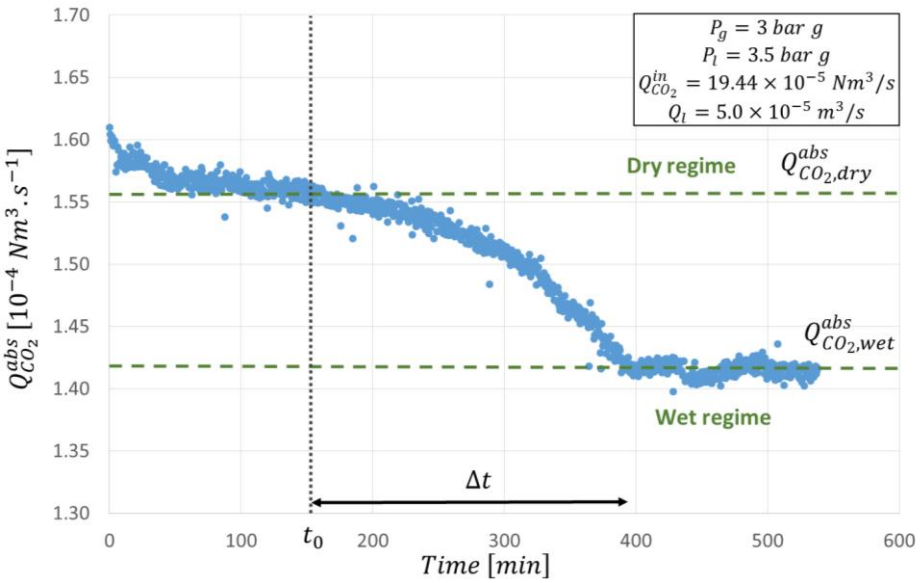

Figure 3.11 – Evolution of CO_2 absorbed flowrate over time

Open-loop configuration

The results of these experiments are presented in Table 3.5: absorbed CO_2 flowrates in both regimes (expressed in $Nm^3.s^{-1}$, equivalent to molar flowrates – see Note on units), time at which humidification starts (t_0) and time laps during which humidification occurs (Δt).

$Q_{CO_2}^{in}$ $\left[\frac{10^{-5}}{Nm^3.s^{-1}}\right]$	Q_l $\left[\frac{10^{-5}}{m^3.s^{-1}}\right]$	P_g $[bar\ g]$	P_l $[bar\ g]$	$Q_{CO_2,dry}^{abs}$ $\left[\frac{10^{-5}}{Nm^3.s^{-1}}\right]$	$Q_{CO_2,wet}^{abs}$ $\left[\frac{10^{-5}}{Nm^3.s^{-1}}\right]$	t_0 $[min]$	Δt $[min]$	Ref.
19.44	1.67	3.00	5.50	6.42	6.33	225	235	1
19.44	1.67	5.00	5.50	9.44	9.11	300	165	
27.78	1.67	5.00	5.50	9.64	9.64	283	240	
27.78	3.33	5.00	5.50	18.33	17.03	195	160	
19.44	3.33	3.00	5.50	12.17	11.25	145	185	
19.44	3.33	3.00	3.50	12.50	11.25	145	255	
19.44	5.00	3.00	5.50	16.67	15.00	105	225	
27.78	5.00	5.00	5.50	24.86	22.22	215	215	
27.78	5.00	3.00	5.50	17.50	16.25	90	165	
36.11	5.00	3.00	5.50	18.19	17.08	50	305	
19.44	5.00	3.00	3.50	15.59	14.17	160	240	
8.95	5.67	0.00	1.50	3.52	3.08	240	60	2
8.95	6.93	0.00	1.88	4.15	3.45	190	460	
8.95	8.18	0.00	2.25	4.77	3.84	220	30	
8.95	9.45	0.00	2.63	5.34	4.19	180	320	
8.95	10.72	0.00	3.00	5.95	3.97	200	550	
8.95	11.97	0.00	3.37	6.47	4.00	220	530	
8.95	14.48	0.00	4.12	7.57	4.45	170	480	
8.95	15.75	0.00	4.50	8.07	4.69	150	430	

Table 3.5 – Experimental values for CO_2 absorbed flow in dry and wet regimes

(1) Present work (2) Mavroudi et al. 2006

3.4.1.1 Influence of liquid flowrate

Experiments were run at two liquid pressures (3.5 and 5.5 $bar\ g$) for a constant gas pressure (3.0 $bar\ g$), resulting in two different transmembrane pressures ΔP. The absorbed CO_2 flowrate linearly increases with the liquid flowrate at constant gas flowrate in the dry regime and does not depend on transmembrane pressure (Figure 3.12).

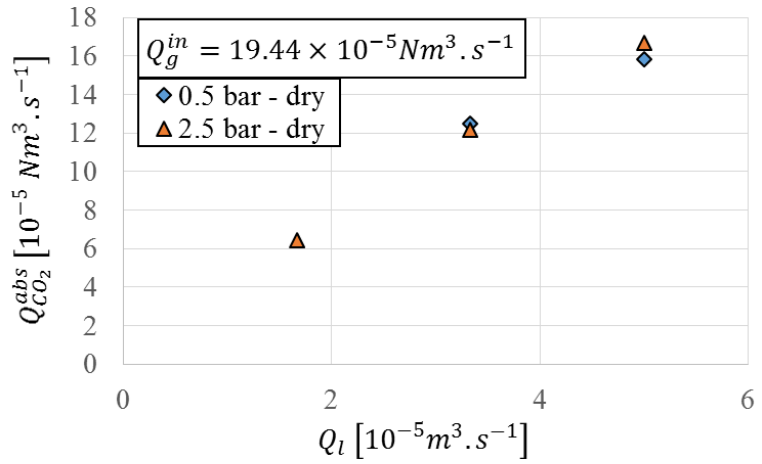

Figure 3.12 – Experimental absorbed CO_2 flow dependence on liquid flowrate at different transmembrane pressures in the dry mode for a constant inlet gas flow in the dry regime

Open-loop configuration – The transmembrane pressure ΔP is specified in the legend

While the CO_2 absorption flowrate increases, the loading rate slightly decreases with the liquid flowrate in the dry regime (Figure 3.13). The solvent is saturated with CO_2 ($\psi_{CO2} = 99.5$ %) for the lowest flowrate ($Q_l = 1.67 \times 10^{-5}\ m^3.s^{-1}$). When the liquid flowrate is increased, the liquid residence time in the membrane module decreases: hence, a kinetic limitation to CO_2 dissolution in the solvent is observed.

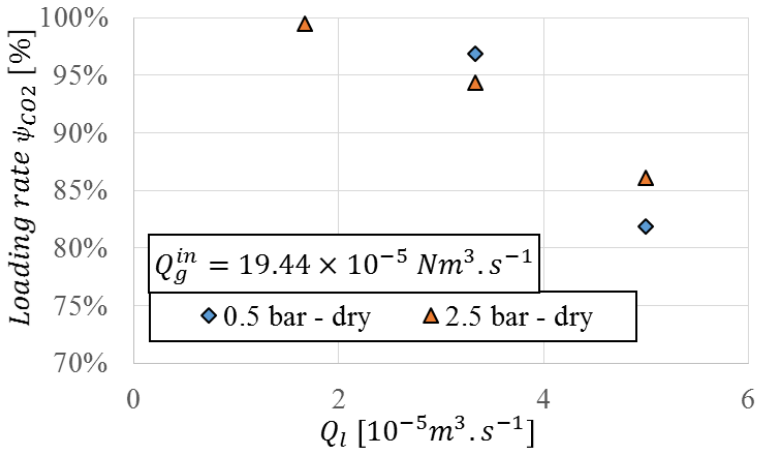

Figure 3.13 – Variation of solvent CO_2 loading rate with liquid flowrate for a constant inlet gas flow in the dry regime

Open-loop configuration – The transmembrane pressure ΔP is specified in the legend

3.4.1.2 Influence of transmembrane pressure

As seen above, in the dry regime, CO_2 absorption does not depend on the transmembrane pressure ΔP. In the wet regime, the same behaviour is observed with differences lower than 5 % (Figure 3.14). When comparing both sets of data (Figure 3.12 and Figure 3.14), the absorption flowrates are slightly lower in the wet regime than in the dry one for the higher liquid flowrates, whereas for the lower the results are quite the same; the trends of CO_2 absorption in both regimes are very similar. It confirms the results

obtained by Mavroudi [197]. The transmembrane pressure has therefore little influence on CO_2 absorption whatever the regime; this experimental result is surprising as this operating parameter was expected to have an influence on the critical pore radius of the membrane and subsequently on its wetting: the transmembrane pressures 0.5 bar and 2.5 bar are respectively equivalent to critical radii of 1530 nm and 306 nm (Eq. 1.50). The range of transmembrane pressures studied might not be large enough to result in a significant difference in membrane wetting. It may also be explained by the shape of the pores, rather ellipsoidal than circular, as observed with the MEB-FEG (2.2.2.2). As long as the shorter axis of the ellipse is below the critical wetting diameter, the solvent will not penetrate in the pore.

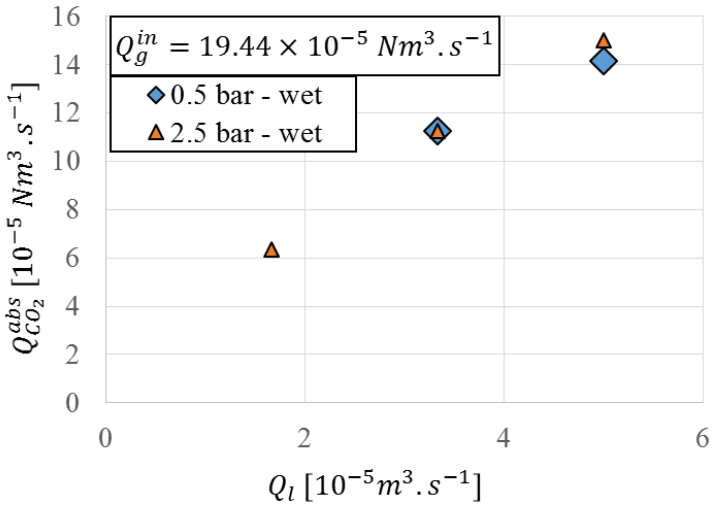

Figure 3.14 – Experimental absorbed CO_2 flow dependence on liquid flowrate at different transmembrane pressures in the wet mode for a constant inlet gas flow

Open-loop configuration – The transmembrane pressure ΔP *is specified in the legend*

3.4.1.3 Average mass transfer coefficient

The overall mass transfer coefficient K_L is calculated applying Eq. 2.10 in both dry and wet regimes (Figure 3.15). In the dry regime, K_L is constant ($8.0 \times 10^{-5}\ m.s^{-1}$) at $\Delta P = 2.5\ bar\ g$ while it decreased from 10.0 to $6.6 \times 10^{-5}\ m.s^{-1}$ with increasing Q_l at $\Delta P = 0.5\ bar\ g$. Though, the related uncertainties are high ($\pm 1.0 - 5.9 \times 10^{-5}\ m.s^{-1}$), especially at low liquid flowrates. This variation might be an artefact.

In the wet regime, the K_L values are decreased by 20-30 % and are all in the same range ($5.0 - 6.7 \times 10^{-5}\ m.s^{-1}$). Therefore, in the studied liquid flowrate range, it seems that the mass transfer does not depend on this parameter. In addition, wetting is affecting K_L coefficient in a similar manner regardless of the transmembrane pressure. Nonetheless, the K_L values and conclusions must be handled with care due to the significant uncertainties.

The average mass transfer coefficients derived from this pure CO_2 experimental campaign are much higher than the values reported in the previous campaign with gas mixtures (Table 3.4). The use of binary mixtures as synthetic biogas may impact the mass transfer coefficient which has been divided

by a factor $2-3$ in similar operating conditions. As a result, the mass transfer resistance in the gas phase may be significant when CO_2 is absorbed in a gas mixture.

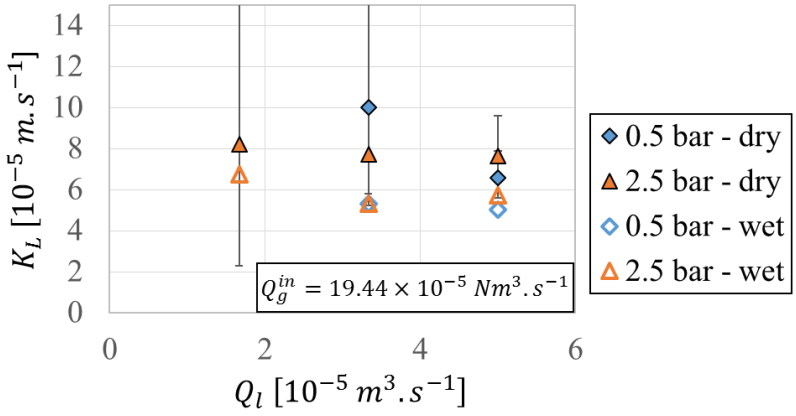

Figure 3.15 – Variation of the overall mass transfer coefficient K_L with liquid flowrate for a constant inlet gas flow

Open-loop configuration – The transmembrane pressure ΔP is specified in the legend

3.4.2 CO_2 absorption in a binary gas mixture

The impact of the mass transfer resistance in the gas phase is investigated through two experimental campaigns performed in the dry mode:

- the inlet gas composition is varied under different flowrate conditions;
- the nature of the complementary gas is tested using both methane and nitrogen.

3.4.2.1 Influence of the gas composition

A synthetic CO_2/CH_4 mixture with a varying composition ($y_{CO_2}^{in} = 10-100\ \%$) was absorbed in an open-loop configuration. In a first set of experiments, the Q_g/Q_l ratio was set to its highest permissible value ($12.5\ NL.L^{-1}$). A high Q_g/Q_l reduces the variation in the gas composition across the membrane contactor, and thus the variation of the CO_2 potential in the gas phase (i.e. its partial pressure P_{CO_2}). In a second experimental set, a medium Q_g/Q_l ratio was used and combined with a higher Q_l. This choice was made to operate under potential biogas upgrading conditions.

The overall mass transfer coefficient K_L decreases with an increasing methane fraction in the gas inlet (Figure 3.16). Under a high Q_g/Q_l ratio ($12.5\ NL.L^{-1}$), K_L is divided by 2.40 from the pure CO_2 experiment ($2.18 \times 10^{-5}\ m.s^{-1}$) to the synthetic biogas run ($0.91 \times 10^{-5}\ m.s^{-1}$ at $y_{CH_4}^{in} = 60\ \%$). This factor is increased to 3.24 for the second series ($4.19 \times 10^{-5}\ m.s^{-1}$ and $1.29 \times 10^{-5}\ m.s^{-1}$ for pure CO_2 and synthetic biogas respectively). An important rise is observed under CO_2-rich gas flow ($y_{CO_2}^{in} = 90 \rightarrow 100\ \%$ and $y_{CH_4}^{in} = 10 \rightarrow 0\ \%$). Therefore, the presence of methane induces a mass transfer limitation.

Comparing both experimental series, the second one displays higher K_L values. This observation may be explained by a higher liquid flowrate, leading a decrease in the liquid mass transfer resistance.

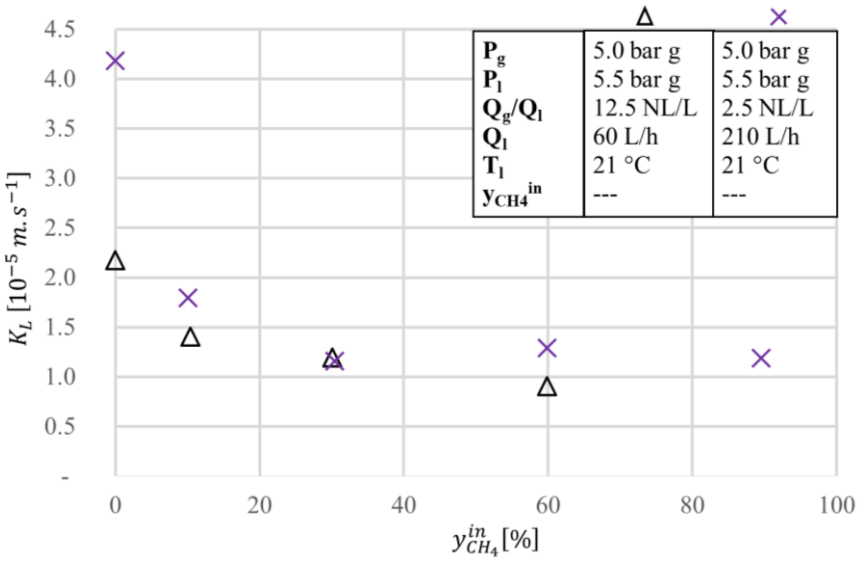

Figure 3.16 – Variation of the overall mass transfer coefficient K_L according to the inlet gas composition

Open-loop configuration

3.4.2.2 Nature of the complementary gas

Two hypotheses are suggested for the observed CO_2 mass transfer limitation in the presence of methane:

- carbon dioxide transfer is limited by the presence of a poorly soluble gas;
- methane molecules interact with water and/or carbon dioxide and limit the transfer and absorption of CO_2.

Methane was replaced by another poorly soluble gas to test the first hypothesis. Oxygen displays a Henry coefficient closer to methane than nitrogen (respectively 3 896, 3 963 and 8 543 MPa for methane, oxygen and nitrogen at $20°C$ - Table 1.10). Though, both for availability and security reasons, nitrogen was preferred. Two batches of tests under similar operating conditions ($y_{CO_2}^{in} = 70 - 100$ %) were then run with mixtures of CO_2 with nitrogen or methane.

Once again, K_L decreases as the inlet molar fraction of methane or nitrogen increases (Figure 3.17). It goes from $4.71 \times 10^{-5}\ m.s^{-1}$ with pure CO_2 to about $2.5 \times 10^{-5}\ m.s^{-1}$ at $y_{CO_2}^{in} = 70$ %. The gap observed between experimental points are within the uncertainty range and both gases can therefore be considered to limit the CO_2 mass transfer in the same manner. As a consequence, the second hypothesis is rejected. Furthermore, the CO_2-CH_4 interaction was already proven to not significantly affect the Henry coefficient values [63]. Thus, the presence of a poorly soluble gas induces a significant mass transfer resistance. This resistance may be located in the gas and/or in the membrane phases.

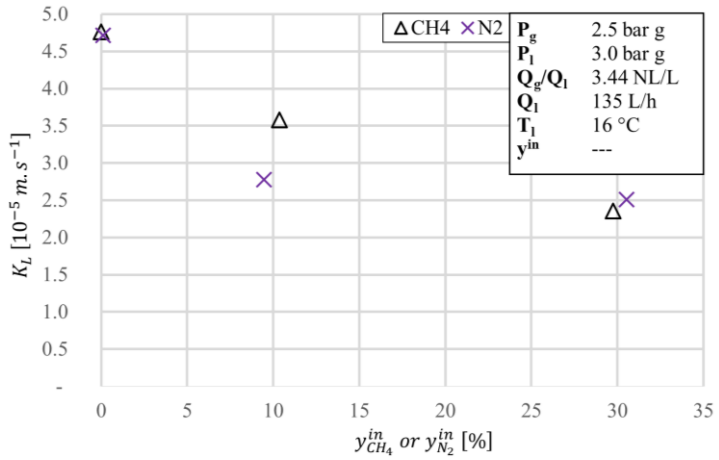

Figure 3.17 – Variation of the overall mass transfer coefficient according to the complementary gas nature

Open-loop configuration

3.4.3 Influence of the inlet gas composition on the average mass transfer coefficient

To further investigate the influence of the inlet gas composition on K_L, all the experiments were compiled to plot the average mass transfer coefficient against the liquid flowrate at different inlet gas compositions in Figure 3.18. Only experiments in the open-loop configuration were selected.

K_L varies in the range $0.9 - 4.8 \times 10^{-5}\ m.s^{-1}$ for this selection of 39 experiments. For a given flowrate, K_L is confirmed to decrease with a diminishing inlet CO_2 fraction. At $Q_l = 5.85 \times 10^{-5}\ m^3.s^{-1}$, three synthetic biogas points ($y^{in}_{CO_2} = 40$ %) are found to have a slightly higher K_L ($2.5 - 3.0 \times 10^{-5}\ m.s^{-1}$) compared to the general trend. These runs were performed with 2 membrane modules in series.

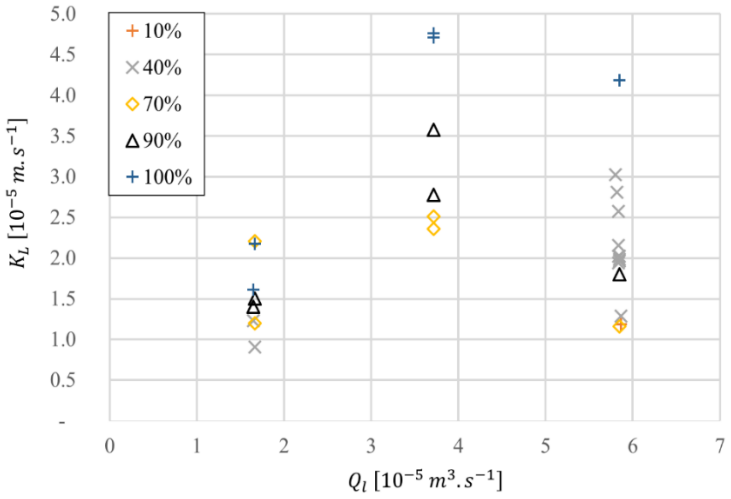

Figure 3.18 – Variation of the overall mass transfer coefficient according to the liquid flowrate and inlet CO_2 molar fraction - synthesis

Open-loop configuration

The presence of a low soluble gas (methane or nitrogen) in the gas mixture is affecting the CO_2 mass transfer coefficient. In a 1D model, the absorbed CO_2 flux in an infinitesimal slice dz of reactor is expressed by:

$$dJ_{CO_2}^{dz} = K_L^0(x^* - x)\, a dz \qquad \text{Eq. 3.6}$$

The presence of this complementary gas is thus affecting the mass transfer rate in two manners:

- it decreases the mass transfer coefficient K_L^0;
- it decreases the mass transfer potential due to a lower CO_2 molar fraction ($x_{CO_2}^* = y_{CO_2}/m_{CO_2}$ ↘).

These experiments provide a solid base to support future modelling or up-scaling works. A range of K_L values for experiments with synthetic biogas was identified ($0.9 - 3.0 \times 10^{-5}\ m.s^{-1}$).

3.5 Process optimization

A membrane contactor is a suitable device to produce biomethane meeting the gas-grid requirements (3.2). Though, at pilot scale, 7 membrane modules in series would be required to operate similarly to an ideal mass exchanger and reach this performance under $Q_g/Q_l = 4.0\ NL.L^{-1}$ (3.3). Indeed, the average mass transfer coefficient K_L is mainly limited by the presence of methane, a poorly soluble gas (3.4). To meet the process developments objectives, several steps were carried out:

- comparison of process performances with a real farm biogas and a synthetic biogas;
- investigation of process architecture (enhanced absorption, alternative degassing system and addition of a methane recycling loop);
- investigation of different absorption solvents.

All experiments were performed in the wet mode to account for real operating conditions.

3.5.1 Upgrading farm raw biogas: influence on process performances

From the DoE experimental campaign (3.3.2), several process parameters were varied to produce the targeted biomethane quality in a liquid closed-loop configuration. For a given gas flowrate ($Q_g = 153$ NL.h^{-1}), a Q_g/Q_l ratio of 1.30 $NL.L^{-1}$ produced biomethane ($y_{CH_4}^{out} = 97.6$ %) with a moderate recovery rate R_{CH_4} of 77.6 %. A higher Q_g/Q_l ratio (1.69 $NL.L^{-1}$) still fulfilled the quality requirement with an improved recovery rate ($R_{CH_4} = 83.7$ %). The average mass transfer coefficient K_L is in the range established in the open-loop configuration (3.4.2).

These recovery rates are still low compared to the available technologies (1.3.2) which allow to recover more than 97 % of the inlet methane flow. Nonetheless, this experimental set-up produces on one side a methane-rich fraction which can be injected into the gas grid, and on the other side a CO_2-rich fraction. Compared to other available technologies, this offgas flow is not diluted with air (as for air stripping in water scrubbing) and still contains a significant methane fraction (respectively $y_{CH_4}^{off} =$

25.3 *and* 20.0 %). This methane content is high enough for this offgas flow to be burnt in a low calorific content burner to cover the digester heat demand. This process point is thus a first proof-of-concept for a biogas upgrading process of industrial interest.

Nevertheless, these results obtained with synthetic biogas had to be confirmed on-site with farm raw biogas. A 2-week experimental campaign took place at a farm from the French Ardennes (GAEC Chateau d'Etrépigny) in December 2015. The farm AD unit, presented in Appendix P, co-digests cow slurry, agroindustrial waste (beet pulp, brewing dregs…), crop residues or grass silage. A by-pass flow is diverted from the average 30 $Nm^3_{biogas}.h^{-1}$ flow to be upgraded in the pilot process. During the 2-week field campaign, the biogas methane content was stable ($y^{in}_{CH_4} = 56.3 - 59.0$ %). An air injection into the digester maintains the H_2S content low ($< 200\ ppmv$) by sulfur oxidation. Though, this air injection results in the presence of nitrogen and oxygen in the biogas flow ($y^{in}_{air} = y^{in}_{O_2} + y^{in}_{N_2} = 1.7 - 2$ %). This air injection was stopped during 3 days for the experimental campaign purpose. Results from this campaign are exclusively presented in this paragraph.

From the previous values of K_L, this experimental campaign was operated with a higher inlet biogas flowrate ($Q_g = 229$ NL.h^{-1}) to test the intensification of the pilot process. In addition, due to biogas compressor limitations, the absorption pressure P_g was set only to 4.5 $bar\ g$. The 97 % biomethane quality was almost reached with a Q_g/Q_l ratio of 1.09 $NL.L^{-1}$ (Table 3.6). The same experimental process point was repeated with a lower inlet air content. The biomethane quality was thus increased from 94.3 to 96.2 %.

Biogas	Q_l $[L.h^{-1}]$	Q_g/Q_l $[NL.L^{-1}]$	P_g $[bar\ g]$	T_l $[°C]$	$y^{in}_{CH_4}$ [%$vol.$]	y^{in}_{air} [%$vol.$]	K_L $[10^{-5} m.s^{-1}]$	$y^{out}_{CH_4}$ [%$vol.$]	R_{CH_4} [%]
Synth.	120	1.30	5.0	27.0	59.5	0.0	2.62	97.6	77.6
	90	1.69	5.0	26.7	59.7	0.0	2.85	97.2	83.7
Raw	210	1.09	4.5	16.3	59.0	1.8	3.07	94.3	83.9
	210	1.09	4.5	16.2	58.0	0.8	2.92	96.2	82.8

Table 3.6 – Comparison of experimental performances in reference architecture 1:1: synthetic and raw farm biogas

Similar biogas upgrading performances were achieved in the reference architecture both with synthetic and raw farm biogases. The process displayed similar average mass transfer coefficients with synthetic and real biogases ($2.62 - 2.85 \times 10^{-5}\ m.s^{-1}$ against $2.92 - 3.07 \times 10^{-5}\ m.s^{-1}$). The slight increase observed for real biogas may be due to an increased liquid flowrate during farm experiments. Therefore, process optimization can be carried out using synthetic biogas in the lab set-up for the sake of convenience. The calculation of the mass transfer indicator K_La ($0.11 - 0.13\ s^{-1}$) demonstrates the intensification potential of the equipment compared to the conventional WS ($0.009 - 0.011\ s^{-1}$ in paragraph 1.3.1.1).

Moreover, within the 2 weeks of on-site campaign, no significant performance degradation was observed. Therefore, the membrane material is not extremely sensitive to the presence of biogas

impurities (like H_2S or VOC[36]). The polymer compatibility with these impurities must however be carefully studied for future industrial developments.

The indicator of energy consumption $W_{process}$ (2.5.1.3) corresponding to these experimental performances was estimated in Table 3.7 according to the procedure detailed in Appendix M. The specific energy consumption is almost equivalent for the three pilot trials ($0.24 - 0.26\ kWh.Nm_{biogas}^{-3}$). Moreover, it is comparable to the specific energy consumption reported for available biogas upgrading processes ($0.2 - 0.3\ kWh.Nm_{biogas}^{-3}$ in Table 1.7). The energy demand for the initial compression and the vacuum pump are equivalent, each of them accounting for about 50 % of the total energy process. As the solvent closed-loop in not depressurized during the regeneration step, membrane contactors offer here a low energy demand for liquid circulation $0.004 - 0.01\ kWh.Nm_{biogas}^{-3}$ (only to compensate the pressure loss along the closed-loop). As a comparison, $0.11\ kWh.Nm_{biogas}^{-3}$ would be required to pressurize the liquid closed-loop from the atmospheric pressure up to the absorption pressure $P_g = 5.0\ bar\ g$ under $Q_g/Q_l = 1.69\ NL.L^{-1}$. If the absorption column is close to an ideal mass exchanger, the Q_g/Q_l ratio may be increased up to $5.29\ NL.L^{-1}$ under similar pressure conditions (3.3.3). Then, the energy consumption associated to the liquid pump may decrease to $0.035\ kWh.Nm_{biogas}^{-3}$.

Biogas	Q_l $[L.h^{-1}]$	Q_g/Q_l $[NL.L^{-1}]$	P_g $[bar\ g]$	$W_{process}$ $[kWh.Nm_{biogas}^{-3}]$	**Compressor** [%]	**Vacuum pump** [%]	**Liquid pump** [%]
Synth.	120	1.30	5.0	0.262	51	46	3
	90	1.69	5.0	0.251	53	45	2
Raw	210	1.09	4.5	0.247	51	45	4

Table 3.7 – Estimated energy consumption in reference architecture 1:1 - see Appendix M

3.5.2 Experimental investigation of process architecture

3.5.2.1 Enhanced absorption: HydroFlow module

In the water conditioning industry, an external device is generally used to prevent and/or remove limescale deposits in pipes, but also to prevent harmful effects of corrosion and bacteria or algae biofilms. This device (HydroFlow module) is positioned on water pipes and acts as a transducer. It results in an electric induced signal ($\pm 150\ kHz$) which is conducted by water throughout the water system. The oscillating induced AC signal favours the formation of ionic suspended clusters in water which prevents ions to attach on the rough surfaces [221].

As it is used to remove limescale deposits, this device was tested as an absorption enhancer and positioned at the liquid inlet of the absorption module in the reference configuration 1:1. The process performances (both $y_{CH_4}^{out}$ and R_{CH_4}) were unaffected for the different process operating conditions tested

[36] Volatile Organic Compounds

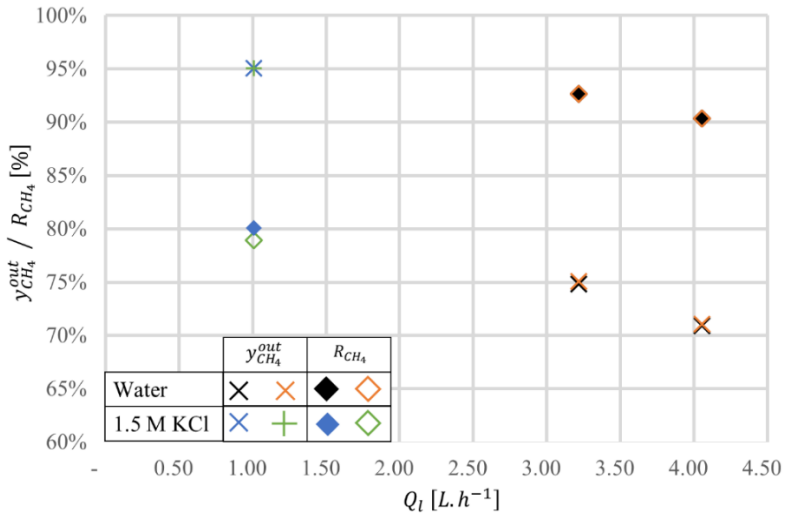

Figure 3.19 – Impact on process performances of an electric signal induced into the water pipe

Left: Reference architecture – Right: Reference architecture with induced electric signal

(Figure 3.19). Anticipating on upcoming results (3.5.3.1), the impact of this device was even tested with a KCl solution as absorbent. In a similar manner, the process performances were unaffected. Therefore, the use of this device was not investigated further.

3.5.2.2 Static mixer and hydroejector as an alternative degassing system

Up to now, the degassing system was a combination of a membrane module and a vacuum pump. It resulted in encouraging performances, but desorption was not complete (3.3.3). It seems interesting to test other devices to improve desorption. Static mixer technology was demonstrated to efficiently accelerate desorption of dissolved gases in a biogas upgrading process [63]. After an imposed pressure drop, the mixing elements located in the cylindrical tube of the static mixer generate intense fluid turbulence which fasten the formation of gas bubbles. An original degassing system was designed (Figure 3.20): it combined a static mixer, a hydro-ejector and a membrane contactor. The energy recovered from the pressure drop was used to generate vacuum in the membrane contactor in order to achieve a quantitative liquid desorption after the gas-liquid separation tank.

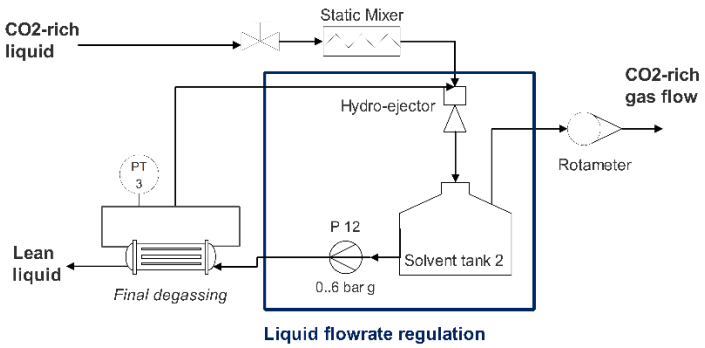

Figure 3.20 – Experimental degassing system combining a static mixer and a hydro-ejector

In this configuration, the energy requirements are modified compared to the reference one. The energy demand is transferred from the vacuum pump in the reference case to the liquid pump in this alternative configuration; this pump is used to pressurize the liquid flow from atmospheric pressure to the pressure of the absorption module.

The results of this new configuration are represented in Figure 3.21, along with the biomethane quality of the reference architecture calculated using the DoE model with similar operating conditions. As established in the reference case, the biomethane quality $y_{CH_4}^{out}$ is increasing with the liquid flowrate. The recovery rate R_{CH_4} is though decreasing. Using the alternative degassing system, $y_{CH_4}^{out}$ is decreased by 3.5 – 5 points compared to the reference configuration. Therefore, carbon dioxide is degassed less effectively than in the reference case.

As a result, the vacuum pump and the membrane contactor were kept as the degassing system. It offers the advantage of a minimal pressure drop in the liquid closed-loop.

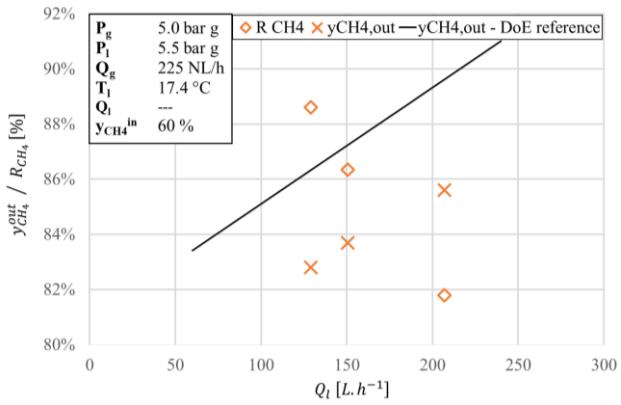

Figure 3.21 – Process performances of an alternative degassing system compared to reference configuration

The DoE curve is the response of the DoE model

3.5.2.3 Methane recycling loop

Commercial biogas water scrubbers are designed with an intermediate step for the regeneration of the CO_2-rich solvent. A flash-tank is set to decrease the pressure at an intermediate level in order to recycle part of the dissolved methane content (Figure 1.9). A new membrane contactor was therefore added in the liquid closed-loop to mimic this architecture (Figure 3.22). This configuration is referred to as 1:1:1 (one membrane module at the absorption step, one at the partial degassing step and one at the final degassing step). The process configurations are referenced in Appendix J.

The process performances were compared against the results obtained in the reference architecture (3.5.1) under the same operating conditions. The recycled flow was controlled by a needle valve to investigate the influence of the gas pressure in the intermediate membrane contactor. The biomethane quality remained constant ($y_{CH_4}^{out} = 95.5 - 95.9$ %) and comparable to the methane content obtained in the reference case. By progressively closing the needle valve, the intermediate gas pressure P_{int} increased from 0.25 to 1.9 $bar\ g$. It increased the methane content in the recycled gas flow $y_{CH_4}^{rec}$ from 57.2 to 76.9 %.

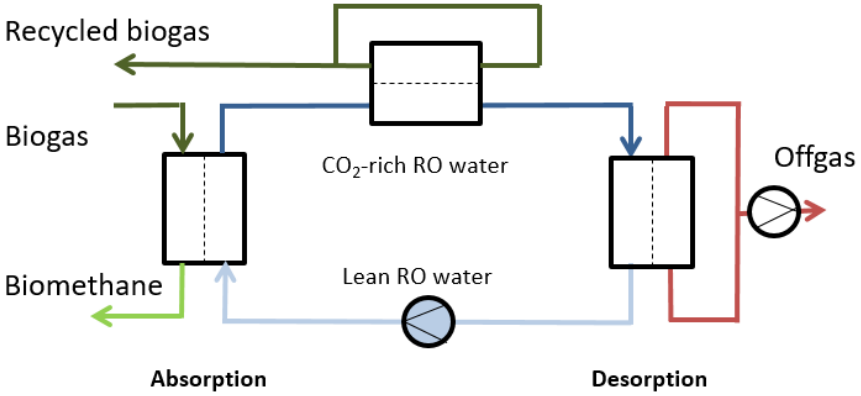

Figure 3.22 – Simplified closed-loop configuration with methane recycling loop 1:1:1

The methane recovery rate R_{CH_4} was calculated by Eq. 2.8 assuming that the recycled gas flow would be mixed with the process inlet biogas flow. Indeed, the recycled gas is close in composition to the inlet biogas ($y_{CH_4}^{in} = 60$ %) and recycling would not significantly affect the feed quality. Completely closing the intermediate needle valve would stop the methane recycling and the process configuration would be similar to the reference case ($R_{CH_4} = 83$ %). By gradually opening the valve, recycling increases and P_{int} decreases: the recovery rate R_{CH_4} is thus increased from 88.5 to 93.5 %. In the meantime, the methane content in the recycled gas $y_{CH_4}^{rec}$ decreases with a decreasing P_{int} from 76.9 to 57.2 %: at $P_{int} = 0.25\ bar\ g$, the inlet gas composition will not be affected by the gas recycling.

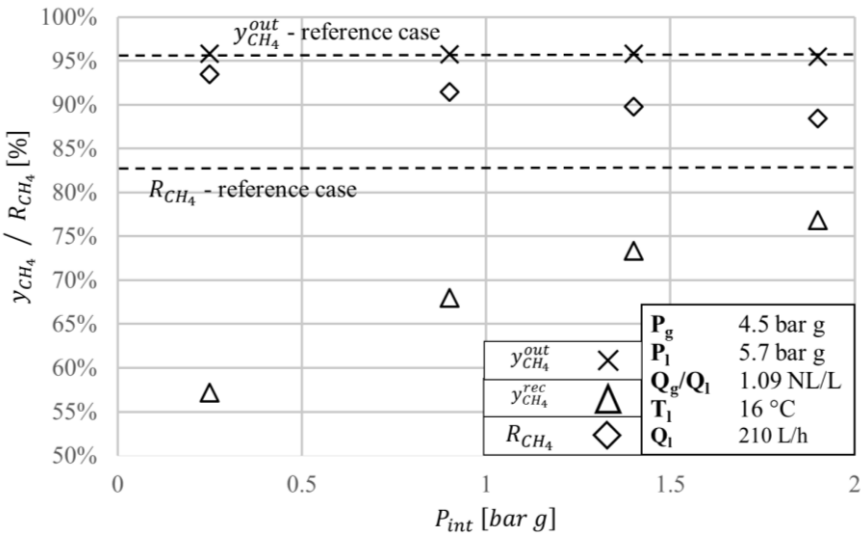

Figure 3.23 – Addition of methane recycling loop: influence of intermediate gas pressure

The best process performances ($y_{CH_4}^{out} = 95.9$ % / $R_{CH_4} = 93.5$ %) were obtained at low intermediate pressure $P_{int} = 0.25\ bar\ g$. The corresponding absorbed flux is $J_{CO_2} = 62\ NL_{CO_2}.m^{-2}.h^{-1}$. The overall mass transfer coefficient calculated from Eq. 2.10 is slightly below previous results in reference configuration ($2.53 \times 10^{-5}\ m.s^{-1}$ against $2.92 - 3.07 \times 10^{-5}$ reported in Table 3.6). As the biomethane quality is kept constant, the absorbed CO_2 flux is equivalent in both

the reference 1:1 and the 1:1:1 configurations. The methane recovery improvement indicates that the addition of the recycling loop mainly impacts the methane mass transfer.

The specific energy consumption was estimated to $0.243\ kWh.Nm_{biogas}^{-3}$ under $P_{int} = 0.25\ bar\ g$. This figure is very slightly below the estimated $0.247\ kWh.Nm_{biogas}^{-3}$ in the reference 1:1 configuration (Table 3.7). In this case, the initial compression requires 52 % of the total energy consumption while the re-compression of the recycled gas accounts for 7 %.

3.5.2.4 Conclusion on process architecture

The enhancement of the absorption step by an induced signal (HydroFlow module) did not prove to be significant compared to the reference configuration. An alternative degassing system combining a static mixer and a hydro-ejector resulted in a degraded biomethane quality as opposed to the reference degassing system in which a vacuum pump degassed the CO_2-rich liquid flowing in a membrane contactor module.

Similarly to commercial water scrubbing, the addition of a methane recycling loop conserved the biomethane quality but also improved the methane recovery rate. Hence, R_{CH_4} was improved from 83.0 % to 93.5 % by addition of an intermediate membrane module. Though, the targeted performances were not experimentally reached yet.

3.5.3 Experimental investigation of solvent influence

To further improve the process performances, two strategies were adopted. Firstly, mineral salts were added to take advantage of the salting out effect and minimize the methane slip. Mineral salts are expected to reduce the gas solubilities but increase the CO_2/CH_4 selectivity π_{CO_2/CH_4} (1.4.2.2). Then, promising amino-acid salts were selected for their CO_2 absorption capacity (5 to 10 fold the absorption capacity of water) and their suitability for industrial operations (1.4.3.2).

3.5.3.1 Mineral salts

This idea of using mineral salts was derived from the low CO_2 loading rate observed ($\psi_{CO_2} = 25 - 30$ %) in the reference configuration (3.3.3). As a reduced fraction of the water absorption capacity was used, the salting out effect was expected to reduce the methane slip without significantly affecting the carbon dioxide absorption efficiency. Two concentrations of KCl in water were successively tested (1.5 and 2.5 M KCl). The selectivity π_{CO_2/CH_4} is theoretically increased by 15.1 and 26.4 % respectively, compared to water (1.4.2.2).

The methane content in the biomethane outlet $y_{CH_4}^{out}$ is found to decrease with an increasing inlet biogas flowrate (Figure 3.24), both for KCl solutions and water (calculated by the DoE model). In addition, for both Q_g/Q_l ratios, the biomethane quality is improved using KCl solutions compared to water. At a low Q_g/Q_l ratio (1.0 $NL.L^{-1}$), the results are comparable whatever the KCl concentration (1.5 or 2.5 M). Though, a greater Q_g/Q_l ratio (1.7 $NL.L^{-1}$) exhibits higher discrepancies between both KCl concentrations and with reverse osmosis (RO) water; in this condition for an inlet gas flowrate

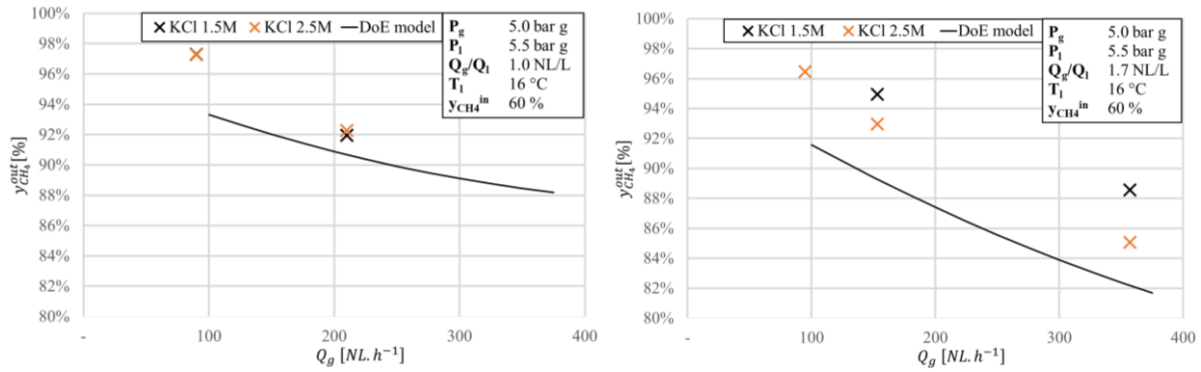

Figure 3.24 – Influence of mineral salt solution: biomethane quality according to inlet biogas flowrate
Left: $Q_g/Q_l = 1.0\ NL.L^{-1}$ - *Right:* $Q_g/Q_l = 1.7\ NL.L^{-1}$

$Q_g = 153\ NL.h^{-1}$, a rich biomethane ($y_{CH_4}^{out} = 94.9$ %) was thus produced with a high recovery rate $R_{CH_4} = 97.0$ %.

The use of mineral salts turned out to significantly improve process performances at the pilot-scale compared to RO water. As a result of this work, a patent application was then filled to protect the use of mineral salts in combination with membrane contactors for a biogas upgrading purpose. Though, due to a reduced carbon dioxide solubility (-27 % for a 1.5 M KCl solution based on literature data), it negatively impacts the process intensification potential (i.e. decrease of the required Q_g/Q_l ratio to produce a gas-grid quality biomethane).

3.5.3.2 Amino-acid salts

Amino-acid salts are expected to enhance carbon dioxide absorption both in capacity and mass transfer rate due to its reactive nature. In an exploratory study, L-alanine was chosen for its moderate cost and its CO_2 absorption capacity [157]. As for mineral salt solutions, the process performances in the reference case using amino-acid solution are compared to RO water results. KOH was added in equimolar proportion to the L-alanine solution. The comparison was made at high Q_g/Q_l ratio ($3.2 - 4.0\ NL.L^{-1}$) due to the strong CO_2 absorption capacity of L-alanine solution ($S_{CO_2} = 0.67\ mol_{CO_2}/mol_{AA}$) [157].

Both with L-alanine solution and RO water, the biomethane quality slightly decreases with the Q_g/Q_l ratio (Figure 3.25). At $Q_g/Q_l = 3.2\ NL/L$, the L-alanine solution and water result in similar biomethane qualities (71.6 % and 70.8 % for L-alanine solution and RO water respectively) for $Q_l = 210\ L/h$. With a lower liquid flowrate $Q_l = 90\ L/h$, the L-alanine solution improves the biomethane quality from 74.5 to 79.8 %. With regards to the amino-acid solution absorption capacity, it appears that the process may be limited by the desorption step instead of the absorption step as opposed to RO water (3.3.4).

Regarding the methane recovery rate, the Q_g/Q_l ratio has little impact with both absorption solutions. However, the L-alanine solution shows higher recovery rates compared to RO water (95.2 % vs 91.1 % and 96.8 % vs 95.4 % for $Q_l = 90\ and\ 210\ L.h^{-1}$ respectively).

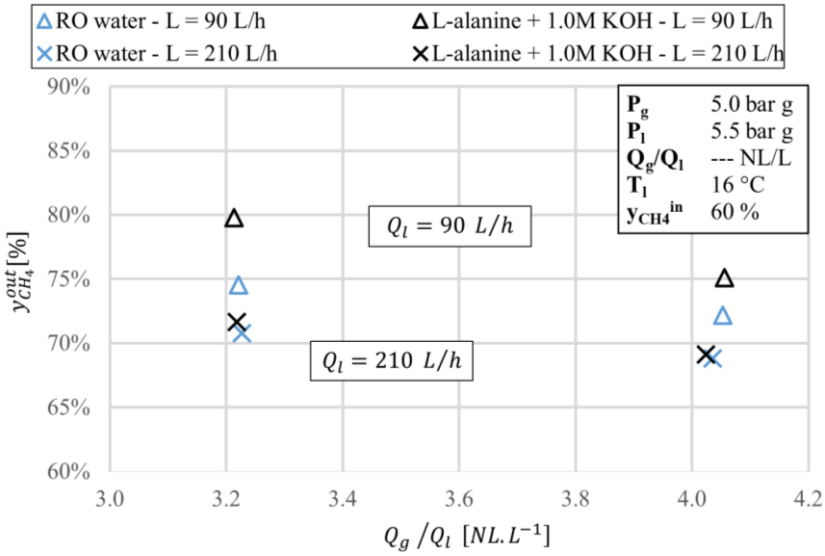

Figure 3.25 – Influence of amino-acid salts: biomethane quality according to gas-to-liquid ratio

Using a solution of L-alanine improves the process performances compared to RO water. This effect is stronger for a lower liquid flowrate ($Q_l = 90\ L.h^{-1}$). CO_2 absorption with amino acids is fast and therefore the desorption unit may be the limiting step (contrary to the use of RO water). Decreasing the absorbent flowrate leads to a more efficient desorption: thus, the absorption capacity of the lean solvent is increased for absorption step. Besides the solvent absorption capacity is more efficiently used at low flowrates. As a result, despite a promising carbon dioxide absorption capacity, the pilot-scale process was far from the targeted performances. More experimental tests must be conducted in order to improve the desorption efficiency either by increasing membrane surface or by adding a promoter for CO_2 desorption.

3.5.4 Combination of solvent and process architecture results

The last experimental campaign set the use of a KCl solution in a methane recycling loop configuration. The impact of solvent temperature ($T_l = 8 - 30°C$) was investigated under two Q_g/Q_l ratios ($1.7 - 1.8\ NL.L^{-1}$). Process performances are displayed in Figure 3.26.

The biomethane quality increases with a colder absorbent for both Q_g/Q_l ratios. Under $Q_g/Q_l = 1.7\ NL.L^{-1}$, it rises from $y_{CH_4}^{out} = 96.5$ % at 29.2°C to 97.7 % at 8.1°C which is above the 94.9% obtained in the reference configuration (3.5.3.1). At the same time, the recovery rate decreases but is kept high from $R_{CH_4} = 99.0$ % to 97.8 %. Comparable recovery rates are obtained under a higher Q_g/Q_l ($1.8\ NL.L^{-1}$); though, the biomethane quality is decreased by 2-2.5 points and drops below the targeted performance.

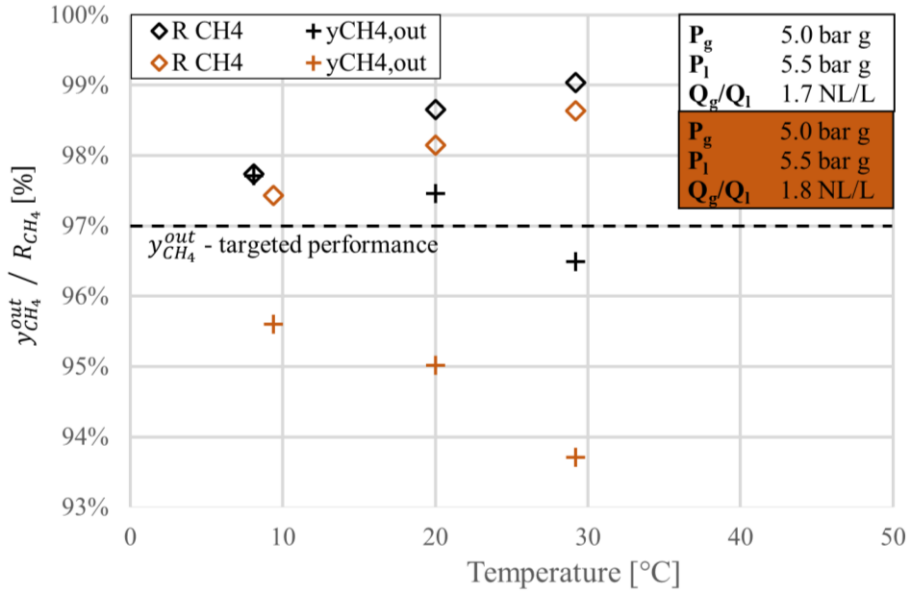

Figure 3.26 – Combination of methane recycling loop and KCl solution: influence of temperature on process performances

This experimental campaign provided two experimental process conditions satisfying the process objectives. The best result was obtained at $T_l = 20°C$ by producing a 97.5 % biomethane with a 98.7 % methane recovery rate. The absorbed flux is $J_{CO_2} = 42\ NL_{CO_2}.m^{-2}.h^{-1}$: it is below the value previous reported for water in paragraph 3.5.2.3 ($62\ NL_{CO_2}.m^{-2}.h^{-1}$) since the inlet biogas flow was also lower in the present case. The corresponding overall mass transfer coefficient ($K_L = 2.81 \times 10^{-5}\ m.s^{-1}$) calculated for a scale-up purpose is slightly above the experimental value obtained with water ($2.53 \times 10^{-5}\ m.s^{-1}$) in a similar configuration. It explains the higher level of performances obtained.

The energy consumption was estimated to $0.225\ kWh.Nm_{biogas}^{-3}$ under these operating conditions (Appendix M). A small improvement is made compared to the case of water in the same 1:1:1 configuration (-7.4 %). This decrease is essentially due to energy consumption of the vacuum pump. It may be explained by the lower offgas flowrate resulting from the addition of mineral salts in the water.

The patent application filled to protect the use of mineral salts in combination with membrane contactors for a biogas upgrading purpose refers to both the 1:1 and the 1:1:1 configurations.

3.6 Conclusion

This experimental chapter aimed at providing data to understand the impact of process parameters and at establishing the proof-of-concept for the biogas upgrading process. The design of experiment methodology identified the flowrates Q_g and Q_l, the absorption pressure P_g and the inlet methane content $y_{CH_4}^{in}$ to be the operating parameters driving the process performances in a reference configuration 1:1. The mass transfer rate was too limited to reach the satisfying biomethane quality on

the pilot equipment, even by doubling the membrane exchange surface for Q_g/Q_l above 2.5 $NL.L^{-1}$. It was thus evidenced that the presence of a poorly soluble gas (i.e. methane) was more limitating than membrane wetting. In a biogas mixture, K_L is divided by a factor 2-3 (compared to the pure CO_2 case) as opposed to a 20-30 % reduction when the membrane shifts from its dry to wet regime.

The process development strategy was carried out in several steps. Firstly, a field campaign demonstrated that comparable performances were obtained by upgrading farm raw and synthetic biogases. Therefore, different configurations were successively tested in the laboratory. Similarly to commercial water scrubbing unit, the addition of a methane recycling loop improved the methane recovery rate from $R_{CH_4} = 83$ % to 93.5 %. The specific energy consumption ($0.243\ kWh.Nm_{biogas}^{-3}$) is estimated comparable to the one of state-of-the-art biogas upgrading processes ($0.2 - 0.3\ kWh.Nm_{biogas}^{-3}$). Then, the salting out effect resulting from mineral salt solutions also improved the methane slip in the reference configuration. The promising potential of amino-acid salt solutions though turned out to be limited by the desorption step due to their high affinity for carbon dioxide. The combination of the methane recycling loop with a KCl solution established a proof-of-concept for biogas upgrading with membrane contactors. A biomethane complying with gas-grid specifications ($y_{CH_4}^{out} = 97.5$ %) was obtained with a satisfying recovery rate ($R_{CH_4} = 98.7$ %): the corresponding absorbed flux is $J_{CO_2} = 42\ NL_{CO_2}.m^{-2}.h^{-1}$. Furthermore, the estimated process energy consumption is competitive ($W_{process} = 0.225\ kWh.Nm_{biogas}^{-3}$). Also, the process is intensified by a factor 10 ($K_L a = 0.11\ s^{-1}$), as compared to the conventional WS in a packed column. A patent application was filled to protect the use of mineral salts in combination with membrane contactors for a biogas upgrading purpose.

Chapter 4

Modelling gas-liquid mass transfer at contactor scale

Chapter 4 Modelling gas-liquid mass transfer at contactor scale

4.1 Introduction

This chapter introduces the original modelling approach carried out to describe the gas-liquid mass transfer in the hollow fiber membrane module (HFMM). This numerical tool is developed for a process upscaling purpose. The choice for an original modelling strategy and the numerical development roadmap are presented in section 4.2. The model is then detailed in paragraph 4.3.1 and 4.3.2 for the case of pure CO_2 absorption; it allows to identify the parameters of the Chilton-Colburn equation based on the local description of hydrodynamic conditions (4.3.3). The model is validated against a batch of experiments in the membrane dry mode. Then, the membrane wetting description presented in the literature is tested as an additional numerical block (4.4). Numerical adaptations are carried out to describe the absorption of CO_2 within a gas mixture (4.5.1). The comparison against experimental data shows a strong numerical overestimation of the CO_2 absorbed flux (4.5.2). As a result, an additional mass transfer resistance is suggested and optimized to fit the experimental results (4.5.3).

4.2 An original modelling tool

The equations governing mass transfer in 1D and 2D models have been presented in paragraph 1.6.2. A critical comparative study carried out for post-combustion carbon capture concluded that 1D, 1D-2D and 2D models have a comparable efficiency to fit experimental results [185]. Though, it was pointed out that these models should conserve the membrane mass transfer coefficient k_m as a fitting parameter. The precise prediction of k_m was identified of major interest although difficult due to large uncertainties on membrane pore size distribution, tortuosity and wetting ratio. Based on this study, the resistance-in-series model (1.6.2.1) was adopted to describe the overall mass transfer resistance; the mass transfer rate is controlled by three resistances (gas, membrane and liquid phases successively).

As pointed out in Chapter 1, the assumption of a parallel flow in membrane modules comprising a center diverting baffle is questionable. To address this issue, a model relying on local liquid hydrodynamic conditions is suggested. By doing so, the model optimization will be valid on industrial modules for upscaling purposes. The model is developed sequentially:

- firstly, the Chilton-Colburn correlation (Eq. 1.44) describing the liquid mass transfer resistance is optimized using pure CO_2 absorption experiments in the dry regime;
- then, the description of membrane wetting available in the literature is tested using the same experiments in their wet regime;
- the optimized model is tested on open-loop biogas absorption experiments;
- an additional resistance in the gas-filled membrane phase is suggested to adapt the pure CO_2 absorption model to biogas upgrading.

Based on experimental observations, two assumptions can be drawn for the absorption of pure CO_2. Firstly, the gas pressure drop being negligible along the module, the partial pressure in CO_2 is kept constant. Moreover, the gas phase and membrane resistances are negligible against the liquid resistance. Hence, the Chilton-Colburn correlation (Eq. 1.44) describing the liquid resistance dependency to hydrodynamic conditions can be derived from experimental results.

4.3 Modelling approach

The modelling approach is detailed for the absorption of pure CO_2 in the gas phase.

4.3.1 Model development

The present model has been developed to provide a predictive tool for the design of physical absorption processes. This model aims at fulfilling the following requirements:

- describe the complex fluid hydrodynamics including the baffle in the shellside (Figure 1.28);
- simulate gas absorption in steady state in both dry and wetted modes.

The following assumptions are made to develop the model:

1. Isothermal operation;
2. Gas flowing in the lumenside under constant gas pressure (no pressure drop);
3. Ideal gas behavior;
4. Henry's law is valid;
5. Membrane features (average pore size, pore size distribution, porosity, thickness, hydrophobicity and tortuosity) are uniform in the module;
6. Membrane properties are constant over time;
7. Solvent evaporation is neglected (low vapor pressure);
8. No phase entrainment across the membrane.

The solvent in the shellside is flowing through the fiber bundle, considered as a porous medium; its hydrodynamics is described by the Darcy equation:

$$\overrightarrow{u_l} = -\frac{\bar{\bar{\kappa}}_l}{\mu_l}\nabla P_l \qquad \text{Eq. 4.1}$$

where $\overrightarrow{u_l}$ is the liquid velocity, P_l the liquid pressure, μ_l the liquid dynamic viscosity and $\bar{\bar{\kappa}}_l$ the permeability tensor of the porous medium.

The fluid is considered incompressible and therefore the mass continuity equation gives:

$$\nabla.\overrightarrow{u_l} = 0 \qquad \text{Eq. 4.2}$$

The mass balance equation on the liquid phase can be written:

$$\frac{\partial \varepsilon_{bed,l} C_{CO2}^{l}}{\partial t} + \nabla.\left(\overrightarrow{u_l}.C_{CO2}^{l}\right) = \frac{\varepsilon_{bed,l}}{\tau_{bed,l}} D_{CO2}^{l} \Delta C_{CO2}^{l} + r_{CO2} \qquad \text{Eq. 4.3}$$

where C_{CO2}^{l} is the dissolved CO_2 concentration in the liquid, D_{CO2}^{l} the CO_2 diffusivity in the liquid, and r_{CO2} is the source term.

The porous medium is characterized by its porosity $\varepsilon_{bed,l}$ (Eq. 4.4) and its tortuosity $\tau_{bed,l}$.

$$\varepsilon_{bed,l} = 1 - \Phi = 1 - \frac{N_f d_{fo}^2}{(2R_o)^2 - (2R_i)^2} \qquad \text{Eq. 4.4}$$

where Φ is the packing fraction in the fiber bundle, N_f is the number of fibers, d_{fo} is the outer fiber diameter, R_o and R_i are respectively the outer and inner radius of the module.

The source term r_{CO2} is the CO_2 flowrate transferred from the gas phase to the liquid phase in $mol.m^{-3}.s^{-1}$:

$$r_{CO2} = \varepsilon_m K_{L,CO2} a\left(H_{CO2}^{cc} C_{CO2}^{g} - C_{CO2}^{l}\right) \qquad \text{Eq. 4.5}$$

where $K_{L,CO2}$ is the local mass transfer coefficient ($m.s^{-1}$), a the specific area ($m^2.m^{-3}$), H_{CO2}^{cc} the dimensionless Henry coefficient, C_{CO2}^{i} the concentration of CO_2 in the bulk of phase i.

The HFMM has an axial geometry. The set of equations is thus reduced to a two dimensions problem and a meshing is applied to the surface. The total mass transfer coefficient $K_{L,CO2}$ is estimated locally based on Eq. 1.43, Eq. 1.44 and Eq. 1.53. Given the inlet composition and flowrates of both phases, the operating pressures and the temperatures (P_l, P_g, T_l, T_g), the model calculates the outlet compositions and flowrates.

The equation system was implemented and solved using the open source CFD[37] framework OpenFOAM. A sequential approach with an implicit formulation and second order numerical schemes was used. The mesh convergence was achieved using a 9000 square cells mesh. Solver tolerance was set below 10^{-4}. Domain imbalance was verified to be below 10^{-6}. The runtime is about 15 minutes on a single thread (Intel Core i7-4910 MQ Haswell at 2.90 MHz, 16 Go DDR3 1600 MHz).

[37] Computational Fluid Dynamics

4.3.2 Geometry and boundary conditions

Data from Table 2.1 and Table 2.2 are used to define the module geometry. Boundary conditions are specified in Figure 4.1. Because of the fiber orientation, the porous medium is anisotropic. The permeability tensor $\overline{\overline{\kappa_l}}$ is estimated from the work of Lemanski and Lipscomb on the shellside flows in hollow fiber modules [222].

$$\overline{\overline{\kappa_l}} = \begin{bmatrix} \kappa_{rr} & 0 \\ 0 & \kappa_{zz} \end{bmatrix} \quad \text{Eq. 4.6}$$

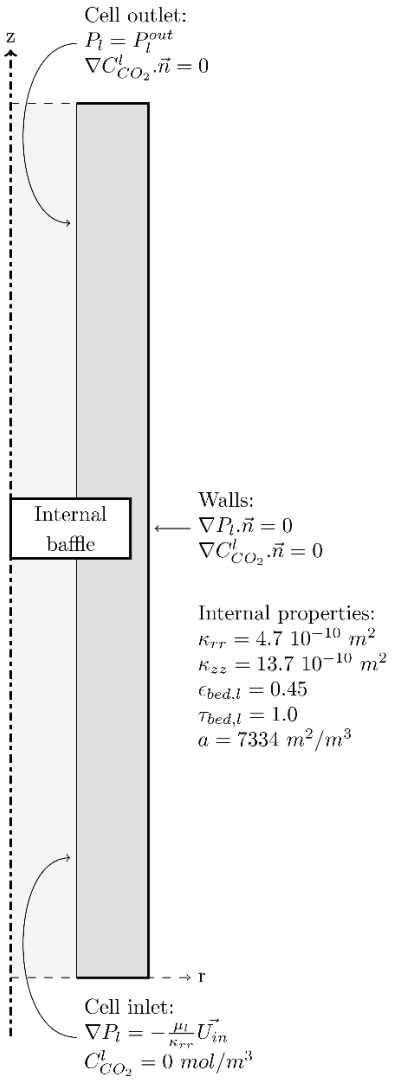

Figure 4.1 – Internal module geometry to simulate liquid shellside flow

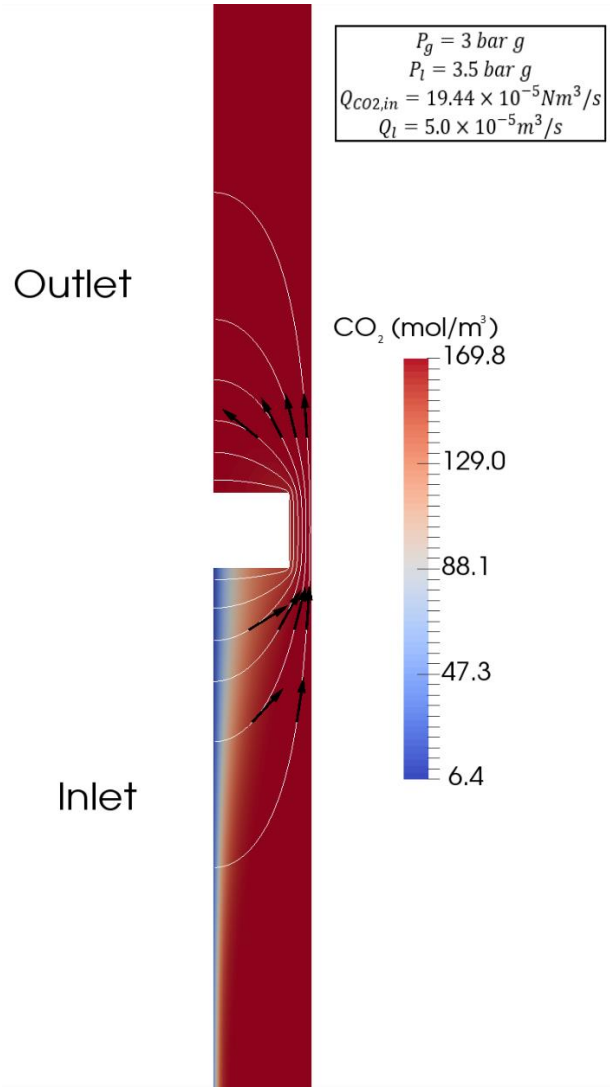

Figure 4.2– Dissolved CO_2 concentration profile along the membrane contactor in dry mode

White lines: liquid flow streamlines

The correlations from literature which are used to estimate physical-chemical data for the model are presented in Appendix E, Appendix F and Appendix G.

The originality of the present model is to integrate the effect of the baffle on the shellside liquid hydrodynamics. Figure 4.2 shows a progressive CO_2 loading of the liquid from fresh water to saturation ($C_{CO_2}^l = 173.0\, mol.m^{-3}$). The fluid streamlines indicate a symmetry in the liquid flow pattern. Interestingly, the lower and upper parts of the module are dead volume which means that the membrane contactor is not fully efficient for gas-liquid mass transfer.

4.3.3 Optimization of Chilton-Colburn parameters

The Chilton-Colburn equation (Eq. 4.11) introduced in paragraph 1.6.2.1 requires to determine values for its parameters ω and c.

$$Sh = f(Re, Sc) = \omega Re^c Sc^{\frac{1}{3}} \quad \text{Eq. 4.7}$$

where Sh, Re and Sc are respectively the Sherwood, Reynolds and Schmidt dimensionless numbers.

As suggested from the literature review (1.6.2.1), the dimensionless numbers are calculated from the local hydrodynamic conditions of the shellside. Therefore, the Reynolds and Sherwood numbers are considered as non-uniform across the membrane module.

$$Sh_l = \frac{k_{l,i} d_{fo}}{D_i^l} \quad \text{Eq. 4.8}$$

$$Re_l = \frac{u_l d_{fo}}{\nu} \quad \text{Eq. 4.9}$$

$$Sc_l = \frac{\nu}{D_i^l} \quad \text{Eq. 4.10}$$

where $k_{l,i}$ is the mass transfer coefficient of the specie i in the liquid phase and ν is the kinematic viscosity.

The objective function F_{obj} is defined to minimize the cumulative relative error between the model and the experimental data:

$$F_{obj} = \sum_{test\ i} \left| \frac{Q_{CO2,exp}^{abs,i} - Q_{CO2,mod}^{abs,i}}{Q_{CO2,exp}^{abs,i}} \right| \quad \text{Eq. 4.11}$$

where $Q_{CO2}^{abs,i}$ is the absorbed CO_2 flowrate for test i, with exp and mod being respectively relative to the experimental and the model results.

Optimization is performed on the absorption flowrates in the dry regime in steady state. Two sets of experimental data in the dry mode are gathered (Table 3.5) : our experimental results and the ones obtained by Mavroudi [197]. Both sets were used to find the optimal parameters of the model.

The model parameters were determined using Particle Swarm Optimization (PSO) method. This method was originally based on the observation of animal groups behavior [223, 224]. Its mathematical relevance has been especially shown in cases requiring the optimization of numerous parameters [225]. This method has already been successful to solve various problems (building cost optimization, solar power plant design, …) [226, 227], including some with highly discontinuous objective functions [228]. The PSO algorithm is run until the parameters are determined with two significant digits.

The Chilton-Colburn parameters optimization leads to the following equation:

$$Sh = 3.51 Re^{0.42} Sc^{\frac{1}{3}} \qquad \text{Eq. 4.12}$$

This correlation allows to estimate the local mass transfer coefficients; it cannot be directly compared with the correlations cited in Table 1.18 which give the overall transfer coefficients for the whole HFMM. Though, the value of the parameter c which describes the dependency on liquid velocity should be in the same range (0.42 – 0.82). The ω value is realistic since it is in the order of magnitude of 1.

4.4 CO_2 absorption as a pure gas

The above optimization was performed in the dry mode. Therefore, the model is first validated in this regime comparing experimental and simulated results. Then, the description of membrane wetting available in the literature (1.6.3) is added to the validated model. The experimental and simulated results are compared in the wet regime.

4.4.1 Non-wetted mode

The CO_2 absorbed flowrates calculated with the model and the experimental results are presented in Figure 4.3. As expected according to Henry's law, the absorbed CO_2 flowrate is higher with increasing gas pressure. Two different trends are observed depending on the data set. The model slightly underestimates the absorption flowrates (- 1 / -13 %) at low liquid flowrates and medium gas pressures ($P_g = 3.0 \; and \; 5.0 \; bar \; g$) in the case of our experimental results. For data from Mavroudi [197] with higher liquid flowrates and atmospheric pressure in the gas, there is a satisfying agreement between experimental and numerical results (-10 / +17 %). Both differences in the experimental set-ups and the operating conditions could explain the discrepancies.

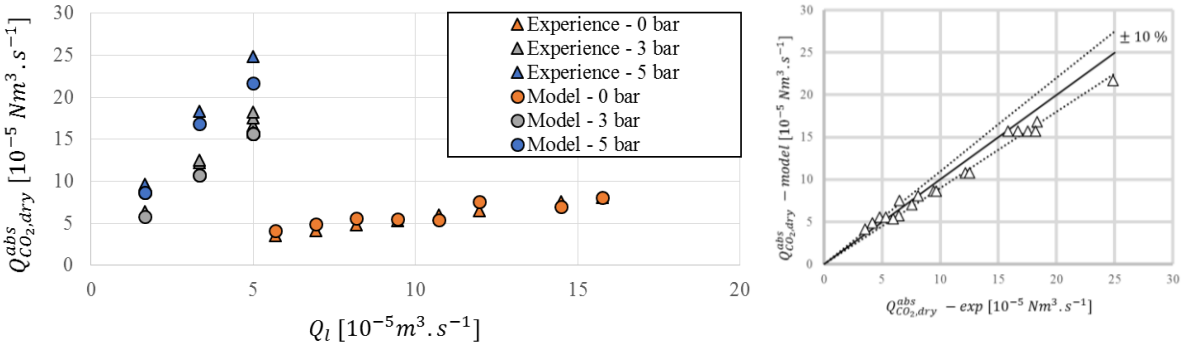

Figure 4.3 – Model validation in the membrane dry mode

Left: Experimental and numerical absorbed CO_2 flows according to the liquid flowrate
Right: Numerical absorbed CO_2 flow as a function of the experimental one

4.4.2 Wetted mode

The model is then run in the wetted mode with the optimized parameters; the calculated and experimental absorption flowrates are compared (Figure 4.4). The results are differentiated according to the gas pressure. At $P_g = 5.0\ bar\ g$, the transmembrane pressure was limited to 0.5 bar and a good agreement is observed between experimental and model results. At $P_g = 3.0\ bar\ g$, the model results are comparable to experimental results for $\Delta P = 0.5\ bar$. However, the results for $\Delta P = 2.5\ bar$ demonstrate a significant underestimation of the absorbed CO_2 flowrate (-52 / -77 %). At $P_g = 0.0\ bar\ g$, the model error increases with the liquid flowrate. For this data set, the transmembrane pressure is also increasing with the liquid flowrate.

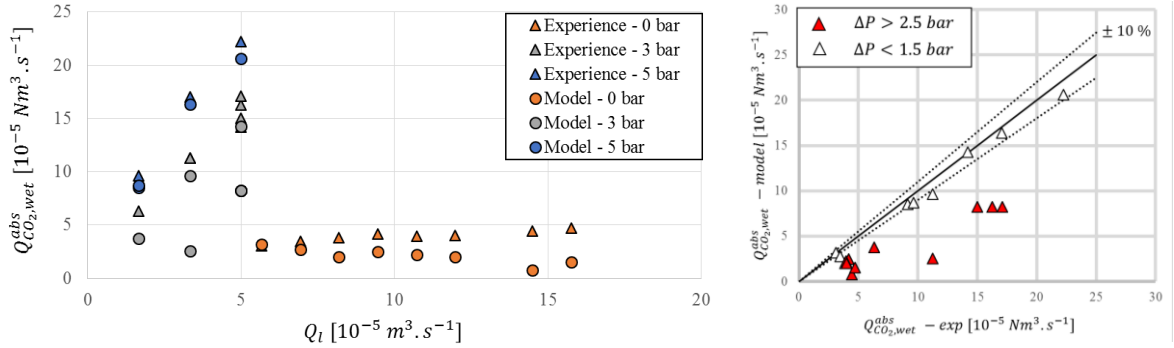

Figure 4.4 – Model validation in the membrane wet mode

Left: Experimental and numerical absorbed CO_2 flows according to the liquid flowrate
Right: Numerical absorbed CO_2 flow as a function of the experimental one

As the transmembrane pressure is supposed to have an impact on wetting according to Eq. 1.50, the relative error of the model ε_{rel} calculated with Eq. 4.13 is plotted against this parameter (Figure 4.5).

$$\varepsilon_{rel} = \frac{Q^{abs}_{mod} - Q^{abs}_{exp}}{Q^{abs}_{exp}} \qquad \text{Eq. 4.13}$$

The absolute relative error significantly increases with transmembrane pressure, for both sets of data. Consequently the wetting phenomenon is not correctly taken into account in the model.

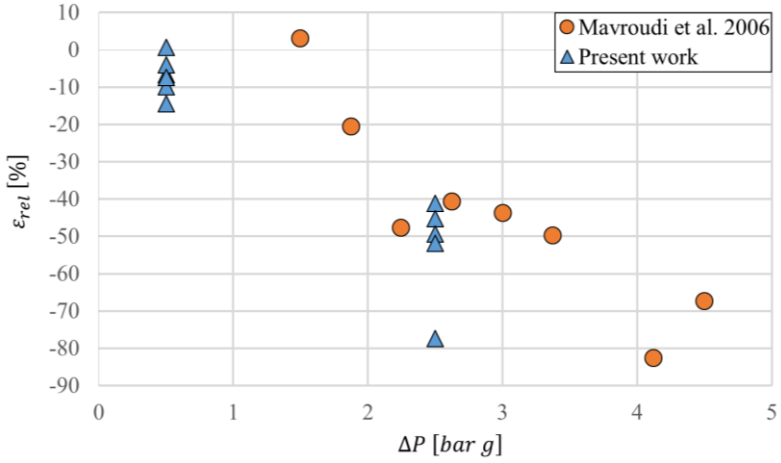

Figure 4.5 – Relative error of the model dependence on transmembrane pressure in the membrane wet mode

The experimental results from Figure 3.14 and their comparison with model results shows that the transmembrane pressure might not be an important factor in the membrane wetting. Therefore, the description provided in the literature and detailed in paragraph 1.6.3 might not capture well the wetting phenomenon. Further experimental tests are needed to suggest a new description.

Modifications in the model of membrane mass transfer in partial wetting mode could bring an explanation. In the literature as well as in this work, the membrane porosity is described by cylindrical non-interconnected pores. Wetting implies that the larger pores are fully wetted while smaller pores are still dry. The resistances of these two categories of pores have been considered in series so far in the literature and in the present model (Eq. 1.53).

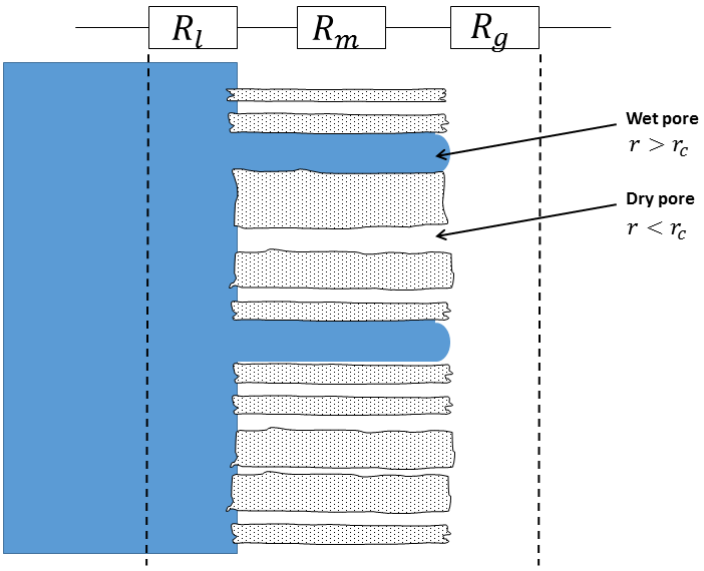

Figure 4.6 – Membrane porosity and membrane wetting modelling

Nonetheless, the membrane porosity model and the membrane wetting description in Figure 4.6 imply to consider the resistances in parallel. This modification will transform Eq. 1.53 into Eq. 4.14, significantly reducing the impact of transmembrane pressure.

$$k_{m,eq} = \eta k_{m,wet} + (1-\eta) k_{m,dry} \qquad \text{Eq. 4.14}$$

where $k_{m,eq}$ is the equivalent mass transfer coefficient of the membrane (including the wet and dry pores), η is the membrane wetting fraction (Eq. 1.51), $k_{m,wet}$ and $k_{m,dry}$ are the membrane mass transfer coefficients when the membrane is respectively fully wetted and fully dry.

4.4.3 Discussion

Both numerical and experimental results are in good agreement (-13 / +17 % error) when the membrane contactor is operated in the dry mode. The liquid mass transfer coefficient is estimated by a Chilton-Colburn correlation, optimized on experimental data with a PSO algorithm. In the wet mode, the membrane pore size distribution is considered. The pores which size is above the Laplace-Young critical radius are considered as totally wetted, the others being dry. Then, the membrane mass transfer coefficient is estimated from the wetting ratio (Eq. 1.51 and Eq. 1.53). The relative error between simulated and experimental results increases with the transmembrane pressure up to 83 %. Therefore, the penetration of water in the membrane is not properly described by the Laplace-Young equation (Eq. 1.50). Additional local measurements and complementary tests would strengthen the newly proposed modelling description of partial wetting (Eq. 4.14). Nevertheless, experimental results proved that membrane wetting is not significantly affecting the absorbed CO_2 flux (<10.5%) in our process conditions (3.4.1). Thus, in the following work, the experimental data are treated as if the membrane was entirely dry.

In addition to simulating mass transfer in a membrane module, this original model offers a new vision of the shellside hydrodynamics which was not previously addressed in the literature. It especially applies to the hollow fiber modules with a diverting baffle, as for the Liqui-Cel® Extra-Flow produced by Membrana. This model is a first step towards the optimization of the inside geometric design of the contactor (addition of new geometrical elements, inner and outer radii of the fiber bundle…). Such a tool can indeed numerically evaluate mass transfer variations induced by a geometric modification.

4.5 CO_2 absorption in a multicomponent gas mixture

The model developed for pure CO_2 absorption is then adapted to a binary gas mixture. The gas molar fractions vary along the module: it thus implies to create numerical fields for both gas molar fractions in the model. Then, the initial model is tested on biogas absorption experiments performed in an open-loop configuration. An explanation for the numerical deviation observed and a correction are subsequently suggested in the last paragraph.

4.5.1 Model adaptation for multicomponent absorption

The model describing CO_2 absorption is adapted to the absorption of a binary gas mixture. Gas and liquid flows are entering the membrane module counter-currently. Two fields describing the bulk molar fractions of the gas phase are created (y_{CO_2} and y_{CH_4}). The progressive biogas upgrading resulting from the numerical model is displayed in Figure 4.7 to better understand the geometry of this 2D model. Hollow fibers are parallel and directed in the module axis.

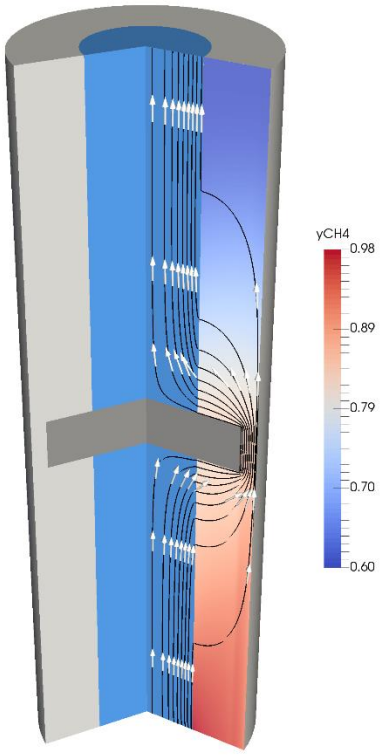

Figure 4.7 – Liquid flow distribution and biogas upgrading in the developed 2D model

The liquid phase mass balance (Eq. 4.3 and Eq. 4.5) written for the pure CO_2 case is still valid. The same equations apply to methane (Eq. 4.15 and Eq. 4.16).

$$\frac{\partial \varepsilon_{bed,l} C^l_{CH_4}}{\partial t} + \nabla.\left(\overrightarrow{u_l}.C^l_{CH_4}\right) = \frac{\varepsilon_{bed,l}}{\tau_{bed,l}} D^l_{CH_4} \Delta C^l_{CH_4} + r_{CH_4} \qquad \text{Eq. 4.15}$$

where $C^l_{CH_4}$ is the dissolved CH_4 concentration in the liquid and $D^l_{CH_4}$ its diffusivity in the liquid.

The source term r_{CH_4} is the CH_4 flowrate transferred from the gas phase to the liquid phase in $mol.m^{-3}.s^{-1}$:

$$r_{CH_4} = \varepsilon_m K_{L,CH_4} a\left(H^{cc}_{CH_4} C^g_{tot} y_{CH_4} - C^l_{CH_4}\right) \qquad \text{Eq. 4.16}$$

where K_{L,CH_4} is the local mass transfer coefficient of methane ($m.s^{-1}$), a the specific area ($m^2.m^{-3}$), $H^{cc}_{CH_4}$ the dimensionless Henry coefficient, $C^{\varphi}_{CH_4}$ the concentration of CH_4 in the bulk of phase φ.

The gas flow in the lumenside is described by the Darcy equation:

$$\overrightarrow{u_g} = -\frac{\overline{\overline{\kappa_g}}}{\mu_g}\nabla P_g \qquad \text{Eq. 4.17}$$

where $\overrightarrow{u_g}$ is the gas velocity, P_g the gas pressure, μ_g its dynamic viscosity and $\overline{\overline{\kappa_g}}$ the permeability of the porous medium. The permeability $\overline{\overline{\kappa_g}}$ is derived from the Poiseuille equation for a viscous flow in a cylindrical tube:

$$\overline{\overline{\kappa_g}} = \varepsilon_{bed,g}\frac{d_{fi}^2}{32}.\begin{pmatrix}0 & 0 & 0\\ 0 & 0 & 0\\ 0 & 0 & 1\end{pmatrix} \qquad \text{Eq. 4.18}$$

The gas flow is controlled by the mass continuity equation in which the gas-liquid mass transfer terms r_i appear:

$$\nabla.\left(\rho_g\overrightarrow{u_g}\right) = -\overline{\overline{\kappa_g}}\nabla.\left(\frac{C_{tot}^g M_g}{\mu_g}\nabla P_g\right) = -\sum_i r_i\, M_i \qquad \text{Eq. 4.19}$$

where ρ_g is the gas density, C_{tot}^g the total gas molar concentration, r_i the source term for species i (Eq. 4.16), M_g and M_i the respective molar masses of the gas phase mixture and species i.

The mass balance equation on the gas phase for component i controls the evolution of its molar fraction y_i:

$$\frac{\partial \varepsilon_{bed,g} C_{tot}^g y_i}{\partial t} + \nabla.\left(\overrightarrow{u_g}.C_{tot}^g y_i\right) = \frac{\varepsilon_{bed,g}}{\tau_{bed,g}} D_i^g C_{tot}^g \Delta y_i - r_i \qquad \text{Eq. 4.20}$$

where $\varepsilon_{bed,g}$ and $\tau_{bed,g}$ are the porosity and tortuosity of the fiber bed regarding the gas phase, y_i is the gas molar fraction, D_i^g the diffusion coefficient in the gas mixture and r_i the source term (Eq. 4.16) of species i. C_{tot}^g is considered constant along the membrane module as no pressure drop has been observed during the experiments ($\Delta P < 0.05\ bar$).

Since the fiber lumenside is not interconnected, the gas is numerically forced to flow only in the direction of the fibers. Additional boundary conditions are set at the gas inlet and outlet (Table 4.1).

Field	**Gas inlet**	**Gas outlet**	**Initial conditions**
$\boldsymbol{y_{CO_2}}$	$y_{\mathrm{CO_2}}^{in}$	$\nabla \mathrm{y_{CO_2}}.\vec{n} = 0$	$y_{CO_2}^{in}$
$\boldsymbol{y_{CH_4}}$	$y_{\mathrm{CH_4}}^{in} = 1 - y_{CO_2}^{in}$	$\nabla \mathrm{y_{CH_4}}.\vec{n} = 0$	$y_{CH_4}^{in}$
$\boldsymbol{P_g}$	$\vec{\nabla} P_g = -\frac{\mu_g^{in}}{\kappa_{g,zz}}\overrightarrow{u_g^{in}}$	$P_g = P_{g,exp}$	$P_{g,exp}$

Table 4.1 – Boundary and initial conditions of the gas phase related fields

The overall mass transfer coefficients relative to the liquid phase K_{L,CO_2} and K_{L,CH_4} are estimated using Eq. 1.43. The liquid mass transfer resistances are derived from the Sh calculation (from the optimized Chilton-Colburn correlation in Eq. 4.12) and its definition (Eq. 4.8). As for the absorption of pure CO_2, the gas phase resistance is considered to be negligible. This assertion is justified by a higher diffusivity coefficient in the gas phase (D^g is approximately 10^{-5} and $10^{-6}\ m^2.s^{-1}$ for respectively $P_g = 0$ and 5 $bar\ g$ while $D^l \sim 10^{-9} m^2.s^{-1}$). The membrane mass transfer coefficient $k_{m,i}$ (Eq. 1.49) implies the calculation of binary diffusion coefficients detailed in Appendix G: they consider both the molecular and Knudsen diffusion mechanisms.

The solver framework is similar to the one presented for the pure CO_2 absorption model (4.3.1).

4.5.2 Model validation

The model is validated using 3 distinct series of experiments previously detailed in paragraph 3.4.3. A binary gas mixture (CO_2/CH_4) is upgraded using an open-loop configuration. The numerical and experimental absorbed CO_2 fluxes J_{CO_2} are compared in Figure 4.8. The equivalent inlet flux (i.e. the maximum absorbed flux) is also provided for an informative purpose. The operating conditions of the 3 experimental series are provided on this figure. Serie 1 investigates the effect of the Q_g/Q_l ratio with a typical biogas mixture at the inlet ($y_{CH_4}^{in} = 60$ %). With the same operating conditions, Serie 2 investigates the impact of the inlet gas composition ($y_{CH_4}^{in} = 10 - 90$ %). Serie 3 was performed with a low liquid flowrate ($Q_l = 60\ L.h^{-1}$) at the maximum Q_g/Q_l ratio (12.5 $NL.L^{-1}$) to test the impact of the gas velocity on the mass transfer efficiency.

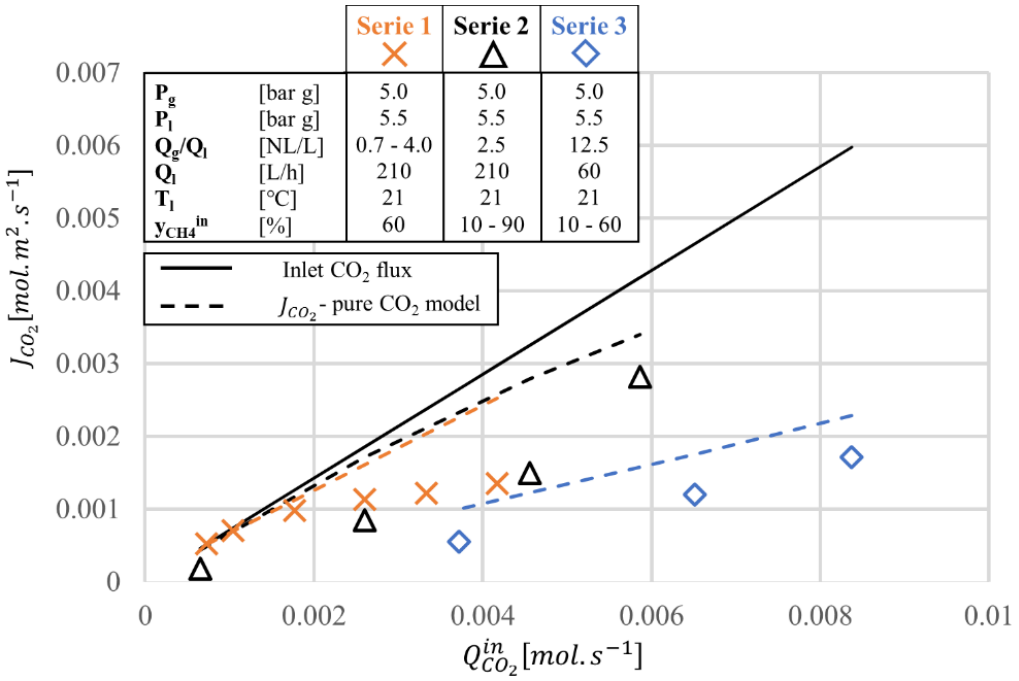

Figure 4.8 – Comparison of experimental and numerical absorbed CO_2 fluxes from a biogas mixture *Open-loop configuration*

The CO_2 absorbed flux J_{CO_2} is rising with the inlet CO_2 flow $Q_{CO_2}^{in}$ (Figure 4.8). This trend is correctly described by the model for the 3 series. Though, a significant error is observed for the 3 experimental series:

- the 3 first points of Serie 1 are not discriminant regarding the mass transfer efficiency since the inlet CO_2 flow is completely absorbed. The error increases with the Q_g/Q_l ratio reaching $\varepsilon_{rel} = 75$ % at $Q_g/Q_l = 4.0\ NL.L^{-1}$. The absorbed flux appears to be limited by a plateau as the inlet gas flowrate increases: this is the maximum CO_2 flux which can be absorbed under these operating conditions with this mass exchanger;
- the convex curvature of Serie 2 is poorly described by the model: as the carbon dioxide fraction is getting close to 100 %, the mass transferred efficiency increases. The relative error is reduced from $\varepsilon_{rel} = 79$ to 33 % with the increasing CO_2 molar fraction ($y_{CO_2}^{in} = 10 - 90$ %);
- Serie 3 is operated at a high Q_g/Q_l ratio. The absorbed flux J_{CO_2} is following a linear increase with an increasing carbon dioxide molar fraction ($y_{CO_2}^{in} = 40 - 90$ %). Under a high Q_g/Q_l ratio, less variations are expected over the carbon dioxide molar fraction along the membrane module ($y_{CO_2}^{out}$ are respectively 34.5 %, 65.4 % and 86.9 %): the absorbed flux J_{CO_2} accounts only for 21-29 % of the equivalent inlet flux. As compared to Serie 2, it may explain the more linear trend.

These initial numerical results indicate that the model is not valid as it is. The absorbed CO_2 flux is overestimated in the simulation; it means that the total mass transfer resistance is underestimated. Indeed, it has been shown that the diminishing molar fraction of CO_2 leads to a reduced mass transfer coefficient K_L (3.4.2.1). This numerical error suggests the presence of an additional mass transfer resistance in the membrane and/or gas phase, as already pointed out by experimental results in paragraph 3.4.2.2.

4.5.3 Model correction

4.5.3.1 Additional resistance in the membrane and gas phase

An additional mass transfer resistance is located in the gas phase or in the membrane filled with the gas mixture. This mass transfer resistance increases as the CO_2 molar fraction decreases. The predominant transport phenomenon in both the gas diffusion layer and the membrane phase is molecular diffusion. Knudsen diffusion is also considered in the membrane pores (see Appendix G). In the case of a binary mixture A/B, the molar flux of a specie A is the sum of a convection term and a diffusion term J_A:

$$\overrightarrow{N_A} = y_A\left(\overrightarrow{N_A} + \overrightarrow{N_B}\right) + \overrightarrow{J_A} \qquad \text{Eq. 4.21}$$

where N_A / N_B are the respective molar fluxes of species A and B, y_A is the molar fraction of specie A.

In the membrane, the diffusion term J_A is expressed by Fick's law:

$$\overrightarrow{J_A} = -\frac{\varepsilon_m}{\tau_m} D_A^{eff} \vec{\nabla} C_A^g = -\frac{\varepsilon_m}{\tau_m} D_A^{eff} \, C_{tot}^g \vec{\nabla} y_A \qquad \text{Eq. 4.22}$$

where ε_m and τ_m are respectively the porosity and tortuosity of the membrane material, D_A^{eff} is the effective diffusion coefficient in the pores in $m^2.s^{-1}$, C_A^g is the molar concentration of the component A in the gas phase in $mol.m^{-3}$.

In the present experiments, the CH_4 molar flux is supposed to be negligible against the CO_2 molar flux due to a ratio ~25 in their Henry coefficients ($N_{CO_2} \gg N_{CH_4}$). In this specific case in which one gas has a negligible flux, Eq. 4.21 is simplified into:

$$\overrightarrow{N_A} = \frac{1}{1 - y_A} \overrightarrow{J_A} \qquad \text{Eq. 4.23}$$

In a 1D problem (Figure 4.9), Eq. 4.23 can be integrated between two positions z_1 and z_2 by the separation of variables leading to:

$$N_A = \frac{\varepsilon_m}{\tau_m} D_A^{eff} \, C_{tot}^g \frac{1}{(z_2 - z_1)} \ln\left(\frac{1 - y_{A2}}{1 - y_{A1}}\right) \qquad \text{Eq. 4.24}$$

At a given height in the hollow fiber module, Eq. 4.24 is applied to the thickness of the membrane (Figure 4.9). The CO_2 molar fraction at the gas-liquid interface is approximated by:

$$y_{A2} = y_{A1} - \varepsilon \qquad \text{Eq. 4.25}$$

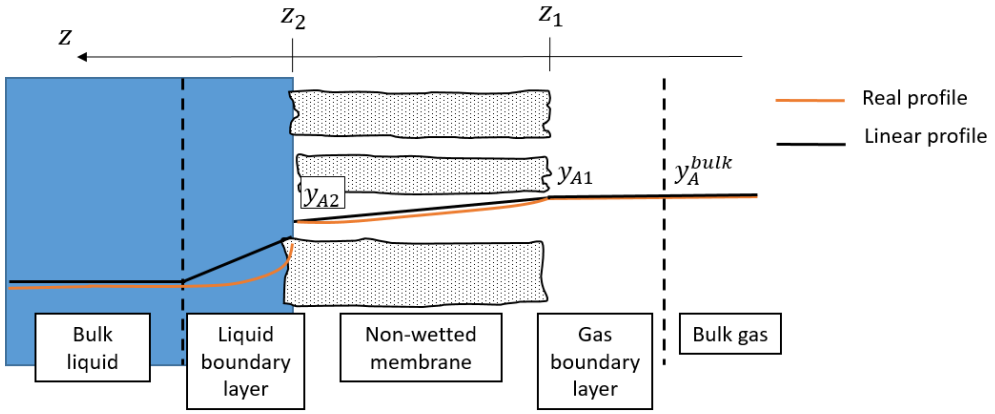

Figure 4.9 – Carbon dioxide molar fraction profile in the membrane in the case of biogas absorption

The approximation to the first order of the combination of Eq. 4.24 and Eq. 4.25 leads to the following expression:

$$N_A = \frac{\varepsilon_m}{\tau_m} D_A^{eff} \, C_{tot}^g \frac{1}{(z_2 - z_1)} \frac{1}{1 - y_{A1}} (y_{A1} - y_{A2}) \qquad \text{Eq. 4.26}$$

k_m (Eq. 1.49) is identified in the above equation as $N_A/(y_{A1} - y_{A2})$. It is thus observed that the equivalent mass transfer coefficient is inversely proportional to $1 - y_{A1}$. It increases with a diminishing CO_2 molar fraction, in accordance with the experimental results. The limit case of a pure gas ($y_{A1} = 1$) leads to an infinite mass transfer coefficient (i.e. no mass transfer resistance).

The shift from a pure gas to a gas mixture may induce a mass transfer resistance in the gas phase also. The same reasoning on diffusion mechanism can be applied to the thin diffusion layer of the gas phase and k_g will be inversely proportionnal to $1 - y_A^{bulk}$, in accordance with the experimental results too. In addition, the resistance-in-series model is built on the hypothesis of a dilute specie. Though, in the present case, both species are major components in equivalent proportion at the gas inlet ($y_{CO_2} = 40\ \%$ / $y_{CH_4} = 60\ \%$).

Based on the form of Eq. 4.26, a corrected mass transfer coefficient k_m^{corr} integrating both the membrane and gas phase resistances is suggested. The optimization factor Λ has been introduced to fit the experimental results.

$$k^{corr} = \mathrm{k}_m^{corr} + \mathrm{k}_g^{corr} = \Lambda \ \frac{1}{1 - y_{CO_2}^{bulk}} k_m \qquad \text{Eq. 4.27}$$

4.5.3.1 Numerical results

The factor Λ has been optimized twice to fit the Series 1 and 3 respectively ($\Lambda = 0.02$ and 0.007). The numerical results of the corrective model are displayed in Figure 4.10. Serie 1 with an

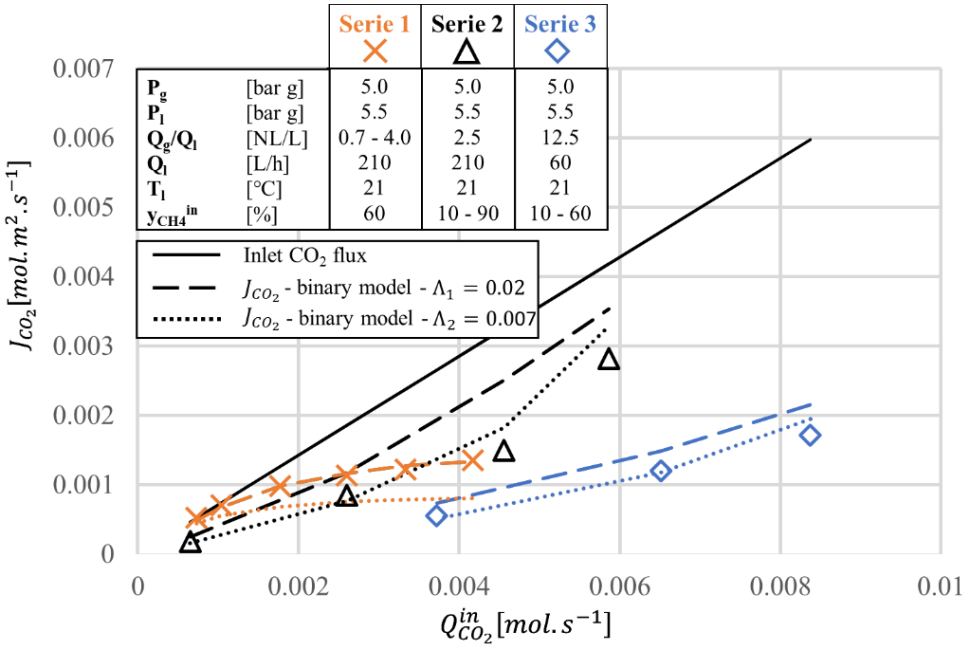

Figure 4.10 – Comparison of experimental absorbed CO_2 fluxes from a biogas mixture with numerical results from corrected model
Open-loop configuration

increasing Q_g/Q_l ratio is correctly described by the numerical model with a corrective parameter $\Lambda = 0.02$ ($\varepsilon_{rel,J_{CO_2}} = -7/+4\,\%$). Though, it overestimates J_{CO_2} in Series 2 and 3 by 25 to 68 %. Dividing the corrective parameter by a factor 2.85 ($\Lambda = 0.007$), the numerical results are in acceptable accordance with the experiments for Series 2 and 3 ($\varepsilon_{rel,J_{CO_2}} = -17/+22\,\%$). On the contrary, in this case, the experimental absorbed flux is numerically underestimated up to -40 % for Serie 1.

Despite the good description of the absorbed flux J_{CO_2} within a single experimental series after the optimization of the fitting parameter, a strong numerical error is observed with different operating conditions. It can be explained by two reasons.

First, the mass balance precision is limited by the analytical sensors (gas flowmeters and gas composition analysis, see paragraph 2.4). Two points from Series 1 and 2 are actually replicates ($Q_{CO_2}^{in} = 2.6 \times 10^{-3}\ mol.s^{-1}$) but exhibit a 25 % difference in the absorbed flux J_{CO_2}. This limitation is explained by the wide range of experimental conditions covered ($Q_g = 147 - 750\ NL.h^{-1}$, $y_{CO_2} = 10 - 90\,\%$) which induces an increased uncertainty on the sensors.

Furthermore, the operating conditions studied in these 3 series fully cover the possibilities of the pilot equipment. Modelling mass transfer is rendered more difficult by such a wide experimental range and the hypothetical change in the mass transfer limiting phenomenon nature.

Considering uncertainty issues and the wide range of operating conditions, the numerical performances obtained with an additional resistance ($\Lambda = 0.007$) is acceptable for a process sizing purpose. Nonetheless, this numerical work has underlined the necessity to investigate the additional mass transfer resistance introduced by the use of a gas mixture. A specific apparatus designed for an accurate control over mass balance uncertainties must be set (real gas calibration, optimized calibration scales …). This original numerical model can be of interest to develop a predictive and local mass transfer description.

4.6 Conclusion

An original predictive model was developed in this chapter for process upscaling purposes. At first, the choice for the development of such a model was made based on the state-of-the-art: the assimilation of the fiber bundle to a porous medium allows to get a description of the local hydrodynamic and mass transfer conditions. It better depicts the specific internal geometry of the membrane module (4.2). The adopted modelling approach is then detailed, and the Chilton-Colburn correlation is optimized in the membrane dry mode based on pure CO_2 absorption experiments (4.3). Numerical results are in good agreement with the experimental data (4.4.1). Though, the results in the membrane wet mode questioned the reported description of membrane wetting (4.4.2): an alternative description based on parallel resistances is suggested (4.4.3). At last, the model is adapted to describe the absorption of a binary gas mixture (4.5). An additional mass transfer resistance located in the membrane and/or the gas phase is optimized based on diffusion equations to fit the experimental results ($\varepsilon_{rel,J_{CO_2}} = -17/+22\,\%$). It provides a suitable model for process upscaling.

Chapter 5

Designing an industrial scale biogas upgrading unit

Chapter 5 Designing an industrial scale biogas upgrading unit

5.1 Introduction

This chapter addresses the question of the industrial process design. Three cases with different inlet biogas flowrates are considered ($100, 250$ and $500\ Nm^3_{biogas}.h^{-1}$) and presented in paragraph 5.2. Then, the range of the commercially available membrane modules is reviewed against our pilot module (5.3). The two strategies initially presented in section 5.4 are then implemented to carry out the process scale-up:

- dimensional analysis is a widespread methodology in process engineering relying on the Pi theorem and the theory of models (5.4.1);
- the second method utilises the validated mass transfer model developed during this PhD on industrial membrane modules to size the process (5.4.2).

In the end, the results from both methods obtained in the wet mode are compared and discussed for the case of water only (5.4.3) to suggest the most reliable industrial set-up at this stage of development. General remarks and points of attention regarding the integration of the CO_2/CH_4 separation unit into the whole biogas upgrading process are also provided (5.5).

5.2 Specifications for the biogas upgrading unit

In order to develop an upscaling framework for the process, specifications for a biogas upgrading unit were set (Table 5.1). Three cases are investigated.

AD case	Q_g $[Nm^3_{biogas}.h^{-1}]$	P_g $[bar\ g]$	$y^{in}_{CH_4}$ $[\%vol.]$	y^{in}_{air} $[\%vol.]$	$y^{out}_{CH_4}$ $[\%vol.]$	R_{CH_4} [%]
Small-scale	100	Atm.	60	< 0.1	> 97	> 97
Medium scale	250	Atm.	60	< 0.1	> 97	> 97
Large scale	500	Atm.	60	< 0.1	> 97	> 97

Table 5.1 – Specifications for the biogas upgrading units

Air injection in the AD unit is to be banned as N_2 (and O_2) ends in the biomethane outlet, thus decreasing the biomethane quality $y_{CH_4}^{out}$. The air fraction is considered low in the raw biogas (< 0.1 %). Furthermore, the impact of the upgrading process on H_2S has not been monitored in the experimental campaigns. The H_2S fraction has thus not been taken into account in the process upscaling. Raw biogas is generally exiting the digester with a very low overpressure (5-10 mbar g).

In the current French context and as a general rule, biogas upgrading and gas-grid injection turn out to be profitable for a minimum raw biogas production of 100 $Nm_{biogas}^3.h^{-1}$. The small-scale case was therefore set to this minimal value. Annual variability in the biogas inlet flow and quality was not included in this exercise.

The targeted performances were to produce a biomethane meeting the French H gas grid specifications ($y_{CH_4}^{out} > 97$ %, see Appendix B) with a satisfactory recovery rate ($R_{CH_4} > 97$ %).

5.3 Commercially available membrane modules

The hollow fiber membrane module (HFMM) used during the experimental campaigns was the smallest item of the Liqui-Cel® industrial range. The module features are compared in Table 5.2.

Model	**2.5"x8"**	**10"x28"**	**14"x40"**
Fiber Type	X-40 / X-50	X-40 / X-50	X-40
Cartridge	Polypropylene (PP)	Fiber Reinforced Plastic (FRP)	Polyvinyl chloride (PVC)
Membrane surface $\boldsymbol{S}$ $[\boldsymbol{m^2}]$	1.4	130	373
Fiber length $\boldsymbol{L_{eff}}$ $[\boldsymbol{m}]$	0.146	0.600	0.795
Module outer radius $\boldsymbol{R_o}$ $[\boldsymbol{m}]$	0.023	0.140	0.178
Specific area $\boldsymbol{a}$ $[\boldsymbol{m^2.m^{-3}}]$	5 671	3 542	4 716
Maximum shellside liquid pressure $\boldsymbol{P_l^{max}}$ $[\boldsymbol{bar\ g}]$	7.2	7.2	7.2
Liquid flow guidelines $[\boldsymbol{m^3.h^{-1}}]$	0.1 – 0.7	10 - 57	16 - 125

Table 5.2 – Characteristics of the Liquid-Cel® Extra-Flow modules

The 10"x28" and 14"x40" models are the largest modules available. Compared to the 2.5"x8" module, the surface is increased by a ratio 93.9 and 266 respectively. The specific area a was calculated from measured data for the 2.5"x8" module, while manufacturer data was used for the other modules. The volume used in this calculation is the overall volume of the module: it integrates the fiber bundle, but also the distribution/collection tube as well as the center baffle. It may explain the observed variations of the specific area a according to the module type.

Both fiber types X-40 and X-50 (Table 2.2) are available on the 10"x28" while the 14"x40" model is equipped only with X-40 fibers.

5.4 Strategy for the process scale-up

Two methods are used to size the biogas upgrading process in the three cases detailed in paragraph 5.2. Dimensional analysis is a general process engineering method based on the use of dimensionless factors to scale-up the process (1.5.2.1). Alternatively, the numerical model developed in Chapter 4 was used for comparison. The numerical method integrates the geometrical features of the modules.

5.4.1 Dimensional analysis method

5.4.1.1 Reduction of problem parameters

The dimensional analysis method is composed of three steps:

- identification of the dimensionless parameters describing the problem;
- establishment of the empirical correlation based on experimental data;
- scale-up and choice of industrial operating conditions.

The process description is focused on the absorption module in which the biogas is upgraded. The process configuration with a methane recycling loop is considered since it provided the best performances at pilot-scale.

The aim of this methodology is to size the membrane area S required for an industrial unit with a given inlet biogas flow Q_g. The relevance list of the problem provides the relevant parameters describing CO_2 absorption in the membrane module. They are divided into target quantity, geometrical, physical and process related properties (Figure 5.1).

1. Target quantity: S membrane area
2. Influencing parameters:
    a. Geometrical: None
    b. Physical properties:
        i. k_{H,CO_2}^{px} Henry coefficient
    c. Process related parameters :
        i. $Q_g^{CO_2}$ CO_2 inlet flowrate
        ii. Q_l Liquid flowrate
        iii. P_g Absorption pressure
        iv. K_{L,CO_2}^0 Overall mass transfer coefficient relative to the liquid phase

Relevance list = $\left\{Q_g^{CO_2}, Q_l, k_{H,CO_2}^{px}, K_{L,CO_2}^0, S, P_g\right\}$

Figure 5.1 – Dimensional analysis – Relevance List

In the provided list, the single parameter K_{L,CO_2}^0 is fully describing the mass transfer. This simplification is enabled by the knowledge gained on the mass transfer description (3.4): CO_2 mass transfer can indeed be fully characterized by its overall mass transfer coefficient K_{L,CO_2}^0. Therefore, fiber geometrical parameter, viscosities and diffusion coefficients are not listed. Among the physical properties, only the Henry coefficient k_{H,CO_2}^{px} is listed (equivalent to liquid temperature T_l). The inlet

gas flow is described by its CO_2 flow $Q_g^{CO_2}$. The total inlet gas flow Q_g could be chosen without affecting the following reasoning.

The dimensional matrix of the problem is presented in Table 5.3. CO_2 absorption in a HFMM module is described by 6 parameters and 3 physical quantities. Molar or mass flowrates and mass transfer coefficient are equivalently expressed in $mol.s^{-1}$ or $kg.s^{-1}$ and $mol.m^{-2}.s^{-1}$ or $kg.m^{-2}.s^{-1}$ respectively.

	S	Q_l	$Q_g^{CO_2}$	P_g	k_{H,CO_2}^{px}	K_{L,CO_2}^0
Mass (M)	0	1	1	1	1	1
Length (L)	2	0	0	-1	-1	-2
Time (T)	0	-1	-1	-2	-2	-1

Table 5.3 – Dimensional matrix

The application of the Pi theorem (1.5.2.1) states that the problem can be described by $6 - 3 = 3$ dimensionless parameters. The flowrates ratio π_1 and the partition coefficient $\pi_2 = m_{CO_2}$ appears to be two dimensionless parameters:

$$\pi_1 = \frac{Q_l}{Q_g^{CO_2}} \quad \text{Eq. 5.1}$$

$$\pi_2 = m_{CO_2} = \frac{k_{H,CO_2}^{px}}{P_g} \quad \text{Eq. 5.2}$$

The two remnants parameters S and K_{L,CO_2}^0 are combined with the liquid flowrate Q_l. The dimensionless factor NTU appears from the recombination of Eq. 1.34:

$$\pi_3 = \frac{K_{L,CO_2}^0 S}{Q_l} = \frac{Z}{HTU} = NTU \quad \text{Eq. 5.3}$$

As a result, processes are considered similar if they have a geometric similarities and if the dimensionless parameters π_1, π_2 and π_3 have the same values. Experimental values obtained in the methane recycling loop configuration are analyzed with these dimensionless parameters to determine the empirical correlation of Eq. 5.4.

$$f\left(\frac{Q_l}{Q_g^{CO_2}}, m_{CO_2}, NTU\right) = 0 \quad \text{Eq. 5.4}$$

5.4.1.2 Process description by empirical correlation

The experimental campaign offering the best results by the combination of the methane recycling loop (configuration 1:1:1) with the use of a KCl solution (3.5.4) is used to determine the form of Eq. 5.4. An experimental campaign with water as solvent was also performed in the same configuration to study the

influence of the intermediate pressure (3.5.2.3): the results are therefore added to the KCl solution dataset. The dimensionless equation is optimized in the form $NTU = \mathrm{B}.\left(\frac{Q_l}{Q_g^{CO_2}}\right)^d m_{CO_2}^f$ as power functions are typically used to describe the relations between dimensionless numbers. In a first approach, it was observed that a good correlation was found for $d = -f$. The optimization result is presented in Figure 5.2. The two dimensionless coefficients π_1 and π_2 are aggregated into a single parameter, the absorption factor A_{CO_2} defined by Eq. 5.5. It is a conventional parameter that takes into account the partition coefficient m_{CO_2} and the flowrates ratio $Q_l/Q_g^{CO_2}$.

$$A_{CO_2} = \frac{\pi_1}{\pi_2} = \frac{P_g}{k_{H,CO_2}^{px}} \frac{Q_l}{Q_g^{CO_2}} = \frac{1}{m_{CO_2}} \frac{Q_l}{Q_g^{CO_2}} \qquad \text{Eq. 5.5}$$

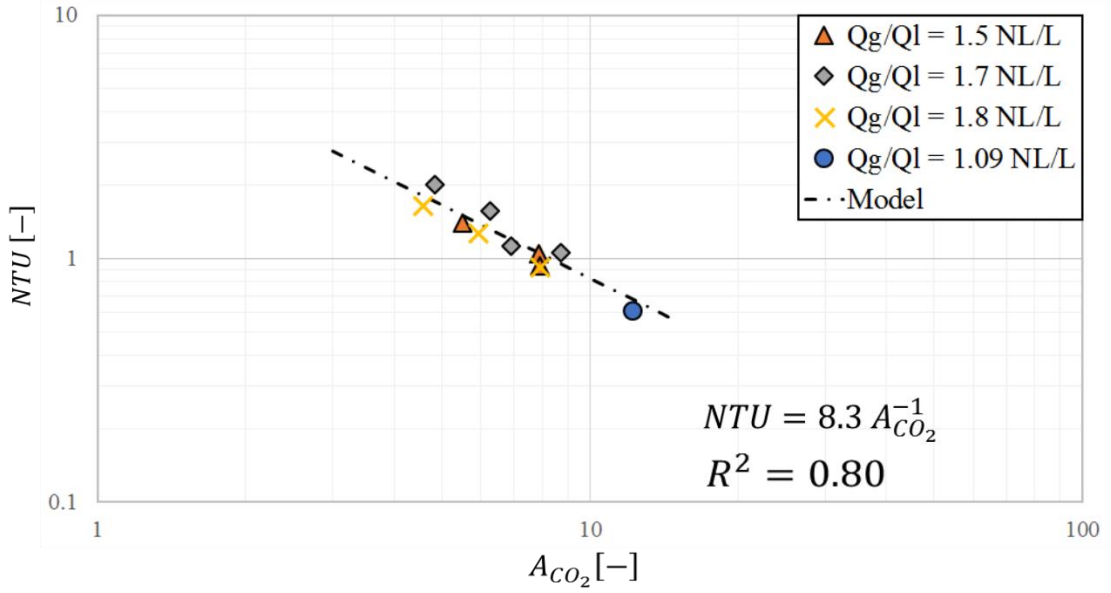

Figure 5.2 – Empirical correlation between dimensionless numbers of the process

As expected, NTU is decreasing with the absorption factor A_{CO_2}. The optimized correlation (Eq. 5.6) describing the equation between dimensionless numbers is acceptable ($R^2 = 0.80$) on the studied range ($A_{CO_2} = 4.58 - 12.2$).

$$NTU = 8.3\ {A_{CO_2}}^{-1.0} \qquad \text{Eq. 5.6}$$

The fact that results obtained both with KCl solution and water are correctly described by the correlation strengthens the reliability of this dimensional analysis method.

5.4.1.3 Industrial unit sizing

This methodology aims at sizing the required membrane area S for the industrial unit. Experimental campaigns are a guidance to choose the operating conditions described by A_{CO_2}. For a specific value of A_{CO_2}, the value of K_{L,CO_2}^0 is set to the pilot scale one. The industrial sizing procedure is as followed:

- definition of the operating conditions ($Q_g^{CO_2}, Q_l, k_{H,CO_2}^{px}$ and P_g) and calculation of A_{CO_2}. These conditions are chosen based on the experimental performances;
- estimation of the NTU of the industrial process by Eq. 5.6;
- calculation of the membrane surface S from Eq. 5.3.

KCl solution as solvent

The best process performances at pilot scale were obtained during the experimental campaign using a KCl solution presented in paragraph 3.5.4.The results of the procedure are presented in Table 5.4. As expected, the membrane area is fully linear with the inlet biogas flow.

AD case	Small-scale	Medium scale	Large scale
$\boldsymbol{Q_g}$ $\boldsymbol{[Nm^3_{biogas}.h^{-1}]}$	100	250	500
$\boldsymbol{A_{CO_2}}$	6.29	6.29	6.29
$\boldsymbol{NTU}$	1.30	1.30	1.30
$\boldsymbol{S}$ $\boldsymbol{[m^2]}$	890	2 225	4 450

Table 5.4 – Membrane area sizing by the dimensional analysis method: case of KCl solution
Indicative expected performances: $y_{CH_4}^{out} = 97.5$ % / $R_{CH_4} = 98.7$ %

Once the membrane size has been determined, the module choice and configuration (parallel vs. serie) may be discussed. Given the process sizing results, the larger membrane area of the 14"x40" module is more adapted. The equivalent number of modules and the corresponding sizing margin Γ are presented in Table 5.5. Industrial equipment are typically oversized with a factor $\Gamma = 20$ %. Therefore, the small, medium and large scale cases require respectively 3, 8 and 15 modules.

AD case	Small-scale	Medium scale	Large scale
$\boldsymbol{N_{module}}$ $\boldsymbol{[14"x40"]}$	3	6 (8)	12 (15)
$\boldsymbol{\Gamma}$ [%]	20.5	0.6 (25.4)	0.6 (20.5)

Table 5.5 – Number of industrial modules and sizing margin - case of KCl solution

Regarding the module configuration, two points are in favour of a serie arrangement:

- a parallel setting would reduce the gas and liquid velocities. It may enhance the mass transfer resistance;
- the experimental campaign (3.3.4) found that a series arrangement of hollow fiber membrane modules (HFMMs) slightly increases the overall mass transfer coefficients.

Though, the maximum inlet flows are limited by the liquid flow guidelines (Table 5.2) set for a minimal pressure drop. Therefore, the maximum inlet biogas flow is constrained to $Q_g = 212.5\ Nm^3.h^{-1}$ for a 14"x40" module ($Q_g/Q_l = 1.70\ NL.L^{-1}$). Then, in the medium and large scale cases, the inlet gas flow is divided into respectively 2 and 3 parallel lines. The suggested module arrangements are displayed in Figure 5.3.

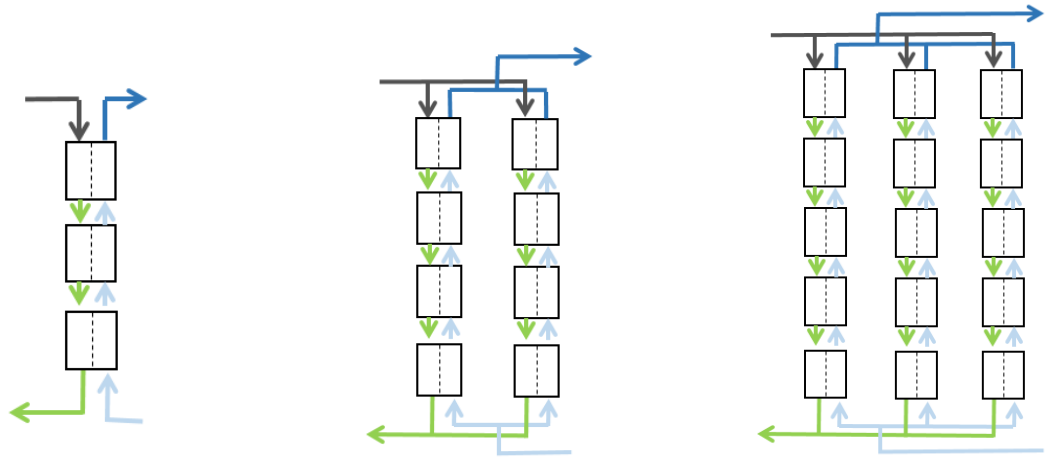

Small scale unit *Medium scale unit* *Large scale unit*

Figure 5.3 – Industrial process design from dimensional analysis method

In the above procedure, the estimation of the mass transfer coefficient K^0_{L,CO_2} is questionable. The best estimation was to set it to the pilot scale value since no empirical correlation could be drawn from experimental data. Two parameters were identified to impact the overall mass transfer coefficient: liquid velocity u_l and gas phase composition along the module y_{CO_2}. In the upscale to the industrial unit, the gas composition profile is expected to be similar from the biogas inlet to the biomethane outlet; thus, the parameter y_{CO_2} will be equivalent from the pilot to the industrial scales. Though, the geometry of the 14"x40" module implies a strong increase of the liquid velocity u_l. At the pilot scale, u_l was $7.1 \times 10^{-3}\ m.s^{-1}$ while in the small-scale unit, it increases to $1.9 \times 10^{-1}\ m.s^{-1}$. It will result in an enhanced mass transfer in the industrial module compared to the pilot scale one. As a consequence, the overall mass transfer coefficient K^0_{L,CO_2} may have been underestimated in the sizing procedure.

Water as solvent

The same procedure was applied to the best experimental results obtained with reverse osmosis (RO) water at $Q_g/Q_l = 1.09\ NL.L^{-1}$ (3.5.2.3). The results of the procedure are presented in Table 5.6.

As for a KCl solution, the liquid flow guidelines (Table 5.2) and the chosen flowrates ratio Q_g/Q_l constrain the gas flowrate to a maximum $Q_g = 136.25\ Nm^3.h^{-1}$ for a 14"x40" module in the case of water. It imposes the process to be arranged respectively into 1, 2 and 4 parallel lines for the small, medium and large scale cases. Thus, it implies an asymmetric arrangement for the medium and large scale cases with respectively 7 and 13 membrane modules: lowering the margin factor Γ to 13.7 % and 15.8 % respectively can allow a symmetric configuration. In such an asymmetric arrangement, the flowrates would be regulated proportionally to the total membrane surface of the process line.

AD case	Small-scale	Medium scale	Large scale
$Q_g\ [Nm^3_{biogas}.h^{-1}]$	100	250	500
A_{CO_2}	12.20	12.20	12.20
NTU	0.65	0.65	0.65
$S\ [m^2]$	773	1 932	3 864
$N_{module}\ [14"x40"]$	3	6 (7)	11 (13)
$\Gamma\ [\%]$	30.9	13.7 (26.0)	5.8 (20.3)

Table 5.6 – Membrane area sizing by the dimensional analysis method: case of water
Indicative expected performances: $y_{CH_4}^{out} = 95.9\ \%$ / $R_{CH_4} = 93.5\ \%$

Regarding the small-scale case showing a high margin factor ($\Gamma = 30.9\ \%$), the use of the 10"x28" module can be considered to optimize the investment costs. 7 modules would indeed meet the exchange area requirements and result in a lower margin factor ($\Gamma = 17.7\ \%$).

The obtained sizing requires a slightly lower total surface compared to the case of the KCl solution (-13 %). Nonetheless, the expected performances based on the pilot experimental results are much better while using a KCl solution ($y_{CH_4}^{out} = 95.9\ \%$ / $R_{CH_4} = 93.5\ \%$ in the case of water as opposed to $y_{CH_4}^{out} = 97.5\ \%$ / $R_{CH_4} = 98.7\ \%$ in the case of the KCl solution).

5.4.2 Mass transfer modelling tool

As a comparison, the mass transfer model developed during this PhD (Chapter 4) is used to upscale the process with industrial membrane modules. Since the mass transfer model was validated for experiments with RO water as the absorbent, the process sizing approach utilizing this numerical tool was carried out for water only. The process design procedure consists of 2 steps:

- process arrangement (number of parallel process lines according to the Q_g/Q_l ratio and the liquid guidelines of the specified module);
- numerical simulations with an increasing number of modules in each parallel process lines.

From the above results, the 14"x40" module is selected as the base module. Similarly to paragraph 5.4.1.3, the process arrangement step results in 1, 2 and 4 parallel lines respectively for the small, medium and large scale cases. Therefore, the inlet biogas flow $Q_{g,line}$ for the parallel lines will be $100\ Nm^3.h^{-1}$ for the small scale case while the medium and large cases result in the same inlet biogas flow $Q_{g,line} = 125\ Nm^3.h^{-1}$.

A Python routine was developed to model a series arrangement of membrane contactors. Each membrane contactor was simulated iteratively until stabilization of both CO_2 and CH_4 outlet liquid concentrations. Mass imbalance for both species were verified to be below 10^{-3}. The runtime is about 60 minutes on a single thread (Intel Core i5-4310M, 8 Go DDR3 2700 MHz).

Simulations were then run for one process line in each case with an increasing number of modules (Figure 5.4).

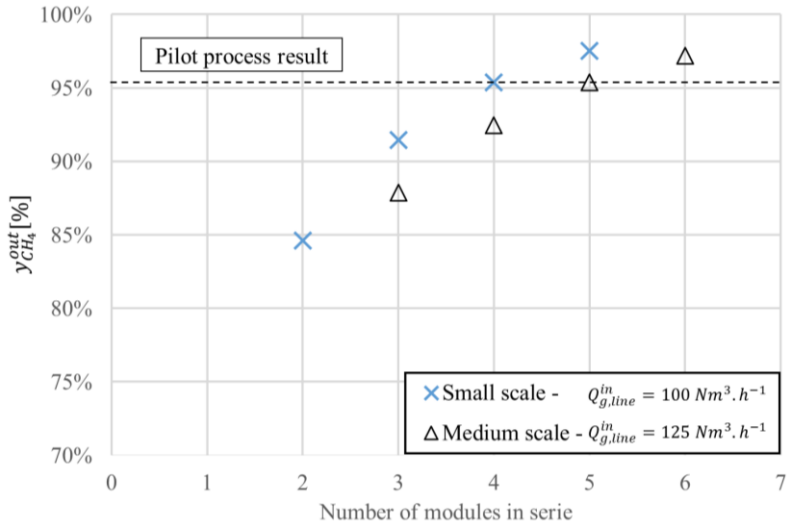

Figure 5.4 – Biomethane quality according to the number of modules

The aim of this process sizing method is to reach the experimental results obtained in similar operating conditions at pilot scale ($y_{CH_4}^{out} = 95.9$ % / $R_{CH_4} = 93.5$ % in paragraph 3.5.2.3). In order to reach the corresponding biomethane quality, 4 membrane modules are required in the small scale case (as opposed to 3 modules according to the dimensional analysis method) while 5 membrane modules per process line are needed for both the medium and large scale cases (10 modules for the complete unit in the medium case as opposed to 7 according to the dimensional analysis method).

The mass transfer model is though only simulating the absorption step. The performances of the partial degassing step recycling the dissolved methane fraction or of the final solvent regeneration step are not described in these simulations. These operations are therefore sized proportionally to the absorption step. However, it also means that the methane recovery rate R_{CH_4} resulting from the simulation is only accounting for the absorption step; it does not take into account the partial methane recovery of the intermediate degassing step. Thus, it is only assumed that the methane recovery rate will be similar to the one obtained experimentally as long as the quality of the biomethane produced is also comparable.

These numerical results were obtained assuming a gas-free absorbent at the absorption liquid inlet. Yet, the comparison between open-loop and closed-loop performances in the reference architecture showed that the inlet CO_2 loading rate ψ_{CO_2} was within 10-25 % in the closed-loop set-up (3.3.3). At a low Q_g/Q_l ratio and with the addition of an intermediate degassing step for methane recycling, the inlet ψ_{CO_2} is likely to decrease to 5–15 %. A sensitivity analysis to this ψ_{CO_2} parameter was performed for the selected number of membrane modules (Figure 5.5). The large scale case is equivalent to the medium scale case since their respective process lines are identical ($Q_{g,line} = 125\ Nm^3.h^{-1}$).

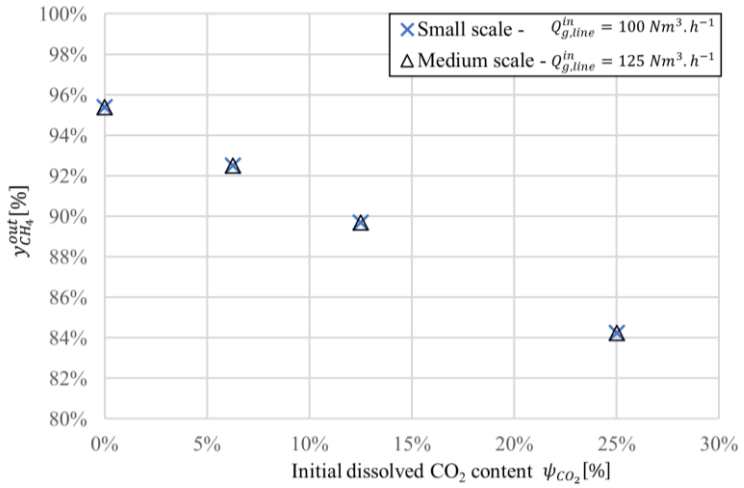

Figure 5.5 – Biomethane quality according the dissolved CO_2 content at the liquid inlet

The large scale case is equivalent to the medium scale one

For all the small, medium and large cases, the biomethane quality is affected in the same way by the inlet CO_2 loading rate ψ_{CO_2}. It is indeed following a linear decrease from $y_{CH_4}^{out} = 95.4$ % to 84.2 % in the studied range $\psi_{CO_2} = 0 - 25$ %. This sensitivity analysis indicates that the biomethane quality will still be high ($89.7 - 95.4$ %) at the industrial scale in the assumed range of ψ_{CO_2} (5-15 %).

Overall, the confidence interval (± 20 %) inferred from the validation of the numerical model at pilot scale and the assumptions made on the efficiency of the regeneration step force to handle these numeric results with care. In a general manner and similarly to the dimensional analysis method, the sizing results and the sensitivity analysis derived from the mass transfer simulation provide only indicative results.

5.4.3 Comparison of the methods

Both above methods were compared when RO water was used as the absorbent. Indeed, no mass transfer simulation results were produced using a KCl solution. The process configurations are compared in Table 5.7. For the dimensional analysis method, only symmetrical configurations are considered to make the comparison per process line possible. The margin factor Γ is then reduced to 13.7 % in both the medium scale and large scale cases.

AD case	**Small-scale**		**Medium scale**		**Large scale**	
$\boldsymbol{Q_{g,process}\ [Nm^3_{biogas}.h^{-1}]}$	100		250		500	
Number of process lines	1	1	2	2	4	4
$\boldsymbol{Q_{g,line}\ [Nm^3_{biogas}.h^{-1}]}$	100	100	125	125	125	125
$\boldsymbol{N_{module,line}}$ [**14"x40"**]	3	4	3	5	3	5

Table 5.7 – Process arrangement and number of modules according to both methodologies - case of water

Left: dimensional analysis – Right: numerical modelling

The sizing resulting from the dimensional analysis requires a smaller number of membrane modules compared to the numerical modelling results (-25 % and -40 % for small and medium cases respectively). While there is only one module of difference in the small scale case, the two modules difference is more significant in the medium and large scale cases. It therefore questions the right sizing approach. Additional steps would test the reliability of both approaches:

Dimensional analysis model

- the correlation optimized with experimental results (mostly using a KCl solution) in Eq. 5.6 can be further validated in the case of water by a set of experiments with a varying absorption factor A_{CO_2}. It would strengthen the method reliability using water as the absorbent;
- doubling the membrane area while keeping the 1:1:1 surface ratio may be an essential step to validate this method. The liquid flowrate can be derived from the NTU targeted value (Eq. 5.3), and then the inlet gas flowrate from the set Q_g/Q_l ratio.

Mass transfer modelling

- modelling the absorption step can only provide indicative results on the overall upgrading process which comprises intermediate and final degassing steps. In order to enhance the reliability of the numerical results on the whole process, the model must be validated also on its ability to simulate the degassing steps. To do so, specific experimental campaigns must be carried out focusing on solvent regeneration (degassing of a saturated solvent in an open-loop configuration). Only then, the absorption and desorption models may be coupled in a single simulation;
- the model must also be validated in the case of the KCl solution. Model parameters can be adapted easily. Though, the main issue is to carry out validation experiments in an open-loop configuration. Indeed, the liquid flowrate is quite significant is the set-up ($Q_l = 90 - 210\ L.h^{-1}$).

5.5 Industrial plant design

The best experimental results obtained at pilot scale under $Q_g/Q_l = 1.7\ NL.L^{-1}$ and $P_g = 5\ bar\ g$ ($y_{CH_4}^{out} = 97.5$ % / $R_{CH_4} = 98.7$ %) combined a methane recycling loop configuration with the use of a KCl solution as the absorbent (3.5.4). As a result, the module arrangement and absorbent are chosen for the industrial scale-up. A module arrangement has been suggested for three biogas flowrates in Figure 5.3 using the dimensional analysis methodology.

Using a KCl solution raises the question of compatibility with the equipment material which must be a point of attention. Though, the use of a KCl solution offers the advantage of a lower freezing temperature compared to the pure water used in conventional packed columns for scrubbing. It is an interesting advantage for Northern Europe which faces negative temperatures in winter.

The question of the CO_2/CH_4 separation has been widely addressed in this work but the process sensitivity to biogas impurities requires additional tests. For instance, the tolerance to H_2S is an

important question since it might affect the absorbent pH and gas-liquid interactions. In this regard, the on-site experimental campaign did not show a strong deviation from results (3.5.1). However, these results need to be confirmed in the case of a KCl solution and on the long-term. While this question has not been addressed, H_2S removal will still need to be performed before the biogas upgrading unit by a conventional technique such as activated carbons. Also, the outlet biomethane exits the process saturated with water due to high water content in the raw biogas and the intense contact between both phases in the membrane module. Therefore, a gas drying unit is required as for water scrubbing to bring the biomethane dew point below its specification (1.2.3.2).

5.6 Conclusion

Two process upscaling methodologies were carried out in this chapter under the membrane wet regime to size biogas upgrading industrial units from three different inlet biogas flowrates ($100, 250$ and $500\ Nm^3_{biogas}.h^{-1}$). The unit specifications were set to meet the market expectations ($R_{CH_4} > 97$ %, $y^{out}_{CH_4} > 97$ %). Then, the range of the commercially available membrane modules was reviewed and compared to our pilot module (5.3). In a first step, dimensional analysis identified three dimensionless numbers (the flowrates ratio $Q_l/Q_g^{CO_2}$, the partition coefficient m_{CO_2} and the NTU) to describe the process (5.4.1). The correlation was optimized: the resulting curve was in good agreement with the available experiments (KCl solution and water), indicating that this approach can be applied to both systems. The NTU was found to be inversely proportional to the CO_2 absorption factor A_{CO_2} (a combination of the flowrates ratio and the partition coefficient). The pilot scale process was thus considered similar to the industrial process. Three module arrangements were suggested for the use of the KCl solution ($y^{out}_{CH_4} = 97.5$ % / $R_{CH_4} = 98.7$ %): 3, 8 and 15 industrial 14"x40" modules are required at the absorption step for the small-scale, medium-scale and large-scale units respectively. However, numerical modelling could not be applied to the use of a KCl solution due to the absence of model validation (5.4.2). Nonetheless, both methods were compared using water as the absorbent: numerical modelling suggested a higher number of modules (+25 % and +40 % for small and medium cases respectively). Additional experimental campaigns are required to strengthen the reliability of both methods separately. The dimensional analysis method should undergo further validation by varying the absorption factor A_{CO_2} or by doubling the surface membrane at absorption while keeping the same level of process performances using the KCl solution. The mass transfer modelling tool should be extended to the whole biogas upgrading process, including the partial and final degassing steps. Furthermore, its extension to the case of the KCl solution still require an experimental validation. In the end, the industrial plant design was discussed to integrate the CO_2/CH_4 separation in the whole biogas upgrading unit (5.5).

General conclusion

The combination of the fossil fuels depletion with climate change issues (linked to the increasing anthropic greenhouse gases emissions) offers mankind to seize a unique opportunity to drastically change the world energy production system (Figure 0.4). In this route towards a sustainable and low-carbon energy mix, biomass and its energy use have an important potential (an estimated $2.32 - 3.51 \times 10^3\ Mtoe$ in 2030) and an essential role to play: it can provide with a base energy production complementarily with intermittent wind and solar energies.

Anaerobic digestion is a naturally occurring biologic process converting biomass sources such as waste streams (agricultural waste, industrial waste, bio-waste, wastewater sludge) into biogas. The conversion of biogas into biomethane offers an attractive process regarding energy production (optimization of energy efficiency, substitution of fossil fuels, storage and transport through existing gas grid). Nonetheless, the costs associated to biogas upgrading processes are still an obstacle to a widespread development across Europe, specifically in the case of farm anaerobic digestion units.

This PhD aimed at the development of an innovative biogas upgrading process by means of membrane contactors. The review of biogas upgrading processes set the projects objectives to market standards ($R_{CH_4} > 97$ %, $y_{CH_4}^{out} > 97$ %); membrane contactors were chosen for their advantages. The membrane contactor technology indeed offers a larger specific area ($> 1\,000\ m^2.m^{-3}$) compared to conventional devices such as packed columns (Figure 0.6). Furthermore, thanks to the membrane hydrophobicity, membrane contactors are an opportunity for the intensification of gas-liquid absorption processes such as water scrubbing. Finally, modularity and ease of operation are two competitive advantages of these devices over packed columns.

A classical approach was adopted to lead this development. At first, the literature review focused on biogas upgrading processes, selection of a suitable solvent for CO_2/CH_4 separation, sizing methodologies from process engineering and mass transfer modelling strategies in membrane contactors. Then, a modular pilot process ($150 - 880\ NL_{biogas}.h^{-1}$) including an absorption and a desorption steps was set up. In the first instance, experimental campaigns were carried out to identify the key process parameters and investigate the observed mass transfer limitations. Project objectives were reached in a second step by the combination of both process configuration and solvent investigations. In the view of process upscaling, mass transfer phenomena were described in an original model. This modelling approach was validated against data from pure CO_2 absorption and extended with a correction for the absorption of a binary mixture. At last, two methodologies are applied to design a biogas upgrading unit in three different cases of inlet gas flowrates from a range of available membrane contactors.

The review of the available technologies evidenced that the biogas upgrading unit is still a financial and operational concern, especially for small-scale farm anaerobic digestion units ($< 250\ Nm^3_{biogas}.h^{-1}$). Hollow fiber membrane contactors may address this issue with advantages of their modularity, operational flexibility and compactness. The solvent review highlighted water, mineral salt solutions and amino-acid salt solutions to be potential suitable solvents. While some studies assessed the separation performances of membrane contactors at the absorption step, at the beginning of this PhD, no study had combined the absorption and regeneration steps in a single process cycle. Gas-liquid mass transfer was approached through available numerical models: for physical absorption, the mass transfer resistance primarily appeared to be located in the liquid phase. For a process scale-up purpose, the need for an original model was identified in order to depict the internal membrane module geometry. In addition, membrane wetting was pointed out to limit mass transfer over long periods of operation and thus this phenomenon deserves a specific care.

A modular pilot process with pressures and flowrates regulation was built from scratch to evaluate the biogas upgrading performances using different solvents and process configurations. A special care was brought to the calibration of gas flow controllers as well as to the set-up of the gas sampling and analysis systems. The biogas upgrading process was evaluated according to biomethane quality, methane recovery rate and specific energy consumption. The overall liquid mass transfer coefficient is also an indicator of the mass transfer efficiency. In addition, two methods were specifically developed to measure the Henry coefficients of considered gases in absorbents and to provide an online measurement of the dissolved gas content in the liquid flow. In the view of mass transfer modelling, the porosity and pore size distribution of the hollow fibers were characterized by Hg intrusion porosimetry and SEM observations: the results slightly differed from manufacturer data.

The design of experiments methodology identified the flowrates Q_g and Q_l, the absorption pressure P_g and the inlet methane content $y^{in}_{CH_4}$ to be the operating parameters driving the process performances in a reference configuration 1:1 (equivalent exchange area at absorption and desorption). The mass transfer rate was too limited to reach the satisfying biomethane quality on the pilot equipment, even by doubling the membrane exchange surface. It was thus evidenced that the presence of a poorly soluble gas (i.e. methane) was more limitating than membrane wetting. In a biogas mixture, K_L is divided by a factor 2-3 as opposed to a 20-30 % reduction when the membrane shifts from its dry to wet regime.

The process development strategy was carried out in several steps. Firstly, a field campaign demonstrated that comparable performances were obtained by upgrading farm raw and synthetic biogases. Therefore, different configurations were successively tested in the laboratory. Similarly to commercial water scrubbing, the addition of a methane recycling loop improved the methane recovery rate from $R_{CH_4} = 83\ \%$ to $93.5\ \%$. The specific energy consumption ($0.243\ kWh.Nm^{-3}_{biogas}$) is estimated comparable to the one of state-of-the-art biogas upgrading processes ($0.2 - 0.3\ kWh.Nm^{-3}_{biogas}$). Then, the salting out effect resulting from mineral salt solutions also reduced the methane slip in the reference configuration. The promising potential of amino-acid salt solutions though turned out to be limited by the desorption step due to the high affinity of these compounds with carbon dioxide. The combination of the methane recycling loop with a KCl solution established a proof-of-

concept for biogas upgrading with membrane contactors. A biomethane complying with gas-grid specifications ($y_{CH_4}^{out} = 97.5$ %) was obtained with the targeted recovery rate ($R_{CH_4} = 98.7$ %). The estimated process energy consumption is competitive ($0.225\ kWh.Nm_{biogas}^{-3}$). The process is intensified by a factor 10 ($K_L a = 0.11\ s^{-1}$), as compared to the conventional WS in a packed column. A patent application was filled to protect the use of mineral salts in combination with membrane contactors for a biogas upgrading purpose.

An original predictive model was developed for process upscaling purposes. The assimilation of the fiber bundle to an anisotropic porous media better depicts the specific geometry of the membrane module including a center diverting baffle than existing mass transfer models: it allows to get a good description of the local hydrodynamic and mass transfer conditions. The Chilton-Colburn correlation was optimized in the membrane dry mode based on pure CO_2 absorption experiments: numerical results are in good agreement with the experimental data ($\varepsilon_{rel,J_{CO_2}} = -10/+17$ %). The results in the membrane wet mode questioned the reported description of membrane wetting: an alternative description based on parallel resistances is suggested. At last, the model is adapted to describe the absorption of a binary gas mixture. An additional mass transfer resistance located in the membrane and/or the gas phase was optimized based on diffusion equations to fit the experimental results ($\varepsilon_{rel,J_{CO_2}} = -17/+22$ %). It provides a suitable model for process upscaling.

As a final step toward industrialization of this work, two process upscaling methodologies were carried out to size biogas upgrading industrial units from three different inlet biogas flowrates ($100, 250$ and $500\ Nm_{biogas}^3.h^{-1}$). In the case of water, dimensional analysis results in a smaller number of industrial membrane modules compared to numerical modelling (-25 % and -40 % for small and medium cases respectively). The experimental results meeting the targeted performances using a KCl solution could only be scaled-up from the dimensional analysis methodology: a specific arrangement is suggested for the small, medium and large scale units with respectively 3, 8 and 15 industrial 14”x40” membrane modules at the absorption step. Additional steps are suggested to strengthen both upscaling approach: new experimental campaigns to validate the dimensional analysis method, extension of the mass transfer model to the whole process and its adaptation to a KCl solution. In the end, general remarks are provided for the integration of the CO_2/CH_4 separation in the whole biogas upgrading unit.

As a general conclusion, an innovative process derived from water scrubbing has been developed and meets the biogas upgrading requirements. The proof-of-concept has been established at the pilot scale and an industrial scale design has been suggested for three different cases ($100, 250$ and $500\ Nm_{biogas}^3.h^{-1}$). The use of membrane contactors offers a more compact and modular design that conventional packed columns. In addition, it shows more operational flexibility due to the phase separation. The investment costs related to the biogas upgrading unit must still be addressed through a demonstration project to answer the question raised in the objectives section.

Perspectives

This PhD has established a proof-of-concept at pilot scale for a biogas upgrading process by means of membrane contactors. Though, several perspectives can be drawn from the present study.

A more in-depth work can be conducted on the characterization of the hollow fiber membrane. The systematic comparison of the membrane characterization techniques (SEM imagery, Hg mercury intrusion, liquid-liquid porosimetry, permporometry…) on different membrane samples could offer a better picture. A focus on the link between the characterization techniques and the mass transfer model would improve the numerical results.

The compatibility of the membrane material with biogas impurities must also be investigated prior to any industrial operations. Despite the good chemical resistance of polypropylene, experiments with exposition of the membrane to organic volatile compounds or high contents of hydrogen sulphide must be undertaken to monitor the material stability.

The proof-of-concept established in the laboratory should undergo a long-term experimental campaigns in real conditions at the farm. It will confirm the low dependency of process performances to membrane wetting and test its H_2S removal capacity.

The developed numerical model must be improved by dedicated experimental campaigns focusing on the mass transfer resistance identified in the membrane and/or the liquid phase. A specific apparatus designed for an accurate control over mass balance uncertainties must be set (real gas calibration, optimized calibration scales …). In the meantime, the numerical results can interestingly be compared to the performances of a 2D model which does not describe the module internal geometry.

In order to better explain the differences in the process sizings derived from the two upscaling methods (dimensional analysis and mass transfer modelling), additional experimental campaigns are required to strengthen the reliability of both methods separately. The dimensional analysis method should undergo further validation by varying the absorption factor A_{CO_2} or by doubling the surface membrane at absorption while keeping the same level of process performances using the KCl solution. The mass transfer modelling tool should be extended to the whole biogas upgrading process, including the partial and final degassing steps. Furthermore, its extension to the case of the KCl solution still require an experimental validation.

As underlined in the general conclusion, the question of investment and operational costs related to the biogas upgrading unit must still be addressed to answer the question raised in the objectives section. In this regard, a significant demonstration project will provide an accurate estimate. Such a project will also confront both sizing methodologies to real industrial performances.

List of original publications and communications

Publications

V. Fougerit, V. Pozzobon, D. Pareau, M.-A. Théoleyre, and M. Stambouli, 'Gas-liquid absorption in industrial cross-flow membrane contactors: Experimental and numerical investigation of the influence of transmembrane pressure on partial wetting', *Chem. Eng. Sci.*, Mar. 2017.

Fougerit V, Pozzobon V, Pareau D, Théoleyre M-A, Stambouli M. 'Experimental and numerical investigation of the effect of the gas composition and flowrate on the physical absorption of carbon dioxide in a gas –liquid membrane contactor'. (Submitted).

Fougerit V, Théoleyre M-A, Stambouli M. Practical use of membrane contactors in a biogas upgrading process based on physical absorption: influence of operating conditions and process configurations. (In preparation).

Patents

Fougerit V, Théoleyre M-A, Smaoui T, Stambouli M (2017) Biogas purification process for biomethane production. Reference INPI 9E98 BT 2 FR (pending).

Conference proceedings

Fougerit V, Lemaire J, Théoleyre M-A, Stambouli M (2017) Experimental Optimization of an Innovative Biogas Upgrading Process Adapted to the Agricultural Context. European Biomass Conference & Exhibition, 12-15 June 2017, Stockholm Sweden.

Oral communications

Fougerit V, Pozzobon V, Pareau D, Théoleyre M-A, Stambouli M (2017) Modelling the absorption of a gas mixture in a cross-flow hollow-fiber membrane module. 13th International Conference on Gas–Liquid and Gas–Liquid–Solid Reactor Engineering (GLS13), 20-23 August 2017, Brussels Belgium.

Fougerit V, Lemaire J, Théoleyre M-A, Stambouli M (2017) Experimental Optimization of an Innovative Biogas Upgrading Process. European Biomass Conference & Exhibition, 12-15 June 2017, Stockholm Sweden.

Fougerit V, Théoleyre M-A, Stambouli M (2016) Développement d'un procédé innovant d'épuration du biogaz adapté aux petites unités. Journées Recherche Innovation, 10-12 February 2016, Limoges France.

Fougerit V, Théoleyre M-A, Stambouli M (2016) Démarche pour un procédé d'épuration du biogaz adapté aux petites unités. Journées Jeunes Chercheurs Condorcet (J2C2), 19-20 January 2016, Reims France.

Posters

Fougerit V, Théoleyre M-A, Stambouli M (2016) How to design a robust, cost-efficient and effective low-scale biogas upgrading process? 3rd European Biogas Association Conference. 27-29 September 2016, Ghent Belgium.

Note on units

Flowrate units

In this manuscript, flowrates are expressed in different units. The most suitable one is selected but they are equivalent to one another. The equivalence relationships are presented here.

$22.4\ NL = 1\ mol$

$3600\ s = 1h$

For instance:

$1\ NL.h^{-1} = 1.24 \times 10^{-5}\ mol.s^{-1} = 2.78 \times 10^{-7}\ Nm^3.s^{-1}$

Energy units

Different energy units are also used in this manuscript. Some are more adapted to describe the global energy consumption (Mtoe, TWh) while others are more suitable for the characterization of a process energy consumption (kWh, MJ).

One tonne of oil equivalent (toe) is defined as defined as the amount of energy released by burning one tonne of crude oil.

1 Mtoe = 11.63 TWh = 41.868 PJ

1 kWh = 3.6 MJ

References

1. Pachauri RK, Allen MR, Barros VR, et al (2014) Climate change 2014: synthesis report. Contribution of Working Groups I, II and III to the fifth assessment report of the Intergovernmental Panel on Climate Change. IPCC

2. U.S. Energy Information Administration (2016) Chapter 1 - World energy demand and economic outlook

3. Climate Change Indicators: Atmospheric Concentrations of Greenhouse Gases | Climate Change Indicators in the United States | US EPA. https://www.epa.gov/climate-indicators/climate-change-indicators-atmospheric-concentrations-greenhouse-gases. Accessed 21 Feb 2017

4. Thrän D, Seidenberger T, Zeddies J, Offermann R (2010) Global biomass potentials — Resources, drivers and scenario results. Energy Sustain Dev 14:200–205 . doi: 10.1016/j.esd.2010.07.004

5. Nakada S, Saygin D, Gielen D (2014) Global Bioenergy. Supply and demand projections. A working paper for REmap 2030. IRENA

6. Tzimas E, Europäische Kommission (2003) Hydrogen storage: state-of-the-art and future perspective. Office for Official Publications of the European Communities, Luxembourg

7. Hydrogen Analysis Resource Center |. http://hydrogen.pnl.gov/. Accessed 27 Jun 2017

8. Zizhou N, Purchase BS, others (2012) The increasing role of anaerobic digestion as a source of energy'. In: Conference paper, Proceedings of the Annual Congress-South African Sugar Technologists' Association

9. Bastide G (2013) Estimation des gisements potentiels de substrats utilisables en méthanisation. ADEME

10. Bauer F, Hulteberg C, Persson T, Tamm D (2013) Biogas upgrading - Review of commercial technologies

11. Roustan M (2003) Transferts gaz-liquide dans les procédés de traitement des aux et des effluents gazeux. Tec & Doc

12. Elhajj J, Al-Hindi M, Azizi F (2014) A Review of the Absorption and Desorption Processes of Carbon Dioxide in Water Systems. Ind Eng Chem Res 53:2–22 . doi: 10.1021/ie403245p

13. Paul EL, Atiemo-Obeng VA, Kresta SM (2004) Handbook of industrial mixing: science and practice. Wiley-Interscience, Hoboken, N.J

14. SGC (2012) Basic Data on Biogas

15. Fachagentur Nachwachsende Rohstoffe (2010) Guide sur le biogaz - De la production à l'utilisation

16. Cresson R (2006) Etude du démarrage de procédés intensifs de méthanisation. Université de Montpellier

17. Moletta R (2011) La méthanisation, 2nd. Editions Tec&Doc

18. Schnurer A, Jarvis A (2010) Microbiological handbook for biogas plants. Swed Waste Manag U 2009:1–74

19. Zehnder AJB (1982) The Carbon Cycle. In: The Natural Environment and the Biogeochemical Cycles. Springer Berlin Heidelberg, pp 83–110

20. Archer DB, Kirsop BH (1990) The microbiology and control of anaerobic digestion. Elsevier Appl Sci SCI Lond N Y 43–92

21. Drosg B, Braun R, Bochmann G, Al Saedi T (2013) Chapter 3 - Analysis and characterisation of biogas feedstocks. In: Wellinger A, Murphy J, Baxter D (eds) The Biogas Handbook. Woodhead Publishing, pp 52–84

22. Wiegel J (1990) Temperature spans for growth: hypothesis and discussion. FEMS Microbiol Rev 6:155–169

23. Lettinga G, Rebac S, Zeeman G (2001) Challenge of psychrophilic anaerobic wastewater treatment. TRENDS Biotechnol 19:363–370

24. Da Costa Gomez C (2013) Chapter 1 - Biogas as an energy option: an overview. In: Wellinger A, Murphy J, Baxter D (eds) The Biogas Handbook. Woodhead Publishing, pp 1–16

25. Wellinger A, Murphy J, Baxter D (2013) The biogas handbook - Science, production and applications. Woodhead Publishing

26. Ryckebosch E, Drouillon M, Vervaeren H (2011) Techniques for transformation of biogas to biomethane. Biomass Bioenergy 35:1633–1645 . doi: 10.1016/j.biombioe.2011.02.033

27. Angeli N (2013) Guide pour l'optimisation de l'efficacité énergétique des installations biogaz. ATEE - Club Biogaz

28. Boulinguiez B, Le Cloirec P (2011) TI - Purification de biogaz - Elimination des COV et des siloxanes

29. Rasi S (2009) Biogas composition and upgrading to biomethane. University of Jyväskylä

30. Rasi S, Veijanen A, Rintala J (2007) Trace compounds of biogas from different biogas production plants. Energy 32:1375–1380 . doi: 10.1016/j.energy.2006.10.018

31. Poulleau J (2002) Caracterisation des biogaz. Institut National de l'Environnement Industriel et des Risques (INERIS)

32. Rasi S, Läntelä J, Rintala J (2011) Trace compounds affecting biogas energy utilisation – A review. Energy Convers Manag 52:3369–3375 . doi: 10.1016/j.enconman.2011.07.005

33. Burning Sulfur Compounds

34. Böhme D, Dürrschmidt W, van Mark M (2010) Renewable Energy Sources in Figures - National and International Development. Federal Ministry for the Environment, Nature Conservation and Nuclear Safety (BMU), Berlin

35. Pöschl M, Ward S, Owende P (2010) Evaluation of energy efficiency of various biogas production and utilization pathways. Appl Energy 87:3305–3321 . doi: 10.1016/j.apenergy.2010.05.011

36. Clarke Energy CHP efficiency for biogas. https://www.clarke-energy.com/fr/2013/chp-cogen-efficiency-biogas/. Accessed 24 Jun 2017

37. Zhang X, Yan J, Li H, et al (2014) Energy Saving for Biogas Production and Upgrading – Thermal Integration. Energy Procedia 61:121–125 . doi: 10.1016/j.egypro.2014.11.921

38. Radovic LR Efficiency of Energy Conversion. Penn State University, Pennsylvania

39. Cullen JM, Allwood JM (2010) Theoretical efficiency limits for energy conversion devices. Energy 35:2059–2069 . doi: 10.1016/j.energy.2010.01.024

40. Budzianowski WM, Brodacka M (2016) Biomethane storage: Evaluation of technologies, end uses, business models, and sustainability. Energy Convers Manag. doi: 10.1016/j.enconman.2016.08.071

41. Götz M, Lefebvre J, Mörs F, et al (2016) Renewable Power-to-Gas: A technological and economic review. Renew Energy 85:1371–1390 . doi: 10.1016/j.renene.2015.07.066

42. Eufores (2015) EU Tracking Roadmap. Eurofores

43. (2011) Gases from non-conventional sources. Injection into natural gas grids. Requirements and recommendations. Green Gas Grids

44. Rachbauer L, Voitl G, Bochmann G, Fuchs W (2016) Biological biogas upgrading capacity of a hydrogenotrophic community in a trickle-bed reactor. Appl Energy 180:483–490 . doi: 10.1016/j.apenergy.2016.07.109

45. COWI (2015) State of the Art on Alternative Fuels Transport Systems in the European Union. European Commission

46. Thrän D (2012) European biomethane potentials. In: Workshop on Biomethane Trade. p 2012

47. Kovacs A (2013) Proposal for a European Biomethane Roadmap. European Biogas Association

48. AEBIOM (2009) A Biogas Roadmap for Europe. European Biomass Association, Brussels

49. Tomescu M, Moorkens I, Wetzels W, et al (2016) Renewable energy in Europe in 2016: recent growth and knock-on effects. European Environmental Agency, Luxembourg

50. European Biogas Association (2010) National Renewable Energy Action Plans: EBA's evaluation of the Biogas contribution. European Biogas Association, Brussels

51. (2014) Biogas barometer 2014. EurObserv'ER

52. Couturier C (2013) Méthanisation agricole: quelle rentabilité selon les projets? Sci Eaux Territ 72–77

53. IRENA (2016) Renewable Energy and Jobs - Annual Review 2016. International Renewable Energy Agency (IRENA)

54. Xu Y, Huang Y, Wu B, et al (2015) Biogas upgrading technologies: Energetic analysis and environmental impact assessment. Chin J Chem Eng 23:247–254 . doi: 10.1016/j.cjche.2014.09.048

55. Muñoz R, Meier L, Diaz I, Jeison D (2015) A review on the state-of-the-art of physical/chemical and biological technologies for biogas upgrading. Rev Environ Sci Biotechnol 14:727–759 . doi: 10.1007/s11157-015-9379-1

56. Andriani D, Wresta A, Atmaja T, Saepudin A (2014) A Review on Optimization Production and Upgrading Biogas Through CO2 Removal Using Various Techniques. Appl Biochem Biotechnol 172:1909–1928 . doi: 10.1007/s12010-013-0652-x

57. Niesner J, Jecha D, Stehlík P (2013) Biogas Upgrading Technologies: State of Art Review in European Region. Chem Eng 35:517–522

58. Bauer F, Persson T, Hulteberg C, Tamm D (2013) Biogas upgrading–technology overview, comparison and perspectives for the future. Biofuels Bioprod Biorefining 7:499–511

59. Vienna University of Technology (2012) DU BIOGAZ AU BIOMETHANE REVUE TECHNIQUE. VIENNA UNIVERSITY OF TECHNOLOGY

60. Warren K (2012) A techno-economic comparison of biogas upgrading technologies in Europe

61. Yang L, Ge X, Wan C, et al (2014) Progress and perspectives in converting biogas to transportation fuels. Renew Sustain Energy Rev 40:1133–1152 . doi: 10.1016/j.rser.2014.08.008

62. Sun Q, Li H, Yan J, et al (2015) Selection of appropriate biogas upgrading technology-a review of biogas cleaning, upgrading and utilisation. Renew Sustain Energy Rev 51:521–532 . doi: 10.1016/j.rser.2015.06.029

63. Benizri D (2016) Epuration du biogaz à la ferme : EPUROGAS, une solution énergétique et économique d'avenir. - Etude expérimentale et modélisation d'un procédé d'absorption de dioxyde de carbone avec de l'eau sous pression à une échelle industrielle -. Université de Toulouse

64. Bortoluzzi G, Gatti M, Sogni A, Consonni S (2014) Biomethane production from Agricultural Resources in the Italian Scenario: Techno-Economic Analysis of Water Wash. Italian Association of Chemical Engineering 37:259–264

65. Rotunno P, Lanzini A, Leone P (2017) Energy and economic analysis of a water scrubbing based biogas upgrading process for biomethane injection into the gas grid or use as transportation fuel. Renew Energy 102:417–432 . doi: 10.1016/j.renene.2016.10.062

66. Abdeen FRH, Mel M, Jami MS, et al (2016) A review of chemical absorption of carbon dioxide for biogas upgrading. Chin J Chem Eng 24:693–702 . doi: 10.1016/j.cjche.2016.05.006

67. Eide-Haugmo I, Lepaumier H, Einbu A, et al (2011) Chemical stability and biodegradability of new solvents for CO2 capture. Energy Procedia 4:1631–1636 . doi: 10.1016/j.egypro.2011.02.034

68. Bishnoi S, Rochelle GT (2000) Absorption of carbon dioxide into aqueous piperazine: reaction kinetics, mass transfer and solubility. Chem Eng Sci 55:5531–5543

69. Bishnoi S, Rochelle GT (2002) Absorption of Carbon dioxide in aqueous Piperazine/Methyldiethanoamine. AIChE Journal 48: . doi: 10.1002/aic.690481208

70. Razi N, Svendsen HF, Bolland O (2013) Validation of mass transfer correlations for CO2 absorption with MEA using pilot data. Int J Greenh Gas Control 19:478–491 . doi: 10.1016/j.ijggc.2013.10.006

71. Rahim NA, Ghasem N, Al-Marzouqi M (2015) Absorption of CO2 from natural gas using different amino acid salt solutions and regeneration using hollow fiber membrane contactors. J Nat Gas Sci Eng 26:108–117 . doi: 10.1016/j.jngse.2015.06.010

72. De Souza G (2009) TI - Purification des gaz par le procédé PSA - Dimensionnement et perspectives

73. Alonso-Vicario A, Ochoa-Gómez JR, Gil-Río S, et al (2010) Purification and upgrading of biogas by pressure swing adsorption on synthetic and natural zeolites. Microporous Mesoporous Mater 134:100–107 . doi: 10.1016/j.micromeso.2010.05.014

74. Auerbach SM, Carrado KA, Dutta PK (2003) Handbook of zeolite science and technology. M. Dekker, New York

75. Pino L, Italiano C, Vita A, et al (2016) Sorbents with high efficiency for CO2 capture based on amines-supported carbon for biogas upgrading. J Environ Sci 48:138–150 . doi: 10.1016/j.jes.2016.01.029

76. Sun L-M (2004) TI - Perméation gazeuse. Ed. Techniques Ingénieur

77. Scholz M, Melin T, Wessling M (2013) Transforming biogas into biomethane using membrane technology. Renew Sustain Energy Rev 17:199–212 . doi: 10.1016/j.rser.2012.08.009

78. Wind JD, Paul DR, Koros WJ (2004) Natural gas permeation in polyimide membranes. J Membr Sci 228:227–236 . doi: 10.1016/j.memsci.2003.10.011

79. Zhang Y, Sunarso J, Liu S, Wang R (2013) Current status and development of membranes for CO2/CH4 separation: A review. Int J Greenh Gas Control 12:84–107 . doi: 10.1016/j.ijggc.2012.10.009

80. Robeson LM (2008) The upper bound revisited. J Membr Sci 320:390–400 . doi: 10.1016/j.memsci.2008.04.030

81. Johansson N (2008) Production of liquid biogas, LBG, with cryogenic and conventional upgrading technology-Description of systems and evaluations of energy balances

82. Clodic D (2016) Bio-LNG and Bio-CO2 measured purities produced by the CryoPur equipment

83. Riva M, Campestrini M, Toubassy J, et al (2014) Solid–Liquid–Vapor Equilibrium Models for Cryogenic Biogas Upgrading. Ind Eng Chem Res 53:17506–17514 . doi: 10.1021/ie502957x

84. Xiong X, Lin W, Jia R, et al (2015) Measurement and Calculation of CO_2 Frost Points in $CH_4 + CO_2$ /$CH_4 + CO_2 + N_2$ /$CH_4 + CO_2 + C_2H_6$ Mixtures at Low Temperatures. J Chem Eng Data 60:3077–3086 . doi: 10.1021/acs.jced.5b00059

85. Tsuji T, Suma K, Tanishita K, et al (1981) Development and clinical evaluation of hollow fiber membrane oxygenator. Trans Am Soc Artif Intern Organs 27:

86. Chabanon E, Belaissaoui B, Favre E (2014) Gas–liquid separation processes based on physical solvents: opportunities for membranes. J Membr Sci 459:52–61 . doi: 10.1016/j.memsci.2014.02.010

87. Gabelman A, Hwang S-T (1999) Hollow fiber membrane contactors. J Membr Sci 159:61–106 . doi: 10.1016/S0376-7388(99)00040-X

88. Mejia Mendez DL, Lemaitre C, Castel C, et al (2017) Membrane contactors for process intensification of gas absorption into physical solvents: Impact of dean vortices. J Membr Sci 530:20–32 . doi: 10.1016/j.memsci.2017.02.016

89. Pabby AK, Sastre AM (2013) State-of-the-art review on hollow fibre contactor technology and membrane-based extraction processes. J Membr Sci 430:263–303 . doi: 10.1016/j.memsci.2012.11.060

90. Luis P, Van der Bruggen B, Van Gerven T (2011) Non-dispersive absorption for CO2 capture: from the laboratory to industry. J Chem Technol Biotechnol 86:769–775 . doi: 10.1002/jctb.2614

91. Zhao S, Feron PHM, Deng L, et al (2016) Status and progress of membrane contactors in post-combustion carbon capture: A state-of-the-art review of new developments. J Membr Sci 511:180–206 . doi: 10.1016/j.memsci.2016.03.051

92. Chabanon E, Roizard D, Favre E (2011) Membrane Contactors for Postcombustion Carbon Dioxide Capture: A Comparative Study of Wetting Resistance on Long Time Scales. Ind Eng Chem Res 50:8237–8244 . doi: 10.1021/ie200704h

93. Hoff KA, Svendsen HF (2013) CO2 absorption with membrane contactors vs. packed absorbers-Challenges and opportunities in post combustion capture and natural gas sweetening. Energy Procedia 37:952–960 . doi: 10.1016/j.egypro.2013.05.190

94. Noble RD, Stern SA (1995) Membrane separations technology: principles and applications. Elsevier, Amsterdam ; New York

95. deMontigny D, Tontiwachwuthikul P, Chakma A (2005) Comparing the Absorption Performance of Packed Columns and Membrane Contactors. Ind Eng Chem Res 44:5726–5732 . doi: 10.1021/ie040264k

96. Gomez-Coma L, Garea A, Irabien A (2016) Carbon dioxide capture by [emim][Ac] ionic liquid in a polysulfone hollow fiber membrane contactor. Int J Greenh Gas Control 52:401–409 . doi: 10.1016/j.ijggc.2016.07.019

97. McLeod A, Jefferson B, McAdam EJ (2013) Quantifying the loss of methane through secondary gas mass transport (or 'slip') from a micro-porous membrane contactor applied to biogas upgrading. Water Res 47:3688–3695 . doi: 10.1016/j.watres.2013.04.032

98. Kim S-J, Park A, Nam S-E, et al (2016) Practical designs of membrane contactors and their performances in CO2/CH4 separation. Chem Eng Sci 155:239–247 . doi: 10.1016/j.ces.2016.08.018

99. McLeod A, Jefferson B, McAdam EJ (2014) Biogas upgrading by chemical absorption using ammonia rich absorbents derived from wastewater. Water Res 67:175–186 . doi: 10.1016/j.watres.2014.09.010

100. Rongwong W, Boributh S, Assabumrungrat S, et al (2012) Simultaneous absorption of CO2 and H2S from biogas by capillary membrane contactor. J Membr Sci 392–393:38–47 . doi: 10.1016/j.memsci.2011.11.050

101. Atchariyawut S, Jiraratananon R, Wang R (2007) Separation of CO2 from CH4 by using gas–liquid membrane contacting process. J Membr Sci 304:163–172 . doi: 10.1016/j.memsci.2007.07.030

102. Marzouk SAM, Al-Marzouqi MH, El-Naas MH, et al (2010) Removal of carbon dioxide from pressurized CO2–CH4 gas mixture using hollow fiber membrane contactors. J Membr Sci 351:21–27 . doi: 10.1016/j.memsci.2010.01.023

103. Marzouk SAM, Al-Marzouqi MH, Teramoto M, et al (2012) Simultaneous removal of CO2 and H2S from pressurized CO2–H2S–CH4 gas mixture using hollow fiber membrane contactors. Sep Purif Technol 86:88–97 . doi: 10.1016/j.seppur.2011.10.024

104. Teplyakov V, Okunev A, Laguntsov N (2007) Computer design of recycle membrane contactor systems for gas separation. Sep Purif Technol 57:450–454 . doi: 10.1016/j.seppur.2006.06.002

105. Van den Broeke LJP, Van de Runstraat A, Sanchez Fernandez E, et al (2012) Method and apparatus for separating mixed gas feed

106. Feron PHM, Volkov V, Khotimsky V, Teplyakov VV (2007) Membrane gas separation

107. Falk-Pedersen O, Dannström H (1998) Method for removing carbon dioxide from gases

108. Birbara PJ, Nalette TA (1994) Continuous carbon dioxide and water removal system

109. Jamal A, Gupta RP, Toy L, Coleman L (2013) Integrated system for acid gas removal

110. Buse G (2015) System and method for treating natural gas that contains methane

111. Vogler S, Braasch A, Buse G, et al (2013) Biogas Conditioning Using Hollow Fiber Membrane Contactors. Chemie Ingenieur Technik 58:1254–1258 . doi: 10.1002/cite.201200235

112. Heile S, Rosenberger S, Parker A, et al (2014) Establishing the suitability of symmetric ultrathin wall polydimethylsiloxane hollow-fibre membrane contactors for enhanced CO2 separation during biogas upgrading. J Membr Sci 452:37–45 . doi: 10.1016/j.memsci.2013.10.007

113. Kerber J, Repke J-U (2016) Mass transfer and selectivity analysis of a dense membrane contactor for upgrading biogas. J Membr Sci 520:450–464 . doi: 10.1016/j.memsci.2016.08.008

114. Belaissaoui B, Claveria-Baro J, Lorenzo-Hernando A, et al (2016) Potentialities of a dense skin hollow fiber membrane contactor for biogas purification by pressurized water absorption. J Membr Sci 513:236–249 . doi: 10.1016/j.memsci.2016.04.037

115. Sales Silva LP, Dalmazzone D, Stambouli M, et al (2016) Phase behavior of simple tributylphosphine oxide (TBPO) and mixed gas (CO2, CH4 and CO2 + CH4)+TBPO semiclathrate hydrates. J Chem Thermodyn 102:293–302 . doi: 10.1016/j.jct.2016.07.022

116. Castellani B, Rossi F, Filipponi M, Nicolini A (2014) Hydrate-based removal of carbon dioxide and hydrogen sulphide from biogas mixtures: Experimental investigation and energy evaluations. Biomass Bioenergy 70:330–338 . doi: 10.1016/j.biombioe.2014.08.026

117. Xia Z-M, Li X-S, Chen Z-Y, et al (2015) Hydrate-based CO2 capture and CH4 purification from simulated biogas with synergic additives based on gas solvent. Appl Energy. doi: 10.1016/j.apenergy.2015.02.016

118. Castellani B, Filipponi M, Rinaldi S, Rossi F (2012) Capture of carbon dioxide using gas hydrate technology. Proc ECOS

119. Sales Silva LP, Dalmazzone D, Stambouli M, et al (2016) Phase equilibria of semi-clathrate hydrates of tetra-n-butyl phosphonium bromide at atmospheric pressure and in presence of CH4 and CO2 + CH4. Fluid Phase Equilibria 413:28–35 . doi: 10.1016/j.fluid.2015.09.042

120. Burkhardt M, Koschack T, Busch G (2015) Biocatalytic methanation of hydrogen and carbon dioxide in an anaerobic three-phase system. Bioresour Technol 178:330–333 . doi: 10.1016/j.biortech.2014.08.023

121. Götz M, Koch AM, Graf F (2014) State of the art and perspectives of CO2 methanation process concepts for power-to-gas applications. In: International Gas Union Research Conference, Copenhagen

122. Bailera M, Lisbona P, Romeo LM, Espatolero S (2017) Power to Gas projects review: Lab, pilot and demo plants for storing renewable energy and CO2. Renew Sustain Energy Rev 69:292–312 . doi: 10.1016/j.rser.2016.11.130

123. Martin MR, Fornero JJ, Stark R, et al (2013) A Single-Culture Bioprocess of *Methanothermobacter thermautotrophicus* to Upgrade Digester Biogas by CO_2 -to-CH_4 Conversion with H_2. Archaea 2013:1–11 . doi: 10.1155/2013/157529

124. Kluckers J (2016) Biological methanation processes

125. Filali R (2012) Estimation and robust control of microalgae culture for optimization of biological fixation of CO2. Supélec

126. Kargupta W, Ganesh A, Mukherji S (2015) Estimation of carbon dioxide sequestration potential of microalgae grown in a batch photobioreactor. Bioresour Technol 180:370–375 . doi: 10.1016/j.biortech.2015.01.017

127. Bhakta JN, Lahiri S, Pittman JK, Jana BB (2015) Carbon dioxide sequestration in wastewater by a consortium of elevated carbon dioxide-tolerant microalgae. J CO2 Util 10:105–112 . doi: 10.1016/j.jcou.2015.02.001

128. Bhola V, Swalaha F, Ranjith Kumar R, et al (2014) Overview of the potential of microalgae for CO2 sequestration. Int J Environ Sci Technol 11:2103–2118 . doi: 10.1007/s13762-013-0487-6

129. Lam MK, Lee KT (2013) Effect of carbon source towards the growth of Chlorella vulgaris for CO2 bio-mitigation and biodiesel production. Int J Greenh Gas Control 14:169–176 . doi: 10.1016/j.ijggc.2013.01.016

130. Meier L, Barros P, Torres A, et al (2017) Photosynthetic biogas upgrading using microalgae: Effect of light/dark photoperiod. Renew Energy 106:17–23 . doi: 10.1016/j.renene.2017.01.009

131. Coquelet C, Richon D (2007) Propriétés thermodynamiques - Détermination pour les mélanges. Techniques de l'Ingénieur

132. Henry W (1802) Experiments on the Quantity of Gases absorbed by Water, at different Temperatures, and nder different Pressures. Philosophical Transactions of the Royal Society of London 29–42

133. Carroll JJ, Slupsky JD, Mather AE (1991) The Solubility of Carbon Dioxide in Water at Low Pressure. J Phys Chem Ref Data 20:1201–1209 . doi: 10.1063/1.555900

134. Loerting T, Bernard J (2010) Aqueous Carbonic Acid (H2CO3). ChemPhysChem 11:2305–2309 . doi: 10.1002/cphc.201000220

135. Musvoto EV, Wentzel MC, Loewenthal RE, Ekama GA (2000) Integrated chemical–physical processes modelling—I. Development of a kinetic-based model for mixed weak acid/base systems. Water Res 34:1857–1867

136. Plummer LN, Busenberg E (1982) The solubilities of calcite, aragonite and vaterite in CO2-H2O solutions between 0 and 90 C, and an evaluation of the aqueous model for the system CaCO3-CO2-H2O. Geochim Cosmochim Acta 46:1011–1040

137. Harned HS, Davis RJ (1943) The Ionization Constant of Carbonic Acid in Water and the Solubility of Carbon Dioxide in Water and Aqueous Salt Solutions from 0 to 50°C. J Am Chem Soc 65:2030–2037

138. Diamond LW, Akinfiev NN (2003) Solubility of CO2 in water from −1.5 to 100 °C and from 0.1 to 100 MPa: evaluation of literature data and thermodynamic modelling. Fluid Phase Equilibria 208:265–290 . doi: 10.1016/S0378-3812(03)00041-4

139. Lekvam K, Bishnoi PR (1997) Dissolution of methane in water at low temperatures and intermediate pressures. Fluid Phase Equilibria 131:297–309

140. Duan Z, Mao S (2006) A thermodynamic model for calculating methane solubility, density and gas phase composition of methane-bearing aqueous fluids from 273 to 523K and from 1 to 2000bar. Geochim Cosmochim Acta 70:3369–3386 . doi: 10.1016/j.gca.2006.03.018

141. Sander R (2014) Compilation of Henry's law constants, version 3.99. Atmospheric Chem Phys Discuss 14:29615–30521 . doi: 10.5194/acpd-14-29615-2014

142. Berg RL, Vanderzee CE (1978) Thermodynamics of carbon dioxide and carbonic acid: (a) the standard enthalpies of solution of Na2CO3(s), NaHCO3(s), and CO2(g) in water at 298.15 K; (b) the standard enthalpies of formation, standard Gibbs energies of formation, and standard entropies of CO2(aq), HCO3−(aq), CO32−(aq), NaHCO3(s), Na2CO3(s), Na2CO3·H2O(s), and Na2CO3·10H2O(s). J Chem Thermodyn 10:1113–1136 . doi: 10.1016/0021-9614(78)90029-0

143. Naghibi H, Dec SF, Gill SJ (1986) Heat of solution of methane in water from 0 to 50. degree. C. J Phys Chem 90:4621–4623

144. Druckenmiller ML, Maroto-Valer MM (2005) Carbon sequestration using brine of adjusted pH to form mineral carbonates. Fuel Process Technol 86:1599–1614 . doi: 10.1016/j.fuproc.2005.01.007

145. Dziedzic D, Gross KB, Gorski RA, Johnson JT (2006) Feasibility Study of Using Brine for Carbon Dioxide Capture and Storage from Fixed Sources. J Air Waste Manag Assoc 56:1631–1641 . doi: 10.1080/10473289.2006.10464568

146. El-Maghraby RM, Pentland CH, Iglauer S, Blunt MJ (2012) A fast method to equilibrate carbon dioxide with brine at high pressure and elevated temperature including solubility measurements. J Supercrit Fluids 62:55–59 . doi: 10.1016/j.supflu.2011.11.002

147. Spycher N, Pruess K (2010) A Phase-Partitioning Model for CO2?Brine Mixtures at Elevated Temperatures and Pressures: Application to CO2-Enhanced Geothermal Systems. Transp Porous Media 82:173–196 . doi: 10.1007/s11242-009-9425-y

148. Schumpe A (1993) The estimation of gas solubilities in salt solutions. Chem Eng Sci 48:153–158

149. Weisenberger S, Schumpe A (1996) Estimation of gas solubilities in salt solutions at temperatures from 273 K to 363 K. AIChE Journal 42:298–300

150. Ramdin M, de Loos TW, Vlugt TJH (2012) State-of-the-Art of CO_2 Capture with Ionic Liquids. Ind Eng Chem Res 51:8149–8177 . doi: 10.1021/ie3003705

151. Freemantle M (1998) Designer solvents: Ionic Liquids may boost clean technology development. Chem Eng News Arch 76:32–37 . doi: 10.1021/cen-v076n013.p032

152. Gómez-Coma L, Garea A, Irabien A (2016) PVDF MEMBRANE CONTACTOR FOR CO_2 CAPTURE USING THE IONIC LIQUID [emim][Ac]: MASS TRANSFER ANALYSIS. Chem Eng Technol. doi: 10.1002/ceat.201600293

153. Gómez-Coma L, Garea A, Irabien A (2014) Non-dispersive absorption of CO2 in [emim][EtSO4] and [emim][Ac]: Temperature influence. Sep Purif Technol 132:120–125 . doi: 10.1016/j.seppur.2014.05.012

154. Xie Y, Ma C, Lu X, Ji X (2016) Evaluation of imidazolium-based ionic liquids for biogas upgrading. Appl Energy 175:69–81 . doi: 10.1016/j.apenergy.2016.04.097

155. Kumar PS, Hogendoorn JA, Versteeg GF, Feron PHM (2003) Kinetics of the reaction of CO2 with aqueous potassium salt of taurine and glycine. AIChE J 49:203–213

156. Holst J van, Versteeg GF, Brilman DWF, Hogendoorn JA (2009) Kinetic study of CO2 with various amino acid salts in aqueous solution. Chem Eng Sci 64:59–68 . doi: 10.1016/j.ces.2008.09.015

157. Song H-J, Park S, Kim H, et al (2012) Carbon dioxide absorption characteristics of aqueous amino acid salt solutions. Int J Greenh Gas Control 11:64–72 . doi: 10.1016/j.ijggc.2012.07.019

158. Lu J-G, Zheng Y-F, Cheng M-D (2009) Membrane contactor for CO2 absorption applying amino-acid salt solutions. Desalination 249:498–502 . doi: 10.1016/j.desal.2009.04.007

159. Yan S, He Q, Zhao S, et al (2014) Biogas upgrading by CO2 removal with a highly selective natural amino acid salt in gas–liquid membrane contactor. Chem Eng Process Process Intensif 85:125–135 . doi: 10.1016/j.cep.2014.08.009

160. Starr K, Ramirez A, Meerman H, et al (2015) Explorative economic analysis of a novel biogas upgrading technology using carbon mineralization. A case study for Spain. Energy 79:298–309 . doi: 10.1016/j.energy.2014.11.015

161. Aines RD (2011) Carbon capture using small-molecule catalysts that mimic carbonic anhydrase

162. Kothandaraman A (2010) Cabon Dioxide Capture by Chemical Absorption: A Solvent Comparison Study. Massachesetts Institute of Technology

163. Hu G, Nicholas NJ, Smith KH, et al (2016) Carbon dioxide absorption into promoted potassium carbonate solutions: A review. Int J Greenh Gas Control 53:28–40 . doi: 10.1016/j.ijggc.2016.07.020

164. Savage DW, Astarita G, Joshi S (1980) Chemical absorption and desorption of carbon dioxide from hot carbonate solutions. Chem Eng Sci 35:1513–1522 . doi: 10.1016/0009-2509(80)80045-5

165. Yong JKJ, Stevens GW, Caruso F, Kentish SE (2015) The use of carbonic anhydrase to accelerate carbon dioxide capture processes: Carbonic anhydrase to accelerate carbon dioxide capture processes. J Chem Technol Biotechnol 90:3–10 . doi: 10.1002/jctb.4502

166. Kanth BK, Lee J, Pack SP (2013) Carbonic anhydrase: Its biocatalytic mechanisms and functional properties for efficient CO_2 capture process development. Eng Life Sci 13:422–431 . doi: 10.1002/elsc.201200157

167. Saeed M, Deng L (2016) Post-combustion CO2 membrane absorption promoted by mimic enzyme. J Membr Sci 499:36–46 . doi: 10.1016/j.memsci.2015.10.014

168. Phan DT, Burns RC, Puxty G, et al (2015) A study of bovine and human carbonic anhydrases as a model enzyme system for CO2 hydration in post combustion capture. Int J Greenh Gas Control 37:85–89 . doi: 10.1016/j.ijggc.2015.03.016

169. Floyd WC, Baker SE, Valdez CA, et al (2013) Evaluation of a Carbonic Anhydrase Mimic for Industrial Carbon Capture. Environ Sci Technol 47:10049–10055 . doi: 10.1021/es401336f

170. Borhani TNG, Azarpour A, Akbari V, et al (2015) CO2 capture with potassium carbonate solutions: A state-of-the-art review. Int J Greenh Gas Control 41:142–162 . doi: 10.1016/j.ijggc.2015.06.026

171. Beggel F, Nowik IJ, Modigell M, et al (2010) A novel gas purification system for biologically produced gases. J Clean Prod 18:S43–S50 . doi: 10.1016/j.jclepro.2010.06.015

172. Capannelli G, Comite A, Costa C, Di Felice R (2013) Effect of Absorbent Type and Concentration on CO_2 Capture from a Gas Stream into a Liquid Phase. Ind Eng Chem Res 52:13128–13136 . doi: 10.1021/ie401376w

173. Penders-van Elk NJMC, van Aken C, Versteeg GF (2016) Influence of temperature on the kinetics of enzyme catalysed absorption of carbon dioxide in aqueous MDEA solutions. Int J Greenh Gas Control 49:64–72 . doi: 10.1016/j.ijggc.2016.02.021

174. Penders-van Elk N, Hamborg ES, Huttenhuis PJG, et al (2012) Kinteics of absorption of carbon dioxide in aqueous amine and carbonate solutions with Carbonic Anhydrase

175. Arazawa DT, Oh H-I, Ye S-H, et al (2012) Immobilized carbonic anhydrase on hollow fiber membranes accelerates CO2 removal from blood. J Membr Sci 403–404:25–31 . doi: 10.1016/j.memsci.2012.02.006

176. Arazawa DT, Kimmel JD, Federspiel WJ (2015) Kinetics of CO2 exchange with carbonic anhydrase immobilized on fiber membranes in artificial lungs. J Mater Sci Mater Med 26: . doi: 10.1007/s10856-015-5525-0

177. Yan S, He Q, Zhao S, et al (2014) Biogas upgrading by CO2 removal with a highly selective natural amino acid salt in gas–liquid membrane contactor. Chem Eng Process Process Intensif 85:125–135 . doi: 10.1016/j.cep.2014.08.009

178. Levin M (2002) Pharmaceutical Process Scale-Up, Marcel Dekker Inc. New York

179. Buckingham E (1914) On physically similar systems; illustrations of the use of dimensional equations. Phys Rev 4:345

180. Atchariyawut S, Jiraratananon R, Wang R (2008) Mass transfer study and modeling of gas–liquid membrane contacting process by multistage cascade model for CO2 absorption. Sep Purif Technol 63:15–22 . doi: 10.1016/j.seppur.2008.03.005

181. Wang R, Zhang HY, Feron PHM, Liang DT (2005) Influence of membrane wetting on CO2 capture in microporous hollow fiber membrane contactors. Sep Purif Technol 46:33–40 . doi: 10.1016/j.seppur.2005.04.007

182. Lu J-G, Zheng Y-F, Cheng M-D (2008) Wetting mechanism in mass transfer process of hydrophobic membrane gas absorption. J Membr Sci 308:180–190 . doi: 10.1016/j.memsci.2007.09.051

183. Bird RB, Stewart WE, Lightfoot E (2002) Transport Phenomena, 2nd edition. John Wiley & Sons, Inc.

184. Bocquet S, Gasconsviladomat F, Muvdinova C, et al (2006) Membrane-based solvent extraction of aroma compounds: Choice of configurations of hollow fiber modules based on experiments and simulation. J Membr Sci 281:358–368 . doi: 10.1016/j.memsci.2006.04.005

185. Chabanon E, Roizard D, Favre E (2013) Modeling strategies of membrane contactors for post-combustion carbon capture: A critical comparative study. Chem Eng Sci 87:393–407 . doi: 10.1016/j.ces.2012.09.011

186. Albarracin Zaidiza D, Wilson SG, Belaissaoui B, et al (2016) Rigorous modelling of adiabatic multicomponent CO2 post-combustion capture using hollow fibre membrane contactors. Chem Eng Sci 145:45–58 . doi: 10.1016/j.ces.2016.01.053

187. Rode S, Nguyen PT, Roizard D, et al (2012) Evaluating the intensification potential of membrane contactors for gas absorption in a chemical solvent: A generic one-dimensional methodology and its application to CO2 absorption in monoethanolamine. J Membr Sci 389:1–16 . doi: 10.1016/j.memsci.2011.09.042

188. Lewis WK, Whitman WG (1924) Principles of Gas Absorption. Industrial and Enineering Chemistry 16:

189. Boributh S, Assabumrungrat S, Laosiripojana N, Jiraratananon R (2011) A modeling study on the effects of membrane characteristics and operating parameters on physical absorption of CO2 by hollow fiber membrane contactor. J Membr Sci 380:21–33 . doi: 10.1016/j.memsci.2011.06.029

190. Cui L, Ding Z, Liu L, Li Y (2015) Modelling and Experimental Study of Membrane Wetting in Microporous Hollow Fiber Membrane Contactors. Can J Chem Eng 93:1254–1265 . doi: 10.1002/cjce.22210

191. Khaisri S, deMontigny D, Tontiwachwuthikul P, Jiraratananon R (2010) A mathematical model for gas absorption membrane contactors that studies the effect of partially wetted membranes. J Membr Sci 347:228–239 . doi: 10.1016/j.memsci.2009.10.028

192. Dupuy A (2010) Stabilisation de l'inerface liquide-liquide dans un contacteur membranaire : application à l'extraction sélective de terpènes oxygénés d'huiles essentielles d'agrumes. AgroParisTech

193. Zheng J, Dai Z, Wong F, Xu Z (2005) Shell side mass transfer in a transverse flow hollow fiber membrane contactor. J Membr Sci 261:114–120 . doi: 10.1016/j.memsci.2005.02.035

194. Lévêque MA (1928) Les lois de la transmission de chaleur par convection. Ann. Mines 13

195. Yang M-C, Cussler EL (1986) Designing hollow-fiber contactors. AIChE J 32:1910–1916

196. Pierre F-X (2002) Les contacteurs membranaires appliqués à l'extraction des composés d'arômes. Institut National Agronomique Paris Grignon

197. Mavroudi M, Kaldis SP, Sakellaropoulos GP (2006) A study of mass transfer resistance in membrane gas–liquid contacting processes. J Membr Sci 272:103–115 . doi: 10.1016/j.memsci.2005.07.025

198. Kreith F, Black WZ (1980) Basic Heat Transfer. Harper & Row, New York

199. Pierre F-X, Souchon I, Athes V, Marin M (2002) Membrane-based solvent extraction of sulfur aroma compounds: influence of operating conditions on mass transfer coefficients in a hollow fiber contactor. Desalination 148:199–204

200. Schöner P, Plucinski P, Nitsch W, Daiminger U (1998) Mass transfer in the shell side of cross flow hollow fiber modules. Chem Eng Sci 53:2319–2326

201. Baudot A, Floury J, Smorenburg HE (2001) Liquid-liquid extraction of aroma compounds with hollow fiber contactor. AIChE J 47:1780–1793

202. Sengupta A, Peterson PA, Miller BD, et al (1998) Large-scale application of membrane contactors for gas transfer from or to ultrapure water. Sep Purif Technol 14:189–200

203. Shen S, Kentish SE, Stevens GW (2010) Shell-Side Mass-Transfer Performance in Hollow-Fiber Membrane Contactors. Solvent Extr Ion Exch 28:817–844 . doi: 10.1080/07366299.2010.515176

204. Kreulen H, Smolders CA, Versteeg GF, van Swaaij WPM (1993) Determination of mass transfer rates in wetted and non-wetted microporous membranes. Chem Eng Sci 48:2093–2102

205. Albarracin Zaidiza D, Billaud J, Belaissaoui B, et al (2014) Modeling of CO2 post-combustion capture using membrane contactors, comparison between one- and two-dimensional approaches. J Membr Sci 455:64–74 . doi: 10.1016/j.memsci.2013.12.012

206. Keshavarz P, Fathikalajahi J, Ayatollahi S (2008) Mathematical modeling of the simultaneous absorption of carbon dioxide and hydrogen sulfide in a hollow fiber membrane contactor. Sep Purif Technol 63:145–155 . doi: 10.1016/j.seppur.2008.04.008

207. Goyal N, Suman S, Gupta SK (2015) Mathematical modeling of CO2 separation from gaseous-mixture using a Hollow-Fiber Membrane Module: Physical mechanism and influence of partial-wetting. J Membr Sci 474:64–82 . doi: 10.1016/j.memsci.2014.09.036

208. Yan Y, Zhang Z, Zhang L, et al (2014) Dynamic Modeling of Biogas Upgrading in Hollow Fiber Membrane Contactors. Energy Fuels 28:5745–5755 . doi: 10.1021/ef501435q

209. Happel J (1959) Viscous flow relative to arrays of cylinders. AIChE J 5:174–177

210. Mosadegh-Sedghi S, Rodrigue D, Brisson J, Iliuta MC (2014) Wetting phenomenon in membrane contactors – Causes and prevention. J Membr Sci 452:332–353 . doi: 10.1016/j.memsci.2013.09.055

211. Kim B-S, Harriott P (1987) Critical entry pressure for liquids in hydrophobic membranes. J Colloid Interface Sci 115:1–8

212. Lv Y, Yu X, Tu S-T, et al (2010) Wetting of polypropylene hollow fiber membrane contactors. J Membr Sci 362:444–452 . doi: 10.1016/j.memsci.2010.06.067

213. Zydney AL, Aimar P, Meireles M, et al (1994) Use of the log-normal probability density function to analyze membrane pore size distributions: functional forms and discrepancies. Journal of Membrane Science 91:293–298

214. Hashemifard SA, Matsuura T, Ismail AF, et al (2015) Characterization of partial pore wetting in hollow fiber gas absorption membrane contactors: An EDX analysis approach. Chem Eng J 281:970–980 . doi: 10.1016/j.cej.2015.07.036

215. Wakao N, Smith JM (1962) Diffusion in catalyst pellets. Chem Eng Sci 17:825–834

216. Agilent (2016) Agilent 490 Data Sheet

217. Hodgkinson J, Tatam RP (2012) Optical gas sensing: a review. Meas Sci Technol 24:012004

218. Bronkhorst Digital Thermal Mass Flow Meters and Controllers for Gases. EL-FLOW Select.

219. Bronkhorst Industrial Mass Flow Meters and Controllers for Gases. IN-FLOW CTA.

220. Mohebbi V, Naderifar A, Behbahani RM, Moshfeghian M (2012) Determination of Henry's law constant of light hydrocarbon gases at low temperatures. J Chem Thermodyn 51:8–11 . doi: 10.1016/j.jct.2012.02.014

221. Technology | HydroFLOW USA, water treatment, water softener, water softening ,non chemical, hydropath, water conditioner,non chemical, non-chemical, s. http://www.hydroflow-usa.com/hydropath_technology. Accessed 26 Apr 2017

222. Lemanski J, Lipscomb GG (1995) Effect of shell-side flows on hollow-fiber membrane device performance. AIChE J 41:2322–2326

223. Eberhart RC, Kennedy J, others (1995) A new optimizer using particle swarm theory. In: Proceedings of the sixth international symposium on micro machine and human science. New York, NY, pp 39–43

224. Reynolds CW (1987) Flocks, herds and schools: A distributed behavioral model. ACM SIGGRAPH Comput Graph 21:25–34

225. Andras P (2012) A Bayesian Interpretation of the Particle Swarm Optimization and Its Kernel Extension. PloS One 7:e48710

226. Banks A, Vincent J, Anyakoha C (2008) A review of particle swarm optimization. Part II: hybridisation, combinatorial, multicriteria and constrained optimization, and indicative applications. Nat Comput 7:109–124 . doi: 10.1007/s11047-007-9050-z

227. Farges O (2014) Conception optimale de centrales solaires à concentration: application aux centrales à tour et aux installations" beam down". Ecole des Mines d'Albi-Carmaux

228. Wetter M, Wright JA (2004) A comparison of deterministic and probabilistic optimization algorithms for nonsmooth simulation-based optimization. Build Environ 39:989–999 . doi: 10.1016/j.buildenv.2004.01.022

229. Hsu C-H, Li M-H (1997) Densities of Aqueous Blended Amines. J Chem Eng Data 42:502–507 . doi: 10.1021/je960356j

230. Atkins P, de Paula J (2006) Physical Chemistry, 8th ed. Oxford University Press, Oxford ; New York

231. Laliberté M, Cooper WE (2004) Model for Calculating the Density of Aqueous Electrolyte Solutions. J Chem Eng Data 49:1141–1151 . doi: 10.1021/je0498659

232. Hsu CH, Li HM (1997) Viscosity of aqueous blended amines. J Chem Eng Data 42:714–720

233. Pérez-Díaz JL, Álvarez-Valenzuela MA, García-Prada JC (2012) The effect of the partial pressure of water vapor on the surface tension of the liquid water–air interface. J Colloid Interface Sci 381:180–182 . doi: 10.1016/j.jcis.2012.05.034

234. Simion AI, Grigoraş C-G, Roşu A-M, Gavrilă L (2015) Mathematical modelling of density and viscosity of nacl aqueous solutions. J Agroaliment Process Technol 21:41–52

235. Reid RC, Prausnitz JM, Poling BE (1987) The Properties of Gases and Liquids, 4th edition. McGraw-Hill Inc., New York

236. Maxwell JC (1860) V. Illustrations of the dynamical theory of gases.—Part I. On the motions and collisions of perfectly elastic spheres. Philos Mag Ser 4 19:19–32 . doi: 10.1080/14786446008642818

237. Fuller EN, Schettler PD, Giddings JC (1966) New method for prediction of binary gas-phase diffusion coefficients. Ind Eng Chem 58:18–27

238. Hirschfelde JO, Curtiss CF, Bird RB (1954) Molecular theory of gases and liquids. J Polym Sci 17:116–116 . doi: 10.1002/pol.1955.120178311

239. He W, Lv W, Dickerson JH (2014) Gas Diffusion Mechanisms and Models. In: Gas Transport in Solid Oxide Fuel Cells. Springer International Publishing, Cham, pp 9–17

240. Wilke CR, Chang P (1955) Correlation of diffusion coefficients in dilute solutions. AIChE J 1:264–270

241. Versteeg GF, van Swaaij WPM (1988) Solubility and diffusivity of acid gases (CO2, N2O) in aqueous alkanolamine solutions. J Chem Eng Data 33:29–34

242. Magalhães AL, Lito PF, Da Silva FA, Silva CM (2013) Simple and accurate correlations for diffusion coefficients of solutes in liquids and supercritical fluids over wide ranges of temperature and density. J Supercrit Fluids 76:94–114 . doi: 10.1016/j.supflu.2013.02.002

243. Le Quéré C, Andrew RM, Friedlingstein P, et al (2017) Global Carbon Budget 2017. Earth Syst Sci Data Discuss 2017:1–79 . doi: 10.5194/essd-2017-123

244. Observatoire France Biométhane - Think Tank du Biogaz. http://france-biomethane.fr/observatoire-sia-partners-2/. Accessed 21 Sep 2016

Appendices

Appendix A Biogas description

The biogas composition is quite variable. It mainly depends on the substrates, the digestion type (liquid Continuously Stirred-Tank Reactor CSTR, plug-flow reactor, batch digester for solid substrates) and the digestion operating conditions. These parameters influence the prevailing biological pathway (Figure 1.1). Spence suggested to correlate the CH_4/CO_2 ratio with the oxidation state of carbon (Figure A.1): the less oxidized, the richer the CH_4 content. It provides an indication of the methane content according to the substrate nature.

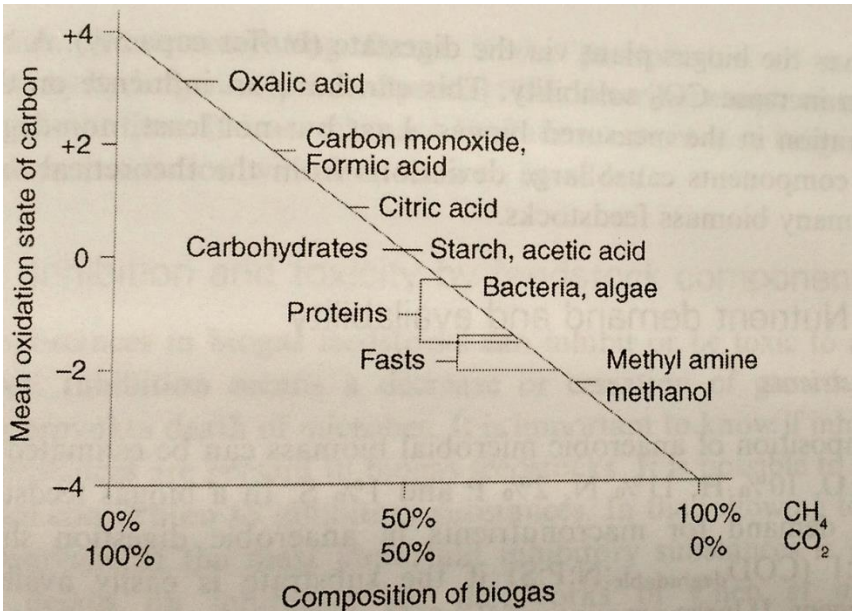

Figure A.1 – Influence of oxidation state on gas composition [21]

The impurities concentrations are also highly variable. For instance, a sulphur-rich protein substrate is more likely to produce a high level of H_2S. For every type of substrate, ranges of concentration are provided for biogas compounds synthetized from available literature (Table A.1). It is also compared to the fossil natural gas composition.

Components	Bio-waste	Activated sludge	Agricultural feedstock	Landfill	Natural gas
CH_4 [% $vol.$]	55-65	60-70	45-70	35-60	81-97
CO_2 [% $vol.$]	35-45	30-40	30-55	30-50	1
H_2S [$ppmv$]	100-6000	500-1500	50-5000	600-10000	5
H_2O	100% saturation	100% saturation	100% saturation	< 100% saturation	60 % saturation
NH_3 [$mg.Nm^{-3}$]		< 0.05	< 2		-
N_2 [% $vol.$]	0-1	0-2	0-5	0-30	< 1
O_2 [% $vol.$]	0.1-0.5	0-1	0-2	0-6	< 3
$Siloxanes$ [$mg.Nm^{-3}$]	1 – 2	< 50	< 1	0 - 50	
$Halogenated\ hydrocarbons$ [$mg.Nm^{-3}$]	Traces	Traces	Traces	0-150	
$Calorific\ value$ [$kWh.Nm^{-3}$]	5 - 8				11.7
$Wobbe\ Index$ [$kWh.Nm^{-3}$]	6.5 – 7.5				14
$Density$	0.9 – 1.1				0.57

Table A.1 – Natural gas and average biogas composition from various feedstocks [27, 28]

Appendix B Specifications for biomethane injection in France

Biomethane injection into the distribution or transportation gas grids must comply with the technical specifications issued by the gas grid operators. The multiplication of biomethane injection points implies a fundamental evolution in the gas grid organization which originally had only very scarce entry points. In France, the decree 2015-1823 imposes the biomethane producers to meet these specifications.

In France, biomethane will be allowed to feed the natural gas grid if it meets the requirements of AFG specifications B562-1 for distribution grid and B562-2 for transportation grid, published respectively in 2010 and 2011. When injected, biomethane has priority access to the grid with non-discriminatory conditions. The complete AFG specification B562-1 is presented in Table B.1

Caractéristique	Spécification
Pouvoir Calorifique Supérieur (conditions de combustion 0 °C et 1,01325 bar)	Gaz de type H[(1)] : 10,7 à 12,8 kWh/m³(n) (combustion 25°C : 10,67 à 12,77) Gaz de type B[(1)] : 9,5 à 10,5 kWh/m³(n) (combustion 25°C : 9,48 à 10,47)
Indice de Wobbe (conditions de combustion 0 °C et 1,01325 bar) [(2)]	Gaz de type H : 13,64 à 15,70 kWh/m³(n) (combustion 25°C:13,6 à 15,66) Gaz de type B : 12.01 à 13,06 kWh/m³(n) (combustion 25°C : 11,97 à 13,03)
Densité	Comprise entre 0,555 et 0,70
Point de rosée eau	Inférieur à -5°C à la Pression Maximale de Service du réseau en aval du Raccordement [(3)]
Point de rosée hydrocarbures [(4)]	Inférieur à -2°C de 1 à 70 bar
Teneur en soufre total	Inférieure à 30 mgS/m³(n)
Teneur en soufre mercaptique	Inférieure à 6 mgS/m³(n)
Teneur en soufre de H_2S + COS	Inférieure à 5 mgS/m³(n)
Teneur en CO_2	Inférieure à 2,5 % (molaire)
Teneur en Tétrahydrothiophène (produit odorisant THT)	Comprise entre 15 et 40 mg/m³(n)
Teneur en O_2	Inférieure à 100 ppmv
Impuretés	Gaz pouvant être transporté, stocké et commercialisé sans subir de traitement supplémentaire
Hg	Inférieur à 1 µg/m³(n)
Cl	Inférieur à 1 mg/m³(n)
F	Inférieur à 10 mg/m³(n)
H_2	Inférieur à 6 %
NH_3	Inférieur à 3 mg/m³(n)
CO	Inférieur à 2 %

Gaz de type H : Gaz à haut pouvoir calorifique.
Gaz de type B : Gaz à bas pouvoir calorifique.

(1) Gaz de type H : Gaz à haut pouvoir calorifique. Gaz de type B : Gaz à bas pouvoir calorifique.

(2) Ces valeurs sont celles discutées dans le cadre de l'association Easee-gas. Concernant la limite supérieure pour l'indice de Wobbe, des vérifications sont en cours pour déterminer à quelle date la valeur de 15.85 kWh/m3(n) (au lieu de15.7) discutée au sein d'Easee-gas serait acceptable en France.

(3) La conversion du point de rosée eau en teneur en eau et inversement est effectuée selon la norme ISO 18 453 « Natural gas – Correlation between water content and water dew point. » (Corrélation de Gergwater).

(4) Il s'agit d'une spécification applicable au gaz naturel qui ne couvre que les hydrocarbures et pas les huiles.

Table B.1 – Gas grid operator (GrDF) specifications for biomethane injection in the distribution network

Appendix C Potential for biomethane production and injection in Europe

Several studies evaluate the forecasted potential of a specific energy source to support policy-making and energy previsions. The biomethane production is relying on two main pathways (Figure C.1). Anaerobic digestion degrades organic matter to produce a mixture of methane and carbon dioxide. Methanation is a process combining hydrogen and carbon dioxide to produce methane according to the Sabatier reaction. The complementarity of these pathways is underlined in the European Commission Report on Alternative Fuels Transport Systems [45]. Methanation is looked upon as a key process to develop a sustainable energy mix. First, it may be used to convert the syngas produced from the gasification of biomass into a chemical form (methane) which can be stored and transported in gas-grid infrastructures. Also, methanation is an attractive solution to store the electricity surplus produced from intermittent renewable energies such as solar and wind energies. Hydrogen is produced by electrolysis and then converted to methane. An overall evaluation of the potential biomethane production and injection capacity in Europe must combine all these pathways.

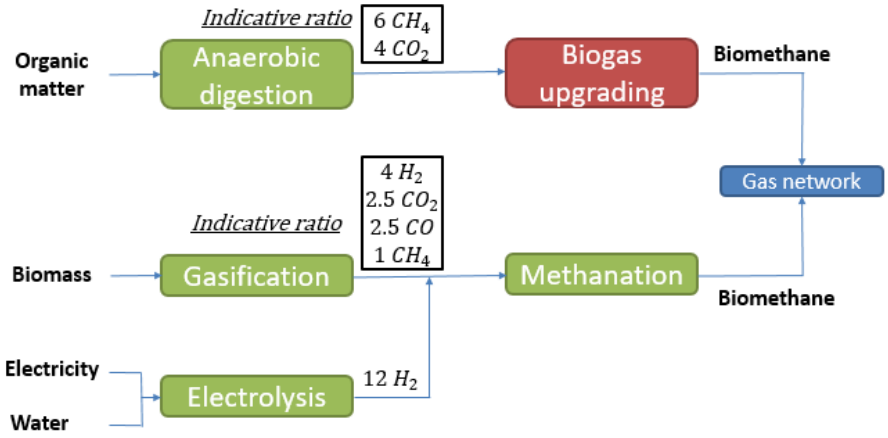

Figure C.1 – Main biomethane production pathways

The figures presented in paragraph 1.2.3.3 are originating from 3 studies which respective scopes are presented in Table C..

Study	Year	Scope	Geographic boundaries
AEBIOM **[48]**	2009	2020 available AD technical potential	EU-27
DBFZ **[46]**	2012	Technical biomethane potential	EU-27
ADEME [9]	2013	2030 available AD technical potential	France

Table C.1 – Scope of several studies assessing the biomethane potential

The DBFZ institute carried out the most exhaustive study on the European biomethane potential. Nonetheless, biomethane development must take advantage of the existing gas-grid infrastructure to become a major renewable source of energy across Europe. Therefore, the comparison of Thrän [46] between the biomethane potential and the gas-grid network is essential to provide a better understanding of the biomethane potential in Europe (Figure C.2 and Figure C.3). It indicates that the production of SNG[38] holds a higher potential than biogas. Moreover, the geographical repartition is quite uniform except for mountainous areas. The case of the Scandinavian countries (Norway, Finland and Sweden) is particular: they hold significant wood resources but the gas grid infrastructure is almost absent.

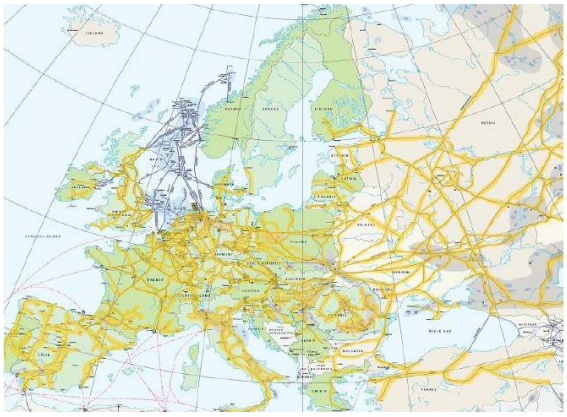

Figure C.2 – Potential along the gas grid: biogas [46]

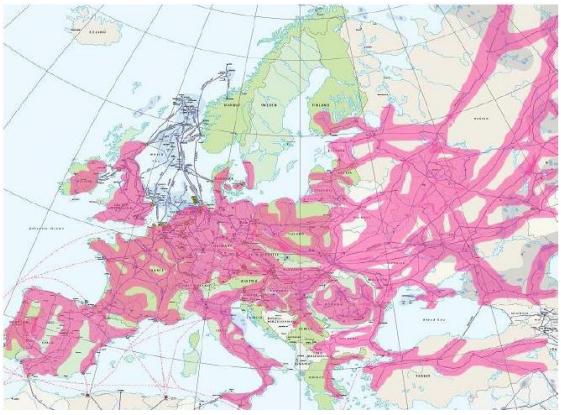

Figure C.3 – Potential along the gas grid: SNG [46]

[38] Synthetic Natural Gas

Appendix D Thermodynamics of CO_2-CH_4 mixtures

The phase diagram of CO_2/CH_4 mixtures has first been of interest for the natural gas industry. CO_2 frost is likely to form at low-temperatures, which may occur during the expansion of LNG[39] at methane terminals. It leads to operational problems in heat exchangers or pipelines. Cryogeny, a biogas upgrading technology, takes advantage of the differences in CO_2 and CH_4 behaviours, as shown in the phase diagram (Table D.1 and Figure D.1). The aim of the process is to frost CO_2 selectively while CH_4 is still in a fluid form.

Fluid	$P_t\,[MPa]$	$T_t\,[K]$	$P_c\,[MPa]$	$T_c\,[K]$
CH_4	0.011696	90.6941	4.5992[229][230]	190.564
CO_2	0.51795	216.592	7.3773	304.1282

Table D.1 – Triple and critical points for CH_4 and CO_2 [83] from NIST Standard Database

An accurate design of a cryogenic biogas upgrading process requires a precise knowledge of the phase boundaries for a biogas mixture. This issue was addressed by surveying the available thermodynamical data (Figure D.1) and comparing them to two different models [83]. Previous experimental studies indicated that the existence of a quadruple point where two immiscible solids are coexisting is very likely. It has though not been confirmed yet by experimental observation.

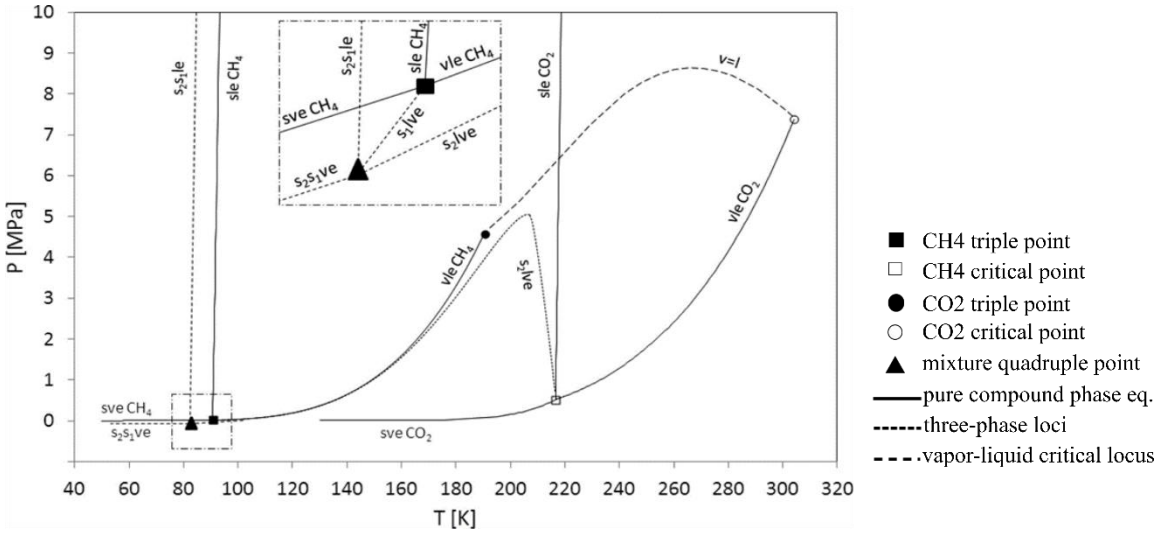

Figure D.1 – Pressure-temperature equilibrium behaviour for the CH_4-CO_2 system [83]

[39] Liquefied Natural Gas

This cryogenic process must therefore be operated below the temperature of the CO_2 triple point: the temperature is in the range 140-200 K depending on the desired biomethane quality [83]. More experimental measurements are needed in this region.

Appendix E Gas-liquid equilibrium

Theoretical considerations and definitions are provided in the main body of the text (1.4.1). The empirical correlation used for the determination of Henry coefficients in water are presented in this appendix. It is based on the survey of Sander [141], compiling gas-liquid equilibrium measurements for a large number of gases. The temperature dependence of Henry coefficient is described with the van't Hoff equation (Eq. E.1), the equilibrium constant being the Henry coefficient H^{cp} [230].

$$\frac{d \ln H^{cp}}{d\,(1/T)} = -\frac{\Delta H_{dis}}{R} \qquad \text{Eq. E.1}$$

where H^{cp} is the Henry coefficient relative to the molar concentration in the liquid phase and the gas partial pressure, ΔH_{dis} is the enthalpy of dissolution of the component and R is the ideal gas constant.

The integration of Eq. E.1 leads to the following expression:

$$H^{cp}(T) = H^{cp*} \exp\left(\frac{-\Delta H_{dis}}{R}\left(\frac{1}{T} - \frac{1}{T^*}\right)\right) \qquad \text{Eq. E.2}$$

where H^{cp*} is the Henry coefficient of the considered compound at the temperature T^*.

k_H^{px}, Henry coefficient related to liquid molar fraction and pressure, is linked to H^{cp} by Eq. E.3. Thus, the form of k_H^{px} derivative is similar to Eq. E.1: its temperature dependence may be described by Eq. E.4.

$$H^{cp}(T) = \frac{C_i^l}{P_i} = \frac{x_i}{P_i} c_{tot}^l = \frac{c_{tot}^l}{k_H^{px}(T)} \qquad \text{Eq. E.3}$$

$$k_H^{px}(T) = k_H^{px*} \exp\left(\frac{\Delta H_{dis}}{R}\left(\frac{1}{T} - \frac{1}{T^*}\right)\right) \qquad \text{Eq. E.4}$$

The van't Hoff equation presented in Eq. E.1 is valid for a temperature range in which the enthalpy of dissolution is not subject to significant variations. Empirical correlations may be used to describe a larger range of temperature.

The parameters $\frac{\Delta H_{dis}}{R}$ and H^{cp*} are listed in the review of Sander from a literature survey. Table E.1 presents the values selected for this work.

Gas	$-\frac{\Delta H_{dis}}{R}\ [K]$	$H^{cp^*}\ [mol.m^{-3}.Pa^{-1}]$
CO_2	2400	3.3×10^{-4}
CH_4	1600	1.4×10^{-5}
O_2	1500	1.3×10^{-5}
N_2	1300	6.4×10^{-6}
H_2S	2100	1.0×10^{-3}

Table E.1 – Parameters describing the Henry coefficients temperature dependence [141]

The values from Table E.1 are in very good agreement with the enthalpy of dissolution listed in paragraph 1.4.2.1. The relative difference for the enthalpy of dissolution ΔH_{dis} is respectively 2.0 % and 0.9 % for CO_2 and CH_4.

Appendix F Solvent properties

The correlations used in this study to determine the values of solvent properties are presented in this appendix. They are issued from specific studies establishing empirical correlations from experimental measurements (Table F.1).

One can find a model applicable to calculate the density of electrolytic solutions according to concentration and temperature [231]. The model, valid for a large number of salts, was used for KCl solutions.

Property	Unit	Correlation (SI)	Source
Water			
$\boldsymbol{\rho_{water}}$	$kg.m^{-3}$	$863.559 + 1.21494\,T - 2.57080 \times 10^{-3}\,T^2$	[229]
$\boldsymbol{\nu_{water}}$	$10^{-6}\,m^2.s^{-1}$	$\exp\left(-3.28285 + \frac{4.56029 \times 10^2}{T - 1.54576 \times 10^2}\right)$	[232]
$\boldsymbol{\gamma_{water}}$	$N.m^{-1}$	$15\,°C: 73.5 \times 10^{-3}$ $20\,°C: 73.0 \times 10^{-3}$	[233]
NaCl solution			
$\boldsymbol{\rho_{NaCl}}$	$kg.m^{-3}$	$b1 + b2\,C_{NaCl,w\%} + b3\,T + b4\,C_{NaCl,w\%}^2 + b5\,T^2 + b6\,C_{NaCl,w\%}\,T$	[234]
$\boldsymbol{ln(\mu_{NaCl})}$	$10^{-3}\,kg.m^{-1}.s^{-1}$	$e1 + e2\,C_{NaCl,w\%}^2 \ln(C_{NaCl,w\%}) + e3\,e^{\frac{C_{NaCl,w\%}}{42.0001357}} + e4 \ln T + e5\,T^{-0.5} + e6\,T^{-1} \ln T$	[234]

Table F.1 – Physico-chemical properties of water and mineral salts

Parameter	Value	Parameter	Value
$\boldsymbol{b_1}$	919.0202567	e_1	-18335.9314
$\boldsymbol{b_2}$	8.661163416	e_2	0.000204573
$\boldsymbol{b_3}$	0.854264859	e_3	0.25824408
$\boldsymbol{b_4}$	0.027175948	e_4	2040.636458
$\boldsymbol{b_5}$	-0.00199299	e_5	185548.199
$\boldsymbol{b_6}$	- 0.00585389	e_6	-211131.092

Table F.2 – Parameters of physico-chemical correlations from Table F.1

Appendix G Diffusion

Diffusion is a mass transport phenomenon. It tends to make the system uniform under the thermal agitation of the molecules and occurs under a gradient of concentration. The description of diffusion in the gas and liquid phases are presented separately.

G.1 Diffusion in the gas phase

G.1.1 Molecular diffusion

In a gas mixture, the molecular diffusion also called continuum diffusion refers to the relative motion of different gas species. The Fick's law is the most popular approach to evaluate the gas diffusion flux $\overrightarrow{J_A}$ in clear fluids and gases.

$$\overrightarrow{J_A} = -D_{AB}\vec{\nabla}C_A \qquad \text{Eq. G.1}$$

The estimation of the binary diffusivity D_{AB} is key for an accurate description of the molecular diffusion. The Chapman-Eskog theory is widely established [235]. The binary diffusivity is derived from the molecular weights M_A and M_B, as well as from parameters that characterize the molecules interactions (the collision diameter σ_{AB} and the dimensionless collision integral Ω).

$$D_{AB} = \frac{0.00186\, T_g^{1.5}}{\sigma_{AB}^2\, \Omega\, P_g}\left(\frac{1}{M_A}+\frac{1}{M_B}\right)^{0.5} \qquad \text{Eq. G.2}$$

The collision diameter σ_{AB} is the mean of the Lennard-Jones parameter σ_A for both considered species (Eq. G.3). The collision integral Ω is typically described by the Lennard-Jones potential.

$$\sigma_{AB} = \frac{1}{2}(\sigma_A + \sigma_B) \qquad \text{Eq. G.3}$$

To describe the diffusivity of ternary gas systems, the Chapman-Eskog theory is not valid anymore and one must use the Maxwell-Stefan model [183, 236].

An empirical correlation (Eq. G.4) that offers a more direct calculation was suggested by Fuller [237]. The interactions between the molecules are here described by the estimation of an equivalent volume of diffusion $\sum \nu$ based on the elements of the gas molecule. The relative error between the

results derived from the Fuller equation and the Chapman-Eskog theory is below 4 % for binary systems [11].

$$D_{AB} = \frac{10^{-7}T^{1.75}}{P\left[(\sum v)_A^{1/3} + (\sum v)_B^{1/3}\right]^2}\left[\frac{1}{M_A} + \frac{1}{M_B}\right]^{\frac{1}{2}} \quad \text{Eq. G.4}$$

The molecular volumes are tabulated. In the case of unavailable data, the molecular volume is estimated by addition of the atomic volumes (Table G.3).

Substance	∇	Substance	∇	Substance	∇
C	16.5	CO_2	26.9	CO	18.9
H	1.98	H_2	7.07	NH_3	14.9
O	5.48	O_2	16.6	H_2O	12.7
N	5.69	N_2	17.9	SO_2	41.1

Table G.3 – Diffusion volumes of atoms and simple molecules [235]

According to the Fuller equation, in the standard conditions, the binary diffusivity of methane and carbon dioxide is $D_{CO2-CH4} = 1.52 \times 10^{-5}\ m^2.s^{-1}$.

Both the Chapman-Eskog theory and the Fuller correlation indicate that an increasing pressure leads to a diffusivity decrease ($D \propto \frac{1}{p}$ for pressures up to 25 atm). It is due to more collisions between gas molecules.

The Fuller empirical correlation was used to estimate binary molecular diffusivities.

G.1.2 Gas diffusion in porous media

In porous media, the Knudsen diffusion can also be at stake. It describes the interactions between the gas molecules and the porous structure: the gas molecule may collide the medium walls more often than other gas molecules. The prevalent diffusion mechanism (molecular and/or Knudsen diffusions) is determined using the Knudsen number Kn (Eq. G.5). It compares the molecules mean free path λ calculated according to the kinetic theory of gases [183] to a characteristic length of the medium microstructure (such as the pore mean diameter $d_{p,mean}$). The mean free path λ represents the average distance one gas molecule can travel before colliding another molecule (Eq. G.6).

$$Kn = \frac{\lambda}{d_{p,mean}} \quad \text{Eq. G.5}$$

$$\lambda = \frac{k_B T}{\sqrt{2}\pi\eta^2 P_g} \quad \text{Eq. G.6}$$

with k_B the Boltzmann constant [$1.3806 \times 10^{-23}\ m^2.kg.s^{-2}.K^{-1}$], T the temperature [$K$], η the particle hard-shell diameter [m] and P_g the gas pressure [Pa].

If the Knudsen number is greater than 10, Knudsen diffusion is the main mechanism: these molecules-wall collisions are dominating the transport phenomena. Under the threshold of 0.1, Knudsen diffusion is negligible against molecular diffusion. In practice, the Knudsen diffusion only occurs for gases since in the liquid state, the mean free path is much shorter (less thermal agitation).

An example of Knudsen number calculation is provided for CO_2 diffusion through the X-50 fiber in Table G.4. The particle hard-shell diameter $\eta_{CO2} = 390 \times 10^{-12} m$ is taken from Hirschfelde [238].

P_g [bar g]	λ [nm]	Kn
3	14.7	0.49
5	9.82	0.33

Table G.4 – Mean free path and Knudsen number of carbon dioxide into the porous X-50 fiber (T=16°C)

Under the process conditions, both molecular and Knudsen diffusions are at stake and must be simultaneously considered.

The Knudsen diffusivity of a gas specie A $D_{A,Kn}$ is estimated by Eq. G.7 [195, 239]. For a given compound, it is only dependent on temperature.

$$D_{A,Kn} = \frac{d_{p,mean}}{3}\sqrt{\frac{8\,RT}{\pi M_A}} \qquad \text{Eq. G.7}$$

When the Knudsen number is in the range 0.1-10, both mechanisms are considered. The effective diffusivity is then expressed by the Bosanquet's law:

$$\frac{1}{D_A^{eff}} = \frac{1}{D_{AB}} + \frac{1}{D_{A,Kn}} \qquad \text{Eq. G.8}$$

The effective diffusivity calculated in the above equation is applicable to straight and perfectly cylindrical pores. To account for the porous medium interconnections and the size distribution of the pores, one must take into account the porosity ε to tortuosity τ ratio.

$$D_A^{eff,porous} = \frac{\varepsilon}{\tau} D_A^{eff} \qquad \text{Eq. G.9}$$

G.2 Diffusion in the liquid phase

The diffusivity of a solute A in a solvent B is well below the diffusivity coefficients in the gaseous phase ($10^{-9}\ m^2.s^{-1}$ in a solvent against $\sim 10^{-5}\ m^2.s^{-1}$ for a gas phase under normal conditions). Roustan reports several correlations to estimate the diffusion coefficients of a solute in a solvent [11]. The diffusivity coefficient under infinite dilution of A, D_{AB}^0, is presented here. This infinite dilution coefficient is considered valid until the solute molar fraction reaches 5-10%. The Wilke-Chang correlation is the most common equation:

$$D_{AB}^0 = 7.4 \times 10^{-12} \frac{(\Phi M_B)^{0.5} T}{\mu_B V_A^{0.6}} \qquad \text{Eq. G.10}$$

where Φ is the solvent association factor, M_B the solvent molar mass $[g.mol^{-1}]$, μ_B the solvent viscosity $[cP]$, V_A the molar volume of the solute A at its normal boiling temperature $[cm^3.mol^{-1}]$ and T the temperature $[K]$. Wilke and Chang suggested tabulated values for various common solvents ($\Phi_{water} = 2.6$) [240]. The molar volume of the solute A may be calculated from:

$$V_A = 10^3 \frac{M_A\ [g.mol^{-1}]}{\rho_{A,liq}\ [kg.m^{-3}]} \qquad \text{Eq. G.11}$$

Several empirical correlations have also been proposed to derive diffusion coefficients in specific solvents. From a survey on available diffusivity measurements, Versteeg suggested an empirical correlation for the diffusion coefficient of CO_2 and N_2O in water [241]:

$$D_{CO_2}^{water} = 2.35 \times 10^{-6} \exp\left(-\frac{2119}{T}\right) \qquad \text{Eq. G.12}$$

Magalhães analyzed different semi-empirical expressions of the diffusivity with temperature, solvent density and viscosity as variables [242]. With appropriate correlations, the diffusivity coefficient can be predicted with solvent parameters available in the literature. For the systems considered ($CO_2 - water$ and $CH_4 - water$), the following equation has been retained:

$$\ln\left(\frac{D_{solute}^{solv}}{T}\right) = a_3 \ln(\mu_{solv}) + b_3 \qquad \text{Eq. G.13}$$

where D_{solute}^{solv} is expressed in $[cm^2.s^{-1}]$, μ_{solv} the dynamic viscosity $[cP]$ and T the temperature $[K]$. The coefficients were correlated from literature data (Table G.5).

Solvent	Solute	$T\ [K]$	$P\ [bar\ a]$	a_3	b_3
Water	CO_2	273 - 368	1	-1.00937 ± 0.02693	-16.65647 ± 0.01086
Water	CH_4	278 - 343	1	-0.89297 ± 0.06817	-16.74168 ± 0.02756

Table G.5 – Coefficients for diffusivity correlation [242]

Appendix H Membrane module data sheets

2.5 x 8 EXTRA-FLOW PRODUCT DATA SHEET

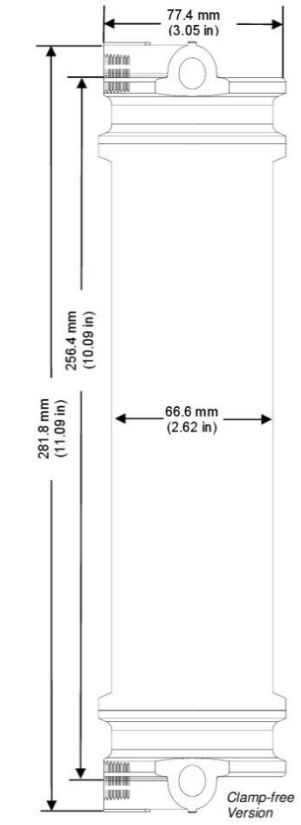

Below: End cap with ¾" or ½" Flaretek® liquid ports

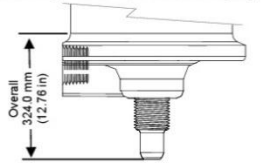

Membrane Characteristics		
Cartridge Configuration	Extra-Flow with Center Baffle	
Liquid Flow Guidelines	0.1 – 0.7 m^3/hr (0.5 – 3 gpm)	
Membrane Type	**X50 Fiber**	**X40 Fiber**
	Recommended for CO_2 removal from liquid and other gas transfer applications	Recommended for O_2 removal from liquid and other gas transfer applications
Membrane/Potting Material	Polypropylene / Polyethylene	
Typical Membrane Surface Area	1.4 m^2 (15.1 ft^2)	
Priming Volume (approximate)		
Shellside	0.40 liters (0.11 gal.)	
Lumenside	0.15 liters (0.04 gal.)	
Pressure Guidelines*		
	X50 or X40 Fiber	
Maximum Shellside LIQUID Working Temperature/ Pressure	5-40° C, 7.2 bar (41-104° F, 105 psig) 70° C, 2.1 bar (158° F, 30 psig)	
If no vacuum is used, 1.05 bar (15 psig) can be added to pressures above.		
Maximum Applied Gas Pressure	4.8 bar (70 psig)	
Max applied gas pressure is for integrity testing at ambient temperatures. Normal operating pressures are typically lower.		
Maximum Lumenside Liquid Temperature/Pressure of Semibody Contactor	5° C, 6.2 bar (41° F, 90 psig) 15-25° C, 4.8 bar (59-77° F, 70 psig) 70° C, 1.0 bar (158° F, 15 psig)	
*Pressures are based on non-dangerous liquids and gasses per the European Union Pressure Equipment Directive /97/23/EC. See Operating Guide for pressure limits in the European Union with dangerous liquids and gasses. Also, see Operating Guide for complete temp/pressure limits for housings and membrane. Note: Liquid pressure should always exceed gas pressure.		
Housing Options and Characteristics		
Material	Polypropylene	
Flange Connections		
Shellside (Liquid Inlet/Outlet)	• ¼ inch NPT female • ¾ inch Flaretek® (nut included) • ½ inch Flaretek® (nut included)	
Note: Overall length with Flaretek connections increases. See website for all housing drawings.		
Lumenside	• ¼ inch NPT female	
Seal Options		
Material	**Applications**	
K-UPW	Ultra Pure Water	
Viton	General Purpose	
K-EXT	Chemical Extraction (Clamped version only)	
Weight		
Dry	0.5 kg. (1.1 lbs.)	
Liquid full (shellside)	0.9 kg. (2 lbs.)	
Shipping weight	1.2 kg. (2.4 lbs.)	
Regulatory		
Meets RoHS threshold limits. Complies with the PED 97/23/EC and is manufactured with sound engineering practice. CFR Title 21 compliant.		

Note: Overall length with Flaretek® fittings increases. See website for all housing option drawings

2.5 x 8 EXTRA-FLOW PRODUCT DATA SHEET

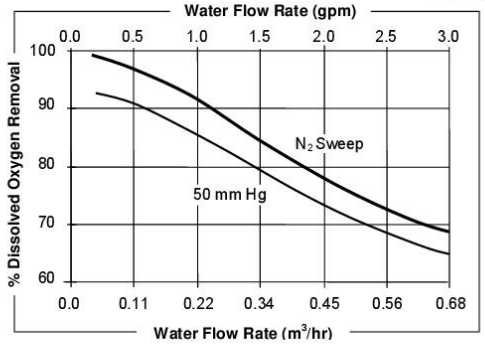

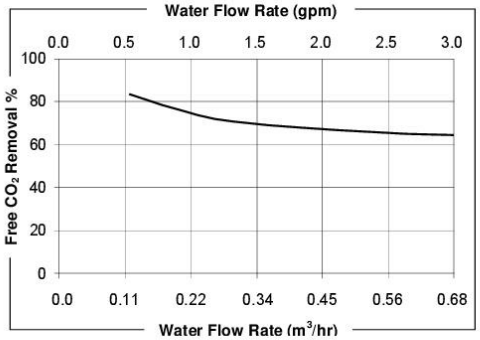

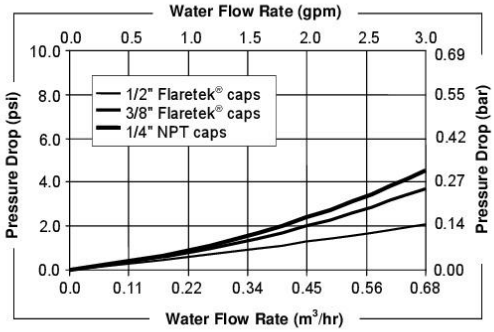

Cartridge Specifications		
Characteristics	**Test Conditions**	**Specifications**
		X50 and X40
Performance O_2 Removal	Shellside water flow: 3 gpm, 20°C (68°F) Lumenside N_2 Flow: 1.0 ft^3/min, 1.0 atm at 20°C	64% minimum
Pressure Drop, psi maximum	Shellside water flow: 3 gpm, 20°C	NPT: 6.8 psi ½ inch Flaretek®: 2.2 psi ¾ inch Flaretek®: 3.9 psi

Curves represent nominal values. Characteristics may change under different operating conditions.

Test condition O_2 Removal with X40 membrane 20°C: N_2 sweep mode, N2 sweep flow rate: 1 scfm. Vacuum mode: 50 mm Hg

Test condition CO_2 Removal with X50 membrane 25°C: Air-combo, vacuum 150 mm Hg, air sweep G/L 0.4.

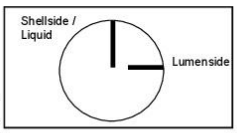

2.5 x 8 end cap ports for NPT connections

Certified System
ISO 9001
ISO 14001

Membrana - Charlotte
A Division of Celgard, LLC
13800 South Lakes Drive
Charlotte, North Carolina 28273
USA
Phone: (704) 587 8888
Fax: (704) 587 8610

Membrana GmbH
Oehder Strasse 28
42289 Wuppertal
Germany
Phone: +49 6126 2260 - 658
Phone: +49 6126 2260 - 41
Fax: +49 202 6099 - 750

Japan Office
Shinjuku Mitsui Building, 27F
1-1, Nishishinjuku 2-chome
Shinjuku-ku, Tokyo 163-0427
Japan
Phone: 81 3 5324 3361
Fax: 81 3 5324 3369

MEMBRANA
A POLYPORE COMPANY

www.liqui-cel.com

Figure H.1 – 2.5"x8" Extra-Flow module data sheet

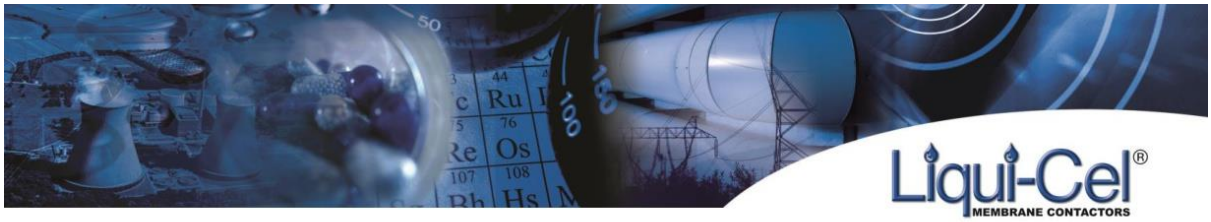

10 x 28 EXTRA-FLOW PRODUCT DATA SHEET

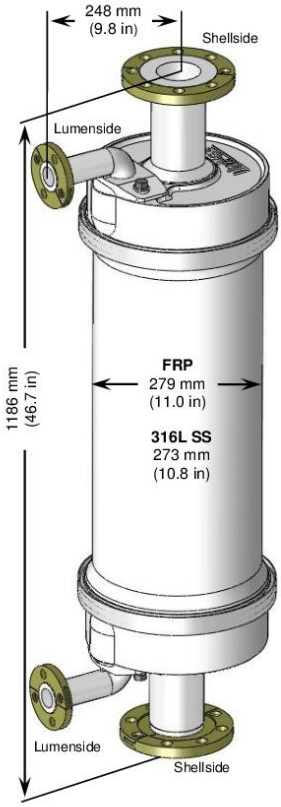

SS Contactors use a different end cap design. Sanitary connections are only available on 316 SS. Complete drawings are available on the web site, **www.liqui-cel.com.**

All dimensions are nominal values.

Membrane Characteristics

Cartridge Configuration	Extra-Flow with Center Baffle	
Liquid Flow Guidelines	10 – 57 m^3/hr (44 – 250 gpm)	
Membrane Type	**X50 Fiber**	**X40 Fiber**
	Recommended for CO_2 removal from liquid and other gas transfer applications	Recommended for O_2 removal from liquid and other gas transfer applications
Membrane/Potting Material	Polypropylene / Epoxy	
Typical Membrane Surface Area	130 m^2 (1400 ft^2)	

Priming Volume (approximate)	**FRP Housing**		**316 SS Sanitary/316 SS ANSI**	
	X50 Fiber	**X40 Fiber**	**X50 Fiber**	**X40 Fiber**
Shellside	26.1 L (6.9 gal)	26.3 L (7.0 gal)	24.3/24.9 L (6.4/6.6 gal)	24.5/25.6 L (6.5/6.8 gal)
Lumenside	10.6 L (2.8 gal)	9.5 L (2.5 gal)	7.5/10.0 L (1.9/2.6 gal)	6.4/9.5 L (1.7/2.5 gal)

Pressure Guidelines*

	X50 Fiber	**X40 Fiber**
Maximum Shellside LIQUID Working Temperature/Pressure	5-50° C, 7.2 barg (41-122° F, 105 psig) 70° C, 2.1 barg (158° F, 30 psig)	5-25° C, 9.3 barg (41-77° F, 135 psig) 50° C, 7.2 barg (77-122° F, 105 psig) 70° C, 2.1 barg (158° F, 30 psig)

If no vacuum is used, 1.0 barg (15 psig) can be added to pressures above.

	FRP	**316 SS**
Maximum Applied Gas Pressure	6.2 barg at 25° C (90 psig at 77° F)	9.0 barg at 25° C (130 psig at 77° F)

Max applied gas pressure is for integrity testing at ambient temperatures. Normal operating pressures are typically lower.

*Pressures are based on non-dangerous liquids and gases per the European Union Pressure Equipment Directive 97/23/EC. See Operating Guide for pressure limits in the European Union with dangerous liquids and gases. Also, see Operating Guide for complete temp/pressure limits for housings and membrane.
Note: Liquid pressure should always exceed gas pressure.

Housing Options and Characteristics

Material	Fiber Reinforced Plastic (FRP) with PVDF for all wetted surfaces and FRP flanges	316L SS Vessel/CF3M SS End Caps. ≤ 32RA (0.8µm SI) on schedule 10S pipe per ASTM A312.
Flange Connections		
Shellside (Liquid Inlet/Outlet)	• 3 inch class 150 raised face flange per ANSI B16.5 • 80A 10K flat face flange per JIS B2238 • 3 inch sanitary flange only available on 316L SS fine finish	
Lumenside	• 1 inch class 150 raised face flange per ANSI B16.5 • 25A 10K flat face flange per JIS B2238 • 1.5 inch sanitary flange only available on 316L SS fine finish	
Mounting Kit		

A Mounting Kit with 2 cradles and 2 straps is available and sold separately. It will hold the contactor horizontally or vertically.

Seal Options

Material	**Applications**
EPDM	All Purpose
HP1 Viton	High Purity/Electronics

Weight (approximate)

	FRP Housing	**Stainless Steel Housing**	
	ANSI/JIS	**ANSI /JIS**	**Sanitary**
Dry	33 kg (73 lbs)	76 kg (168 lbs)	81 kg (177 lbs)
Liquid Full (shellside)	57 kg (126 lbs)	99 kg (218 lbs)	107 kg (235 lbs)
Cartridge only – dry	10 kg (23 lbs)	10 kg (23 lbs)	10 kg (23 lbs)
Shipping weight (max)	44 kg (98 lbs)	133 kg (294 lbs)	138 kg (303 lbs)

Regulatory

Complies with the limits as set by RoHS Directive 2011/65/EU Annex II; recasting 2002/95/EC. Constructed of FDA CFR title 21 compliant materials for wetted parts only. For CFR title 21 compliance on the PVDF-lined FRP vessel 20,000 gallons of liquid should be flushed through the contactor prior to use.

10 x 28 EXTRA-FLOW PRODUCT DATA SHEET

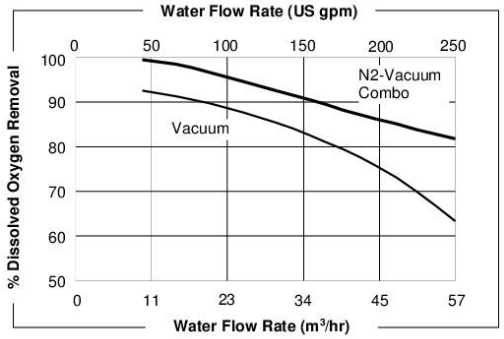

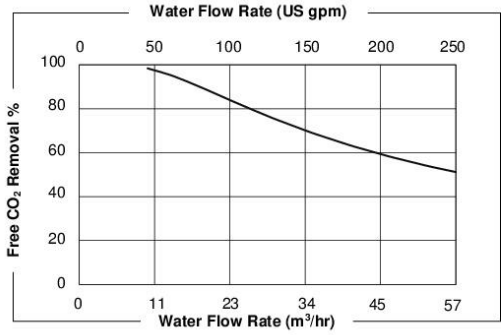

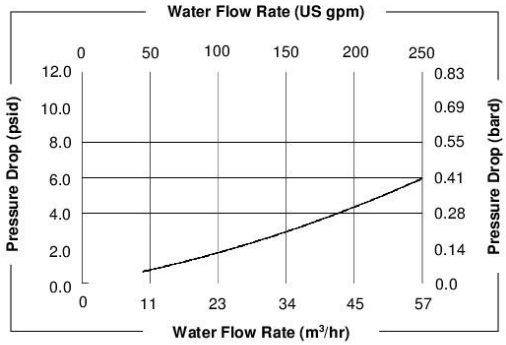

Curves represent nominal values using water. Characteristics may change under different operating conditions.

Test condition O_2 Removal with X40 membrane 20° C (68° F): N_2-vacuum combo mode, vacuum: 50 mm Hg N_2 sweep flow 0.40 Nm^3/hr (0.25 scfm).

Test condition CO_2 Removal with X50 membrane 25° C: Air-vacuum combo mode, vacuum 75 mm Hg, air sweep flow 1.6 Nm^3/hr (1 scfm).

Liqui-Cel® Membrane Contactors are tested and certified by WQA against NSF/ANSI 61.

ISO 9001

Industrial Business Group
Membranes Business Unit
13840 South Lakes Drive
Charlotte, North Carolina 28273
USA

Phone: +1 704 587 8888
Fax: +1 704 587 8610

3M Deutschland GmbH
Membranes Business Unit
Öhder Straße 28
42289 Wuppertal
Germany

Phone: +49 202 6099 - 658
Fax: +49 202 6099 - 750

3M Japan Ltd.
Membranes Business Unit
6-7-29, Kita-Shinagawa,
Shinagawa-ku, Tokyo | 141-8684
Japan

Phone: +81 3 6409 5732
Fax: +81 3 6409 5827

MEMBRANA
Now proudly part of 3M

www.liqui-cel.com

Figure H.2 – 10”x28” Extra-Flow module data sheet

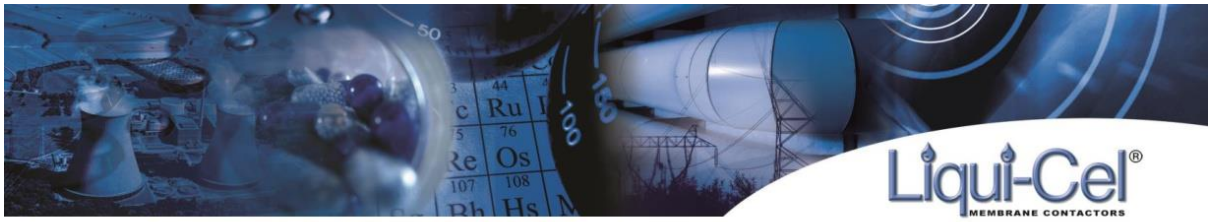

14 x 40 EXTRA-FLOW PRODUCT DATA SHEET

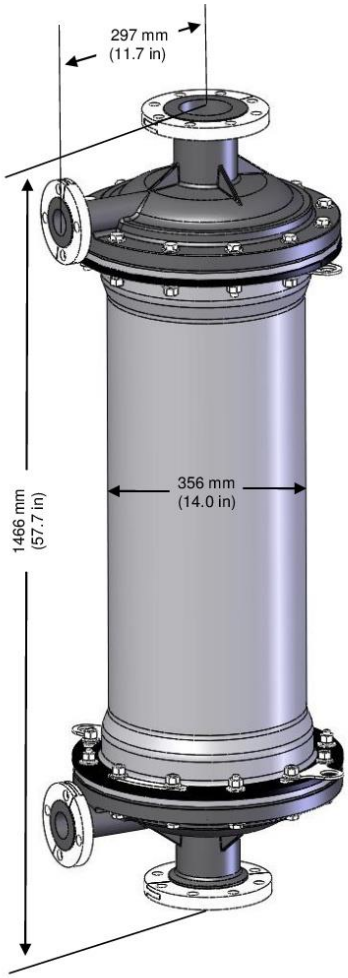

***NOTE:** All dimensions are nominal values*

Cartridge Characteristics	
Cartridge Configuration	Extra-Flow with Center Baffle
Liquid Flow Guidelines	16 – 125 m^3/hr (70 – 550 gpm)
Membrane Type	**X40 Fiber**
	Recommended for O_2 removal from liquid and other gas transfer applications
Membrane/Potting Material	Polypropylene / Epoxy
Typical Active Membrane Area	4015 ft^2 (373 m^2)
Priming Volume (approximate)	
Shellside Lumenside	53.2 L (14.1 gal) 25.9 L (6.9 gal)
Pressure Guidelines	
Maximum Shellside LIQUID Working Temperature/Pressure in vacuum or combo mode	5-25° C, 7.2 barg (41-77° F, 105 psig) 50° C, 2.1 barg (122° F, 30 psig)
If no vacuum is used, 1 barg (15 psig) can be added to pressures above.	
Maximum Applied Gas Pressure	4.1 barg at 25° C (60 psig at 77° F)
Max applied gas pressure is for integrity testing at ambient temperatures. Normal operating pressures are typically lower.	
*Pressures are based on non-dangerous liquids and gasses per the European Union Pressure Equipment Directive /97/23/EC. See Operating Guide for pressure limits in the European Union with dangerous liquids and gasses. Also, see Operating Guide for complete temp/pressure limits for housings and membrane. Note: Liquid pressure should always exceed gas pressure.	
Housing Options and Characteristics	
Housing Material	PVC Vessel with Engineered Thermoplastic End Caps
Flange Backing Rings	SMC (Sheet Molded Compound)
Flange Connections	
Shellside (Liquid Inlet/Outlet)	• 4 inch class 150 raised face flange per ANSI B16.5 • 100A at 10K raised face flange per JIS B2238
Lumenside	• 2 inch class 150 raised face flange per ANSI B16.5 • 50A at 10K flat face flange per JIS B2238
Mounting Kit	
A Mounting Kit with 2 cradles and 2 straps is available and sold separately. It will hold the contactor horizontally or vertically.	
Seal Options	
Material	**Applications**
EPDM (ANSI / NSF 61)	All Purpose
Weight (approximate)	
Dry	64 kg (141 lbs)
Liquid Full	116 kg (256 lbs)
Regulatory	
Complies with the limits as set by RoHS Directive 2011/65/EU Annex II; recasting 2002/95/EC.	

3M

14 x 40 EXTRA-FLOW PRODUCT DATA SHEET

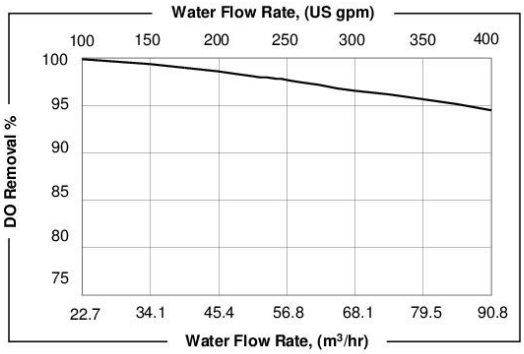

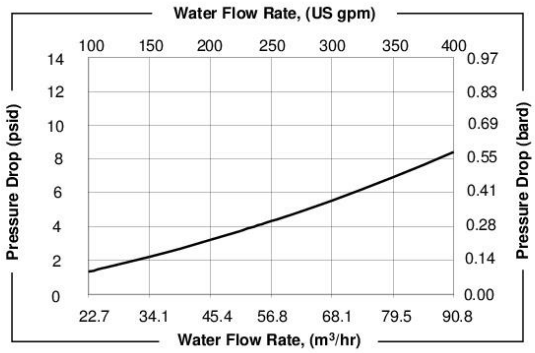

Curves represent nominal values, generated using water at 20°C.

Test condition O_2 Removal: X40 membrane, N_2-vacuum combo mode, Vacuum: 50 torr, N_2: 0.8 scfm.

Characteristics may change under different operating conditions.

Technical Information: The technical information, recommendations and other statements contained in this document are based upon tests or experience that 3M believes are reliable, but the accuracy or completeness of such information is not guaranteed.

Product Use: **Many factors beyond 3M's control and uniquely within user's knowledge and control can affect the use and performance of a 3M** product in a particular application. Given the variety of factors that can affect the use and performance of a 3M product, user is solely responsible for evaluating the 3M **product and determining whether it is fit for a particular purpose and suitable for user's method of application.**

Warranty, Limited Remedy, and Disclaimer: Unless an additional warranty is specifically stated on the applicable 3M product packaging or product literature, 3M warrants that each 3M product meets the applicable 3M product specification at the time 3M ships the product. 3M MAKES NO OTHER WARRANTIES OR CONDITIONS, EXPRESS OR IMPLIED, INCLUDING, BUT NOT LIMITED TO, ANY IMPLIED WARRANTY OR CONDITION OF MERCHANTABILITY OR FITNESS FOR A PARTICULAR PURPOSE OR ANY IMPLIED WARRANTY OR CONDITION ARISING OUT OF A COURSE OF DEALING, CUSTOM OR USAGE OF TRADE. If the 3M product does not conform **to this warranty, then the sole and exclusive remedy is, at 3M's option, replacement of the 3M product or refund** of the purchase price.

Limitation of Liability: Except where prohibited by law, 3M will not be liable for any loss or damage arising from the 3M product, whether direct, indirect, special, incidental or consequential, regardless of the legal theory asserted, including warranty, contract, negligence or strict liability.

Liqui-Cel® Membrane Contactors are tested and certified by WQA against NSF/ANSI 61.

Certified System ISO 9001

Industrial Business Group
Membranes Business Unit
13840 South Lakes Drive
Charlotte, North Carolina 28273
USA

Phone: +1 704 587 8888
Fax: +1 704 587 8610

3M Deutschland GmbH
Membranes Business Unit
Öhder Straße 28
42289 Wuppertal
Germany

Phone: +49 202 6099 - 658
Fax: +49 202 6099 - 750

3M Japan Ltd.
Membranes Business Unit
6-7-29, Kita-Shinagawa,
Shinagawa-ku, Tokyo | 141-8684
Japan

Phone: +81 3 6409 5732
Fax: +81 3 6409 5827

MEMBRANA
Now proudly part of 3M

www.liqui-cel.com

Figure H.3 – 14”x40” Extra-Flow module data sheet

Appendix I Technical description of the pilot process

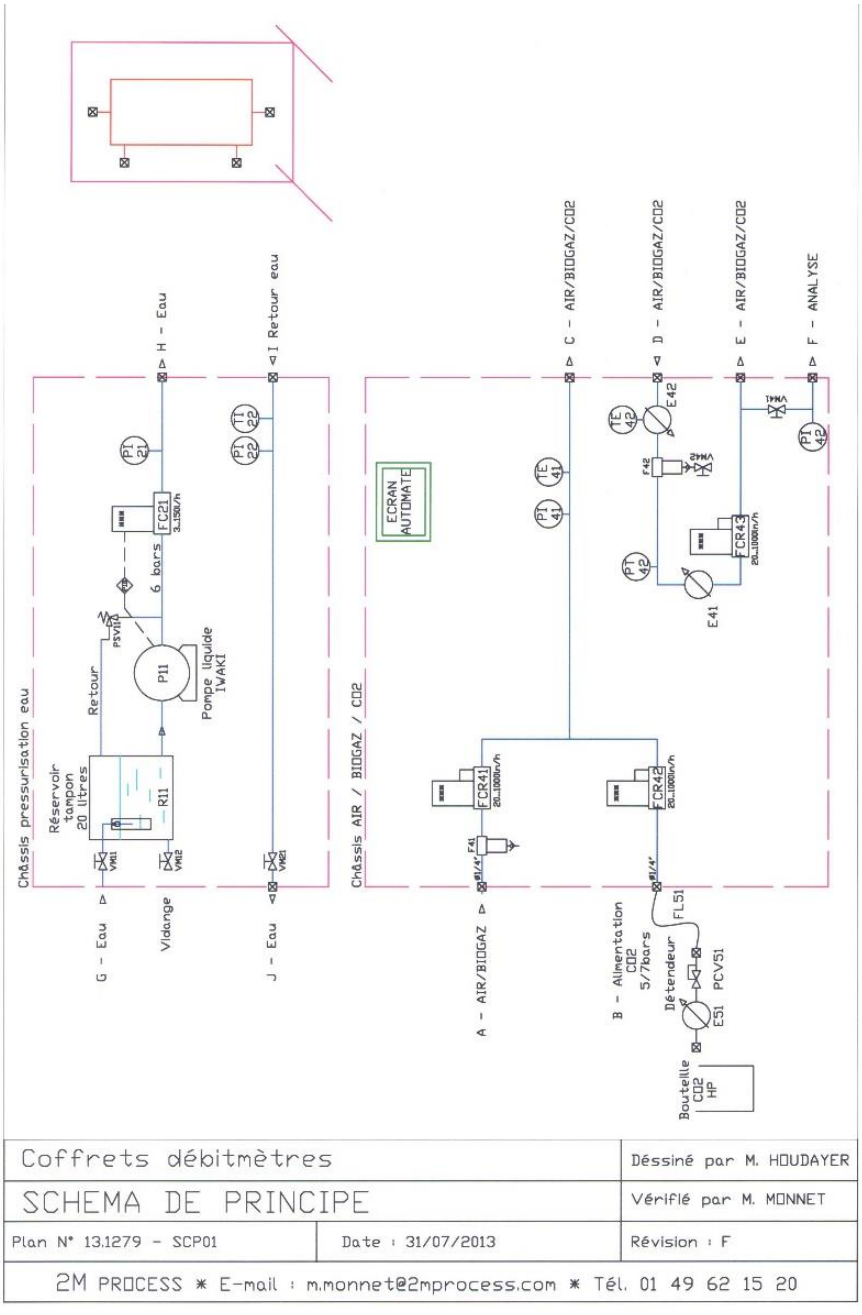

Figure I.1 – Pilot process flow diagram

FL51	1	Flexible en PTFE	SS-4BHT-120	Swagelok	T 1/4"
PCV51	1	Détendeur	SAM - type C - ZA0312	Cahouet	Type C
E51	1	Réchauffeur électrique	500W - type C - ZH2101	Cahouet	Type C
E42	1	Echangeur effet Peltier	DA-075-24-02-00-00	Alcyon	
E41	1	Cable auto régulant	Gamme Flextrace	Flexelec	
PT42	1	Transmetteur Pression	PBSN12B79RA144224	Baumer	G 1/4" M
TE42	1	Sonde PT100	Diamètre 3 lg 150	Pyro-Systèmes	
TE41	1	Sonde PT100	Diamètre 3 lg 150	Pyro-Systèmes	
PI42	1	Manomètre -1/3 bars	MEX3D20B79/-1+3B	Baumer	G 1/4" M
PI41	1	Manomètre -1/9 bars	MEX3D20B79/-1+9B	Baumer	G 1/4" M
FCR43	1	Régulateur débit massique	F-202EV-MGD-22-K	Bronkhorst	DB 1/4"
FCR42	1	Régulateur débit massique	T22-MGD-22-K	Bronkhorst	DB 1/4"
FCR41	1	Régulateur débit massique	T22-MGD-22-K	Bronkhorst	DB 1/4"
F42	1	Filtre coalesceur	AA213.271.5CK	Power Uti.	NPT 1/4"
F41	1	Filtre coalesceur	AA213.271.5CK	Power Uti.	NPT 1/4"
VM42	1	Vanne manuelle BS	SS-4P4T	Swagelok	DB 1/4"
VM41	1	Vanne manuelle laminage	SS-1RS4	Swagelok	DB 1/4"
TI22	1	Thermomètre 0/60°c	TBI80.211.144.11T	Baumer	T 6
PI22	1	Manomètre -1/9 bars	MEX3D20B79/-1+9B	Baumer	G 1/4" M
PI21	1	Manomètre -1/9 bars	MEX3D20B79/-1+9B	Baumer	G 1/4" M
FC21	1	Débitmètre Vortex	FLM2S-1	Bronkhorst	G 3/8" M
VM21	1	Vanne manuelle laminage	SS-1RS4	Swagelok	DB 1/4"
R11	1	Capacité 20 litres	36M2	Manutan	
P11	1	Pompe à engrenages	MDGM4S6B	Iwaki	NPT 1/4"
PSV11	1	Soupape tarage 5 bars	SS-RL3S4	Swagelok	DB 1/4"
VM12	1	Vanne manuelle BS	486340	RS	G 3/8" F
VM11	1	Vanne manuelle BS	486340	RS	G 3/8" F
Rep.	Qté	Désignation	Référence	Fournisseur	Observation
CHASSIS DEBITMETRES					
NOMENCLATURE				Document: 13.1279-NOM01	
Dés.	B. HOUDAYER		Date : 31/07/2013	Folio 1	Rév. A
2M PROCESS - E-mail : m.monnet@2mprocess.com - Tél. 01 49 62 15 20					

Table I.1 – Nomenclature of the pilot process equipments

Appendix J Experimental process configurations

The pilot process was progressively developed to reach the final experimental set-up presented in Figure J.1. In its reference configuration, it comprises 5 distinct parts: one chassis for gas regulation, the gas composition analytical system, two chassis for liquid regulation and the gas-liquid absorption/desorption units with two membrane contactors.

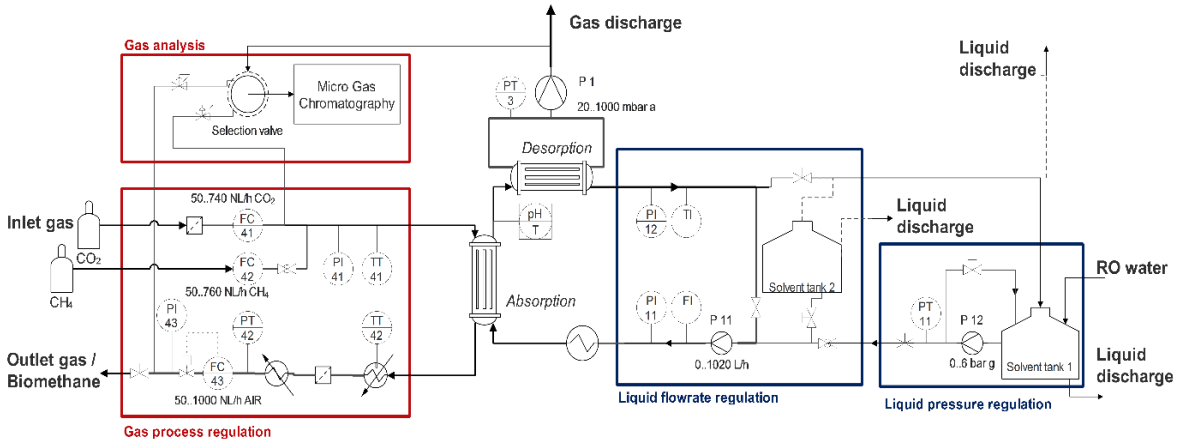

Figure J.1 – Process flow diagram for the reference process architecture

Several process architectures have been investigated in a closed-loop or in an open-loop configuration. The reference case in Figure 2.10 presents an equivalent exchange area 1:1 in the absorption and desorption steps (one membrane module each). Simplified process flow diagrams of other investigated architectures are displayed in Table J.1. Only 2.5”x8” membrane modules were used in the experimental section. Thus, the notation x:y is introduced to describe the reference architecture equipped with x and y membrane modules in series respectively at the absorption and desorption steps. A similar notation x:y:z is adopted to describe the ratio of membrane modules between the absorption, partial recycling and final degassing step respectively. The abbreviation OL or CL stands for open-loop and closed-loop configurations.

	Open-loop	Closed-loop
1:1 Ref.	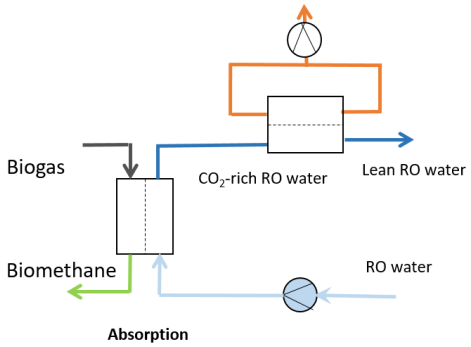	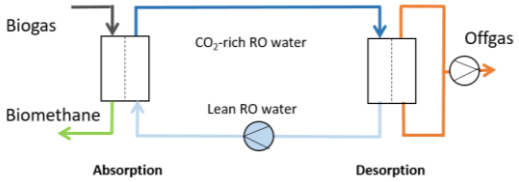
2:1	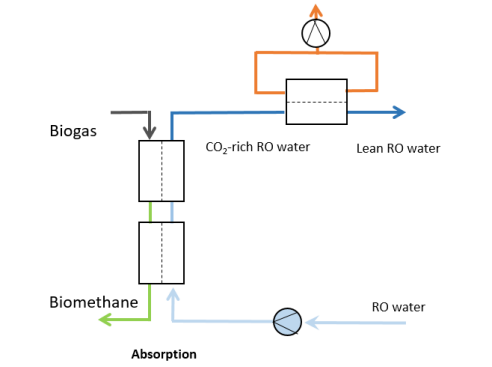	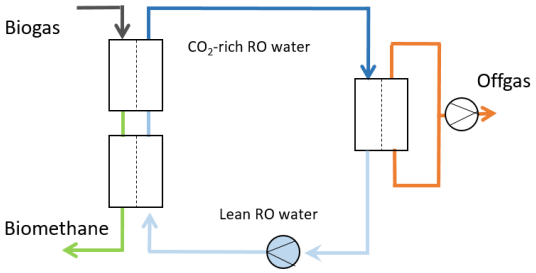
1:1:1	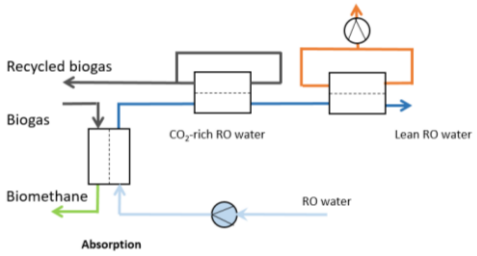	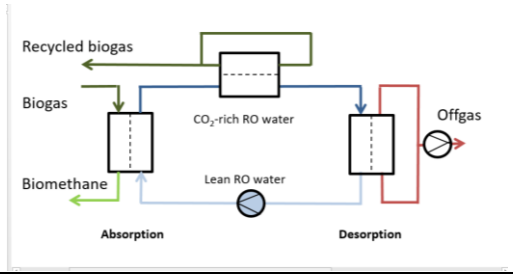
2:1:1	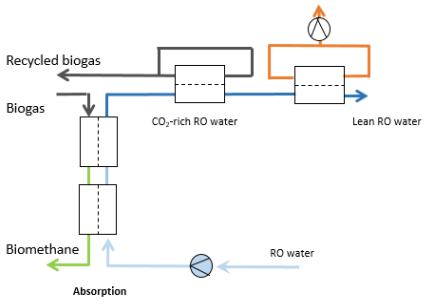	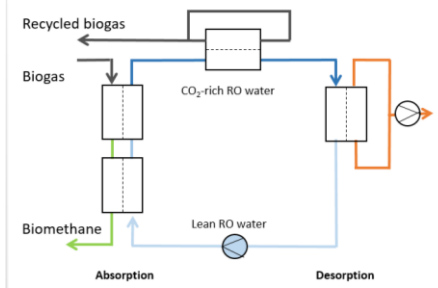

Table J.1 – Simplified process flow diagrams

Appendix K Methods developed for Micro Gas Chromatography

An analytical method was developed and optimized for the purpose of this study. For a CO_2/CH_4 mixture, the analytical conditions listed in Table K.1 lead to a minimal analysis time of 110 s.

Module	Backflush, RTS	Backflush	
Entrée chauffée (°C)	100	Durée balayage (s)	30
Chauffage injecteur (°C)	100 °C	100 °C	
Chauffage colonne (°C)	99 °C	60 °C	
Durée injection (ms)	40 ms	40 ms	
Temps backflush (s)	4.00 sec	16.00 sec	
Durée analyse (s)	80 sec	80 sec	
Pression colonne (psi)	He 29 psi	29 psi	
Temps initial (sec)			
Gradient (psi/min)			
Pression finale (psi)			
Filament	ON	ON	
Sensibilité	Auto	Auto	
Contrôle Temp TCD	ON	ON	

Table K.1 – Analytical conditions of the micro GC for a CO_2/CH_4 mixture

Left: 10m Molsieve 5Å – Right: 10m PoraPLOT U

The sweeping time is set to 30s to ensure the analytical line is fully flushed by the sample to be analysed. The backflush time is optimized on both columns to prevent unwanted molecules to enter the analytical column. For instance CO_2 molecules would clog the Molsieve 5Å column due to their larger size.

Once the analytical conditions were optimized, the retention times of each compound and their relative windows are set (Table K.2). Higher pressures or higher temperatures in the analytical column would diminish the retention time of a compound.

Compound	Column	Retention time $[s]$	Relative window [%]
O_2	*10m Molsieve 5Å*	28.30	8
N_2	*10m Molsieve 5Å*	37.26	10
CH_4	*10m Molsieve 5Å*	50.49	17
CO_2	*10m PoraPLOT U*	36.99	10

Table K.2 – Table of components in micro GC method

In the meantime, integration parameters are optimized to automatically detect the peaks present in the chromatogram (Table K.3 and Table K.4). These parameters were suitable to detect a large range of CO_2/CH_4 concentrations from gas grid quality biomethane to CO_2-rich offgas. The slope sensitivity is the parameter that determines the peak boundaries while the peak absolute width is an indication on its spread.

Time $[s]$	Parameter	Value	Unit
0.0	Slope sensitivity	60.00	$[\mu V.s^{-1}]$
0.0	Peak absolute width	1.00	$[s]$
44.0	Peak absolute width	6.00	$[s]$
46.0	Slope sensitivity	200.00	$[\mu V.s^{-1}]$

Table K.3 – Chromatogram integration parameters: 10m Molsieve 5Å

Time $[s]$	Parameter	Value	Unit
0.0	Slope sensitivity	120.00	$[\mu V.s^{-1}]$
0.0	Peak absolute width	0.80	$[s]$
0.0	Peak detection	Off	
30.0	Peak detection	On	

Table K.4 – Chromatogram integration parameters: 10m PoraPLOT U

Once both the analytical conditions and integration parameters are set, the method is calibrated using standard gases. Four standard gases are available (Table K.5). The calibration range had to cover a large range of concentrations for both CO_2 and CH_4 $(0 - 100\ \%)$.

Standard gas	CH_4	CO_2	O_2	N_2
1	60.00	40.00		
2	99.95			
3		99.95		
4		5.00	20.00	75.00

Table K.5 – Standard gas mixtures for micro GC calibration

Methane and carbon dioxide have respectively two and three different standard concentrations. The resulting calibration curve is not fully linear for both components (Figure K.1 and Figure K.2). Methane curvature is concave while carbon dioxide curvature is convex.

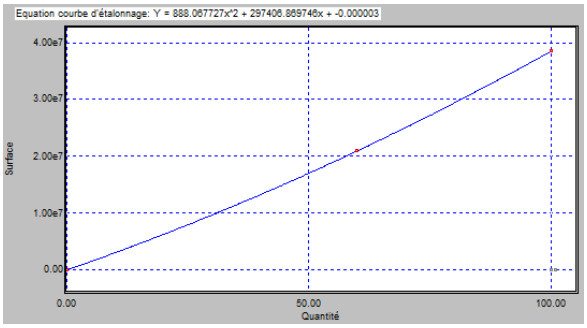

Figure K.1 – Methane calibration curve

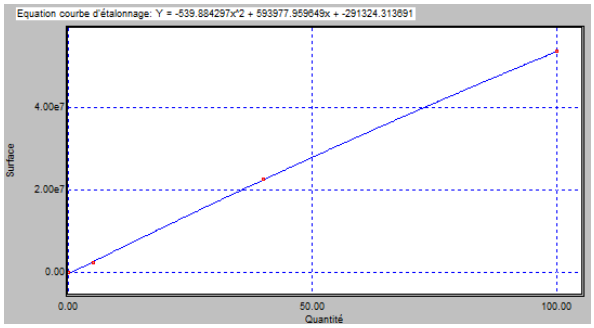

Figure K.2 – Carbon dioxide calibration curve

Appendix L Rotameters: scale conversion

The speed of the fluid is derived from the dynamic equilibrium between the buoyant force, the upward force and the float weight. Similarly to mass thermal flowmeters, the scale of the rotameter is calibrated for a specific gas under given pressure and temperature conditions. For a different gas mixture and/or under process operating conditions, a correction factor must be applied.

The correction factor F to be applied to a rotameter scale calibrated with a gas named *scale* under the conditions P_{scale}/T_{scale} is derived from a balance of the forces applying to the float. It depends on the ratio of the real gas and scale gas densities (ρ_{real} and ρ_{scale} respectively):

$$F = \left(\frac{\rho_{scale}}{\rho_{real}}\right)^{0.5} = \left(\frac{M_{scale}}{M_{real}}\frac{P_{scale}}{P_{real}}\frac{T_{real}}{T_{scale}}\right)^{0.5} \quad \text{Eq. L.1}$$

$$Q^{g}_{real} = F \times Q^{g}_{scale} \quad \text{Eq. L.2}$$

The real gas flowrate Q^{g}_{real} is expressed under the measurement operating conditions P_{real}/T_{real}. The following transformation applies to express it under standard conditions (STP) $P^* = 1\ atm\ a / T^* = 273.15K$:

$$Q^{g}_{STP}\ [Nm^3.s^{-1}] = Q^{g}_{(T_{real},P_{real})}\frac{P_{real}}{P^*}\frac{T^*}{T_{real}}\ [m^3.s^{-1}] \quad \text{Eq. L.3}$$

Appendix M Energy consumption

Energy consumption is calculated on the biogas upgrading process considering three steps:

- Inlet biogas compression to process absorption pressure P_g;
- Vacuum pump compression work on the degassed offgas flow;
- Work of the liquid circulation pump to compensate the pressure losses ΔP_l in the liquid closed-loop.

In the case of the methane recycling loop architecture, the recompression of the recycled flow from atmospheric pressure to absorption pressure is also considered.

The isentropic approach is preferred over the polytropic approach because it compares the energy conversion of the real case to the ideal isentropic transformation from an overall point of view. A polytropic transformation is a succession of isentropic infinitesimal transformations: it is a local description which accounts for the heat dissipation. For compressors, they are characterized by Eq. M.1.

$$\zeta_{is} < \zeta_{poly} < 1 \qquad \text{Eq. M.1}$$

For the sake of comprehension, the process power calculated is divided by the raw biogas inlet flow. The unit $kW.Nm_{biogas}^{-3}$ is a reference point to compare the energy consumption of biogas upgrading processes (see paragraph 1.3.2)

M.1 Compression work

The calculations regarding both the initial biogas compression and the compression in the vacuum pump are similar. The isentropic ratio expressed in Eq. M.2 is the ratio of enthalpy variations between the isentropic and real transformations (Figure M.1).

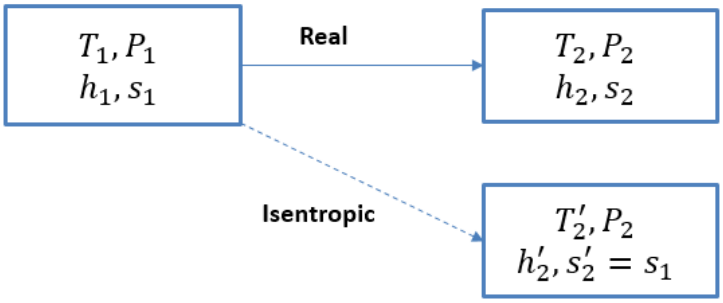

Figure M.1 – Real and isentropic transformations

$$\zeta_{is} \overset{\text{def}}{=} \frac{h_2' - h_1}{h_2 - h_1} = \frac{T_2' - T_1}{T_2 - T_1} \quad \text{Eq. M.2}$$

The isentropic transformation of an ideal gas follows the Laplace law (Eq. M.3 and Eq. M.4).

$$PV^{\gamma} = b_1 \quad \text{Eq. M.3}$$

$$T^{\gamma} P^{1-\gamma} = b_2 \quad \text{Eq. M.4}$$

where γ is the Laplace coefficient of the considered gas.

Thus, the temperature T_2' is derived from initial temperature and compression factor Γ.

$$T_2' = T_1 \Gamma^{\frac{\gamma-1}{\gamma}} \quad \text{Eq. M.5}$$

The compression work is then calculated in the case of the isentropic transformation (Eq. M.6). Assuming the isentropic efficiency, the real mechanical work transferred is derived from Eq. M.2.

$$\Delta h_{1\to 2} = h_2 - h_1 = C_p T_1 \left(\Gamma^{\frac{\gamma-1}{\gamma}} - 1 \right) \quad \text{Eq. M.6}$$

where C_p is the molar specific heat capacity.

Electrical and mechanical efficiencies of the equipment are considered on top of isentropic efficiency. Electrical efficiency is rising with the mechanical power of the compressor (generally in the range 40-95 %): it is assumed to 75 %. Mechanical efficiency is generally around 90 %. The isentropic efficiency is set to 75 % for this calculation. As a result, electrical energy is transferred to the compressed gas flow with a 50.6 % overall efficiency.

The Fluidat database is used to calculate the properties of the gases under different temperature and pressure conditions (Table M.1). The γ coefficient is stable under moderate pressure conditions for both CO_2 and CH_4.

Property	Unit	Air [0 $bar\ g$]	CO_2 [0 $bar\ g$]	CO_2 [5 $bar\ g$]	CH_4 [0 $bar\ g$]	CH_4 [5 $bar\ g$]
c_p	$J.K^{-1}.kg^{-1}$	1006	846.9	889.3	2204	2236
c_v	$J.K^{-1}.kg^{-1}$	717.8	652.9	667.4	1681	1687
$\gamma = \frac{c_p}{c_v}$	–	1.40	1.30	1.33	1.31	1.33
M	$g.mol^{-1}$	28.96	44.01		16.04	
ρ	$kg.m^{-3}$	1.189	1.815	11.20	0.6594	3.992
ν	$10^{-5}\ m^2.s^{-1}$	1.525	0.7979	0.1299	1.662	0.2753

Table M.1 – Properties of carbon dioxide, methane and air under moderate pressures and 20°C - Data from Fluidat database

The temperatures of the different gas flows are assumed to be the same as in industrial conditions. The raw biogas enters the initial compressor after its pretreatment: in case of a mesophilic digester, it may have cooled down from 40 to 30 °C. Before flowing through the vacuum pump, the offgas flow is supposed to be at the liquid temperature (20 °C in the calculations).

M.2 Liquid circulation work

The energy required to circulate the liquid in a closed-loop is induced by the pressure loss along the process. The energy W_{liq} $\left[kWh.Nm^{-3}_{biogas}\right]$ to be transmitted to the fluid per cubic meter of inlet biogas is calculated by:

$$W_{liq} = \frac{Q_l}{Q_g}\Delta P_l \times 10^{-3} = \frac{Q_l}{Q_g}\gamma_{liq}h_{liq} \times 10^{-3} = \frac{Q_l}{Q_g}\rho_{liq}gh_{liq} \times 10^{-3} \quad \text{Eq. M.7}$$

where $\frac{Q_l}{Q_g}$ is the liquid-to-gas ratio $[L.NL^{-1}]$, ΔP_l is the pressure loss $[Pa]$, γ_{liq} the liquid specific weight ($\gamma_{water}(20°C) = 9.79\ kN/m^3$) $[N.m^{-3}]$, h_{liq} is the equivalent liquid column height $[m]$ and ρ_{liq} the liquid density $[kg.m^{-3}]$. A one meter water column height is equivalent to a pressure of 98.1 $mbar$.

As for the compression work, the transmitted energy is subject to additional losses: mechanical and electrical efficiencies are respectively set to 75 %.

The maximum pressure loss on the pilot process ($\Delta P_l = 0.3\ bar$) was recorded during experiments combining three membrane contactors. The membrane contactor manufacturer also provides the pressure loss curves on each module data sheet. Experimental measurements were in excellent agreement.

Appendix N Determination of solvent loading rates

In this work, we have introduced the loading rate ψ of a gas component i. This indicator is defined by:

$$\psi_i = \frac{x_i}{x_i^{sat}(\mathrm{P}_i, \mathrm{T})} \qquad \text{Eq. N.1}$$

where x_i is the dissolved gas content (molar fraction) in the liquid and x_i^{sat} the same parameter when the liquid is saturated. x_i^{sat} is calculated from thermodynamical data and operating conditions P_i, T.

The loading rate ψ_i is an indicator of the solvent saturation regarding the component i. The loading rate is equal to 100 % if the absorbent is at equilibrium with the partial pressure P_i.

In a counter-current absorption process, the absorbent at the outlet is at equilibrium with the inlet gas only if the contacting equipment is of infinite dimension (ideal equipment). Therefore, the partial pressure P_i considered for calculating the loading rate is the partial pressure at the gas inlet. The loading rate indicates the fraction of the solvent absorption capacity which is actually used; it is then an indicator of the gap to equilibrium at the gas inlet.

Two methods were developed to calculate solvent loading rates. The first method is based on a direct analytical measurement using an additional set-up in which the gas liquid-equilibrium is assumed. The second method is derived from mass balance calculations.

N.1 Method 1: Direct analytical measurement

The liquid flow, with a dissolved gas content to be analysed, flows through an additional membrane contactor in the shellside (Figure N.1). The gas lumenside is a closed atmosphere: it is depressurized and flushed 3 times to remove the initial atmosphere before an analytical measurement. The gas composition and pressure are progressively reaching the equilibrium conditions with the dissolved gas content of the liquid phase. The partial pressure of each gas component is derived both from the manometer indication and from the gas analysis. Application of Henry's law provides an estimation of the liquid molar fraction x_i.

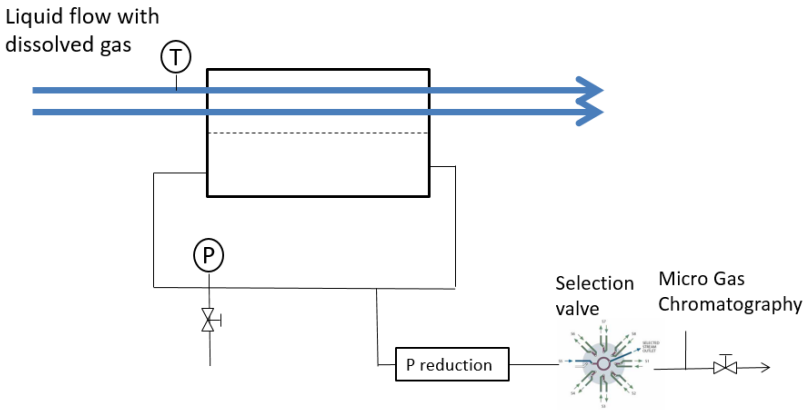

Figure N.1 – Dissolved gas analytical module set-up

This apparatus can be connected at any position on the liquid closed-loop: before the absorption step to assess the loading rate of the inlet absorbent or after the absorption step to evaluate the solvent absorption capacity fraction used. Though, due to the micro GC specifications, the gas must reach an equilibrium pressure above atmospheric pressure. The device was then mainly used after the absorption step.

N.2 Method 2: Outlet/Inlet mass balance

If a counter-current absorption unit is considered, the dissolved gas content at the outlet ψ_i^{out} is the sum of the dissolvent gas content at the inlet ψ_i^{in} and the gas content variation that was transferred from the gas to the liquid phase within the unit $\Delta\psi_i^{transfer}$ (Eq. N.2).

$$\psi_i^{out} = \psi_i^{in} + \Delta\psi_i^{transfer} \quad \text{Eq. N.2}$$

The mass balance method can only account for the transfer term. Therefore, this method can only be used assuming that the inlet liquid is free of any dissolved gas ($\psi_i^{in} = 0$ %).

The term $\Delta\psi_i^{transfer}$ is calculated from $x_i^{transfer}$, the liquid molar fraction of component i relative to the mass transfer through the membrane. It is calculated from the ratio of the absorbed flow against the total liquid flow:

$$x_i^{transfer} = \frac{Q_i^{abs}}{Q_l} \quad \text{Eq. N.3}$$

The gas flow absorbed through the membrane Q_i^{abs} is calculated by difference between the inlet and outlet flows, Q_{tot}^{in} and Q_{tot}^{out} being the total gas inlet and outlet flowrates:

$$Q_i^{abs} = Q_{tot}^{in} y_i^{in} - Q_{tot}^{out} y_i^{out} \quad \text{Eq. N.4}$$

Therefore, this method measures the solvent absorption capacity used during the absorption step, but does not consider the dissolved gas content at the contactor liquid inlet. When the inlet absorbing solvent is free of dissolved gas, the mass balance method and the direct measurement method performed after the absorption step are expected to provide the same results.

Appendix O Design of Experiments

The Design of Experiments (DoE) methodology was adopted to compare the relative influence of the process parameters and their interactions in a large range of operating conditions. The reference architecture was used. Five parameters were selected and three levels were defined to investigate the quadratic influences and interactions (Table O.1). The temperature of the absorbent was measured but not regulated ($T_l = 25°C \pm 3°C$). The influence of liquid pressure on membrane wetting was specifically studied in a different campaign.

Level	$\boldsymbol{Q_l}$ $[\boldsymbol{L.h^{-1}}]$	$\boldsymbol{Q_g}$ $[\boldsymbol{NL.h^{-1}}]$	$\boldsymbol{P_g}$ $[\boldsymbol{bar\ g}]$	$\boldsymbol{P_{vac}}$ $[\boldsymbol{mbar\ a}]$	$\boldsymbol{y_{CH_4}^{in}}$ $[\%\boldsymbol{vol.}]$
Parameter	P1	P4	P3	P2	P5
-β= -2.378	60	205.0	1.10	100.0	30.0
-1	103.5	355.7	2.2	157.9	47.4
0	135	465.0	3.0	200.0	60.0
+1	166.5	574.3	3.8	242.1	72.6
+β= +2.378	210	725.0	4.90	300.0	90.0

Table O.1 – Definition of parameters' levels for the Design of Experiments

A central composite design was used to reduce the number of experiments (243 tests initially). The complete table with the parameters values and the obtained response is presented in Table O.2.The central composite design is divided into 3 matrices:

- A factorial design with 2 levels (-1 and +1): 32 tests;
- A series of tests at the center of the domain: N_0 tests;
- A series of tests on the axis of the domain (-β and +β for each parameter): 10 tests.

The value of β is chosen from tables (Table 3.3) to satisfy the optimality criteria: rotability, orthogonality and uniform precision.

A design is **rotatable** if the variance of the predicted response at any point x depends only on the distance of x from the design center point. It means that the error of the response is only dependent on the distance from the center point (and not on the direction).

An experimental design is **orthogonal** if the effects of any factor balance out (sum to zero) across the effects of the other factors. This criteria is verified when the variance-covariance matrix $(X^tX)^{-1}$ is diagonal. The diagonal terms are representative of the variance of the model coefficients $Var(b_i) = \alpha_{i,i}\sigma^2$.

An experimental design satisfies **uniform precision** when the variance is constant over the domain. This criterion implies the rotatability of the design.

The criteria of orthogonality and uniform precision cannot be satisfied at the same time. Therefore, the design is qualified as quasi-orthogonal instead of orthogonal.

Ref.	$Q_l - P1$ $[L.h^{-1}]$	$P_{vac} - P2$ $[mbar\ a]$	$P_g - P3$ $[bar\ g]$	$Q_g^{in} - P4$ $[NL.h^{-1}]$	$y_{CH_4}^{in} - P5$ $[\%v/v]$	$y_{CH_4}^{out} - R$ $[\%v/v]$
C	135.0	200	3.00	465	60.0	69.3
1	103.5	158	2.20	356	47.4	56.6
2	166.5	158	2.20	356	47.4	60.2
3	103.5	242	2.20	356	47.4	56.8
4	166.5	242	2.20	356	47.4	59.8
5	103.5	158	3.80	356	47.4	60.0
6	166.5	158	3.80	356	47.4	68.1
7	103.5	242	3.80	356	47.4	65.2
8	166.5	242	3.80	356	47.4	70.3
9	103.5	158	2.20	574	47.4	52.9
10	166.5	158	2.20	574	47.4	59.9
11	103.5	242	2.20	574	47.4	52.8
12	166.5	242	2.20	574	47.4	55.2
13	103.5	158	3.80	574	47.4	55.8
14	166.5	158	3.80	574	47.4	60.5
15	103.5	242	3.80	574	47.4	57.5
16	166.5	242	3.80	574	47.4	61.3
17	103.5	158	2.20	356	72.6	77.9
18	166.5	158	2.20	356	72.6	78.7
19	103.5	242	2.20	356	72.6	75.4
20	166.5	242	2.20	356	72.6	76.9
21	103.5	158	3.80	356	72.6	78.8
22	166.5	158	3.80	356	72.6	81.0
23	103.5	242	3.80	356	72.6	78.3
24	166.5	242	3.80	356	72.6	79.8
25	103.5	158	2.20	574	72.6	74.8
26	166.5	158	2.20	574	72.6	75.9
27	103.5	242	2.20	574	72.6	74.4
28	166.5	242	2.20	574	72.6	75.4

Ref.	$Q_l - P1$ $[L.h^{-1}]$	$P_{vac} - P2$ $[mbar\ a]$	$P_g - P3$ $[bar\ g]$	$Q_g^{in} - P4$ $[NL.h^{-1}]$	$y_{CH_4}^{in} - P5$ $[\%v/v]$	$y_{CH_4}^{out} - R$ $[\%v/v]$
29	103.5	158	3.80	574	72.6	72.7
30	166.5	158	3.80	574	72.6	72.8
31	103.5	242	3.80	574	72.6	72.7
32	166.5	242	3.80	574	72.6	72.7
33	210.0	200	3.00	465	60.0	71.6
34	135.0	300	3.00	465	60.0	69.0
35	135.0	200	4.90	465	60.0	76.2
36	135.0	200	3.00	725	60.0	66.9
37	135.0	200	3.00	465	90.0	92.6
38	60.0	200	3.00	465	60.0	66.0
39	135.0	100	3.00	465	60.0	69.1
40	135.0	200	1.10	465	60.0	65.3
41	135.0	200	3.00	205	60.0	77.5
42	135.0	200	3.00	465	30.0	39.9

Table O.2 – Table of tests for the DoE using a central composite design

Appendix P Anaerobic digestion unit at the farm GAEC Chateau d'Etrépigny

The results initially obtained with synthetic biogas in the laboratory had to be confirmed on-site with farm raw biogas. The 2-week experimental campaign took place at a farm from the French Ardennes (GAEC Chateau d'Etrépigny) in December 2015.

This farm is a typical example of the average livestock farm in France. It produces organic milk from 80 dairy cows. The mesophilic anaerobic digestion unit under operation since 2008 was designed by Aria Energie (named Aria-Innovent since then). The unit (Figure P.1) is equipped with one mixing unit, two digesters in series (100 m^3 and 700 m^3) and one post-digester (700 m^3).

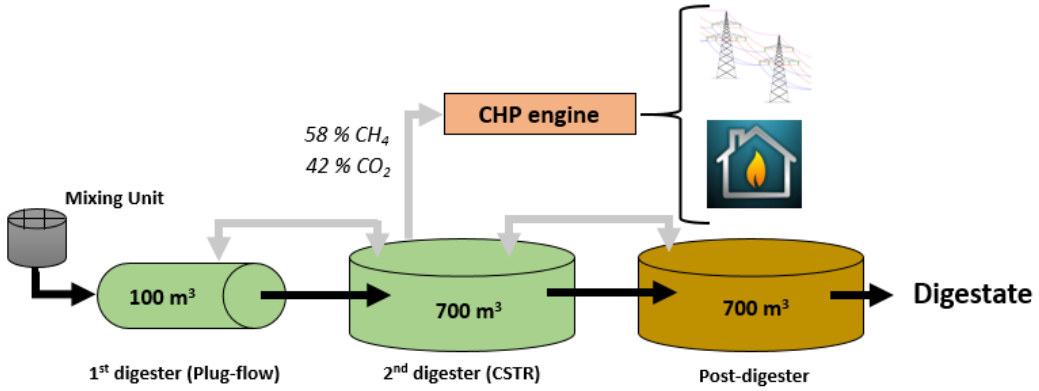

Figure P.1 – Anaerobic digestion unit at GAEC Chateau d'Etrépigny

The digester substrate is mainly composed of cow slurry (about 75 %). The cow slurry is scraped from the stable twice a day. Then, agroindustrial waste (beet pulp, brewing dregs…), crop residues or grass silage are added occasionally to enhance the gas production. They are added and mixed together with the slurry in the mixing unit.

The biogas is collected from the second digester. Its atmosphere is connected to both the first digester and the post-digester. Biogas is cooled down in the ground and condensates are collected in a water trap. It then enters the cogeneration unit (60 kW) presented in Figure P.2. The electricity production goes to the grid while the heat production is used to heat the digester and four houses of the neighbourhood thanks to a heat network (about 100m long).

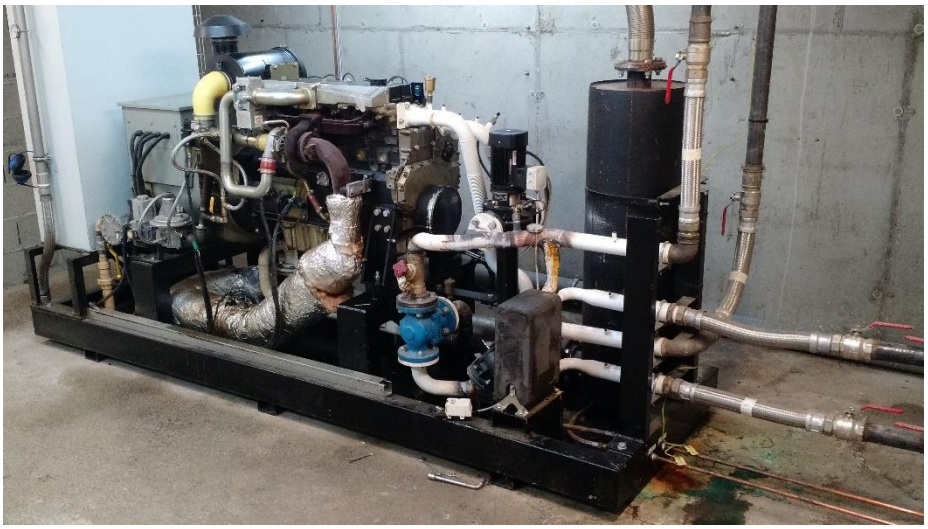

Figure P.2 – CHP engine at GAEC Chateau d'Etrépigny

For the purpose of the field campaign, a by-pass flow was set: the biogas flow needed for the experiments was diverted from the main biogas pipe to be upgraded in the pilot process. Both the biomethane and the offgas flows were then reinjected in the water trap, 20 meters ahead of the by-pass uptake. During the 2-week field campaign, the biogas methane content was stable ($y_{CH_4}^{in} = 56.3 - 59.0\ \%$). An air injection into the digester maintains the H_2S content low ($< 200\ ppmv$) by sulfur oxidation. Though, this air injection results in the presence of nitrogen and oxygen in the biogas flow ($y_{air}^{in} = y_{O_2}^{in} + y_{N_2}^{in} = 1.7 - 2\ \%$). This air injection was stopped during 3 days for the experimental campaign purpose.

Appendix Q Extended abstract in French / Résumé long en français

Q.1 Introduction

L'entrée du monde dans l'ère industrielle s'est enjointe d'une consommation mondiale croissante d'énergie depuis le 19ème siècle. Les ressources fossiles telles que le pétrole, le charbon ou le gaz sont les sources d'énergie les plus utilisées aujourd'hui pour des raisons de prix et d'accessibilité [2]. Leur utilisation est largement responsable du changement climatique (84 % des émissions de CO_2 en 2016 sont liés à la combustion des énergies fossiles [243]), qui fait émerger des effets dévastateurs de long-terme sur les sociétés humaines (sècheresses, famines, augmentation du niveau de la mer, nouvelles maladies, modifications des écosystèmes marins et terrestres…) [1]. La société est donc contrainte de passer d'une consommation d'énergie émettrice de gaz à effet de serre et dont les stocks sont limités, à un système de production renouvelable et neutre en carbone.

Pour relever ce défi, la biomasse offre une production énergétique de base contrairement aux énergies renouvelables intermittentes telles que le solaire et l'éolien. La production d'énergie mondiale correspondante en 2030 est estimée entre $2.32 \times 10^3\ Mtep$ et $3.51 \times 10^3\ Mtep$ par l'agence internationale des énergies renouvelables (IRENA) [5]. En particulier, les biocarburants (gaz ou liquide) offrent des solutions pour la décarbonisation du secteur des transports.

La méthanisation permet de dégrader la matière organique sous forme de méthane comme vecteur de stockage d'énergie. Le biogaz, mélange de CH_4 et de CO_2, peut être purifié en biométhane en séparant ces composés. Ce biométhane constitue une alternative renouvelable au gaz naturel fossile.

L'objectif de ce projet de recherche est de concevoir un procédé d'épuration du biogaz adapté au contexte agricole sur la base de deux constats. D'une part, le gisement organique est dispersé sur le territoire et repose sur des fermes agricoles petites et moyennes (< 200 UGB[40]) [9]. D'autre part, le coût d'investissement spécifique augmente lorsque le débit nominal de biogaz diminue [10]. Pour répondre aux besoins du marché actuel, les développements technologiques ont été guidés par 4 choix :

- le procédé utilisera un principe d'absorption simple et robuste tel que le lavage à l'eau ;

[40] Unité Gros Bétail

- le contacteur à membranes, dérivé du poumon artificiel, sera l'équipement de contact gaz-liquide. Il offre à la fois un coût d'investissement spécifique constant et une aire interfaciale supérieure aux équipements conventionnels (Figure Q.1);
- sur la base des compétences du laboratoire, le périmètre d'investigation de la thèse s'est limité aux conditions opératoires, à la nature du solvant et à l'arrangement des modules ;
- les contacteurs utilisés font partie d'une même gamme industrielle pour faciliter l'industrialisation du procédé.

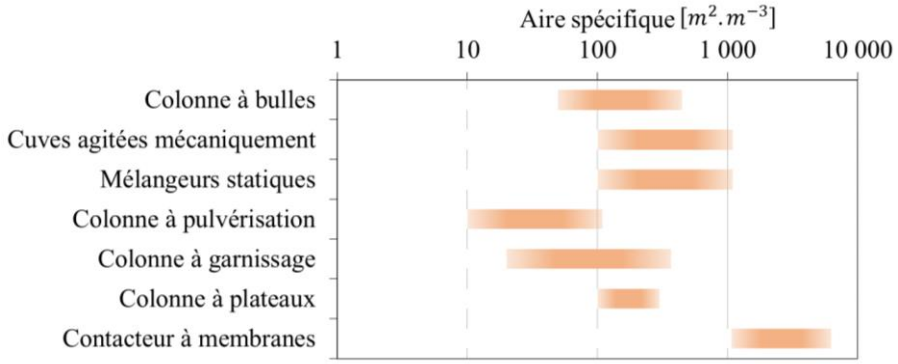

Figure Q.1 – Aire spécifique des équipements de contact gaz-liquide (adapté de [11–13])

Les développements de cette thèse sont présentés en 5 chapitres. Dans un premier temps, un état de l'art est réalisé, relatif aux différents sujets abordés (production d'énergie par méthanisation, revue technico-économique de l'épuration du biogaz, solvants pertinents pour la séparation CH_4/CO_2, méthodologies de changement d'échelle). Le Chapitre 2 présente les dispositifs expérimentaux et méthodes utilisés pour caractériser les performances du procédé d'épuration de biogaz. Les principaux résultats expérimentaux relatifs au développement du procédé sont ensuite exposés dans le Chapitre 3 : étude de l'influence des paramètres opératoires, puis démarche d'optimisation par étapes ont découché sur la production de biométhane ($y_{CH_4}^{out} > 97$ %) avec un taux de récupération satisfaisant ($R_{CH_4} >$ 97 %). Le Chapitre 4 présente le développement d'un modèle de transfert de matière original dans l'objectif de changement d'échelle du procédé. Enfin, le Chapitre 5 met en œuvre et compare le dimensionnement procédé obtenu par 2 méthodologies de changement d'échelle (analyse dimensionnelle et utilisation du modèle de transfert) pour trois débits de biogaz différents (100, 250 et 500 $Nm^3_{biogaz}.h^{-1}$).

Q.2 Etat de l'art

La revue technico-économique des procédés d'épuration du biogaz est synthétisée dans le Tableau Q.1. Le lavage à l'eau est un procédé très établi en Europe (environ 35 % des unités), mais les nouvelles installations tendent majoritairement vers la perméation gazeuse [244]. La comparaison des coûts spécifiques d'investissement indique que les différentes technologies sont sensiblement équivalentes (Figure Q.2) : le choix dépendra du cahier des charges et des spécificités de chaque installation. Néanmoins, l'investissement spécifique double lorsque le débit nominal passe de 500 à 100 $Nm^3_{biogaz}.h^{-1}$. Parmi les procédés émergents, l'utilisation des contacteurs à membranes pour les procédés d'absorption offre différents avantages grâce au matériau membranaire microporeux et

	Lavage à l'eau	*Lavage aux amines*	*PSA*	*Perméation gazeuse*	*Cryogénie*
Avantages	Robustesse Facile à piloter Tolérant aux impuretés	Compacité Forte sélectivité	Compacité	Compacité Modularité Bonne fiabilité Facilité de maintenance	Production de bio-GNL et de bio-CO_2 Forte flexibilité
Inconvénients	Réduction de la taille de l'installation limitée (hausse du coût d'investissement spécifique)	Nécessite des étapes de prétraitement (H_2S, COV) Consommation d'agents chimiques Forte demande en chaleur pour la régénération	Nécessite des étapes de prétraitement (H_2S, siloxanes, eau)	Nécessite des étapes de prétraitement drastiques Expérience opérationnelle limitée	Forte demande en énergie Haut coût capitalistique
Points de vigilance opérationnels	Bouchons dus à la croissance de biofilms Formation de mousses	Dégradation des amines par O_2 et H_2S	Etanchéité des électrovannes		Formation de glace carbonique
Pertes méthane [%]	1	0.1	2	0.5	
Pureté méthane [%]	98	>99	98	>97	>99.4
Consommation d'eau [$L.Nm^{-3}$ biogas]	0.04 - 0.4	0.03	0	0	0
Consommation électrique [$kWh.Nm^{-3}$]	0.23 - 0.3	0.12 - 0.14 + 0.55 $kWh_{th}.Nm^{-3}$	0.2 - 0.3[2]	0.2 - 0.3	0.60
Consommables chimiques	Agent anti-mousse	Charbon actif Agent anti-mousse	Charbon actif	Charbon actif	Charbon actif

Tableau Q.1 – Comparaison technique des procédés disponibles pour l'épuration du biogaz(adapté de [10, 26, 61, 82])

hydrophobe : flexibilité opérationnelle, aire interfaciale fixe, modularité et compacité [90, 91]. Néanmoins, aucune mise en œuvre n'a permis de produire un biométhane de haute qualité ($y_{CH_4}^{out} >$ 97 %) avec un taux de récupération satisfaisant ($R_{CH_4} > 97$ %).

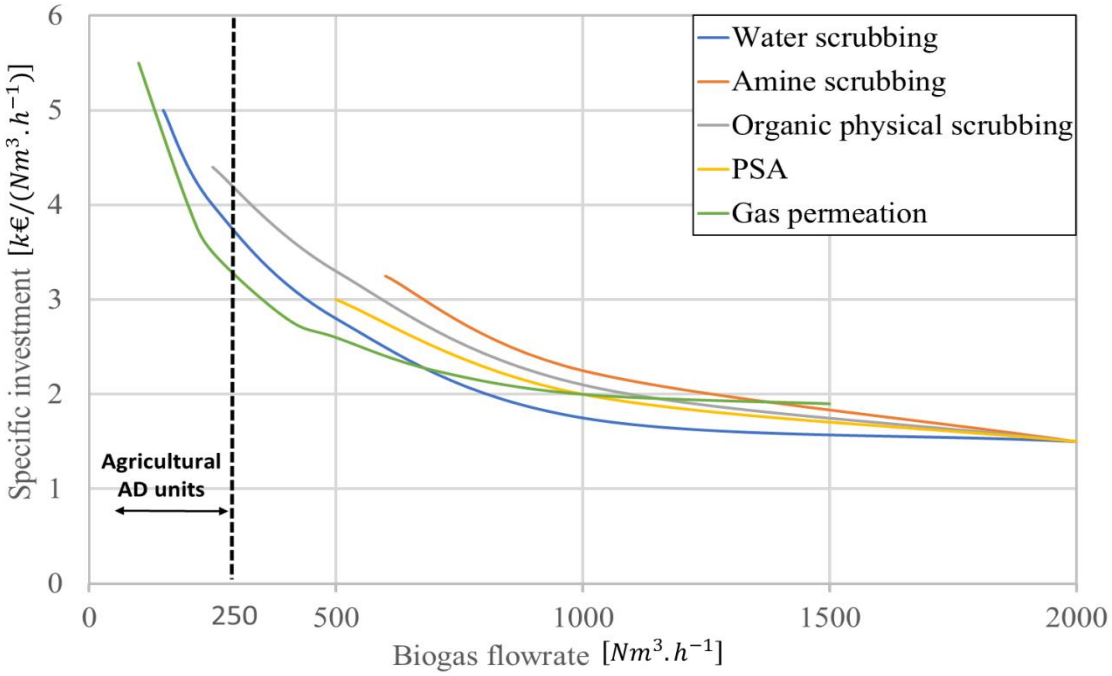

Figure Q.2 – Investissement spécifique d'une unité d'épuration de biogaz en fonction du débit nominal [10]

Des solvants d'absorption physique et chimique sont comparés selon leur pertinence pour la séparation CH_4/CO_2 (Tableau Q.2). Parmi les absorbants physique, l'eau et les solutions de sels sont sélectionnés pour leur robustesse (non-sensible aux polluants, peu favorable à l'humidification de la membrane) et leurs faibles coûts. Parmi les solvants chimiques qui offrent un potentiel d'intensification (capacité et vitesse d'absorption), les sels d'acides aminés sont choisis pour leur faible volatilité et leur résistance à l'oxydation par rapport aux amines.

	Eau	Solution de sels	Solvants organiques	Liquides ioniques	MEA	Sels acides aminés	K_2CO_3
Avantages	Sans agent chimique Tolérant aux impuretés	Sélectivité CO_2/CH_4 améliorée Tolérant aux impuretés	Forte solubilité en CO_2	Forte solubilité en CO_2	Très réactif Forte solubilité en CO_2	Très réactif Faible volatilité Résistant à la dégradation oxydative Forte solubilité en CO_2	Forte solubilité en CO_2 Dégazage peut être réalisé par changement de pression
Inconvénients	Faible solubilité en CO_2	Faible solubilité en CO_2	Faible tension de surface Viscosité du solvant plus élevée Empoisonnement solvant par H_2S	Coût actuel élevé Forte viscosité Faible tension de surface	Température élevée de désorption ($T > 120\ °C$) Empoisonnement solvant par H_2S Faible tension de surface Viscosité modérée	Prix élevé Faible tension de surface Viscosité modérée Empoisonnement solvant par H_2S	Cinétique lente
$J_{CO_2}^{abs}$ $[10^{-3}\ mol.m^{-2}.s^{-1}]$	0.08 – 0.16	0.08-0.15		NS	1.50 – 4.67	0.4 – 5.5	0.5
Coût du solvant $[\$.kg^{-1}]$	-	KCl : 0.2	MeOH : 0.7 NMP : 4 DMPEG : 2.5	1 000 (échelle labo) 40 (grande échelle)	1.5-2	> MEA	2.4

Tableau Q.2 – Applicabilité des solvants à la séparation CH_4/CO_2 utilisant des contacteurs à membranes [10, 71, 97, 150, 158, 172, 177]

Le dimensionnement des procédés d'absorption est utile dans deux phases distinctes. D'une part, la détermination théorique du ratio des débits Q_g/Q_l en fonction des conditions du procédé permet d'identifier la zone pertinente de travail pour les essais pilote. D'autre part, deux méthodologies sont identifiées pour le dimensionnement industriel : l'analyse dimensionnelle semi-empirique et une méthode numérique prédictive. Dans l'optique de construire un modèle de transfert de matière robuste valable aussi bien pour le module pilote que pour le module industriel, il est essentiel de modéliser les échanges dans le contacteur à l'échelle locale. Dans cette perspective, les stratégies de modélisation sont synthétisées dans le Tableau Q.3. Le phénomène d'humidification de la membrane est particulièrement clé dans ces modèles. Il induit une baisse du flux de transfert dans la membrane dû à la présence d'eau dans les plus gros pores de la membrane.

Stratégie de modélisation	Hypothèse sur le régime d'écoulement		Avantages	Commentaires
	Phase gazeuse	*Phase liquide*		
Résistance en série (1D)	Piston	Piston	Approche classique	Repose sur une bonne prédiction des coefficients de transfert de matière
Modèle 1D-2D	Piston	Convection axiale et diffusion radiale	Compromis en termes de complexité	Suppose une configuration à courants croisés
Convection diffusion (2D)	Convection axiale et diffusion radiale	Convection axiale et diffusion radiale	L'influence du solvant et de l'hydrodynamique peut être analysée indépendamment	Suppose une configuration à courants croisés

Tableau Q.3 – Synthèse des différentes stratégies de modélisation disponibles dans la littérature (adapté de [91, 185])

Cet état de l'art couvre les facettes relatives au développement expérimental d'un procédé pilote innovant d'épuration du biogaz en biométhane, ainsi qu'à sa transposition à l'échelle industrielle. Il souligne les avantages de l'épuration du biogaz par absorption dans des contacteurs à membranes. Néanmoins, aucune mise en œuvre n'a été identifiée à ce jour permettant de répondre aux exigences du marché. Cette thèse s'attache donc à expérimenter un tel procédé pilote, et à définir la méthodologie adéquate pour concevoir l'unité industrielle.

Q.3 Matériel et méthodes

Pour tester les performances d'un procédé d'absorption par contacteur à membranes, un pilote expérimental a été construit. Le module pilote a été choisi dans une gamme industrielle pour réaliser la preuve de concept à une taille significative et pour faciliter la mise à l'échelle.

La caractérisation des deux types de membrane en fibres creuses choisies (porosimétrie Hg, imagerie MEB-FEG) a questionné les données constructeurs (pour la membrane X-50, porosité de 29 % contre 40-45 % pour le constructeur).

Le procédé pilote (Figure Q.3) permet de réaliser un mélange synthétique de biogaz ($150 - 880\ NL_{biogaz}.h^{-1}$), et d'épurer ce flux par un liquide d'absorption circulant en boucle ouverte ou en boucle fermée (avec une étape de dégazage). Des débitmètres massiques thermiques et une micro-chromatographie en phase gazeuse mesurent les débits et compositions des entrées/sorties gaz.

Trois indicateurs principaux caractérisent les performances du procédé d'épuration : la qualité du biométhane produit ($y_{CH_4}^{out}$), le taux de récupération du méthane (R_{CH_4}) et la consummation énergétique du procédé ($W_{process}$, généralement exprimée en $kWh.Nm_{biogaz}^{-3}$). Dans le cas du lavage à l'eau conventionnel, les coûts opérationnels sont essentiellement dus à la consommation énergétique. De plus

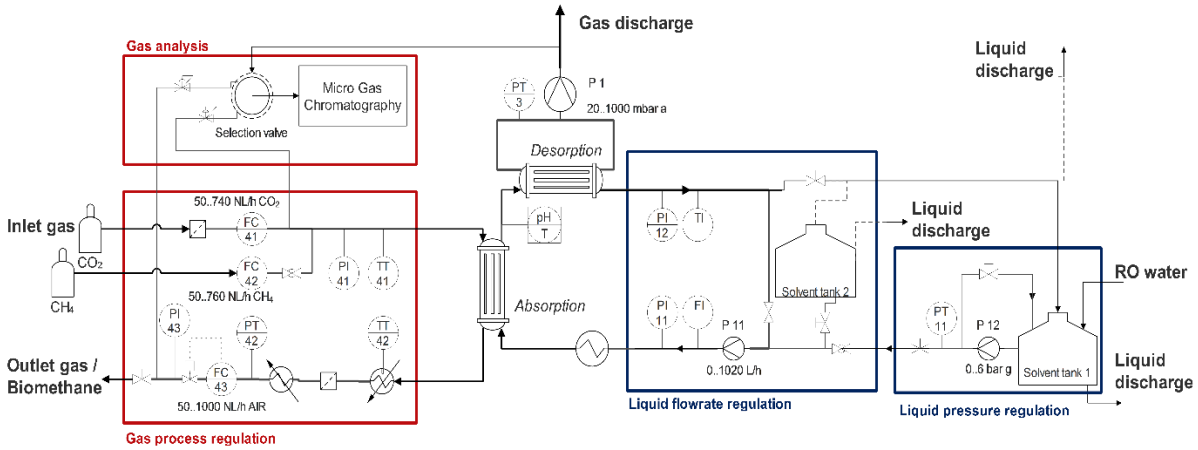

Figure Q.3 – Diagramme procédé pour l'architecture de référence 1:1

le coefficient global de transfert de matière K_L permet de caractériser l'efficacité du transfert en première approximation. Ces indicateurs sont calculés sur la base des mesures expérimentales.

En outre, deux dispositifs spécifiques ont été développés. L'intégration d'un module membranaire annexe dans le circuit liquide a permis d'évaluer la quantité de gaz dissous en exploitant l'équilibre gaz-liquide. Le second dispositif est indépendant et permet de caractériser l'équilibre gaz-liquide des solvants testés dans le pilote principal.

Le pilote expérimental développé permet de mettre en œuvre un plan d'études pour comprendre les paramètres opératoires influant sur les performances du procédé, puis de construire une démarche d'optimisation grâce à son caractère modulable.

Q.4 Développement d'un procédé pilote d'épuration du biogaz

Une étape préliminaire a validé que le contacteur à membranes est capable de produire un biométhane de qualité réseau (> 97 %) avec un solvant circulant en boucle ouverte. Ensuite, une étude paramétrique a mis en évidence que, dans une architecture de référence comprenant une étape d'absorption et une étape de désorption, le ratio des débits Q_g/Q_l, la pression du gaz à l'absorption P_g et la qualité du gaz d'entrée $y_{CH_4}^{in}$ sont les paramètres principaux affectant la qualité du gaz produit $y_{CH_4}^{out}$. La comparaison des résultats expérimentaux avec des échangeurs idéaux (Figure Q.4) montre que le pilote expérimental est éloigné du régime idéal. Deux hypothèses sont alors testées. La comparaison expérimentale des performances en boucle ouverte et en boucle fermée montre une baisse de la qualité du biométhane allant jusqu'à 5 points, qui souligne une désorption non-totale du liquide en boucle fermée. Par ailleurs, l'augmentation de la surface d'échange permet de tendre vers un échangeur idéal. Néanmoins, il est mis en évidence que 7 modules en série seraient nécessaires pour s'approcher du régime idéal.

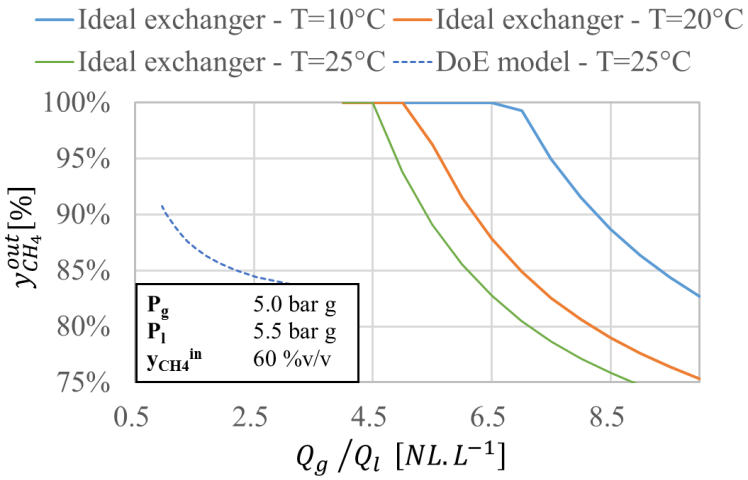

Figure Q.4 – Influence du ratio Q_g/Q_l sur la qualité du biométhane : comparaison du modèle quadratique issu du plan d'expérience avec les performances d'un échange idéal

Le modèle du plan d'expérience est appliqué pour $Q_g = 205\ NL.h^{-1}$

L'influence du phénomène d'humidification sur le coefficient de transfert global K_L est mesurée sous différentes conditions de pression transmembranaires. Dans des conditions fixes, la dynamique du flux d'absorption distingue deux régimes permanents (Figure Q.5) ; le régime humidifié s'établissant au bout de plusieurs heures. Le coefficient de transfert global diminue alors d'un facteur 20-30 % pour s'établir dans la gamme $5.0 - 6.7 \times 10^{-5}\ m.s^{-1}$. Néanmoins, dans la gamme de pression transmembranaire étudiée (0.5 ou 2.5 bar), ce paramètre affecte peu le flux d'absorption en CO_2 (< 5 %) quel que soit le régime.

Ensuite, l'absorption du CO_2 en mélange avec un autre gaz peu soluble (CH_4 ou N_2) montre que le coefficient de transfert est divisé significativement par un facteur 2 à 3. Le phénomène observé est dépendant de la composition du gaz, mais semble peu affecté par la nature du gaz complémentaire peu soluble.

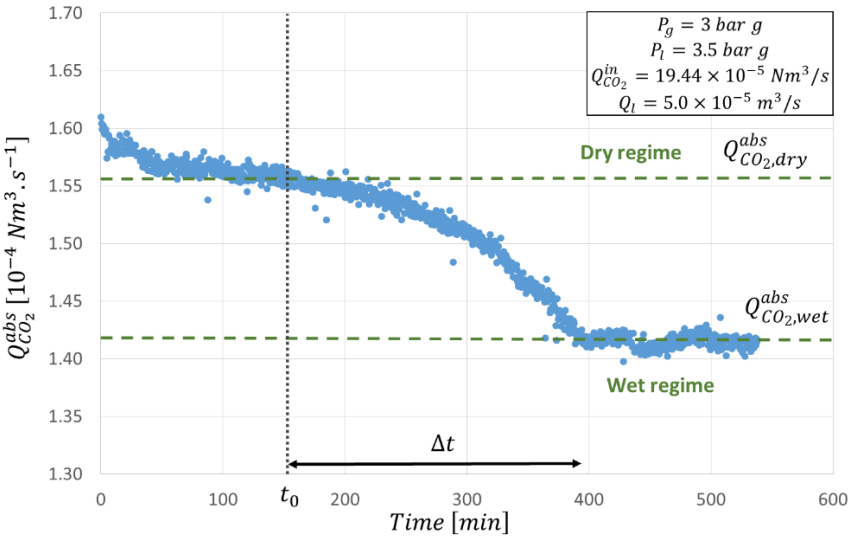

Figure Q.5 – Evolution du débit de CO_2 absorbé en fonction du temps

Configuration en boucle ouverte

Avant d'entreprendre la démarche d'optimisation, une campagne d'essais sur site agricole a été conduite pour valider le bon comportement du procédé avec du biogaz réel. Dans des conditions intensifiées, les performances obtenues sont comparables (Tableau Q.4). Les 2 semaines de campagne n'ont pas relevé de dégradation significative des performances. La consommation énergétique de ce premier point d'optimisation est compris entre 0.247 et 0.262 $kWh.Nm^{-3}_{biogaz}$.

Biogaz	Q_l $[L.h^{-1}]$	Q_g/Q_l $[NL.L^{-1}]$	P_g $[bar\ g]$	T_l $[°C]$	$y^{in}_{CH_4}$ $[\%vol.]$	y^{in}_{air} $[\%vol.]$	K_L $[10^{-5}m.s^{-1}]$	$y^{out}_{CH_4}$ $[\%vol.]$	R_{CH_4} [%]
Synth.	120	1.30	5.0	27.0	59.5	0.0	2.62	97.6	77.6
	90	1.69	5.0	26.7	59.7	0.0	2.85	97.2	83.7
Brut	210	1.09	4.5	16.3	59.0	1.8	3.07	94.3	83.9
	210	1.09	4.5	16.2	58.0	0.8	2.92	96.2	82.8

Tableau Q.4 – Comparaison des performances expérimentales dans l'architecture de référence 1:1 : biogaz synthétique et biogaz brut

Des améliorations sur l'architecture du procédé (conditionneur d'eau, mélangeur statique, boucle de recyclage méthane) et le solvant (solutions de sels minéraux ou d'acides aminés) sont successivement testées. Parmi les avancées pertinentes, l'intégration d'un contacteur intermédiaire (Figure Q.6) a permis de recycler une partie d'une méthane dissous vers la tête du procédé pour augmenter son taux de récupération de 83 à 93.5 %, sans affecter pour autant la qualité du biométhane produit.

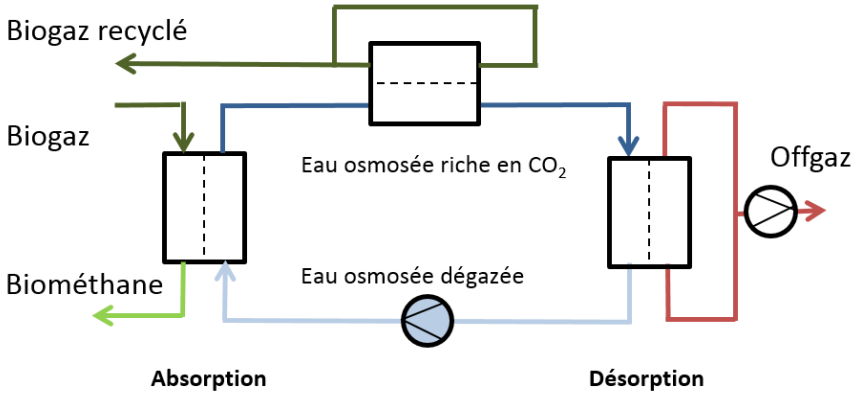

Figure Q.6 – Schéma simplifié de la configuration en boucle fermée avec recyclage de méthane 1:1:1

Par ailleurs, l'usage d'une solution de KCl, combinant une sélectivité π_{CO_2/CH_4} supérieure à l'eau et une capacité d'absorption du méthane réduite, a également permis d'augmenter la qualité du biométhane produit de 4 points par rapport à de l'eau osmosée.

Enfin, ces deux étapes ont été combinées. L'augmentation de température permet alors d'augmenter le taux de récupération méthane mais diminue la qualité du biométhane (Figure Q.7). Un optimum est obtenu à 20°C pour la production d'un biométhane de qualité réseau (97.5 %) avec un taux de récupération satisfaisant ($R_{CH_4} = 98.7$ %). Le flux de CO_2 absorbé est de $J_{CO_2} = 42\ NL_{CO_2}.m^{-2}.h^{-1}$ avec un coefficient de transfert global $K_L = 2.81 \times 10^{-5}\ m.s^{-1}$. La consommation énergétique est

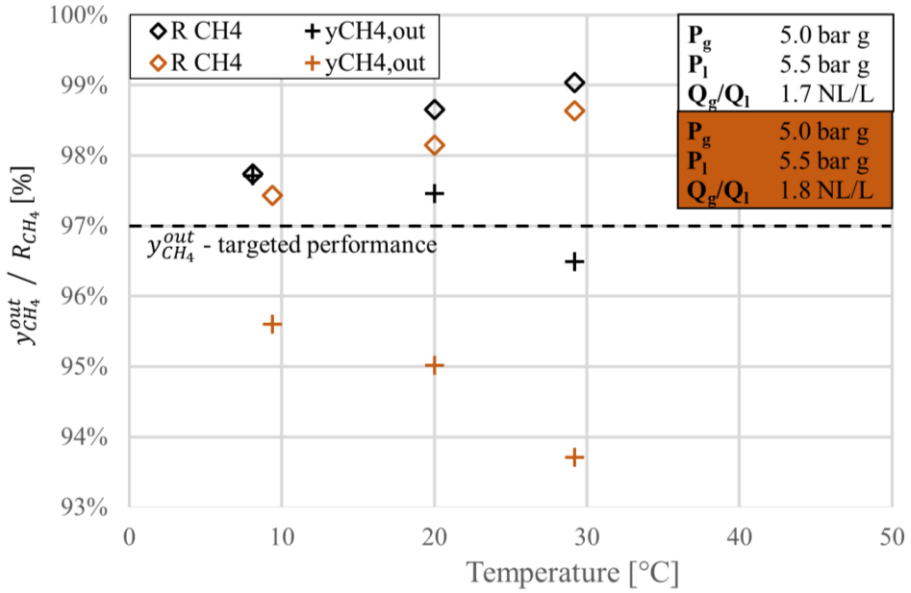

Figure Q.7 – Combinaison de la boucle de recyclage méthane et de la solution de KCl : influence de la température sur les performances procédé

estimée à $0.225\ kWh.Nm_{biogaz}^{-3}$. En outre, le procédé offre un facteur 10 d'intensification comparé aux tours de lavage ($K_La = 0.11\ s^{-1}$ contre $0.009 - 0.011\ s^{-1}$). Un brevet a été déposé pour protéger l'usage de solutions de sels en combinaison avec des contacteurs à membranes.

La démarche expérimentale a permis d'identifier les paramètres clés du procédé (Q_g/Q_l, P_g et $y_{CH_4}^{in}$), de valider les performances en conditions réelles, et de conduire une stratégie d'optimisation ayant menée à une preuve de concept.

Q.5 Modélisation des transferts gaz-liquide à l'échelle du contacteur

Pour construire une méthodologie de changement d'échelle, un modèle de transfert gaz-liquide devait être construit pour simuler les régimes permanents secs et humidifiés. Pour décrire la géométrie interne spécifique de la gamme de contacteurs (déflecteur interne dans la calandre) et modéliser les transferts à l'échelle locale (dans le but de transposer le modèle à un module industriel), un modèle original a été développé. Il repose sur l'assimilation du faisceau de fibres à un milieu poreux pour décrire l'hydrodynamique du liquide dans la calandre. La résistance au transfert est décrite par un modèle des résistances en série à l'échelle locale, agrégeant les résistances de la phase gazeuse, de la membrane et de la phase liquide.

Sur la base des essais expérimentaux d'absorption du CO_2 pur, les paramètres de la relation de Chilton-Colburn, permettant d'évaluer la résistance au transfert en phase liquide, sont déterminés. En régime sec, le modèle permet une bonne prédiction ($\varepsilon_{rel,J_{CO_2}} = -10/+17\ \%$) des débits de CO_2 absorbés (Figure Q.8 – gauche). En ajoutant un bloc provenant de la littérature pour décrire l'humidification de la membrane, le modèle conduit à sous-estimer le débit d'absorption pour les fortes

pressions transmembranaires (Figure Q.8 – droite). Une description du phénomène d'humidification mettant en parallèle plutôt qu'en série les résistances internes à la membrane conduit à une surestimation pour la même catégorie de points. Décrire la porosité par un modèle de pores cylindriques non-interconnectés pourrait être limitant pour simuler tous les ressorts de l'humidification de la membrane.

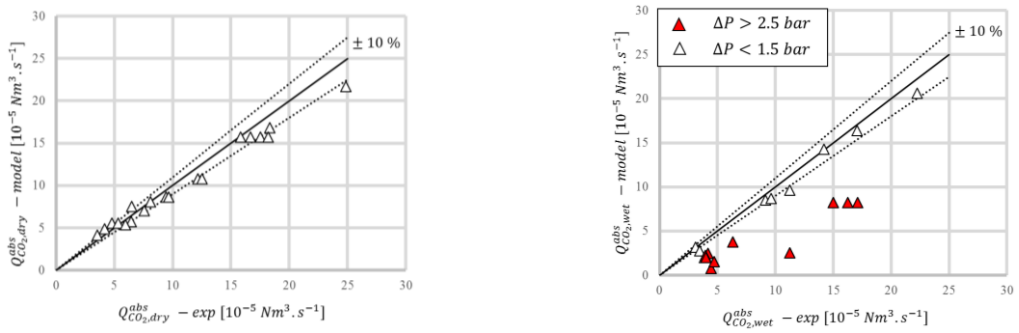

Figure Q.8 – Comparaison des débits d'absorption CO_2 numériques et expérimentaux

Gauche : membrane sèche – Droite : membrane humidifiée

Le modèle a été adapté pour décrire l'absorption d'un mélange binaire (ici, le biogaz). La composition du gaz évolue au sein du contacteur (Figure Q.9). La confrontation des résultats expérimentaux et numériques a conduit à une forte surestimation initiale du flux de CO_2 absorbé : cela met en évidence l'impact de la présence de méthane sur le transfert de CO_2. Pour prendre en compte cette résistance additionnelle située dans la membrane ou dans la phase gazeuse, une correction empirique est proposée sur la base des lois de diffusion. Le calage du paramètre permet de capturer les tendances expérimentales et d'aboutir à une description raisonnable ($\varepsilon_{rel,J_{CO_2}} = -40/+22$ %) dans une large gamme de conditions expérimentales (Figure Q.10).

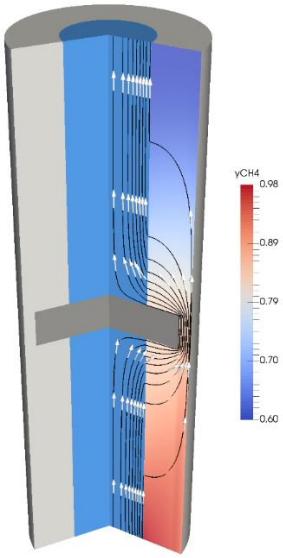

Figure Q.9 – Distribution de l'écoulement liquide et variation de composition gaz dans le modèle original 2D

Le modèle original de transfert de matière gaz-liquide a été développé dans une perspective de changement d'échelle. Il permet notamment d'intégrer la géométrie interne et les conditions hydrodynamiques locales. La confrontation avec les résultats expérimentaux démontre un bon accord pour l'absorption du CO_2 en gaz pur dans le cas d'une membrane sèche. Il questionne également le

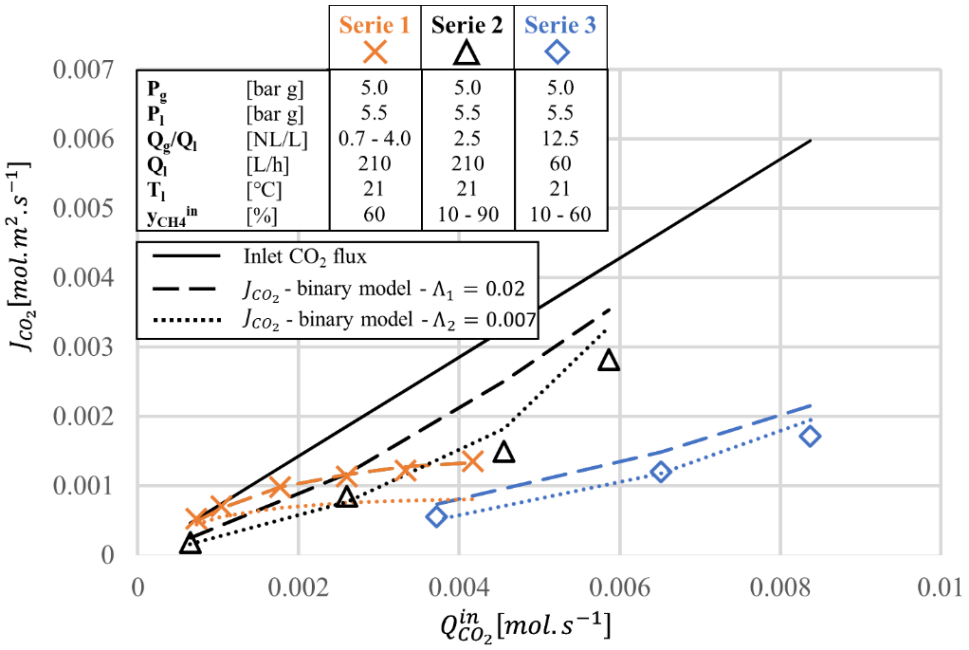

Figure Q.10 – Comparaison des flux expérimentaux de CO_2 absorbés à partir d'un biogaz avec les résultats numériques issus du modèle corrigé
Configuration en boucle ouverte

modèle d'humidification de la membrane, et son comportement face à une modification de la pression transmembranaire. Enfin, l'utilisation d'un gaz binaire démontre l'influence de la présence de méthane sur l'efficacité du transfert en CO_2. Les mécanismes sous-jacents ont été intégrés au modèle par une correction empirique pour la bonne prédiction des performances du procédé.

Q.6 Conception d'une unité industrielle d'épuration du biogaz

Pour valider la preuve de concept expérimentale par une unité de démonstration, deux méthodologies de changement d'échelle ont été mises en œuvres pour dimensionner le procédé d'épuration de biogaz pour 3 débits nominaux différents (100, 250 et 500 $Nm^3_{biogaz}.h^{-1}$). L'objectif assigné est de dimensionner l'unité pour fonctionner dans les performances du pilote expérimental.

La méthodologie classique d'analyse dimensionnelle permet de dimensionner la surface de membrane nécessaire à l'absorption du flux de CO_2. Une relation entre les nombres adimensionnels caractéristiques du transfert (Eq. Q.1) est identifiée sur la base des essais expérimentaux, valide à la fois pour l'utilisation de l'eau et d'une solution de KCl comme solvants.

$$NTU = 8.3\ {A_{CO_2}}^{-1.0} \qquad \text{Eq. Q.1}$$

Par ailleurs, l'adaptation du modèle numérique du module pilote au module industriel permet de simuler les performances du procédé. Une routine met en série des modules membranaires dans l'étape d'absorption. Le modèle ayant été validé pour l'utilisation de l'eau, le dimensionnement est valide pour les résultats obtenus avec ce même solvant.

Le tableau Q.5 synthétise les résultats de dimensionnement obtenus par les deux méthodes pour l'utilisation d'eau. Le dimensionnement par analyse dimensionnelle conduit à une surface d'échange réduite par rapport à l'utilisation du modèle numérique de transfert (-25 % / -40 %).

Cas considéré	**Débit réduit**		**Débit moyen**		**Débit fort**	
$\boldsymbol{Q_{g,process}\ [Nm^3_{biogaz}.h^{-1}]}$	100		250		500	
Nombre de lignes procédé	1	1	2	2	4	4
$\boldsymbol{Q_{g,line}\ [Nm^3_{biogas}.h^{-1}]}$	100	100	125	125	125	125
$\boldsymbol{N_{module,line}}$ [**14"x40"**]	3	4	3	5	3	5

Tableau Q.5 – Arrangement et nombre de modules selon chacune des méthodologies - cas de l'eau
Gauche : analyse dimensionnelle – Droite : modélisation numérique

Seule l'analyse dimensionnelle est appliquée pour les essais pilotes les plus performants avec une solution de KCl : 3, 8 et 15 modules industriels sont respectivement nécessaires pour l'étape d'absorption pour les cas des petite, moyenne et grande unités.

De nouvelles campagnes expérimentales sont nécessaires pour renforcer la fiabilité des méthodes de dimensionnements. L'analyse dimensionnelle doit être validée par une augmentation de la surface d'échange, tandis que le modèle numérique doit être adapté pour simuler les dégazages intermédiaires et finaux. Ce dernier devra également être validé pour une solution de KCl.

Deux approches de dimensionnement ont été proposées, testées et comparées pour 3 débits de biogaz. L'analyse dimensionnelle, méthode semi-empirique, conduit à un dimensionnement inférieur à celui obtenu par la simulation des transferts gaz-liquide appliquée à un module industriel. Ce travail pose les bases pour la conception d'une unité de démonstration du procédé. Des perspectives sont proposées pour renforcer et valider les deux méthodologies.

Q.7 Conclusion générale

Pour construire une production énergétique durable et décarbonée, la biomasse, et en particulier la méthanisation, ont un rôle essentiel à jouer pour une production de base, complémentaire des autres énergies renouvelables intermittentes. Dans cette optique, l'épuration du biogaz en biométhane offre une solution de valorisation énergétique pertinente (optimisation de l'efficacité énergétique, substitution au gaz naturel fossile, réseau de stockage et de transport existant). Pour accélérer l'exploitation du potentiel européen, cette thèse s'est attachée à développer un procédé d'épuration du biogaz, adapté aux unités de méthanisation agricole, et visant à une réduction des importants coûts d'investissement. En particulier, l'usage de contacteurs membranaires a été évalué en remplacement des tours à garnissage dans le procédé robuste du lavage à l'eau.

L'état de l'art relatif aux différents aspects du projet de recherche a conduit à :

- établir un benchmark techno-économique des procédés disponibles ;
- sélectionner les solvants applicables à l'épuration du biogaz par contacteurs à membranes (eau et solutions de sels pour l'absorption physique, sels d'acides aminés pour l'absorption chimique) ;
- définir la gamme de conditions opératoires du procédé pilote ;
- identifier des stratégies de dimensionnement pour ce procédé ;
- identifier les paramètres-clés du transfert et les limitations associées.

Un pilote expérimentale modulaire ($150 - 880\ NL_{biogaz}.h^{-1}$) a été construit pour évaluer les performances du procédé selon 3 indicateurs principaux : la qualité du biométhane, le taux de récupération de méthane et la consommation énergétique du procédé. En outre, deux dispositifs ont été spécifiquement développés pour mesurer la quantité de gaz dissous d'une part, et caractériser l'équilibre gaz-liquide d'autre part.

Le développement expérimental a tout d'abord identifié les débits Q_g et Q_l, la pression d'absorption P_g et la qualité du biogaz entrant $y_{CH_4}^{in}$ comme les paramètres opératoires clés dans une architecture de référence comportant un module d'absorption et un module de désorption. Le contacteur ne fonctionnant pas comme un échangeur de matière idéal, il a été mis en évidence que la présence d'un gaz peu soluble (comme le méthane) était une limitation plus importante au transfert de CO_2 que l'humidification de la membrane (le coefficient de transfert de matière global K_L est divisé par un facteur 2-3 contre une baisse de 20-30 % dans le cas de l'humidification).

La campagne expérimentale sur site a confirmé la stabilité des performances du procédé avec du biogaz réel. Cela a permis de conduire une stratégie d'optimisation en laboratoire par étapes successives : amélioration de l'architecture du procédé et comparaison de différents solvants. La combinaison des approches a permis d'aboutir à une preuve de concept par la mise en œuvre d'une solution de sels KCl dans une configuration à trois contacteurs membranaires (recyclage partiel du méthane dissous vers la tête du procédé). Les performances sont comparables aux procédés disponibles ($y_{CH_4}^{out} = 97.5\ \%/R_{CH_4} = 98.7\ \%$) avec une consommation énergétique estimée dans la fourchette basse du benchmark ($0.225\ kWh.Nm_{biogaz}^{-3}$). La technologie offre un facteur d'intensification de 10 en comparaison des tours conventionnelles de lavage à l'eau. Un brevet a été déposé pour protéger l'usage de solutions de sels en combinaison avec des contacteurs à membranes.

Un modèle prédictif original a été développé pour fournir un outil de changement d'échelle. L'assimilation du faisceau de fibres à un milieu poreux anisotrope permet d'intégrer la géométrie interne spécifique du module membranaire disposant d'un déflecteur central : cela permet une bonne description de l'hydrodynamique locale et des conditions de transfert. Le modèle simule bien le flux de CO_2 absorbé dans un régime sec pour l'absorption de gaz pur ($\varepsilon_{rel,J_{CO_2}} = -10/+17\ \%$). Néanmoins, la confrontation numérique/expérimentale en régime humidifié pour différentes pressions transmembranaires questionne la description de l'humidification de la membrane. L'adaptation du modèle à l'absorption d'un gaz binaire met en évidence l'impact de la présence de méthane sur

l'efficacité du transfert de CO_2 et nécessite l'ajout d'une résistance additionnelle empirique, inspirée des lois de diffusion ($\varepsilon_{rel,J_{CO_2}} = -40/+22$ %).

Enfin, deux méthodologies sont menées pour concevoir une unité de démonstration dans 3 cas différents (100, 250 et 500 $Nm^3_{biogaz}.h^{-1}$) et poser les bases d'une industrialisation. Dans le cas de l'eau, la comparaison montre un dimensionnement inférieur par analyse dimensionnelle plutôt que par l'adaptation du modèle de transfert à un module industriel (-40 à -25 % selon le débit nominal de biogaz). Seule l'analyse dimensionnelle peut être conduite pour le cas de la solution de KCl : 3, 8 et 15 modules industriels sont respectivement nécessaires pour l'étape d'absorption dans les trois cas considérés.

La conclusion générale de ce travail est le développement d'un procédé innovant d'épuration du biogaz combinant le lavage à l'eau à la mise en œuvre de contacteurs à membranes. La preuve de concept a été faite à l'échelle pilote et un dimensionnement industriel a été proposé pour 3 cas d'études. Les contacteurs à membranes offre un procédé plus compacte, flexible et modulaire que les colonnes à garnissage. La baisse des coûts d'investissement d'un tel procédé reste néanmoins à confirmer au travers d'un projet de démonstration pour répondre à l'ensemble des objectifs fixés.

Q.8 Perspectives

Dans la continuité de la preuve de concept établi et de cette étude, plusieurs pistes apparaissent primordiales :

- malgré la bonne stabilité chimique du polypropylène, la compatibilité du matériau membranaire avec les impuretés du biogaz doit faire l'objet d'une validation spécifique avant toute opération industrielle ;
- la preuve de concept établie en laboratoire doit être validée par une campagne sur site avec une conduite continue du procédé (comportement en conditions réelles, humidification, capacité d'épuration du H_2S) ;
- le modèle de transfert de matière peut être amélioré par la conduite d'essais spécifiques pour comprendre les mécanismes induisant la résistance identifiée dans la membrane et/ou la phase gazeuse dans le cas d'un mélange. Un dispositif spécifique avec une meilleure précision sur la débitmétrie gaz est nécessaire ;
- la validité des deux méthodologies de changement d'échelle devra être testée à une échelle intermédiaire. De manière spécifique, la modélisation des transferts gaz-liquide pourra être étendue aux étapes de dégazage du procédé, et devra être validée pour la mise œuvre d'une solution de KCl.

Enfin, la question des coûts d'investissement et d'opération du procédé est primordiale. Dans cette optique, un projet de démonstration permettra d'affiner l'estimation de ces coûts. Dans le même temps, il confrontera les deux méthodologies de dimensionnement proposées aux performances d'une unité industrielle.

ÉCOLE DOCTORALE
Sciences mécaniques et énergétiques, matériaux et géosciences (SMEMAG)

université PARIS-SACLAY

CentraleSupélec

Titre : Développement d'un procédé innovant d'épuration du biogaz par mise en œuvre de contacteurs à membranes

Mots clés : Epuration de biogaz ; Absorption gaz-liquide ; Contacteurs à membranes ; Transfert de matière

Résumé : L'épuration est une solution attractive pour la valorisation du biogaz. Néanmoins, les coûts associés à ces procédés constituent un frein au développement, en particulier pour l'épuration du biogaz d'origine agricole.

Ces travaux ont évalué le contacteur à membranes, technologie issue du poumon artificiel, pour le développement d'un procédé d'absorption physique, robuste et répondant aux exigences de la filière. Un pilote expérimental modulaire ($150 - 880\ NL_{biogaz}.h^{-1}$) a permis d'investiguer les performances du procédé en termes de rendement méthane R_{CH_4} et de qualité méthane $y_{CH_4}^{out}$.

Le contacteur à membranes permet de produire un biométhane répondant aux spécifications de l'injection réseau. Les paramètres opératoires clés ont été mis en évidence par un plan d'expérience. Parmi les limites connues du procédé, l'effet de l'humidification de la membrane sur le débit d'absorption du CO_2 reste limité (< 10.5%) : une nouvelle description de l'humidification des pores a été proposée. La composition du gaz est plus limitante : le coefficient de transfert du CO_2 est divisé par un facteur 2-3 lorsque celui-ci est présent en mélange plutôt qu'en gaz pur. Plusieurs configurations et solvants ont été testés pour améliorer les performances. L'intégration d'une boucle de recyclage et le remplacement de l'eau par une solution de sels (KCl) ont permis de déployer un procédé breveté atteignant les performances visées ($R_{CH_4} = 98.7\%$, $y_{CH_4}^{out} = 97.5\%$) : le flux membranaire est de $42\ NL_{CO_2}.m^{-2}.h^{-1}$.

En vue d'un dimensionnement industriel, un modèle original de transfert a été développé pour intégrer la géométrie interne spécifique du module membranaire. Optimisé et validé pour l'absorption de CO_2 pur, cet outil numérique a nécessité l'optimisation d'une correction additionnelle inspirée des lois de diffusion pour décrire la limite observée en présence d'un mélange de gaz.

Une mise à l'échelle est proposée pour 3 unités industrielles (100, 250 et $500\ Nm^3_{biogaz}.h^{-1}$) sur la base des équipements disponibles. Les dimensionnements obtenus par analyse dimensionnelle ou par modélisation numérique diffèrent de 25 à 40 % et doivent encore être validés.

Title: Development of an innovative biogas upgrading process by means of membrane contactors

Keywords: Biogas upgrading ; Gas-liquid absorption ; Membrane contactor ; Mass Transfer

Abstract: Upgrading is an attractive pathway for biogas utilization. Yet, the costs associated to these processes are still an obstacle to a widespread development, specifically in the case of farm anaerobic digestion units.

This PhD has assessed membrane contactor, a technology derived from the artificial lung, for the development of a robust gas-liquid physical absorption process meeting the biogas industry expectations. A modular experimental pilot ($150 - 880\ NL_{biogas}.h^{-1}$) was designed to investigate the performances in terms of methane recovery R_{CH_4} and methane quality $y_{CH_4}^{out}$.

The membrane contactor technology turned out to be suitable to produce a gas-grid quality biomethane. Key operating parameters were identified through a Design of Experiments. Among known process limitations, membrane wetting was found to have little influence on CO_2 absorption (< 10.5%): a new pore wetting description was suggested. Gas composition was a stronger limitation: the CO_2 mass transfer coefficient was divided by a factor 2-3 in the presence of a gas mixture instead of as a pure gas. Process configurations and solvents were successively tested to improve the performances. The addition of a methane recycling loop and the replacement of water by a saline solution (KCl) were combined into a patent and reached the targeted performances ($R_{CH_4} = 98.7\%$, $y_{CH_4}^{out} = 97.5\%$): the corresponding absorbed flux is $42\ NL_{CO_2}.m^{-2}.h^{-1}$.

For a process upscaling purpose, an original mass transfer model was developed to describe the specific internal geometry of the membrane module. Firstly optimized and validated for the absorption of pure CO_2, this numerical tool has required an optimized additional correction inspired from diffusion laws to account for the mass transfer limitation observed for a binary gas mixture.

Process designs are suggested for 3 industrial cases (100, 250 and $500\ Nm^3_{biogas}.h^{-1}$) based on an available membrane contactor range. The process sizings resulting from the dimensional analysis methodology or numerical simulation differ from 25 to 40 % and must then be confirmed.

Université Paris-Saclay
Espace Technologique / Immeuble Discovery
Route de l'Orme aux Merisiers RD 128 / 91190 Saint-Aubin, France